Monitoring Charge Carrier Dynamics at Atomic Length Scales by STM-induced Luminescence

PAR

Christoph GROßE

EPFL

ÉCOLE POLYTECHNIQUE
FÉDÉRALE DE LAUSANNE

Suisse
2015

Groß wird nur
wer über sich hinauswächst!

Meinen Eltern Ulrich & Christiane Große
für ihre unentwegte Unterstützung
meinen Weg zu finden.

Acknowledgements

It has been a great privilege for me to work at the Max Planck Institute for Solid State Research in Stuttgart and do my PhD on such an outstanding microscope as the "Photon-STM" in Prof. Klaus Kern's group. Therefore, first and foremost I would like to thank *Prof. Klaus Kern* for giving me the great opportunity to be part of his group. He always expected and encouraged me to develop and verify my own ideas and left it up to my own creativity on how to realize them. This I appreciated really a lot. However, this thesis would not exist without the numerous other people that have been supporting me over the years of this journey. I am deeply grateful to ..

.. the members of my PhD committee: Prof. Richard Berndt, Prof. Jascha Repp, Prof. Anna Fontcuberta i Morral, and Prof. Minh Quang Tran who agreed to evaluate this thesis.

.. my supervisor *Dr. Klaus Kuhnke* for his great technical and scientific expertise and his compelling patience during the occasionally hours-long discussions where I once again tried to hammer the point home. In the end, your arguments almost always convinced me. Although your countless corrections of the first abstract and paper drafts brought me to the verge of despair, your meticulousness has continuously egged me on to improve and specify my ideas and, finally, made this thesis what it is.

.. the many scientific stockholders of this work: *Dr. Sebastian Loth* for realizing the first pulse measurements together with *Dr. Markus Etzkorn* who initiated them – Sebastian, you deeply impressed me with your incredible fascination for science and the way you approach arising questions; *Dr. Rico Gutzler* for the help with the DFT calculations, the virtually daily scientific and non-scientific discussions after lunch, as well as our shared addiction to running; *Dr. Olle Gunnarsson* for programming the initial tight-binding code for the electronic structure of the C_{60} multilayers and the many discussions that arose from the work on and with it. – it was always fascinating to discover another bizarre peculiarity of Fortran; *Dr. Pablo Merino Mateo* for the photon–photon correlation measurements on the C_{60} multilayers – even though you joined us just at the end of my scientific marathon, I will always remember the Frankfurt Marathon we ran together; *Dr. Alexander Kabakchiev* for enhancing the microscope by the optical detection system and thus making it into the versatile machine it is today – your work paved the way for all these beautiful experiments, in particular the studies of the single $Ir(ppy)_3$ molecules; *Dr. Theresa Lutz* for familiarizing me with the microscope and the initial supervision – I mostly followed your advise of always having a bar of (dark) chocolate in my drawers, especially for long night shifts. *Romain Froidevaux* for characterizing the new high-frequency wiring of the microscope after relocating it to the Precision Laboratory as well as programming the software for the new pulse generator; *Dr. Frank Schramm* and *Prof. Mario Ruben* from the Karlsruhe Institute of Technology (KIT) for synthesizing the $Ir(ppy)_3$ molecules; *Dr. Stephan Rauschenbach* and *PD Konstantin Amsharov* for the characterization of evaporated $Ir(ppy)_3$ films by laser desorption ionization mass spectrometry; and *Dr. Uta*

Abstract

The goal of this thesis is the combination of the high spatial resolution of scanning tunneling microscopy (STM) with the high temporal resolution of optical spectroscopy. To this end, the light excited by the highly localized tunnel current in the tunnel junction is exploited as fast readout signal. By this means, technical limitations of the time resolution in STM – caused by the necessary high-gain current amplifier – can be overcome. Two complementary techniques are presented, which allow (a) access to the local photon statistics and (b) following the luminescence response to nanosecond voltage pulses at atomic length scales. The versatility of these methods is demonstrated by using two different model systems: pure C_{60} films ($<$10 molecular layers) on Ag(111) and Au(111) substrates, as well as single $Ir(ppy)_3$ molecules adsorbed on them. These two model systems reveal the possibility to investigate both the local charge carrier dynamics of mesoscopic systems as well as individually and selectively addressable quantum systems. Furthermore, these methods are not limited to pure emission processes such as the recombination of electron hole pairs; rather, it is also possible to study the dynamics of non-emitting processes via the excitation and radiation of surface plasmon polaritons (SPPs) from the tunnel junction.

To achieve high time resolutions in the luminescence response of an investigated system, the voltage pulses arriving at the tunnel junction should exhibit high edge steepnesses. Therefore, a further technique is developed that permits a quantitative mapping of the voltage at the tunnel junction with millivolt and nanosecond accuracy. Knowing the precise shape of the voltage pulses arriving at the tunnel junction offers compensation for ubiquitous pulse distortions arising from reflections and attenuations of the pulses on their way to the tunnel junction, thus enabling pulse rise and falling times of a few nanoseconds.

The detailed investigation of the electronic structure of pure C_{60} films shows that the electronic states of C_{60} multilayers experience a band bending in STM due to the electric field between the STM tip and the metal substrate. Indeed, this effect can also be employed to quantify the absolute film thickness in a specific experiment. As soon as the band bending is sufficiently high to align the lowest unoccupied molecular orbitals with the Fermi energy of the substrate, electrons can be injected into theses states by the substrate. At structural defects in the C_{60} film, these electrons can recombine with holes in the highest occupied molecular orbitals, which are injected by the STM tip. At such defects, local deviations from the highly ordered structure of the C_{60} film result in localized electronic states within the band gap. These states act as traps for the injected electrons and holes and increase their lifetime such that they can recombine with each other. It is shown that the underlying injection dynamics are accessible by the luminescence time response of these defects to nanosecond voltage pulses. Measurements of the second-order intensity correlation function additionally prove that these defects act as single photon sources with exciton lifetimes of $<$0.7 ns. Therefore, this work demonstrates that structural defects alone – in otherwise homogeneous organic films – are sufficient to guarantee an emission of single photons one after the other. Furthermore, this

thesis provides a molecular picture about the role of disorder, the localization of electronic states and the resulting charge carrier dynamics in molecular solids.

To clarify whether thin C_{60} films can be used as electronic decoupling layers – for example, to study the intrinsic properties of single molecules – the electronic structure of individual $Ir(ppy)_3$ molecules adsorbed on C_{60} films is investigated as a function of the C_{60} film thickness. Whereas the adsorption of the single molecules on a C_{60} monolayer leads to a vacuum level alignment, their electronic structure on C_{60} bi- and trilayers suggests a charge transfer to the C_{60} film. Hence, the high electron affinity of C_{60} makes it rather unfavorable as an inert decoupling layer. Nevertheless, single $Ir(ppy)_3$ molecules adsorbed on various C_{60} film thicknesses prove to be an ideal model system to study the influence of molecules on the SPP excitation in tunnel junctions and reveal different methods for controlling their generation. Surprisingly, the level of control systematically increases from one to three C_{60} layers due to the changing electronic structure. In this context, the results presented provide new avenues to control light at its quantum limit by individual quantum systems, which is an important challenge for future quantum interfaces bridging nanoelectronics and nanophotonics.

Key words: C_{60}, $Ir(ppy)_3$, organic semiconductors, plasmonics, second-order intensity correlation, STM-induced luminescence, time-resolved STM

Zusammenfassung

Ziel dieser Arbeit ist es, die atomare Ortsauflösung der Rastertunnelmikroskopie (STM) mit der hohen Zeitauflösung spektroskopischer Methoden zu kombinieren. Die Grundidee besteht dabei darin, das durch den hochlokalisierten Tunnelstrom innerhalb des Tunnelkontakts angeregte Licht als sehr schnell auslesbares Messsignal zu nutzen. Die technisch bedingte geringe Zeitauflösung des Tunnelstroms infolge der notwendigen hohen Stromverstärkung kann somit umgangen werden. Es werden zwei sich ergänzende Methoden präsentiert, die es ermöglichen, auf atomaren Längenskalen (a) die lokale Photonenstatistik und (b) die lokale Lumineszenzantwort auf nanosekundenkurze Spannungspulse zu untersuchen. Die Vielseitigkeit dieser Methoden wird an zwei verschiedenen Modellsystemen demonstriert: reinen C_{60}-Multilagen (<10 molekulare Lagen) auf Ag(111)- und Au(111)-Substraten sowie darauf adsorbierten *fac*-tris(2-phenylpyridine)iridium(III) $(Ir(ppy)_3)$-Einzelmolekülen. Diese beiden Modellsysteme offenbaren, dass sich sowohl die lokalen Ladungsträgerdynamiken mesoskopischer Systeme als auch die einzeln und selektiv adressierbaren Quantensysteme untersuchen lassen. Auch beschränkt sich der Einsatzbereich dieser Methoden keinesfalls nur auf die Dynamiken reiner Emissionsprozesse, etwa die Rekombination von Elektron-Loch-Paaren. Alternativ lassen sich auch die Dynamiken nicht-emittierender Prozesse mittels der in dem Tunnelkontakt angeregten bzw. abgestrahlten Oberflächenplasmonpolaritonen auslesen.

Für eine maximale Zeitauflösung der zeitabhängigen Lumineszenzintensität bzw. der Lumineszenzantwort eines zu untersuchenden Systems ist es wichtig, Spannungspulse mit hohen Flankensteilheiten im Tunnelkontakt zu realisieren. Aus diesem Grund wurde eine weitere Methode entwickelt, mittels derer die an dem Tunnelkontakt ankommenden Spannungspulse mit einer Genauigkeit von wenigen Millivolt und Nanosekunden abgebildet werden können. Die genaue Kenntnis der an dem Tunnelkontakt ankommenden Pulse erlaubt es ihrerseits, allgegenwärtige Verzerrungen der Pulse auf ihrem Weg zu dem Tunnelkontakt, etwa durch Dispersion und Reflexionen in der Zuleitung, zu kompensieren und Pulsflanken von wenigen Nanosekunden zu realisieren.

Die detaillierte Charakterisierung der elektronischen Struktur der reinen C_{60}-Schichten zeigt, dass das zwischen dem Metallsubstrat und der STM-Spitze herrschende elektrische Feld eine Bandverbiegung der C_{60}-Zustände bewirkt. Dieser Effekt kann beispielsweise dazu genutzt werden, die exakte Dicke der C_{60}-Schicht in einem spezifischen Experiment zu bestimmen. Ist die Bandverbiegung groß genug, um die niedrigsten unbesetzten Molekülzustände mit der Fermi-Energie des Substrats auszurichten, ist eine Injektion von Elektronen in diese Zustände möglich. An strukturellen Defekten der C_{60}-Schicht können diese Elektronen mit über die STM-Spitze injizierten Löchern in den höchst besetzten Molekülzuständen rekombinieren. Lokale Abweichungen von der hochgeordneten Struktur der C_{60}-Schicht sorgen hier für die Entstehung lokalisierter elektronischer Zustände innerhalb der Bandlücke. Diese Zustände können als Fallen für injizierte Elektronen und Löcher wirken und deren Lebensdauer so

weit erhöhen, dass eine Rekombination beider möglich wird. Es wird gezeigt, dass die zugrunde liegenden Ladungsträgerdynamiken über die Lumineszenzantwort dieser Defekte auf nanosekundenkurze Spannungspulse zugänglich sind. Messungen der Intensiätskorrelation zweiter Ordnung beweisen zudem, dass diese Defekte als Einzelphotonenquellen mit Exzitonen-Lebensdauern $<0.7\,$ns fungieren. Folglich demonstriert diese Arbeit, dass strukturelle Defekte in ansonsten homogenen organischen Schichten bereits ausreichen, um eine Emission einzelner Photonen zu gewährleisten. Darüber hinaus ermöglicht sie ein umfassendes molekulares Bild über die Rolle lokaler Unordnung, die Lokalisation elektronischer Zustände und die daraus resultierenden Ladungsträgerdynamiken in molekularen Festkörpern.

Um zu klären, inwieweit sich dünne C_{60}-Schichten als elektronische Entkopplungsschichten eignen, etwa zur Erforschung der intrinsischen Eigenschaften einzelner Moleküle, wurde die elektronische Struktur einzelner $Ir(ppy)_3$-Moleküle auf unterschiedlich dicken C_{60}-Schichten untersucht. Während die Adsorption der $Ir(ppy)_3$-Moleküle auf einer C_{60}-Monolage zu einer Vakuumniveauangleichung der elektronischen Zustände führt, deutet ihre elektronische Struktur auf C_{60}-Doppel- und -Dreifachlagen auf einen Ladungstransfer zu der C_{60}-Schicht hin. Als inerte Entkopplungsschicht ist C_{60} aufgrund seiner hohen Elektronenaffinität folglich eher ungeeignet. Trotz allem entpuppen sich die auf unterschiedlich dicken C_{60}-Lagen adsorbierten $Ir(ppy)_3$-Moleküle als ideale Modellsysteme zur Untersuchung des Einflusses von Molekülen auf die Plasmonpolaritonanregung in Tunnelkontakten und offenbaren verschiedene Methoden zu deren Kontrolle. Interessanterweise nimmt der Grad der Kontrolle infolge der sich ändernden elektronischen Struktur systematisch mit der Anzahl der C_{60}-Lagen zu. Die präsentierten Ergebnisses eröffnen damit neue Wege, Licht auf der Quantenebene und mittels einzelner Quantensysteme zu kontrollieren – eine wichtige Voraussetzung hinsichtlich künftiger Quantenschnittstellen zwischen Nanoelektronik und Nanophotonik.

Stichwörter: C_{60}, $Ir(ppy)_3$, organische Halbleiter, Plasmonics, Intensitätskorrelation zweiter Ordnung, STM-induzierte Lumineszenz, zeitaufgelöste Rastertunnelmikroskopie

Contents

Abbreviations and Symbols

2PPE	two-photon photoemission spectroscopy		τ_{tunnel}	time constant related to the measured tunneling current
Δz_{rel}	relative STM tip–sample distance		ψ_{s}	wavefunction of the substrate
ϵ_r	dielectric constant		ψ_{t}	wavefunction of the tip
ρ_{t}	density of states of the tip		AC	alternating current
ρ_{s}	density of states of the sample		APD	avalanche single photon diode
τ	observed time constant		C_{60}	Buckminsterfullerene C_{60}
τ_{e}^1	effective time constant related to the injection of an electron without the presence of a hole		CBP	4,4',bis(N-carbazolyl)biphenyl
			CCD	charged-coupled device
			d_{C60}	thickness of the C_{60} film
τ_{e}^2	effective time constant related to the injection of an electron during the presence of a hole		d_{dec}	thickness of the decoupling layer
			d_{vac}	thickness of the vacuum barrier
$\tau_{\mathrm{e}}^{\mathrm{diff}}$	time constant related to the diffusion of an electron to the surface		$d_{\mathrm{dI/dU}}$	thickness of the vaccum barrier during the acquisition of the $\mathrm{d}I/\mathrm{d}U$ spectrum
$\tau_{\mathrm{e}}^{\mathrm{inj}}$	time constant related to the injection of an electron		DC	direct current
			DFT	density functional theory
$\tau_{\mathrm{e}}^{\mathrm{loss}}$	time constant related to the loss of electrons by tunneling to the STM tip		$\mathrm{d}I/\mathrm{d}U$	differential conductance
			DOS	density of states
τ_{ex}	lifetime of an electron–hole pair		E	electric field strength
			E_{C60}	electric field strength within the C_{60} film
$\tau_{\mathrm{ex}}^{\mathrm{rad}}$	time constant related to the radiative decay of an electron–hole pair		E_{F}	Fermi energy
			$E_{\mathrm{F,s}}$	Fermi energy of the substrate
$\tau_{\mathrm{ex}}^{\mathrm{non\text{-}rad}}$	time constant related to the non-radiative decay of an electron–hole pair		$E_{\mathrm{F,t}}$	Fermi energy of the tip
			E_{vac}	electric field strength in the vacuum barrier
τ_{h}^1	effective time constant related to the injection of a hole without the presence of an electron		EELS	electron energy loss spectroscopy
			fcc	face-centered cubic
τ_{h}^2	effective time constant related to the injection of a hole during the presence of an electron		FWHM	full width at half maximum
			$g^2(\Delta t)$	second-order intensity correlation function
			HOMO	highest occupied molecular orbital
$\tau_{\mathrm{h}}^{\mathrm{inj}}$	time constant related to the injection of a hole		HREELS	high resolution electron energy loss spectroscopy
			I_{SD}	source–drain current

I_{set}	set point current of STM images and $\mathrm{d}I/\mathrm{d}U$ spectra
IPES	inverse photoelectron spectroscopy
Ir(ppy)$_3$	*fac*-tris(2-phenylpyridine)iridium(III)
k_{ex}	decay rate of an electron–hole pair
$k_{\mathrm{ex}}^{\mathrm{rad}}$	radiative decay rate of an electron–hole pair
$k_{\mathrm{ex}}^{\mathrm{non\text{-}rad}}$	non-radiative decay rate of an electron–hole pair
KPFM	Kelvin probe force microscopy
LCD	liquid-crystal display
LDOS	local density of states
LEED	low energy electron diffraction
LUMO	lowest unoccupied molecular orbital
ML	molecular layer
M_{st}	tunneling matrix element
n	number of C_{C60} layers
n_{phot}	photon emission rate
$\overline{n}_{\mathrm{phot}}$	mean photon emission rate
$N(\Delta t)$	measured distribution of photon arrival time
NEXAFS	near edge X-ray absorption fine structure
NIR	negative ion resonance
OLED	organic light-emitting diode
P	luminescence intensity
$P(t)$	time-dependent luminescence intensity
PIR	positive ion resonance
PMMA	poly(methyl methacrylate)
ppy	2-(pyridin-2-yl)phenyl
S^{e}	injection of an additional electron into the SOMO
S^{h}	removal of the single electron from the SOMO
S_{C}	C_{60} SOMO
$S_{\mathrm{C}}^{\mathrm{e}}$	electron injection into the C_{60} SOMO via the STM tip
$S_{\mathrm{C}}^{\mathrm{e}}{}'$	electron injection into the C_{60} SOMO via the substrate
$S_{\mathrm{C}}^{\mathrm{h}}$	hole injection into the C_{60} SOMO via the STM tip
$S_{\mathrm{C}}^{\mathrm{h}}{}'$	hole injection into the C_{60} SOMO via the substrate
S_{I}	Ir(ppy)$_3$ SOMO
$S_{\mathrm{I}}^{\mathrm{e}}$	electron injection into the Ir(ppy)$_3$ SOMO
$S_{\mathrm{I}}^{\mathrm{h}}$	hole injection into the Ir(ppy)$_3$ SOMO
sc	simple cubic
SOC	spin–orbit coupling
SOMO	singly occupied molecular orbital
SPP	surface plasmon polariton
STM	scanning tunneling microscopy
TIP	tip-induced surface plasmon polariton
TCSPC	time-correlated single-photon counting
TDDFT	time-dependent functional theory
THF	tetrahydrofuran
$T(\nu)$	transfer function of the transmission line from the pulse generator to the STM tunnel junction
U	Hubbard energy
$U_0(t)$	voltage pulse sent to the tunnel junction
$U_{0,\mathrm{com}}(t)$	compensated voltage pulse sent to the tunnel junction
U_{bias}	applied bias voltage
u_{C60}	relative voltage drop across the C_{60} layer
U_{C60}	absolute voltage drop across the C_{60} layer
u_{dec}	relative voltage drop across the decoupling layer
U_{dec}	absolute voltage drop across the decoupling layer
U_{G}	gate voltage
U_{LUMO}^{0}	potential of the LUMO-derived C_{60} states at zero electric field
$U_{\mathrm{LUMO}}^{\mathrm{obs}}$	LUMO potential observed in $\mathrm{d}I/\mathrm{d}U$ spectra
$U_{\mathrm{S}}(d_{\mathrm{vac}})$	switching voltage
$U_{S_{\mathrm{C}}^{\mathrm{e}}}^{0}$	zero-field potential to charge the C_{60} SOMO with an

	additional electron
$U^0_{S^h_C}$	zero-field potential to charge the C_{60} SOMO with an additional hole
$U^{obs}_{S^e_C}$	bias voltage to charge the C_{60} SOMO by an additional electron from the tip
$U^{obs\prime}_{S^e_C}$	bias voltage to charge the C_{60} SOMO by an additional electron from the substrate
$U^{obs}_{S^e_C}$	bias voltage to charge the C_{60} SOMO by an additional hole from the tip
$U^{obs\prime}_{S^e_C}$	bias voltage to charge the C_{60} SOMO by an additional hole from the substrate
U_{set}	set point voltage of STM images and dI/dU spectra
$U_T(t)$	time-dependent bias voltage at the tunnel junction
u_{vac}	relative voltage drop across the vacuum barrier
U_{vac}	absolute voltage drop across the vacuum barrier
UHV	ultra-high vacuum
UPS	ultraviolet photoelectron spectroscopy
XPS	X-ray photoelectron spectroscopy
XRD	X-ray diffraction

Chapter 1

Introduction

Just as the 20th century is regarded as the century of the electron, due its substantial impact on technological developments, the 21st is predicted to be the century of the photon.[1] Indeed, the United Nations have proclaimed the year 2015 as the international year of light and light-based technologies and consider "applications of light science and technology are vital for existing and future advances in, inter alia, medicine, energy, information and communications, fibre optics, agriculture, mining, astronomy, architecture, archaeology, entertainment, art and culture, as well as many other industries and service .."[2] The European Comission even sees photonics as the *key enabling technology* with the largest market potential in 2015.[3] For the year 2020 its market size is predicted to be worth € 615 billion.[4]

Almost all existing and upcoming applications in this field will rely on the conversion of electrical currents – as the most readily available form of energy – to light. The efficiency of this conversion is substantially determined by the dynamics of the underlying and competing processes. For the following three branches of photonics an understanding of these dynamics on a molecular and atomic level is of particular importance:

- **Organic light emitting diodes** (OLEDs) promise to be perfect devices for large-scale light sources. Their quantum efficiency – that is the efficiency by which electrons can be converted into photons – can reach values of almost $100\,\%$.[5] Furthermore, they allow an easy and cost-efficient production and enable novel applications, such as flexible lighting elements or displays. Although consisting of macroscopically extended films, the performance of such devices crucially depends on the charge carrier dynamics on the molecular level.

- **Exploiting the quantum properties of light** requires the generation of photons one after the other. This special variation of light cannot be described using classical electromagnetism and thus is referred to as *non-classical light.* Macroscopic light sources, such as light bulbs or conventional OLEDs, even lasers, are not able to emit this special variation of light. Instead, it can only be generated by nanostructures with confined electronic states. The realization and further characterization of such non-classical light sources, therefore, demands study of local luminescence dynamics on the nanoscale.

- **Confining and Manipulating light on the nanoscale** is another important challenge. Controlling light in a similar way as we are able to control electric currents, or even beyond that by exploiting its quantum properties, offers completely new concepts for future computer chips.[6] However, the diffraction limit of free propagating

light generally prohibits its confinement to structures smaller than about half of its wavelength – that is a few hundred nanometers. This issue can be circumvented by coupling light to metal surfaces,[7,8] which results in quasi-particles known as surface plasmon polaritons (SPPs). For many applications a direct electrical generation of this "nanoscopically-defined" light without the irradiation of diffraction-limited light would be desirable. One possible approach to achieve this is the excitation of SPPs in tunnel junctions.[9] Additional quantum systems, such as single molecules or nanostructures, could take over the task of controlling the excited SPPs and could thus allow to rule light at its ultimate quantum limit.

In all the above examples, it is essential to use methods that enable studying the conversion dynamics of electric currents into light on the level of individual molecules and atoms. In this context, optical pump–probe techniques have the advantage that they possess the highest time resolution among all experimental methods. Indeed, ultrafast laser spectroscopy grants a time resolution down to the attosecond time scale.[10] However, like free propagating light, this technique is generally subject to the diffraction limit; hence, its spatial resolution is limited to half of the wavelength used. Again, this issue can be circumvented by coupling the ultrafast laser pulses to a plasmonic structure, such as a sharp metal tip, and exploiting its near-field.[11,12] In most (organic) electronic devices, however, charge carriers are generated electrically by the injection of charges instead of optically. One step closer to electrically driven devices is the combination of similar pump–probe excitation schemes with scanning tunneling microscopy (STM).[13–15] These techniques measure the mean current through a system of interest as a function of the time delay between a pump pulse, which excites the system, and a probe or read-out pulse. Both the excitation and read-out processes can be carried out by either optic,[14] electric[15] or optically-generated electric pulses.[13] In either case, the pump–probe approach overcomes the technical limitations caused by the high-gain but low-bandwidth (~1 kHz) current amplifier necessary for STM. Compared to the near-field methods mentioned above, these methods additionally profit from the supreme high spatial resolution of STM and from its possibility to characterize the local electronic structure. The latter is particularly important as it determines the charge carrier dynamics within the investigated system. Although these methods provide information on the dynamics involved in the optical or electrical generation of charge carriers, however, their recombination dynamics remain hidden. In summary, none of the discussed techniques is able to access the full dynamics involved in the conversion of electric current into photons.

The primary goal of this thesis is the development and application of techniques that combine the highly localized injection of charges in STM with the fast detection of photons generated in the STM tunnel junction. Besides the measurable tunneling current and its derivative with respect to the applied bias voltage, which reflects the local density of states (LDOS), the emitted light provides additional information about the investigated system (see Fig. 1.1). The locally excited light can be studied (I) spatially by photon maps, which represent the integrated photon intensity simultaneously recorded during a constant current or constant height image; (II) spectrally by a spectrograph; and (III) as a function of the tunnel parameters, that is, the applied bias voltage and the tip–sample distance. When the detected intensity is multiplied by the elementary charge and divided by the measured current, one obtains the photon yield of the underlying process in photons per tunneling electron. In the time domain, the set-up used in this thesis allows measurement of (IV) the luminescence time response to nanosecond voltage pulses sent to the tunnel junction as well as (V) the second-order intensity correlation function.

The latter evaluates the time between the emission of two photons and provides information defining whether the luminescence process results in the emission of classical or non-classical light. In addition to the development of these techniques, a second objective of this thesis is to apply them for studying the local luminescence dynamics in organic semiconductors as the building block of OLEDs.

Besides evaluating the full dynamics involved in the conversion of electric currents into light, monitoring the light emitted from the tunnel junction offers the following advantages: Compared to pump–probe excitation schemes, (I) it works without a second probe pulse, which possibly perturbs or interferes with the investigated system. (II) It is not based on a pulse cross-correlation, but provides direct mapping of the development of the studied system. (III) In contrast to the measured electric current, the detection of individual photons and their
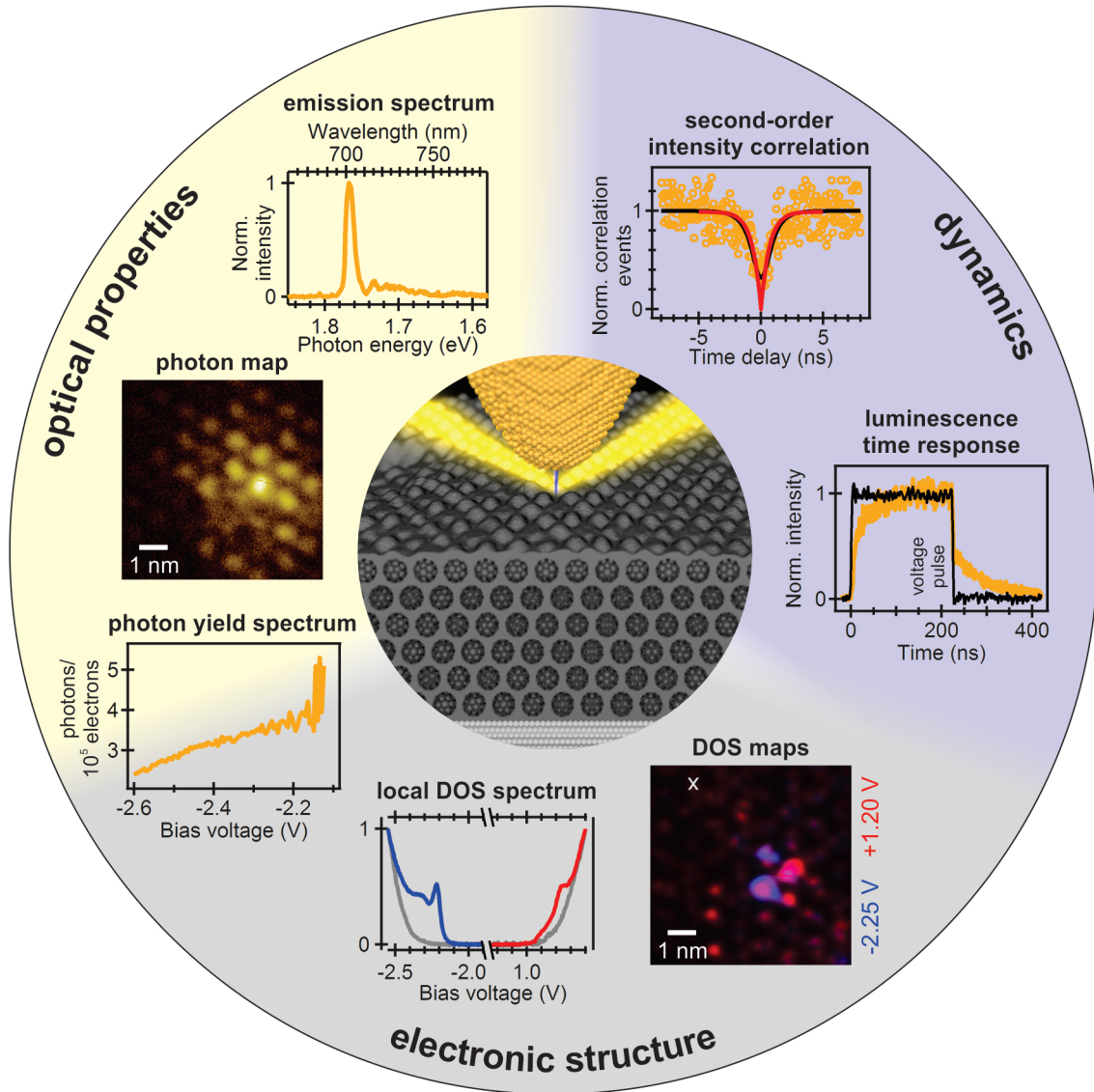
Fig. 1.1: STM modes available due to the detection of the luminescence excited in the tunnel junction using the example of the STM-induced luminescence on thin C_{60} films. For details see chapter 5.

precise emission time provides information on individual quantum processes. And (IV) measuring the energy of the emitted photons reveals the energetic situation during their creation and for a given parameter set, for example, at a certain bias voltage. For the energy of the tunneling electrons, strictly speaking, this does not apply. Although the differential conductance (dI/dU) signal provides information about the relative number of electrons tunneling at a particular energy, this value may change when increasing the bias voltage as a result of the modified tunnel barrier.

In fact, the generation of photons in an STM tunnel junction does not necessarily require the recombination of electron–hole pairs. An alternative mechanism is the excitation of SPP modes in the tip–sample cavity by inelastic tunneling charge carriers.[16, 17] Theses SPP modes typically decay on sub-picosecond time scales[18, 19] by emission of a photon. Hence, it should be possible to exploit the SPPs excited in the STM tunnel junction as an ultrafast read-out signal to monitor even the dynamics of non-emitting processes. Therefore, a third objective of this thesis is to verify this approach. However, in order to apply this idea to various molecular processes, it is necessary to understand the precise relation between the molecules in an STM junction and the SPPs excited therein – a fourth objective of this thesis.

To work toward these objectives, this thesis studies the STM-induced luminescence of thin C_{60} films up to 10 molecular layers (MLs) as well as single *fac*-tris(2-phenylpyridine)iridium(III) ($Ir(ppy)_3$) molecules adsorbed on them. $Ir(ppy)_3$ was chosen because it is one of the leading compounds for second-generation OLEDs,[5] enabling a quantum efficiency of almost 100 %.[20–22] C_{60} was primarily chosen because of its epitaxial growth on noble metal substrates and should be evaluated with respect to its use as molecular decoupling layer for the single $Ir(ppy)_3$ molecules. Moreover, C_{60} has been found as an effective hole injection layer for OLED devices[23–26] and provides an ideal model system to study the local charge carrier dynamics in organic semiconductors (see chapter 4).

This thesis is structured in three parts. The first part provides the technical background by briefly introducing scanning tunneling microscopy (STM) and STM-induced luminescence as well as describing the instrumentation used (chapter 2). This part also includes an approach that enables the quantitative mapping of nanosecond voltage pulses arriving at the STM tunnel junction by exploiting the SPPs excited on bare noble metal surfaces (chapter 3). By enabling a compensation of ubiquitous distortions of the voltage pulses sent to the tunnel junction, this technique is a prerequisite to maximize the edge steepness of the pulses and thus the achievable time resolution in the later experiments. The second and third parts of this thesis then discuss the STM-induced luminescence of C_{60} films with a thickness up to 10 MLs (chapter 5) and single $Ir(ppy)_3$ molecules adsorbed on 1–3 MLs of C_{60} (chapter 8), respectively. In both cases, the observed STM-induced luminescence is decisively determined by the local electronic structure. Therefore, each part starts with a detailed characterization of the electronic structure of the corresponding system (chapter 4 and 7 respectively). In the case of the single $Ir(ppy)_3$ molecules, the electronic structure varies substantially for the different C_{60} layer thicknesses. Hence, the corresponding chapter is preceded by a discussion of the calculated electronic structure of free $Ir(ppy)_3$ as well as the measured electronic structure of $Ir(ppy)_3$ on the bare metal substrates and on a C_{60} monolayer (chapter 6).

Chapter 2

Scanning Tunneling Microscopy (STM) and STM-induced Luminescence

2.1 Scanning Tunneling Microscopy

Scanning tunneling microscopy (STM) is one of the most versatile techniques in surface science and allows, more than almost any other technique, a "direct" view on molecular processes and the underlying electronic structure. It is based on the concept of quantum tunneling and exploits the exponential dependence of the tunneling current between a sharp metallic tip and a metallic or semiconducting sample with respect to their separation. A precise measurement of the flowing current thus enables detection of very small changes in the distance between the tip and the sample up to one thousandth of the size of an atom. Since the flowing current is typically restricted to only a few atoms of the tip apex, the spatial resolution of STM can be as high as 0.1 nm. When the surface of the sample is scanned in the x- and y-directions, this technique thus enables imaging of surfaces on atomic length scales. For precise positioning of the tip usually piezoelectric materials are employed, which expand or contract when applying a high voltage across them. Two imaging modes can be distinguished. In the

constant height mode, the z-coordinate of the tip is kept constant and the flowing tunneling current is measured as a function of the lateral position. Typically, this mode is only employed for very flat surfaces; for example, when taking detailed images of a single substrate terrace or flat adsorbed molecular films. To account for the exponential dependence of the tunneling current with respect to the tip–sample distance, all constant height images in this thesis are plotted with a logarithmic color scale. In contrast, in the constant current mode, the current is monitored by an electronic feedback loop that continuously adjusts the z-coordinate of the tip–sample distance, such that the current is constant. In this case, the primary measure is the z-coordinate of the tip. This imaging mode can be used also for much rougher surface; hence, it is the mode of choice when imaging large and/or initially unknown regions of a sample.

2.1.1 Vacuum Tunneling Between Two Metals

When two conductive surfaces, from here on two metals, are brought in close proximity to one another (~1 nm), electrons can cross over from one metal to the other. Classically, this process is forbidden because the absence of electronic states between the two metals creates a potential barrier that is higher than the energy of the electrons in the metals. However, from a quantum mechanical point of view, the electrons can be described as waves that possess a finite probability to penetrate into and through this barrier. These waves arise as solutions of Schrödinger's equation

$$-\frac{\hbar^2}{2m}\nabla^2\psi(\boldsymbol{r}) + \left[V(\boldsymbol{r}) - E\right]\psi(\boldsymbol{r}) = 0, \tag{2.1}$$

with $\hbar$ as the reduced Planck constant $h/2\pi$, m and E as the mass and energy of the electron, respectively, and $V(\boldsymbol{r})$ as the position dependent potential. For a rectangular potential barrier Schrödinger's equation can be solved analytically. Within the barrier eq. (2.1) has two solutions, one wavefunction that exponentially decays in $+z$ direction and one wavefunction that exponentially decays in $-z$ direction:

$$\psi(z) \propto \mathrm{e}^{\pm\kappa z}, \tag{2.2}$$

with the decay constant

$$\kappa = \frac{\sqrt{2m(V-E)}}{\hbar}. \tag{2.3}$$

These solutions describe the penetration of electrons in $+z$ or $-z$ direction, respectively. As the probability to observe an electron at a position z is proportional to the square of the wavefunction $|\psi(0)|^2\mathrm{e}^{\pm 2\kappa z}$, electrons have a non-zero probability to penetrate through the barrier.

In reality, the potential may not be rectangular and constant across the potential barrier, as image forces acting on the electrons will round its edges. However, at the moment this point will be neglected. In the simplest case, the potential V equals the vacuum level; hence, $(V-E)$ can be assumed as the mean work function of both metals $\phi = (\phi_1 + \phi_2)/2$, as long as $\phi_1 \approx \phi_2$.

When applying a weak bias voltage (few millivolts) between the two metals, the Fermi energies E_F of both metals shift with respect to one another and a net current arises. This current is proportional to the transmission probability of the electrons through the potential barrier and thus proportional to the wavefunction squared:

$$I \propto T \propto |\psi(0)|^2 \cdot \mathrm{e}^{-2\kappa z}, \tag{2.4}$$

where $\psi(0)$ is the electron wavefunction near E_F of the metal where it originates from. For most metals, the work function is around $5\,\mathrm{eV}$. Insertion of this value into eq. (2.3), together with the corresponding values for m and $\hbar$, results in a decay constant of $\kappa = 11.4\,\mathrm{nm}^{-1}$. Therefore, changing the distance between both metals by $0.1\,\mathrm{nm}$ leads to a decrease in the current of $\exp\left[-2\kappa \cdot 0.1\,\mathrm{nm}\right] = 0.101$. In other words, a one angstrom change in the separation of both metals leads to a one order of magnitude change in the tunneling current. This result explains why such a tunneling current can only be measured for very small separations of two metals.

2.1.2 Bardeen's Approach − Quantitative Description of the Tunneling Current

The first analytic expression for the tunneling current between two metals was developed by John Bardeen.[27] His tunneling theory is based on the following assumptions:[28]

a) tunneling is weak so that the process can be described by a first-order approximation

b) the states of both metals are nearly orthogonal

c) electron–electron interactions can be neglected

d) the occupation probabilities for both metals are independent of each other and do not change despite the tunneling

e) both metals are in electrochemical equilibrium

Instead of solving Schrödinger's equation for the combined system consisting of both metals, Bardeen's approach starts with an independent solution of Schrödinger's equation for both metals. The tunneling current between both electrodes is then treated as the transfer of electrons from one metal to the other under the influence of the Hamiltonian of the whole junction. When tunneling is weak, the temporal evolution of an electron in the ψ_s state of a metal, let's call it "s", can be described by

$$\psi_\mathrm{s}(t) = \psi_\mathrm{s}(0)\mathrm{e}^{-itE_\mathrm{s}/\hbar} + \sum_k c_\mathrm{t}(t)\psi_\mathrm{t}\mathrm{e}^{-itE_\mathrm{t}/\hbar}, \tag{2.5}$$

where the sum is over all bound states ψ_t of the metal "t". Assuming the wavefunctions of the individual subsets s and t as (approximately) orthogonal, eq. (2.5) can be inserted into the time-dependent Schrödinger equation. When neglecting second and higher order terms, one obtains

$$i\hbar\frac{\mathrm{d}c_\mathrm{t}(t)}{\mathrm{d}t} = \int \psi_\mathrm{s} V \psi_\mathrm{t}^* \mathrm{d}^3\boldsymbol{r}\,\mathrm{e}^{-i(E_\mathrm{s}-E_\mathrm{t})t/\hbar}. \qquad (2.6)$$

By defining a matrix tunneling element

$$M_\mathrm{st} = \int \psi_\mathrm{s} V \psi_\mathrm{t}^* \mathrm{d}^3\boldsymbol{r}, \qquad (2.7)$$

that describes the transmission probability of an electron in the ψ_s state of metal s through a potential barrier V into a state ψ_t in metal t, an explicit expression for the tunneling current can be obtained. As long as the density of states (DOS) of both electrodes, ρ_s and ρ_t, do not vary appreciably near E_F on the range of the applied bias voltage (U_bias), the tunneling current is given as

$$I = \frac{2\pi e^2}{\hbar}|M_\mathrm{st}|^2 \rho_\mathrm{s}(E_\mathrm{F})\rho_\mathrm{t}(E_\mathrm{F})U_\mathrm{bias}. \qquad (2.8)$$

According to Bardeen, the tunneling matrix element (M_st) can be expressed by a surface integral over any separation surface lying entirely within the barrier region. When considering only elastic tunneling processes, in which the energy of the tunneling electrons does not change, it can be shown that the tunneling matrix element is given by[29]

$$M_\mathrm{st} = \frac{\hbar^2}{2m} \int \left(\psi_\mathrm{s}\vec{\nabla}\psi_\mathrm{t}^* - \psi_\mathrm{t}^*\vec{\nabla}\psi_\mathrm{s} \right) \mathrm{d}\boldsymbol{S}. \qquad (2.9)$$

It is noteworthy that the potential barrier does not appear explicitly in this formula. Instead, electron tunneling is described only by the wavefunctions of both metals at the separation surface. Using eq. (2.8), the total tunneling current at a given bias voltage (U_bias) is accessible by summing over all available states:

$$I = \frac{4\pi e}{\hbar}\int_{-\infty}^{\infty} \left[f(E_\mathrm{F} + eU_\mathrm{bias} + \epsilon) - f(E_\mathrm{F} + \epsilon) \right] \rho_\mathrm{t}(E_\mathrm{F} + eU_\mathrm{bias} + \epsilon)\rho_\mathrm{s}(E_\mathrm{F} + \epsilon)|M_\mathrm{st}|^2 \mathrm{d}\epsilon, \qquad (2.10)$$

with $f(E)$ as the Fermi distribution function. For low temperature, $f(E)$ can be approximated by a step function. At the limit of small voltages eq. (2.10) further simplifies to

$$I = \frac{4\pi e}{\hbar}\int_{0}^{eU_\mathrm{bias}} \rho_\mathrm{t}(E_\mathrm{F} + eU_\mathrm{bias} - \epsilon)\rho_\mathrm{s}(E_\mathrm{F} - \epsilon)|M_\mathrm{st}|^2 \mathrm{d}\epsilon. \qquad (2.11)$$

If the magnitude of M_st does not change appreciably in the investigated bias interval, the tunneling current thus equals a convolution of the DOS of both metals.

2.1.3 The Tersoff–Hamann Model – Contrast Mechanism in STM

Shortly after the invention of the scanning tunneling microscope by Binnig and Rohrer,[30] Tersoff and Hamann developed a first model of the tunneling current and the contrast mechanism in STM[31,32] based on Bardeen's description of the tunneling current in (planar) tunnel junctions. In their model, the wavefunction of the sample electrons is treated exactly, but expanded in reciprocal lattice vectors of the surface

$$\psi_{\mathrm{s}} = \frac{1}{\sqrt{\Omega_{\mathrm{s}}}} \sum_{G} a_{\mathrm{G}} \cdot \exp\left[-\sqrt{\kappa^2 + |\boldsymbol{k}_{\parallel} + \boldsymbol{G}|^2} z\right] \times \exp\left[i(\boldsymbol{k}_{\parallel} + \boldsymbol{G}) \cdot \boldsymbol{x}\right], \qquad (2.12)$$

with Ω_{s} as the sample volume, κ defined as in eq. (2.3), $\boldsymbol{k}_{\parallel}$ as the Bloch wave vector of the state and $\boldsymbol{G}$ as the surface reciprocal lattice vector. For a non-periodic surface the sum over all surface vectors becomes an integral. The wavefunction of the tip is modeled as a local spherical potential well at a position $\boldsymbol{r}_0 = (0, 0, z)$ and a radius of curvature R. Hence, the tip states are modeled as pure s-like states, without any angular dependence. Expanding the tip wavefunctions analogously to those of the sample yields

$$\psi_{\mathrm{t}}(\boldsymbol{r}) = \frac{1}{2\pi} \int \mathrm{d}^2 q \cdot \frac{\exp\left[-\sqrt{\kappa^2 + q^2}|z|\right]}{\kappa^2 \sqrt{1 + q^2/\kappa^2}} \cdot \exp\left[i\boldsymbol{q} \cdot \boldsymbol{x}\right]. \qquad (2.13)$$

Substituting the wavefunctions of the tip and the sample into Bardeen's expression for the tunneling matrix element give by eq. (2.9) results in

$$M_{\mathrm{st}} = \frac{4\pi\hbar^2}{2m\sqrt{\Omega_{\mathrm{t}}}} R e^{\kappa R} \psi_{\mathrm{s}}(\boldsymbol{r}_0). \qquad (2.14)$$

Hence, the tunneling matrix element reflects the value of the sample wavefunction $\psi_{\mathrm{s}}(\boldsymbol{r}_0)$ at the center of the tip $\boldsymbol{r}_0$. Insertion of the matrix element into Bardeen's expression for the tunneling current eq. (2.11) and comparison with the wavefunction of the the sample eq. (2.12) shows that

$$I \propto \rho_{\mathrm{t}} |\psi_{\mathrm{t}}|^2 \int\limits_{0}^{eU_{\mathrm{bias}}} \rho_{\mathrm{s}}(E_{\mathrm{F}} - \epsilon) \mathrm{d}\epsilon, \qquad (2.15)$$

as long as the tip wavefunction has a pure s-like character, i.e. is spherically symmetric, the tunneling matrix element as well as the tip DOS do not depend on the applied bias voltage and the thermal broadening of the Fermi level is negligible. Therefore, the tunneling current is proportional to the surface LDOS at the position of the tip. This means an STM image reflects the contours of the LDOS of the probed surface. Moreover, the derivative of the current with respect to the bias voltage is proportional to the LDOS at the energy $E_{\mathrm{F}} + eU_{\mathrm{bias}}$ at the center of the tip:

$$\frac{\mathrm{d}I}{\mathrm{d}U} \propto \rho_\mathrm{s}(E_\mathrm{F} - \epsilon, \boldsymbol{r}_0). \tag{2.16}$$

In STM experiments, the derivative of the tunneling current is typically measured by modulating the applied bias voltage with millivolt amplitudes and determine the derivative by a phase-sensitive lock-in technique to improve the signal-to-noise ratio. In this thesis, the bias voltage is modulated by voltage amplitudes between 1 and 20 mV and frequencies between 500 and 800 Hz.

2.2 STM-induced Luminescence

The idea of investigating the photon emission from individual molecules by tunneling low-energy electrons dates back to the year 1971 when Russel Young suggested the use of a *topografiner* for this purpose[33] – ten years before the invention of the scanning tunneling microscope. After its invention by Binnig and Rohrer[30] this idea came within reach, but it still took a further seven years until Gimzewski *et al.* reported the first observation of light excited in the tunnel junction of a scanning tunneling microscope on polycrystalline tantalum and a Si(111)(7 × 7) surfaces.[34] Motivated by these first experiments, the initial studies focused on the light emission on bare metal surfaces[16, 17, 35] and, shortly thereafter, on molecules adsorbed on them.[36, 37] Since then, the STM-induced luminescence of a large number of different systems have been investigated, for example, single molecules,[38, 39] molecular layers,[40, 41] and nanocrystals,[42, 43] metal clusters,[44, 45] semiconductor surfaces[46] and various quantum structures.[47–49] At moderate currents (<10 nA) and bias voltages (<5 V) two fundamental emission processes can be distinguished: (I) the excitation of tip-induced surface plasmon polaritons (TIPs) by inelastic tunneling processes from states of the STM tip into sample states, or vice versa, and (II) intrinsic transitions within a single molecule, molecular film or nanostructure, initiated by an additional electron in the lowest unoccupied molecular orbital (LUMO) or conduction band states and an additional hole in the highest occupied molecular orbital (HOMO) or valence band states, respectively. Often both processes (I) and (II) can only hardly be separated because they mutually depend on each other and the intrinsic transitions within molecules or nanostructures can be induced, enhanced or quenched by the tip–sample cavity. However, section 8.1 will show one possible approach that allows discrimination between these two processes by comparing the spatial dependence of the excited light with the shape of the electronic states. In addition to these two prevalent luminescence processes, at higher bias voltages and/or currents further luminescence processes have been observed which, for example, involve field-emission states.[50, 51] Because of their ubiquitous presence and their importance for this thesis, the following two sections will review the radiative decay of TIPs and electron–hole pairs in more details.

2.2.1 Radiative Decay of Tip-induced Surface Plasmon Polaritons

The radiative decay of tip-induced surface plasmon polaritons (TIPs) was first discovered on polycrystalline silver substrates.[16] TIPs represent localized surface plasmon polariton (SPP) modes – collective charge oscillations of the free electrons in metal surfaces – which are confined

to the tip–sample cavity. They strongly couple to the electrons tunneling through the STM junction and are excited by their shot noise.[52] The photon emission yield of this processes has been calculated as 10^{-3}–10^{-4} photons per electron.[53] The emission characteristics of TIPs resemble those of surface plasmon polarition modes in planar tunnel junction:[9] Their emission spectra are rather broad, typically several hundred millielectronvolts, because the electrons exciting them may tunnel into and/or out of a continuum of final states. Furthermore, the emission spectra are independent of the bias polarity and, at moderate currents ($<10\,\text{nA}$), exhibit a quantum cutoff defined by the energy of the tunneling electrons. At higher currents, the formation of hot holes and electron–electron interactions can result in photon energies that exceed the energy of the tunneling electrons,[54] known as electroluminescence up-conversion. The specific shape of the emission spectra sensitively depends on the nanoscopic structure of the STM tip apex and the dielectric properties of tip and sample. Noble metals, in particular silver and gold, have been found to lead to the strongest emission intensities[17, 55] because of their weak internal damping and the small imaginary part of their dielectric function. The influence of molecules adsorbed on such noble metal surfaces will be discussed in chapter 8.

2.2.2 Radiative Decay of Electron–Hole Pairs

In order to permit an electrical generation and subsequent radiative recombination of electron–hole pairs in a single molecule, a molecular film, or a nanostructure, generally these must be sufficiently decoupled from a supporting metallic substrate. This is necessary for two reasons. First, for a simultaneous injection of electrons into the LUMO-derived or conduction band states and holes into the HOMO-derived or valence band states, the corresponding electronic states must not be pinned to the substrate. Instead, it must be possible to align at least one of these states with the Fermi level of the substrate. Otherwise, only one type of charge carrier, either electrons or holes, can be injected by the STM, which cannot encounter the complementary charge carrier. A second point that necessitates a sufficient decoupling from the metal substrate concerns the radiative recombination of created electron–hole pairs. In close proximity to a metal surface, the decay of electron–hole pairs is generally dominated by non-radiative decay channels. For chemisorbed molecules that possess a direct wavefunction overlap with the metal substrate states these non-radiative decay channels arise from resonant electron (tunneling) processes.[56] For physisorbed molecules, they mostly result from a dipole coupling of the excited quantum system with the underlying metal substrate.[56–59] The magnitude of the latter quenching mechanism decreases with the third power of the distance to the metal surface; hence, it can be effectively suppressed by an additional decoupling or buffer layer. Such a decoupling layer can be provided by a thin insulating layer,[38, 39] molecular films of several molecular layers,[40, 41, 60–69] or a combination of both.[42, 43, 70] In the second case, the decoupling of the topmost layer can be achieved either by the same type of molecules[40, 41, 64–69] (typically ~6 ML) or by a second type.[60–63] Recently it has been shown that the necessary decoupling from the metal substrate is also possible by the molecule itself, as long as it is large enough, such as a single polymer chain.[71]

The emission spectrum of an electron–hole recombination process typically exhibits a main emission line occasionally followed by a vibrational progression pattern at the lower energy side.[38, 39, 42, 43, 70] However, whether individual vibronic states can be resolved or not depends on the number and energy difference of the vibrational modes that are able to couple to the

electronically excited state(s). In the case of many coupling vibrational modes with similar vibrational frequencies, the resulting vibronic states typically collocate in multiplets. This can lead to rather broad emission spectra that may be difficult to discriminate from a radiative decay of TIP modes. Furthermore, these cavity modes often substantially influence the detectable emission spectra by selectively increasing the local density of available photonic states. Similar to pure plasmonic spectra on bare metal substrates, the precise shape of the obtained spectra thus often depends on the nanoscopic shape of the STM tip apex. To obtain the intrinsic emission spectrum of the molecules or nanostructure, the obtained spectra are typically divided by the plasmonic spectrum of the tip on a bare metal substrate. In contrast to the excitation of TIP modes on metals, the radiative decay of electron–hole pairs generally requires a specific threshold bias voltage. Below this threshold none or only one type of charge carrier can be injected, which precludes a recombination of electrons and holes. In most cases, this voltage threshold is larger than the HOMO–LUMO gap of the molecule or the gap between the conduction and valence band of the nanostructure due to the necessary alignment of electronic states with the Fermi level of the substrate. However, for some systems an electron–hole recombination for bias voltages smaller than the electronic gap (electroluminescence up-conversion) has been observed. Examples of such processes are an Auger-like mechanism observed on sodium-copper quantum well structures,[72] a triple-triple annihilation process observed on phthalocyanines,[68] or the STM-induced luminescence of porphyrin molecules, which has been interpreted by a two-electron processes[69] as well as a population of higher vibrational states through plasmonic pumping of the tip–sample cavity.[41]

2.3 Technical Details

2.3.1 Instrumentation Used

All experiments discussed in this work were carried out in an in-house built low-temperature (4 K) ultra-high vacuum (UHV) scanning tunneling microscope. During this PhD, the microscope was relocated to the Precision Laboratory of the Max Planck Institute for Solid State Research in Stuttgart, inaugurated in 2012. The experimental data discussed in chapter 3, 4 and parts of chapter 5, as well as in section 6.3 and 8.1 were acquired in the old lab; the remaining parts of this thesis arose from measurements in the Precision Laboratory. For a detailed description of the set-up before the relocation, the reader is referred to the two previous PhD theses in references [73] and [74]. The following sections describe the current set-up.

Precision Laboratory

The experiment is located in one of the eleven experimental rooms ("boxes") of the Precision Laboratory of the Max Planck Institute for Solid State Research in Stuttgart (see Fig. 2.1a). These experimental rooms ensure a seismic, acoustic, and electromagnetic shielding of the experiment from the immediate laboratory environment, necessary for highly-sensitive STM studies. The set-up itself resides on a 150 t fiberglass reinforced concrete block set on six air springs, which reduce the vibrational level below 10 nm/s (Fig. 2.1b). Figure 2.1c depicts a frequency spectrum of the measured tunneling current with opened feedback loop in the old lab (black) and the Precision Laboratory (red) after stabilizing the STM tip at a current of
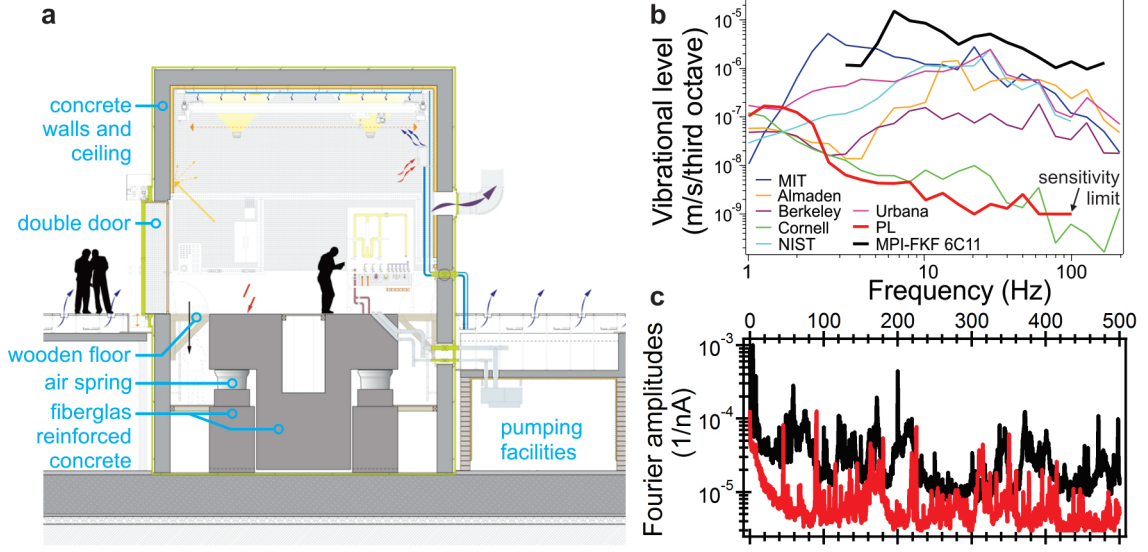
Fig. 2.1: Structure of and vibrational level in the experimental rooms in the Precision Laboratory. (a) Scheme of one of the eleven experimental rooms in the Precision Laboratory (courtesy of hammeskrause architects). (b) Vibrational level in the Precision Laboratory (PL, red), the old laboratory (MPI-FKF 6C11, black) and various other laboratories reproduced from ref. [76]. (c) Fourier transform of the tunneling current measured with opened feedback in the Precision Laboratory (red) and the old laboratory (black) after stabilizing the STM tip at a set point current of 1 nA.

1 nA. In most of the frequency regions, the relocation of the microscope increased the stability of the tunnel junction by one order of magnitude. The standard deviation of the measured tunneling current after an initial stabilization at 1 nA is 3.2 pA. Assuming a one order of magnitude change of the tunneling current for a 1 Å change of the tip–sample distance (see section 2.1.1), the stability of the STM tunnel junction is <0.2 pm.

Ultra-high Vacuum System

The actual experiment consist of two UHV chambers separated by a plate valve, as well as a load-lock that enables the transfer of STM tips and samples into and out of the UHV environment. The first chamber, inter alin, provides a sputter gun and two molecule evaporators, which allow an *in situ* preparation of samples (base pressure: 1×10^{-10} mbar). The second chamber accommodates the scanning tunneling microscope, which is mounted on a liquid helium bath cryostat surrounded by liquid nitrogen radiation shields (base pressure: $<1 \times 10^{-11}$ mbar). For an additional vibrational isolation of the microscope, the helium cryostat hangs on a platform residing on three passive air springs. The original design of the experiment traces back to a previous PhD thesis by Michael Vogelgesang;[75] the optical detection system was added within the scope of a subsequent PhD thesis by Alexander Kabakchiev.[73]

Microscope Head

The microscope head comprises an exchangeable sample holder, held in position by a magnet, as well as an exchangeable tip holder, guided by rails and held by springs (see Fig. 2.2a).

To guarantee a constant adjustment of the optical detection system during coarse motion and STM operation, the STM tip is fixed and all relative motion between tip and sample is realized by the motion of the sample. The movement during STM operation is achieved by an eight-segment scan piezo, with one ring of four segments providing horizontal scanning and the other four segments enabling the control of the tip–sample distance. A second slip-stick piezo system allows for a horizontal and vertical coarse positioning of the sample over a range of several millimeters.

Optical Detection System

The optical detection system of the microscope provides three independent light paths to the tunnel junction, which can be used to couple light in, out, or image the tunnel junction.[73,77] The latter facilitates the orientation on the sample as well as its coarse approach and enables adjustment of the optical detection system (see below). Each of the three optical paths consists of an aspherical lense that couples the light emitted from the tunnel junction via an *ex situ* adjusted mirror through holes in the cryogenic shields and UHV viewports out of the UHV chamber (Fig. 2.2b). Currently, the three optical paths are equipped with two avalanche single photon diode (APD, PerkinElmer SPCM-AQRH-15) and an optical spectrograph (Acton Research Spectra Pro 300i, 150 lines/inch blazed grating, combined with a peltier-cooled intensified charged-coupled device (CCD), see section 2.3.2) outside the UHV chamber.

The distance of the lenses (numerical aperture: 0.42) to the STM tip of a few millimeters is chosen such that the lenses create an intermediate focus between the liquid helium and nitrogen radiation shield. As a consequence, the corresponding holes in the radiation shields can have diameters of a few millimeters (He shield: 4 mm, N_2 shield: 6 mm), which reduces the thermal radiation entering the microscope. To allow an alignment of the optical paths to different STM tips, the position of the apertures in the nitrogen shield can be adjusted by a wobble stick. As part of the microscope, the lenses are cooled to the same temperature as the microscope itself, i.e., in usual operation mode to 4.2 K. Their vertical axes are mounted at an angle of 60° with respect to the sample surface normal and an azimuthal angle of 90° with respect to each other. Accounting for reflection losses at the uncoated surfaces of the
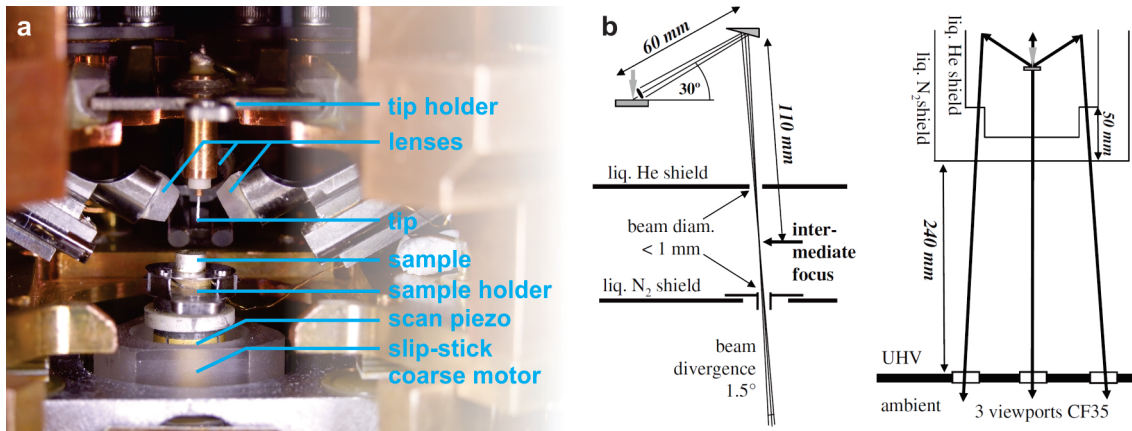

Fig. 2.2: Scanning tunneling microscope and beam geometry of the optical paths. (a) View inside the microscope. (b) Schematic beam geometry obtained from ref. [77].

lenses and the UHV viewports, each lens leads to a collection efficiency of 7 % and 12 % for the two limiting cases of an isotropic radiation and an exclusive radiation on the 60 ° cone, respectively.[73] The value for the isotropic radiation is typically of minor importance because the emission intensity vanishes for altitude angles close to 0 ° and 90 °.

The position of each lens can be adjusted *in situ* in all three spatial directions by a corresponding slip-stick piezo motor to adapt the optical paths to different STM tips. For this purpose, each lens is mounted on a four-segment piezo tube, which enables a positioning of the lenses over a distance of ±3 mm and ±1 mm along the beam direction and perpendicular to it, respectively. The motion of the lenses is controlled by the sign and amplitude of a saw-tooth voltage applied to the four piezo segments with respect to the inner electrode.

2.3.2 Acquisition and Presentation of Emission Spectra

Emission spectra are acquired by a two-dimensional CCD chip. Wavelength spectra are obtained by integration along the direction perpendicular to the grating vector of the blazed grating. For a more convenient analysis, these spectra are plotted as a function of the photon energy throughout this thesis. For this purpose, the emission intensity is corrected by the varying bin size.

2.3.3 Measuring Time-dependent STM-induced Luminescence Intensities

In this thesis, the time-dependent luminescence intensity from the STM tunnel junction is studied in two ways: First, by the luminescence time response upon a train of short voltage pulses sent to the STM tunnel junction and, second, by the second-order intensity correlation function. The latter reflects the time delay between the emission of two photons, which quantifies the photon statistics of the emission process, that is, the temporal fluctuations in the photon intensity. Both techniques are realized by a time-correlated single-photon counting (TCSPC) unit (Becker & Hickl SPC-130), which measures the delay time between the detection of a single photon by one of the avalanche single photon diodes (APDs) (stop signal) with respect to a trigger signal (start signal, see Fig. 2.3). In the case of the photon statistics, the trigger or start signal is provided by a second APD. For monitoring the luminescence response to short voltage pulses, the trigger signal is provided by the pulse generator creating the pulses. In either case, the tunneling current and the photon intensity is chosen to be low enough that the number of trigger signals is much larger than the number of stop signals.

For the pulse measurements, three different pulse generators have been employed in this thesis, one pulse pattern generator (Agilent 81110A: section 3.1) and two arbitrary waveform generators (Agilent 81150A: section 3.2 and 3.3; Agilent M8190A: section 8.2.5). For the experiments described in chapter 3 and 5, the pulses were sent to the tunnel junction via standard low-temperature stainless steel cables (Lake Shore Cryotronics, type SS[78]) with a length of ~1.5 m and an attenuation of −3 dB/m at approximately 20 MHz. The experiments in section 8.2.5 were performed after the relocation of the microscope to the Precision Laboratory with a semi-rigid coaxial stainless steel cable (Coax Co. Ltd, SC-119/50-O-SS) and a specified attenuation of −1.93 dB/m at 500 MHz. Counting many photon detections events
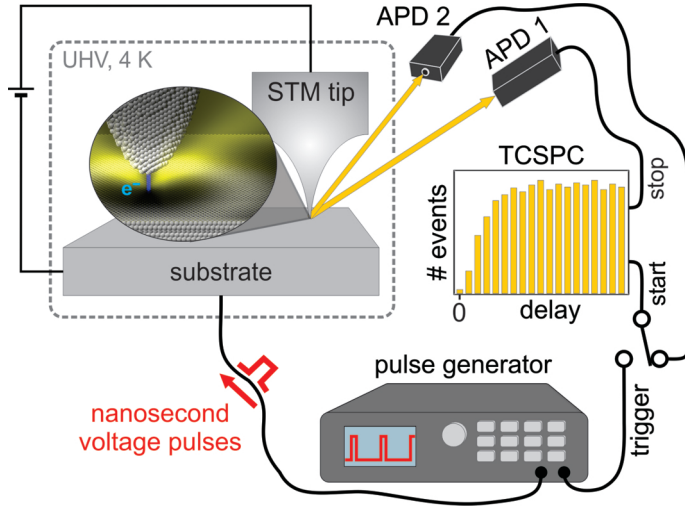
Fig. 2.3: Measuring time-dependent STM-induced luminescence intensities. Two types of measurements are possible: (1) For monitoring the luminescence response to nanosecond voltage pulses, the start and the stop signals for the time-correlated single-photon counting (TCSPC) unit are the trigger signal from the pulse generator and the detection signal from one of the two avalanche single photon diodes (APDs), respectively. (2) For the measurement of the second-order intensity correlation function – that is, the fluctuations in the photon intensity of the emitted light – the TCSPC unit measures the time delay between two photons detected by the two APD.

(typically 10^8 for an integration time of $500\,\mathrm{s}$) into time bins results in a histogram reflecting the distribution of photon arrival times $N(\Delta t)$. Since the number of detection events by the APD is kept much smaller than the number of trigger pulses from the pulse generator, $N(\Delta t)$ is proportional to the time-dependent luminescence intensity $P(t)$. The achievable experimental time resolution is limited by the time jitter of the photon detector and estimated to be less than $1.1\,\mathrm{ns}$ for the APD used here.[79]

2.3.4 Correction of the Experimental Drift

The lateral drift between successive STM images, such as those in Fig. 4.7, 6.6, 6.9, 7.3, 7.7, 8.3, 8.10, and 8.12, is corrected by linearly fitting the position of a common feature, for example, a specific C_{60} molecule. Depending on the "history" of previous measurements and the direction (fast or slow scan direction), the lateral drift typically amounts to ±50 to ±300 pm/h. For measurements as a function of the tip–sample distance, such as those in Fig. 5.10, 7.4, 7.5, and 8.8, the vertical drift is corrected by repeatedly measuring either the STM tip height (feedback on) or the current (feedback off) of a distinct feature. In the case of a current measurement (feedback off), the time-dependent current is fitted by an exponential function. The fitted exponent then allows one to estimate the drift by assuming a one order of magnitude change in current for a 0.1 nm displacement (see section 2.1.1). In the case of successively measuring the tip height of a certain feature (feedback on), the drift is fitted by a linear function.

2.3.5 Sample and Tip Preparation

Preparation of Metal Substrates

The STM samples are prepared under UHV conditions ($<3 \times 10^{-10}\,\mathrm{mbar}$) on either a Au(111) or a Ag(111) substrate. These substrates are cleaned by several (typically three) cycles of Ar

sputtering and annealing to 830 K. Afterwards the samples are coated with pure C_{60} films of varying thicknesses, single $Ir(ppy)_3$ molecules, or single $Ir(ppy)_3$ molecules on top of a thin C_{60} film. Shadowing half of the substrate by a shutter located ~2 mm above the sample enables the deposition of molecules on only one side of the sample. This enables preparing the STM tip on the uncovered, clean metal surface prior to the measurements on the molecules (see below).

Preparation of the Pure C_{60} films

For the experiments in chapter 4 and 5, the afore prepared Au(111) or Ag(111) substrate is coated with a multilayer coverage of C_{60} from an effusion cell, with the substrate held at room temperature. The typical evaporation temperature is 823 K; the evaporation time varied between 20 and 40 min.

Preparation of the Single $Ir(ppy)_3$ Molecule Samples

$Ir(ppy)_3$ was synthesized by Dr. Frank Schramm and Prof. Mario Ruben from the Karlsruhe Institute of Technology (KIT) according to the literature.[80, 81] Final purification after column chromatography (SiO_2, CH_2Cl_2) of the reaction material was achieved by vacuum sublimation (453 K, 2×10^{-3} mbar). The nondestructive evaporation of $Ir(ppy)_3$ was regularly verified by laser desorption ionization mass spectra of evaporated $Ir(ppy)_3$ films.

For the STM samples a submonolayer-coverage of $Ir(ppy)_3$ is deposited from an effusion cell (Dodecon 4× evaporator). The evaporation temperature and time varied between 523 K to 543 K and 4 min to 7 min, respectively. In the majority of experiments shown in this thesis, the sample was held at room temperature during the evaporation of $Ir(ppy)_3$. However, for the measurements on single $Ir(ppy)_3$ molecules on a bilayer of C_{60} on Au(111) (section 8.2), the sample was cooled to ~240 K to reduce the diffusion of the single molecules to the step edges of the rather small substrate terraces. For the experiments on C_{60} monolayers (section 6.3 and 8.1), C_{60} bilayers (section 7.2 and 8.2) and C_{60} trilayers (section 7.3 and 8.3), prior to the evaporation of $Ir(ppy)_3$ molecules, the cleaned substrate was coated with a mean coverage of one (788 K, 20 min) or two molecular layers of C_{60} from a second molecule evaporator (on Ag(111): 788 K, 70 min; on Au(111): 823 K, 25 min).

Preparation of STM Tips

The STM tips are produced by electrochemical etching of gold wires (voltage: 3 V) using a 1:1 mixture of concentrated hydrochloric acid (Roth, ROTHIPURAN 37%, p.a.) and ethanol (Roth, ROTIPURAN ≤ 99.8%, p.a.) as the electrolyte. After the etching process, the tips were rinsed with deionized water as well as *iso*-propanol and transferred into UHV. Occasionally, the tips were evaporated under UHV conditions with silver to enhance their plasmonic luminescence.[82] Before the STM measurements, the tip is typically prepared on a clean metal surface, either Ag(111) or Au(111), by voltage pulses up to ±10 V or indentation into the surface. The tip is prepared until it: (I) does not produce any multiple-tip features, (II) leads to

a featureless $\mathrm{d}I/\mathrm{d}U$ spectrum only exhibiting the surface-specific surface state, and (III) radiates a broad, featureless plasmonic spectrum with (IV) an integrated luminescence efficiency of $>10^{-5}$ photons/electrons.

Chapter 3

Mapping and Edge Optimization of Nanosecond Voltage Pulses

Scanning probe microscope studies focus increasingly on measuring fast time-dependent processes at atomic dimensions, such as spin[15,83–85] and charge[14,86] dynamics or molecular motion.[87–90] Heterodyne frequency mixing[91] and pump–probe excitation schemes[15,92–95] have been put forward as techniques to measure repetitive variations of the tunneling current in scanning tunneling microscopy (STM). Such techniques overcome practical limitations caused by the limited bandwidth of high-gain current amplifiers. One essential prerequisite to quantitatively analyze such measurements is the exact knowledge of the time-dependent bias voltage at the tunnel junction $U_{\mathrm{T}}(t)$. For nanosecond pulses, absorption and reflection in the wiring and connectors can significantly distort the input pulses $U_0(t)$ as they propagate to the tunnel junction. However, due to its enclosure inside an experimental setup, the voltage at the point of the measurement, here the STM tunnel junction, is generally not directly accessible.

In this chapter an optical read-out technique is demonstrated that enables mapping the time-dependent electrostatic potential in a tunnel junction with millivolt and nanosecond accuracy. For this purpose, the time-dependent luminescence intensity emitted from a metallic tunnel junction of a scanning tunneling microscope is measured upon excitation with nanosecond voltage pulses. The photons arise from the decay of tip-induced surface plasmon polaritons (TIPs) modes in the tip–sample cavity, which are excited by inelastically tunneling electrons.[16] Plasmons at surfaces and on clusters have typical lifetimes on the femtosecond time scale.[18,19] Therefore, the emitted photons can be used as an instantaneous probe for processes down to at least the picosecond range. The luminescence intensity is found to be a quantitative measure of the voltage between the STM tip and the sample. This permits a non-invasive mapping of fast voltage transients directly at the tunnel junction. In the present case, knowledge of the

pulse profile at the tunnel junction enables optimization of the experimental time response by a factor of 16 by actively shaping the pulses sent to the junction. Parts of this chapter have been published in reference [96].

3.1 Mapping Voltage Pulses at the Tunnel Junction

Since the photon emission is instantaneous on the experimental time scale (see above), the only requirement to use the photon intensity as a probe of the voltage at the tunnel junction is a strictly monotonic dependence between both quantities. Once known, this dependence can be used to convert the measured photon intensity back to the transient voltage at the tunnel junction. Indeed, this criterion holds for bias voltages larger than the energy threshold of the avalanche single photon diode (APD) of about $1.2\,\text{eV}$ (Fig. 3.1). The origin of the monotonic behavior most lies in the increasing number of inelastic tunneling channels, although details of the functional dependence may vary between (microscopically) different tips. For different data sets, therefore, individual calibration curves are used to ensure a quantitative evaluation.
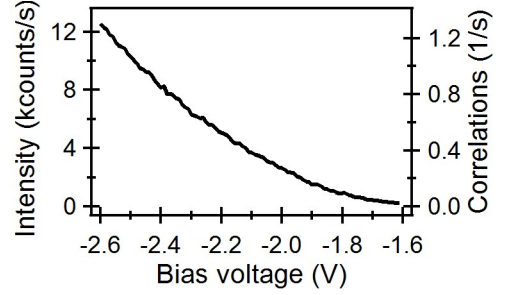
Fig. 3.1: Intensity–voltage calibration curve for mapping voltage pulses at the STM tunnel junction. The number of correlation events per bin (right axis) arises from the total intensity measured by the APD (left axis) by multiplication with the bin size and the pulse repetition rate.

3.1.1 Mapping of Microsecond Voltage Pulses

In order to check the validity of the proposed technique, microsecond long bias pulses are sent to the tunnel junction (Fig. 3.2, red dashed curve). These slow pulses should experience, if at all, only minor distortions because of the small bandwidth necessary for them. Thus, the
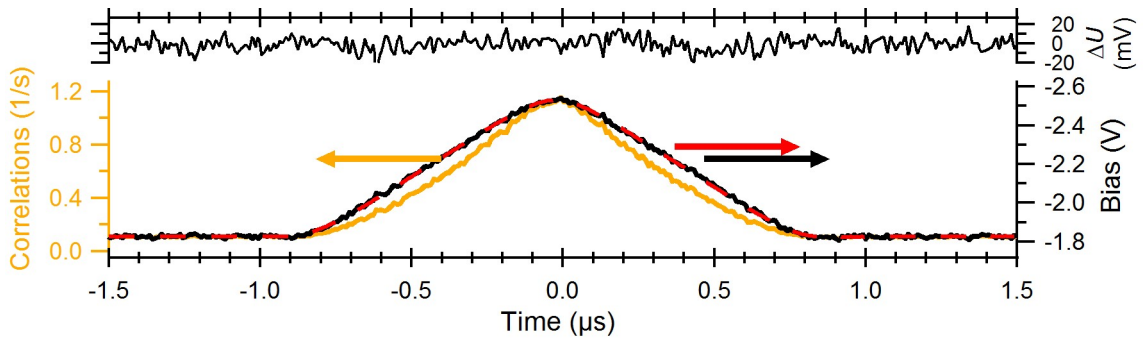
Fig. 3.2: Mapping of microsecond voltage pulses. Lower part: voltage pulse from the pulse generator ($U_0(t)$, red dashed curve) with a full width at half maximum (FWHM) of $870\,\text{ns}$, photon arrival time ($N(\Delta t)$, orange curve), and voltage profile at the tunnel junction ($U_\text{T}(t)$, black curve) derived from the photon signal. Upper graph: Difference between the pulses at the tunnel junction and the original pulses sent to the junction, $\Delta U = U_\text{T}(t) - U_0(t)$. Experimental bin width: $10\,\text{ns}$.

pulses reaching the junction should be the same as those produced by the pulse generator, that is, $U_T(t) = U_0(t)$. Indeed, the transient voltage $U_T(t)$ (solid black curve) calculated from the photon arrival time $N(\Delta t)$ (orange curve) by the calibration curve in Fig. 3.1 agrees very well with the input pulse. The difference between the transient voltage and the input pulses $U_T(t) - U_0(t)$ (black curve, upper graph) shows a uniform spread around zero. The error in the optically measured voltage profile mainly results from the statistical (Poisson) noise in the measured photon signal $N(\Delta t)$ and the accuracy of the calibration curve $N(V)$. The root mean square of the difference $U_T(t) - U_0(t)$ yields an error for $U_T(t)$ of less than $6\,\mathrm{mV}$, which corresponds to less than $0.4\,\%$ of the applied voltage.

3.1.2 Mapping of Nanosecond Voltage Pulses

When injecting triangular voltage pulses that are faster than $50\,\mathrm{ns}$ (Fig. 3.3a, dashed curves), the voltage transients at the tunnel junction (Fig. 3.3a, solid curves) deviate significantly from the injected pulses. For the shortest pulses with a width of $10\,\mathrm{ns}$, a more than 60% reduction in their pulse height as well as persistent voltage oscillations extending for more than $300\,\mathrm{ns}$ and amplitudes up to 20% of the main pulse can be observed. In order to verify that these oscillations are variations of the voltage at the tunnel junction, the calculated autocorrelation of the optically measured voltage transients (Fig. 3.3b) is compared with the measured pulse autocorrelation using only STM electronics (Fig. 3.3c). For the latter, two identical voltage pulses are added by a power combiner and sent to the STM tunnel junction. The delay $\Delta\tau$ between the two pulses is scanned and the resulting time averaged tunneling current $\langle I(\Delta\tau)\rangle$ is recorded as a function of $\Delta\tau$. Compared to the pulses in Fig. 3.3a, the data in Fig. 3.3c are obtained with slightly different pulse parameters (see caption Fig. 3.3) to cover a bias range with a non-linear current–voltage characteristic. The rectifying property of this nonlinearity causes the time-averaged tunneling current to change when parts of the pulses overlap in time.
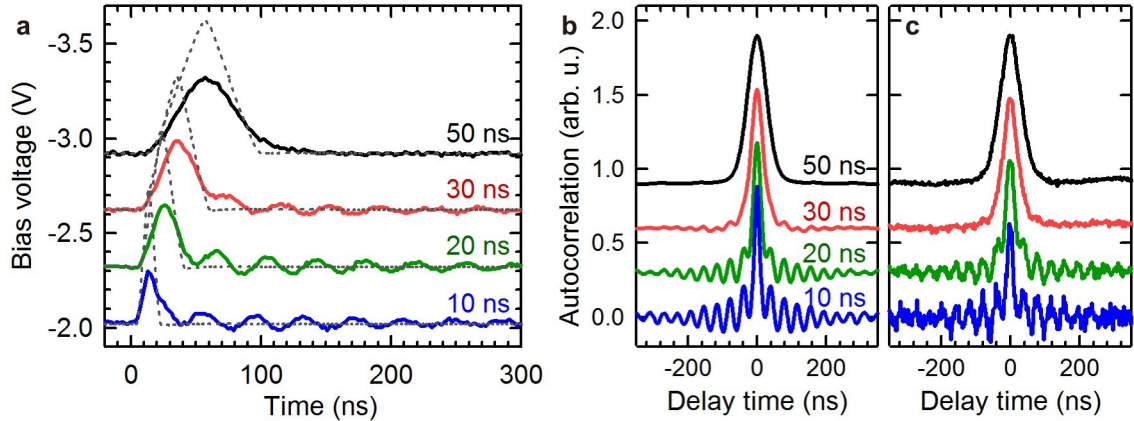
Fig. 3.3: Mapping of nanosecond fast triangular pulses. (a) Optically measured voltage profiles at the tunnel junction (colored curves) for fast triangular pulses of different widths sent to the STM tunnel junction (dashed curves, pulse widths denoted). All curves were recorded with a voltage offset of $-2.02\,\mathrm{V}$ and are shifted for clarity by increments of $-0.3\,\mathrm{V}$. Bin width in the time-correlated single-photon counting (TCSPC) experiment: $2\,\mathrm{ns}$. (b) Numerically derived autocorrelation of the optically measured pulses from panel a. (c) Electronically measured autocorrelation using the same (color-coded) pulse lengths as in panel a, but a voltage offset of $-1.5\,\mathrm{V}$ and a pulse amplitude of $-0.5\,\mathrm{V}$.

The all-electronic autocorrelation measurements (Fig. 3.3c) agree very well with the calculated autocorrelations of the optically measured voltage transients (Fig. 3.3b) and show the same "ringing" behavior. This confirms the reliability of the optical approach for measuring fast voltage transients.

3.2 Transfer Function of the Transmission Line

Figure 3.4 depicts the transient voltage $U_T(t)$ upon the injection of nanosecond fast rectangular pulses of different length. The pulses generated by the function generator exhibit a rising and falling edge of $2\,\text{ns}$, whereas the pulses arriving at the tunnel junction have falling edges of approximately $50\,\text{ns}$ width ($90\% - 10\%$ amplitude). This is most likely due to the finite bandwidth of the wiring of $20\,\text{MHz}$. As observed for the triangular pulse, again a strong ringing follows the pulses. Such strong deviations from the injected pulses are undesired and will obscure the dynamics in any time-resolved STM measurement.

By knowing the precise shape $U_0(t)$ of the pulses sent to the junction as well as the pulses arriving at the junction $U_T(t)$, the transmission through the bias line, i.e., its transfer function $T(\nu)$ can be determined by the ratio of the respective Fourier transforms of $U_T(t)$ and $U_0(t)$:

$$T(\nu) = \frac{\mathcal{F}[U_T(t)]}{\mathcal{F}[U_0(t)]}. \tag{3.1}$$

The resulting transfer function is depicted by the black curve in Fig. 3.4b. Alternatively, the real part of the transfer function is accessible by using only electronics (Fig. 3.4b, green curve) – analogous to the pulse autocorrelation discussed above – by adding a sine wave voltage to a DC bias and using the same nonlinearity as for the all-electronic autocorrelation.

From the two independent measurements of the transfer function, the ringing can be traced to three strong resonances at $25\,\text{MHz}$, $90\,\text{MHz}$, and $130\,\text{MHz}$. They most likely result from standing waves between the high-impedance tunnel junction and impedance mismatches at the intersections between different wire segments along the transmission line. It is worth noting that similar resonances and low passing behavior are likely to occur in any STM system that does not utilize special high-frequency wiring. Use of high-frequency connectors and wires can reduce such resonances,[93, 94] but may not always be implementable in commercial or existing STM systems, in which vibration isolation, the ultra-high vacuum (UHV) environment, low temperatures or high magnetic fields may limit the choice of high-frequency components.

3.3 Shaping of Pulses Arriving at the Tunnel Junction

Knowing the amplitude *and* phase of the transfer function, it is possible to compensate imperfections of the experimental setup by a proper choice of input pulses. Mathematically, the Fourier amplitudes of the desired pulse $A_0(\nu) = \mathcal{F}[U_0(t)]$ only need to be divided by the transfer function $T(\nu)$ to obtain the compensated pulse amplitudes:

$$A_{\text{comp}}(\nu) = \frac{A_0(\nu)}{T(\nu)}. \tag{3.2}$$

The back transformation then leads to the compensated voltage pulses that need to be sent to the tunnel junction:

$$U_{0,\text{com}}(t) = \mathcal{F}^{-1}[A_{\text{comp}}(\nu)] \tag{3.3}$$

This method is akin to pulse shaping in optical experiments[97] or pulse optimization in the transmission of digital signals.[98] Figure 3.4c shows some compensated voltage pulses from this approach. After propagation through the transmission line, these pulses lead to near-perfect
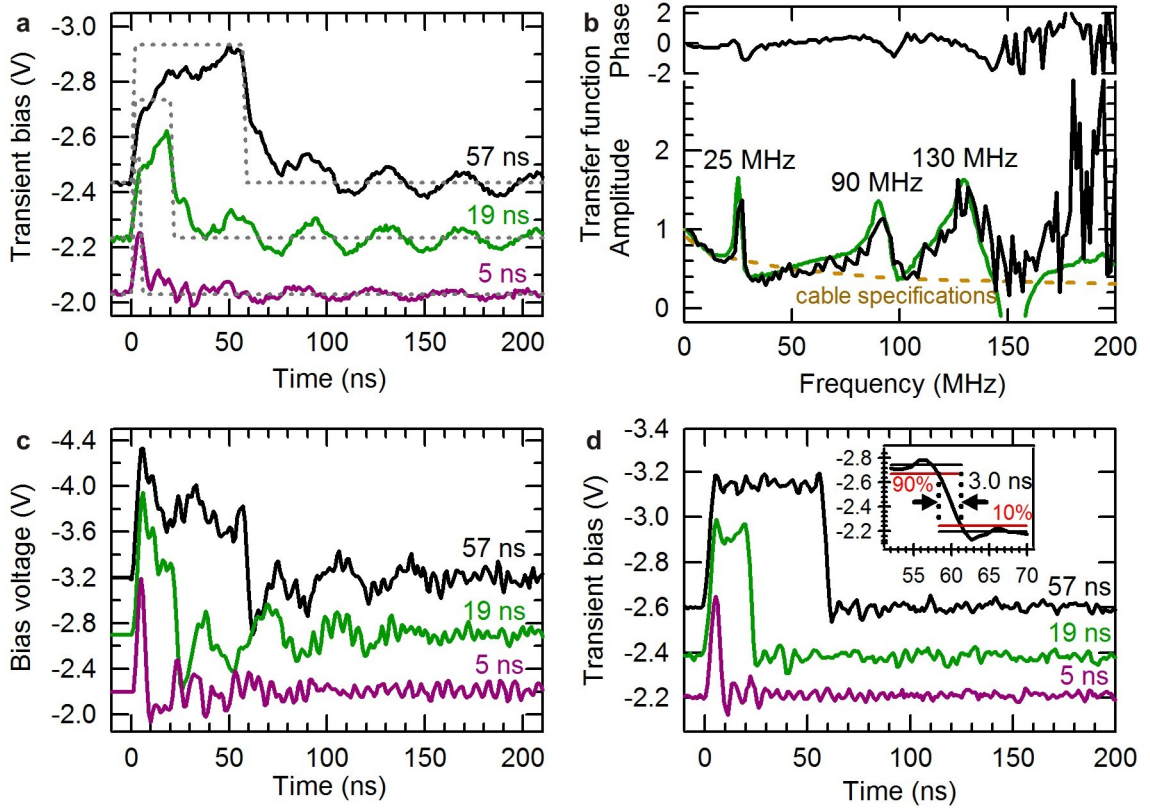
Fig. 3.4: Mapping of nanosecond fast rectangular pulses (a) Optically measured transient voltages (colored curves) for pulses of different lengths sent to the STM tunnel junction (dashed curves, pulse length denoted). (b) Transfer function of the transmission line between pulse generator and tunnel junction. Black curves: amplitude (normalized to 1 at 0 MHz) and phase (in radians) derived from the optically recorded data in panel a; green curve: electronically measured transfer function using a nonlinear current–voltage characteristic; brown dashed curve: cable specifications.[78] (c) Shaped voltage pulses sent to the STM tunnel junction to compensate for the distortion by the cables. (d) Optically measured transients at the tunnel junction for the pulses in panel c. The inset in (d) shows a zoom in on the falling edge of the 57 ns pulse. TCSPC bin width in panel a, c, and d: 1 ns. All curves in panel a were measured at an offset of −2.03 V and in panel c and d at an offset of −2.2 V. For clarity, curves are shifted by multiples of −0.2 V in panel a and d and by 0.5 V in panel c.

rectangular pulses with considerably reduced ringing and falling edges of 3 ns (90% − 10%) width (Fig. 3.4d). The residual voltage variations visible in Fig. 3.4d mostly arise from noise in the transfer function, which is calculated from data (Fig. 3.4a) and thus itself contains noise. In total, the pulse shaping used here leads to a sixteen-fold increase in performance and time response without physical modification of the wiring.

The experimental limit with respect to the compensation of cable imperfections will be given by the bandwidth and the maximum output amplitude of the arbitrary waveform generator. It may reach values well below 1 ns. For cables with good high-frequency performance, switching times will be limited by parasitic capacitances of the STM head. However, with an optimized design, voltage pulses as fast as 8 ps can be realized.[92] Regarding the optical detection scheme, the time resolution will be determined by the time jitter of the employed photon counting detector. The ultimate limit is, finally, defined by the plasmon lifetime, which is in the subpicosecond range.[18, 19]

3.4 Conclusions

This chapter has demonstrated a method to map nanosecond short voltage pulses sent to the tunnel junction of a scanning tunneling microscope with millivolt and nanosecond accuracy. By using the monotonic dependence of the plasmon emission on the applied bias voltage, the time-dependent voltage at the junction $U_T(t)$ can be directly determined from the time-dependent intensity. This quantitative knowledge of the transient voltage at the tunnel junction can be used to optimize the signal quality in the tunnel junction considerably. In this experiment, a time resolution of 3 ns could be achieved, which exceeds the bandwidth of the wiring by more than one order of magnitude.

The presented technique is non-invasive and can be used in any tunneling transport experiment in which plasmon-induced light emission is detectable. It may be applied to measure fast changes in the local electrostatic potential at the tunnel junction as caused by non-equilibrium effects, such as fluctuating charges on dopants or molecules, or transient screening by dipoles. Applied in STM, the generation of precisely defined, sharp voltage pulses at the tunnel junctions will provide the foundation to study luminescence dynamics on (sub)nanometer length scales. The first applications of the concepts developed in this chapter will be presented in section 5.6 and 8.2.5.

Chapter 4

Morphology and Electronic Structure of C_{60} Multilayers

After the discovery of C_{60} in 1985 by Kroto *et al.*,[99] the simple and efficient method of producing fullerenes developed by Krätschmer *et al.*[100] and the discovery of superconductivity in alkali-doped C_{60} by Hebard *et al.*[101] spurred intensive research on fullerenes and its most prominent member, the buckminsterfullerene C_{60}. Because of this intensive study and its unique properties, C_{60} has become a popular model system for a variety of different fields. It has been employed for investigating the nucleation and growth of molecules on surfaces,[102] for the realization of a single-molecule transistor[103] or even a superconducting single-molecule transistor,[104] and to prove the wave–particle duality of individual molecules.[105]

In this and the subsequent chapter, C_{60} films adsorbed on Ag(111) and Au(111) substrates are employed as model systems to investigate the local electronic structure of molecular solids and the dynamics governing the recombination of electron–hole pairs therein. In chapter 5 it will be demonstrated that the key for understanding the charge carrier dynamics lies in a proper understanding of the alignment of electronic states as well as their local variations.

Both factors will thus be discussed in section 4.4 and section 4.5 of this chapter. There, it will become evident that the local electronic structure of C$_{60}$ films decisively depends on the local degree of order and the orientation of the individual molecules. Therefore, this chapter will start with an overview about the structure and the morphology of thin C$_{60}$ films on the coinage metal substrates copper, silver, and gold.

4.1 Molecular and Solid State Structure of C$_{60}$

C$_{60}$, also known as buckminsterfullerene, is the most prominent and most abundant member of the fullerenes – spherical allotropes of carbon. By definition, fullerenes are polyhedral closed cages made up of n three-coordinated carbon atoms with 12 pentagonal and $(n/2 - 10)$ hexagonal faces, where $n \geq 20$.[106]

Molecular Structure

The buckminsterfullerene molecule C$_{60}$ consists of 60 carbon atoms forming the vertices of a truncated icosahedron (Fig. 4.1). As such, it is built up of 12 pentagonal faces and 20 hexagonal faces. All carbon atoms are equivalent and possess an sp^2-hybridization with weak sp^3 admixtures due to the curved surface. However, the three bonds emanating from each carbon are not equivalent. Two of the three bonds form the edges of the pentagons exhibit a length of $0.1455\,\mathrm{nm}$,[107] and are rather electron-poor, while the third bond, which fuses two hexagonal faces, has a length of $0.1391\,\mathrm{nm}$[107] and is rather electron-rich. Nevertheless, C$_{60}$ has the highest degree of symmetry of any known molecule and belongs to the icosahedral point group I_h.[108] This allows 120 symmetry operations consisting of the identity operation, 6 five-fold axes through the centers of the pentagonal faces, 10 three-fold axes through the centers of the hexagonal faces, 15 two-fold axes through the centers of the bonds fusing two hexagonal faces, plus the corresponding inversion operations. As a consequence of the very rigid structure and the absence of dangling bonds, C$_{60}$ is the largest stable molecule formed by a single elementary species.[108] It withstands heating to above 1000°C and collisions with other species in the energy range of hundreds of electronvolts.
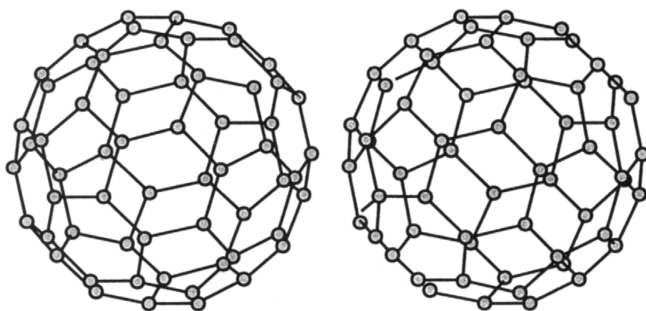
Fig. 4.1: Stereographic projection of C$_{60}$. In order to visualize a 3D image of the molecule, the eyes must focus at infinity between both structures. Obtained from ref. [108].

Solid State Structure

At room temperature, C$_{60}$ crystallizes in a face-centered cubic (fcc) structure held together only by van der Waals forces; thus, it is referred to as a van der Waals solid. The unit cell

of the lattice consists of four equivalent molecules with a lattice constant of $a_0 = 1.42$ nm and the symmetry of the $Fm\bar{3}m$ space group. Occasionally, the room temperature phase of C_{60} is referred to as a (orientatianally) *disordered phase* because the molecules rotate freely and uncorrelated from each other at their lattice positions.

When the temperature is lowered to ~260 K, the solid undergoes a first-order phase transition,[109, 110] in which the molecules lose two of their three degrees of orientational freedom. At the same time, the beforehand mentioned four equivalent molecules of the unit cell become inequivalent, and the fcc lattice changes to a simple cubic (sc) lattice with a $Pa\bar{3}$ space group. Because of the decreasing entropy, this sc-phase of C_{60} is commonly referred to as the (orientationally) *ordered phase*. The residual rotational motion of the molecule occurs around the [111] axis and three symmetry equivalent $[\bar{1}10], [0\bar{1}1], [10\bar{1}]$ axes – one axes for each of the four molecule of the unit cell.[107] Figure 4.2 depicts the orientation of these four axes. Strictly speaking, each molecule performs a site-specific, uniaxial jump reorientation between two stable configurations separated from each other by a rotational angle of ~60°.[110] The energy difference between these two configurations is

Fig. 4.2: Rotational axes of the four inequivalent molecules in the ordered phase of C_{60} below 260 K. The arrows indicate the sense of the rotation. Obtained from ref. [108].

~11.4 meV with an activation barrier of 290 meV.[108] In the thermodynamically favored configuration, electron-poor pentagonal faces of a C_{60} molecule oppose an electron-rich bond between two hexagons of a neighboring molecule or vice versa.[107] In the slightly less stable second configuration, on the other hand, a pentagonal face of a C_{60} molecule opposes a hexagonal face of a neighboring molecule or vice versa.[110] Both configurations can be described by a specific rotational angle around the various ⟨111⟩ axes or multiples of 120° added to these angles. It is noteworthy that different setting angles with respect to an anticlockwise rotation have been reported in the literature[110–114] ranging from 98° to 102° for the thermodynamically most stable configuration and 38° to 44.8° for the second configuration. Various surface sensitive techniques, such as low energy electron diffraction (LEED), electron energy loss spectroscopy (EELS) or Helium atom scattering have shown that the freezing of the two degrees of rotational freedom of surface molecule occurs about 30 K below the bulk phase transition.[115–117] Hence, the surface molecules are the last molecules that pass the first-order phase transition.

Around 90 K, the bulk molecules pass a further, second-order phase transition, by losing their last degree of rotational freedom and randomly latch into one of the two most stable configurations described above.[110, 118] Below this second phase transition, the abundance of both configurations is fixed and equals the equilibrium ratio at the transition temperature.[118] Because the configurations of neighboring molecules are not correlated to one another, this leads to *merohedral disorder* and the solid forms an orientational glass state.[110] At 5 K the lattice constant of this low-temperature phase at is 1.4042 nm.[118]

4.2 Morphology and Growth of C$_{60}$ Films

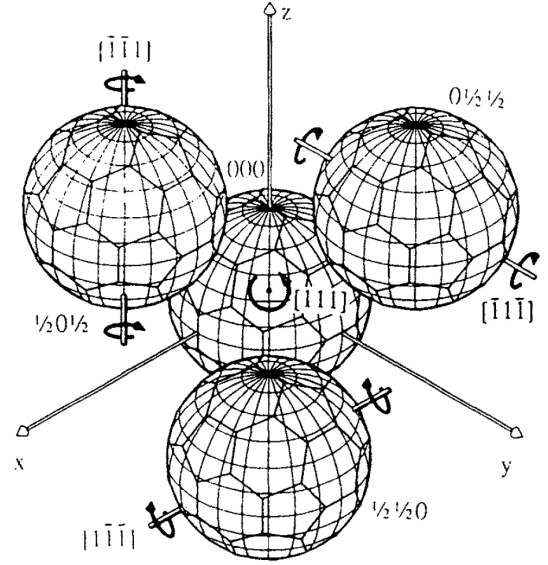The adsorption behavior of C$_{60}$ has been investigated by a variety of scanning tunneling microscopy (STM) studies on various substrates. Besides semiconducting surfaces, such as GaAs,[119] silicon,[120–124] layered materials,[125–127] and thin insulating layers,[128] most studies have focused on the group 11 or coinage metals: copper,[129–135] silver,[131–133, 136–144] and gold.[37, 131, 136, 138, 143, 145–157] Because of the high degree of order of grown C$_{60}$ films, this thesis focuses on the adsorption of C$_{60}$ on the (111) surface of these coinage metals. The following sections will shown that the properties of a single C$_{60}$ monolayer are primarily determined by the molecule–substrate interactions, whereas the properties of C$_{60}$ bi- and multilayers are governed by the much weaker intermolecular interactions.

4.2.1 C$_{60}$ Monolayers on Coinage Metal Substrates

On all (111) coinage metal surfaces, the thermodynamically most stable arrangement of C$_{60}$ molecules consists of a hexagonal close packing. However, the orientation of the hexagonal lattice with respect to the substrate lattice, as well as the orientation of the C$_{60}$ molecules, varies among the three metals (see below). The close-packed structures either form a commensurate superstructure with respect to the substrate or induce a reorganization of the metal surface to accommodate the C$_{60}$ overlayer. At low substrate temperatures, the formation of these structures is kinetically hindered; hence, the deposition of C$_{60}$ at cryogenic temperatures results in unordered or metastable structures.[134, 135, 154] In contrast, at room temperature the C$_{60}$ molecules possess enough thermal energy to diffuse to substrate step edges and narrow terraces, where they form close-packed overlayers. For the Au(111) surface minor deviations in the growth process and a greater tendency toward a growth on the terraces before a complete saturation of step edges have been reported.[137] The origin of this behavior was ascribed to the necessary lifting of the herringbone reconstruction of Au(111)[158] as well as the presence of more reactive fcc and less reactive hcp sites.

STM images acquired at room temperature have revealed different internal patterns of the individual C$_{60}$ molecules within the close-packed monolayers on Cu(111),[129] Ag(111),[136] and Au(111).[136, 147, 153] Hence, the free rotation of the molecule observed in the bulk must be inhibited for all three coinage metals and the molecule–substrate interaction must be substantially larger than the molecule–molecule interaction. Indeed, the adsorption energies of single C$_{60}$ molecules within a monolayer on Cu(111), Ag(111) and Au(111) have been calculated as $-2.2\,\mathrm{eV}$,[159] $-1.5\,\mathrm{eV}$[160] and $-1.2\,\mathrm{eV}$,[160] respectively, which is considerably larger than the intermolecular binding energy of ~$0.6\,\mathrm{eV}$.[161] The adsorption energy thus follows the reactivity of the metals and decreases down the periodic table. As the binding energy provides the driving force to form highly ordered structures, the degree of (orientational) order within the corresponding monolayers decreases and the variability of stable overlayer structures increases from copper, via silver, to gold. For example, on Cu(111) C$_{60}$ predominantly adsorbs in a $(4 \times 4)R0°$ superstructure in which all molecules of the unit cell occupy equivalent substrate sites and exhibit the same molecular orientation.[129, 132, 133] Additional metastable phases only exist below $370\,\mathrm{K}$.[134, 162] On Ag(111), the most stable phase comprises a $(2\sqrt{3} \times 2\sqrt{3})R30°$ superstructure in which the close-packing direction of the C$_{60}$ molecules is rotated by 30° with respect to the substrate lattice.[136, 137, 144, 163] In addition, two further phases exist in which

the close-packing direction is rotated by 12° or 46° with respect to substrate lattice.[132, 133, 136] Whereas the molecule in the $R12°$ and $R46°$ phase appear uniformly in STM images, the $(2\sqrt{3} \times 2\sqrt{3})R30°$ exhibits a mixture of *bright* and *dim* molecules, indicating two different adsorption geometries.

Finally, the Au(111) surface leads to hexagonal overlayers with the lowest degree of (orientational) order and the largest variability in different bonding scenarios. As on the Ag(111) surface, several hexagonal structures with close-packing directions along various substrate directions have been reported. Besides phases with a rotational angle of 30°, such as the thermodynamically most stable $(2\sqrt{3} \times 2\sqrt{3})R30°$ phase,[145, 150, 153, 155] structures with rotational angles of 0°,[145, 147, 153, 155] 14°,[145, 149, 150, 153, 155] and 34°[153] have been observed. To further complicate the situation, the individual molecules within these structures can occupy several different adsorption sites on the substrate and/or occur in various orientations. The unit cell of the $(\sqrt{589} \times \sqrt{589})R14.5°$ phase first reported by Schull *et al.*[149], for example, consists of 49 molecules in 11 different orientations.

4.2.2 C$_{60}$ Bi- and Multilayers on Coinage Metal Substrates

STM images acquired at increasing C$_{60}$ coverage show that the growth of a second C$_{60}$ layer does not start before the surface of the coinage metals is fully covered with a complete monolayer.[137, 145] Like the molecules in the monolayer, the molecules of the second layer arrange in hexagonal structures with their close-packing rows residing halfway between the rows of the first layer.[137, 145] The observed C$_{60}$ step heights of ~0.8 nm,[137, 145, 148] furthermore, matches the expected value for an molecular step edge between two (111) surfaces of bulk fcc C$_{60}$ (0.81 nm).* Both observations indicate that the second layer occupies the threefold hollow sites of the first layer; hence, C$_{60}$ grows epitaxially. As a result of the much higher diffusion barrier (~ 540 mV[102]), at room temperature the tendency to nucleate at step edges is less pronounced than for the monolayer and the bilayer edges appear rougher. In other words, their shape is kinetically hindered.[137, 145, 156] Room temperature STM images indicate a dynamic reorganization of the step edges and do not reveal any submolecular features. Together with the low desorption temperature of 570 K, which is ~200 K below the desorption of the monolayer on Ag(111) and Au(111), this suggests a much weaker interaction of the C$_{60}$ molecules within the second layer.

The observation of submolecular features within C$_{60}$ bilayers requires imaging at cryogenic temperatures. At liquid nitrogen temperature (77 K) Tang *et al.*[156] found a clear submolecular pattern solely for some molecules within a C$_{60}$ bilayer on Au(111), possibly an indication that not all surface molecules lost their last degree of rotational freedom. Nevertheless, the authors reported a (2×2) superstructure with a basic structural unit consisting of seven molecules. Similar (2×2) superstructures have been also observed on ~10 molecular layers (MLs) of C$_{60}$ on Si(100)[124] as well as on 2–4 MLs on NaCl.[128] The latter study was carried out at 50 K and reveals clear submolecular patterns on all surface molecules. By comparing the observed orbital patterns with calculated projections of a free C$_{60}$ molecule, this

---

*The (111) step height is accessible via $h_{(111)} = D \cdot \sqrt{6}/3$ from the diameter of a C$_{60}$ molecule D, which can be determined from the fcc latice constant of $a = 1.4042$ nm[118] by $D = a \cdot \sqrt{2}/2$

and previous studies[124, 129, 140, 142, 143] have demonstrated that it is possible to determine the molecular orientation within the surface layer from such STM images.

When the coverage is further increased, C$_{60}$ grows in pyramid-like structures at room temperature; that is, the third and higher layers begin to grow before the second layer is completed. The growth on the coinage metals thus resembles that on GaAs(110)[119] and VSe$_2$(0001)[127] surfaces. The origin of this growth mode lies in the rather large edge diffusion (Ehrlich–Schwoebel) barrier of 110 meV.[102] At elevated substrate temperatures these barriers can be overcome so that high quality films with out-of-plane coherence length of several hundred nanometers and in-plane coherence lengths comparable to those of the substrates become possible on Cu(111),[162] Ag(111)[164] and Au(111).[165, 166]

4.3 Electronic Structure of C$_{60}$ Films

4.3.1 C$_{60}$ Monolayers on Coinage Metal Substrates

As discussed in section 4.2.1, the molecule–substrate binding energy within a C$_{60}$ monolayer substantially exceeds the molecule–molecule interaction. This suggests that the bonding to the substrate must go beyond pure van der Waals interactions. Indeed, a number of experimental and theoretical techniques reveal a hybridization of the lowest unoccupied molecular orbital (LUMO) of the C$_{60}$ molecules with the metal substrate, as well as a charge transfer to the C$_{60}$ molecules, for all three coinage metals. A summary of studies performed on the corresponding (111) surfaces can be found in Tab. 4.1. Although the reported degree of hybridization and the amount of charge transferred to the C$_{60}$ molecules varies among different studies, most of them indicate an increase in interaction strength according to Au<Ag<Cu.

In X-ray photoelectron spectroscopy (XPS), the increasing charge transfer can be observed by an increasing asymmetry, width and shift of the $C\,1s$ core-level peak with respect to spectra acquired on C$_{60}$ multilayers.[167, 175, 177, 178] At the same time, techniques probing the electronic unoccupied states of surfaces, such as inverse photoelectron spectroscopy (IPES) and near edge X-ray absorption fine structure (NEXAFS) measurements indicate an increasing shift of the C$_{60}$ LUMO-derived states toward the Fermi level compared to the corresponding multilayer

Tab. 4.1: Studies indicating a charge transfer from coinage metal substrates to a C$_{60}$ monolayer. If reported the amount of electrons transfered per C$_{60}$ molecule (Δe) and the work function of the surface (Φ in eV) are denoted.

Surface	Δe	Φ	Method	Ref.
Au(111)	0.8	4.7	UPS, NEXAFS	[167]
	0.2	4.95	DFT	[160]
	0.9		DFT	[168]
	0.01		DFT-based tight binding	[169]
		4.8	DFT	[161]
		4.53	KPFM	[170]
			STM	[147]
			STM	[171]
Ag(111)	0.75	4.7	UPS	[172]
	0.3		DFT-based tight binding	[169]
	0.5	4.95	DFT	[160]
		5.19	KPFM	[170]
			UPS	[173]
			UPS	[174]
			STM	[136]
Cu(111)	1.5–2	4.86	UPS, NEXAFS	[175]
	0.8	5.15	DFT	[159]
	1.6		HREELS	[176]
		5.07	KPFM	[170]
			STM	[171]

spectra.[167,175,177] In particular, inverse photoemission spectra show that the C_{60} LUMO-derived states exhibit a tail that extends down to the Fermi level – a clear indication for the hybridization between C_{60} and metal states. UPS studies, which probe the electronic occupied states of surfaces, confirm the LUMO tail and reveal a non-zero density of states (DOS) within the entire HOMO–LUMO gap (see Fig. 4.3a).[167,175] Similar results have also been observed in various STM studies on Au(111),[147,171] Ag(111),[136] and Cu(111).[171] Therefore, C_{60} monolayers adsorbed on the coinage metals copper, silver and gold have a metallic character. Two additional consequences that follow from the hybridization and the redistribution of charges are a reduction of the observed HOMO–LUMO energy gap and the formation of an interfacial dipole layer. As a consequence, the LUMO is pinned near the substrate Fermi level and the work function is changed accordingly.[177] Hence, C_{60} layers adsorbed on coinage metals show a Fermi level alignment of their states instead of a vacuum level alignment.

4.3.2 C_{60} Bi- and Multilayers on Coinage Metal Substrates

When additional C_{60} layers are adsorbed on the monolayer they follow the Fermi level pinning of the first layer,[177] albeit their electronic structure differ substantially due to the absence of a direct contact and their larger separation from the metal substrate. The different electronic structures of C_{60} monolayers and multilayers has two origins: First, the absence of a direct hybridization with the metal substrates precludes charge transfer to, and thus a partial occupa-
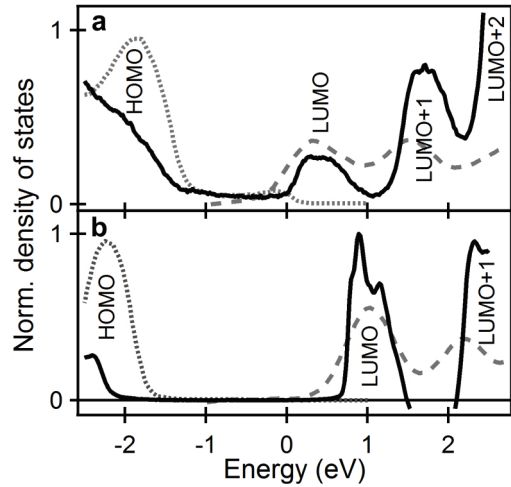
Fig. 4.3: Electronic structure of various C_{60} layers. (a) Tunneling spectrum (solid line), photoelectron spectrum (dotted line) and inverse photoelectron spectrum (dashed line) of a C_{60} monolayer on Ag(111). (b) Tunneling spectrum (solid line) of a C_{60} bilayer as well as photoelectron spectrum (dotted line) and inverse photoelectron spectrum (dashed line) of a few tens of nanometers thick C_{60} film adsorbed on Ag(111). Tunneling spectra were acquired at 4 K; photoelectron and inverse photoelectron spectra were acquired at room temperature and are reproduced from ref. [173]. (c) Summary of reported values for the HOMO- and LUMO-derived states of various C_{60} film thicknesses on different substrates.

c Substrate	C_{60} layers	HOMO [eV]	LUMO [eV]	Method	Ref.
Ag(111)	1	−1.95	0.3	UPS, IPES	[173]
Ag(110)	1	−1.8	–	UPS	[179]
Ag	1	−1.8	–	UPS	[178]
Ag(111)	multilayer	−2.2	1	UPS, IPES	[173]
Ag(110)		−2.2	–	UPS	[179]
Ag		−2.2	–	UPS	[178]
Au(111)	1	−1.7	–	UPS	[167]
Au(110)	1	–	0.9	IPES	[180]
Au	1	−1.8	–	UPS	[178]
Au	1	–	0.9	IPES	[177]
Au(111)	2	−2.0	–	2PPE	[181]
Au(111)	3	−2.0	–	2PPE	[181]
Au(111)	3	−2.1	–	UPS	[167]
Au(111)	multilayer	−2.0	–	2PPE	[181]
Au(110)		–	1.5	IPES	[180]
Au		−2.2	1.5	UPS, IPES	[177]

tion of, the LUMO-derived states. Therefore, the C$_{60}$ LUMO-dervied states do not show a tail extending to the Fermi level and C$_{60}$ bi- and multilayers are semiconducting. Second, the larger distance to the metal surface reduces the substrate screening, which cannot be compensated by the increased polarizability of the C$_{60}$ film due to the three additional neighbors per molecule.[†] Both factors result in a shift of the electronic levels of C$_{60}$ bi- and multilayers in UPS and IPES (Fig. 4.3b) compared to the spectra on a C$_{60}$ monolayer. A summary of reported energies for the HOMO- and LUMO-derived states on various gold and silver surfaces can be found in Fig. 4.3c. Some of the denoted studies found weak shifts of the electronic states between C$_{60}$ bi- and multilayers. However, all of them agree that the observed electronic states of three and more C$_{60}$ layers are identical to those observed for the surface of bulk C$_{60}$. The slightly different energy levels of C$_{60}$ bi- and trilayers might result from the decreasing screening by the substrate, which becomes negligible for thicker layers.

4.4 Band Bending of C$_{60}$ States in STM

Compared to photoemission and inverse photoemission spectra, the energy levels of C$_{60}$ multilayers observed in differential conductance ($\mathrm{d}I/\mathrm{d}U$) spectra seem to linearly shift with film thickness. Figure 4.4a displays a set of such $\mathrm{d}I/\mathrm{d}U$ spectra (black curves) acquired on the different terraces of a C$_{60}$ pyramid formed (Fig. 4.4b). The height difference of the individual terraces of 0.79 nm is within the calibration accuracy of the microscope with the expected value of 0.81 nm for a molecular step edge between two (111) surfaces of bulk C$_{60}$ at 5 K. The $\mathrm{d}I/\mathrm{d}U$ spectra in Fig. 4.4a show that the three-fold degeneracy of the LUMO is lifted and it splits into three separated states. In UPS and IPES spectra acquired at room temperature (Fig. 4.4a, gray curve), this splitting is most likely obscured by the larger temperature broadening of the peak, albeit the electric field in the STM junction might further increase the splitting of the LUMO-derived states. $\mathrm{d}I/\mathrm{d}U$ spectra acquired on C$_{60}$ films of the same thickness show only minor variations, with the position of the three LUMO-derived peaks being essentially independent of the lateral position and the orientation of the surface molecules. Only the peak intensities vary slightly. Therefore, the C$_{60}$ states might form band-like states, similar to that observed for a C$_{60}$ monolayer on thin insulating films.[182]

A fit of the three LUMO-derived states on the various C$_{60}$ terraces in Fig. 4.4a as the sum of three Gaussians reveals that the apparent peak positions shift linearly with increasing film thickness (Fig. 4.4c). By a comparison of the peak positions with those observed on C$_{60}$ bilayers [(0.80 ± 0.02) V; (0.93 ± 0.03) V; (1.15 ± 0.01) V] and C$_{60}$ trilayers [(1.14 ± 0.16) V; (1.38 ± 0.16) V; (1.6 ± 0.2) V], the lowest layer in Fig. 4.4a–c can be identified as a C$_{60}$ trilayer. $\mathrm{d}I/\mathrm{d}U$ spectra on the same C$_{60}$ terrace, but at different tip–sample distances Δz_{rel} show a shift in the opposite direction; that is, with increasing vacuum barrier thickness the LUMO-derived states shift toward lower voltages (Fig. 4.4d). Both observations – the shift of the LUMO-derived states as function of the C$_{60}$ film thickness and as a function of the vacuum barrier thickness – can be rationalized by regarding the STM tunnel junction as a plate capacitor that is partially filled with a dielectric. The following paragraphs will employ this model of a plate capacitor to derive an emperical formula (eq. (4.6)), which quantifies

---

[†]each molecule within the monolayer has six neighbors, while each surface molecule in a multilayer has nine neighbors

the bending of the C$_{60}$ state due to the electric field in the STM junction. This formula will provide an important keys to unveil the STM-induced luminescence and the charge carrier dynamics discussed in chapter 5.

4.4.1 Assumptions for the Quantitative Evaluation of the Band Bending

The picture of a plate capacitor is justified if the curvature of the STM tip is much larger than the effective distance between the STM tip and the metal substrate. In this context is is noteworthy that, because of the dielectric properties of the C$_{60}$ film, the effective thickness of the C$_{60}$ film is a factor of its dielectric constant ($\epsilon_r \sim 4$) smaller than its real thickness. If
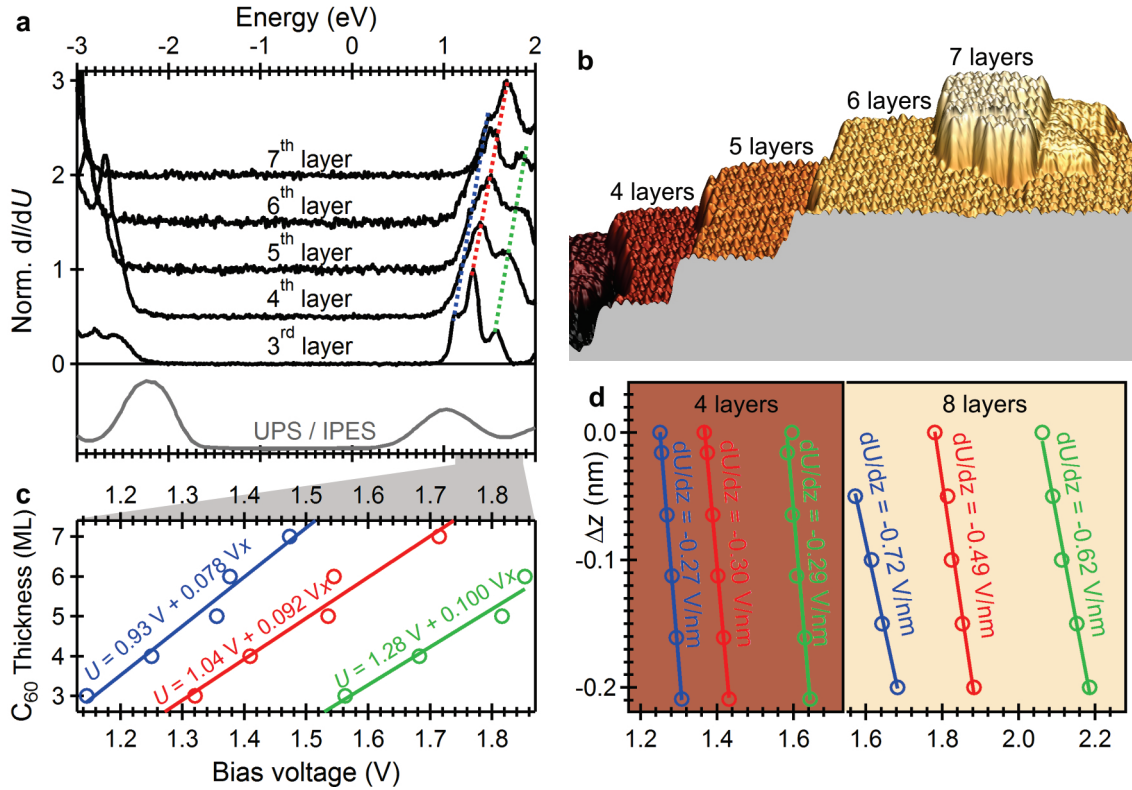
Fig. 4.4: Electronic structure of C$_{60}$ multilayers in STM. (a) dI/dU spectra acquired on the different terraces of a C$_{60}$ pyramid imaged by the STM topography in (b) (U_{set} = 1.7 V, I_{set} = 20 pA). The lowest layer could be identified as a C$_{60}$ trilayer. For clarity, the spectra in panel a are shifted by multiples of 0.5. All dI/dU spectra were acquired at the same set point parameters (U_{set} = 2 V, I_{set} = 50 pA) and on a C$_{60}$ molecule with a hexagonal face pointing to the STM tip, which was located in the center of the corresponding terrace. The gray curve at the bottom of panel a depicts a room temperature UPS spectrum and an IPES spectrum of a few ten nanometers thick C$_{60}$ film on Ag(111), which were reproduced from ref. [173] (c) Shift of the three LUMO-derived peaks (colored circles) in panel a, determined from a fit with three Gaussians, as a function of the C$_{60}$ film thickness. The colored lines show a linear fit of the corresponding peak positions, with the fit function being denoted next to them. (d) Shift of the three LUMO-derived states on a 4 and 8 MLs thick C$_{60}$ film as a function of the relative STM tip–sample distance (Δz_{rel}). The colored lines show linear fits of the peak positions with the corresponding slopes of the fit functions being denoted next to them.

the dielectric properties of the C$_{60}$ film are further assumed to be independent of the electric field in the junction as well as independent of the film thickness, the electric field in the vacuum barrier and in the C$_{60}$ film is homogeneous. Finally, as the work function of the metal substrate and the STM tip are comparable to each other, the electric field strength (E) in the vacuum barrier and the electric field strength in the C$_{60}$ film are simply related to the corresponding effective thickness (d) and the voltage drop (U) according to:

$$E_{\mathrm{vac}} = \frac{U_{\mathrm{vac}}}{d_{\mathrm{vac}}}; \qquad E_{\mathrm{C}60} = \frac{U_{\mathrm{C}60}}{d_{\mathrm{C}60}} \qquad (4.1)$$

4.4.2 Implications of the Assumptions

When the voltage drop across the vacuum barrier (U_{vac}) equals the potential of one of the LUMO-derived states, electrons can tunnel from the STM tip into the corresponding state (Fig. 4.5) and the dI/dU signal exhibits a maximum. Because the applied bias voltage is the sum of the voltage drop across the vacuum barrier (U_{vac}) and the voltage drop across the C$_{60}$ film ($U_{\mathrm{C}60}$):

$$U_{\mathrm{bias}} = U_{\mathrm{vac}} + U_{\mathrm{C}60}, \qquad (4.2)$$

the LUMO-derived states are thus observed at a bias voltage of:

$$U_{\mathrm{LUMO}}^{\mathrm{obs}} = U_{\mathrm{LUMO}}^{0} + U_{\mathrm{C}60}, \qquad (4.3)$$

where U_{LUMO}^{0} is the potential of the LUMO-derived states at zero electric field.

4.4.3 Shift of LUMO-derived States as a Function of the C$_{60}$ Thickness

When the C$_{60}$ layer thickness is increased while keeping the vacuum barrier thickness constant, the voltage drop across the C$_{60}$ layers rises at the expense of the voltage drop across the vacuum barrier. According to eq. (4.3), this must lead to a shift of the observed peak positions toward higher bias voltage. Rearrangement of eq. (4.1) to $U_{\mathrm{C}60}$ and insertion into eq. (4.3) yields:

$$U_{\mathrm{LUMO}}^{\mathrm{obs}} = U_{\mathrm{LUMO}}^{0} + E_{\mathrm{C}60} \cdot d_{\mathrm{C}60} \qquad (4.4)$$

Therefore, a plot of $U_{\mathrm{LUMO}}^{\mathrm{obs}}$ as a function of the C$_{60}$ layer thickness $d_{\mathrm{C}60}$ is linear, with the electric field in the C$_{60}$ film as its slope. When $U_{\mathrm{LUMO}}^{\mathrm{obs}}$ is plotted as a function of the number of C$_{\mathrm{C}60}$ layers (n), the corresponding slope equals the electric field divided by the thickness of one C$_{60}$ layer (0.81 nm). Presuming that the first C$_{60}$ layer is energetically
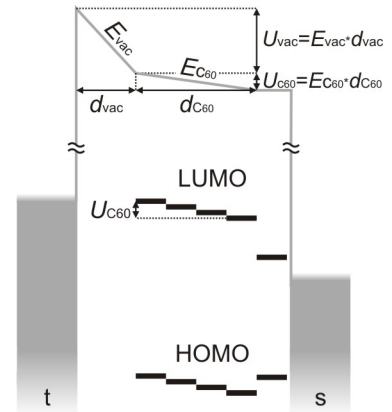

Fig. 4.5: Voltage drops and electric fields strength within the STM junction.

pinned to the metal substrate (see section 4.3.1), the extrapolation of the obtained linear fit functions (see Fig. 4.4) to one layer results in the potentials of the LUMO-derived states at zero field (U_{LUMO}^{0}). The determined zero-field potentials are: $U_{\mathrm{LUMO}1}^{0} = (1.01\pm0.035)$ V; $U_{\mathrm{LUMO}2}^{0} = (1.14 \pm 0.05)$ V; $U_{\mathrm{LUMO}3}^{0} = (1.38 \pm 0.06)$ V. The mean energy of these three states, 1.18 V, reasonably agrees with the 1 eV found in IPES spectra of C_{60} multilayers on Ag(111).[173]‡

Knowing the zero-field potentials of the LUMO-derived states, it is now possible to determine the relative voltage drop across the C_{60} film for a given number of molecular layers (n):

$$u_{\mathrm{C60}}(n) = \frac{U_{\mathrm{C60}}}{U_{\mathrm{bias}}} = 1 - \frac{U_{\mathrm{vac}}}{U_{\mathrm{bias}}} \tag{4.5}$$

At the observed peak positions, U_{vac} equals the zero-field potential of the LUMO-derived states. Inserting these into eq. (4.5), together with the fit functions from Fig. 4.4c, yields

$$u_{\mathrm{C60}}(n) = 1 - \frac{1}{a + b \cdot n} \tag{4.6}$$

with the two empirical parameters $a = 0.92 \pm 0.01$ and $b = 0.077 \pm 0.004$. This formula allows one to estimate the absolute band bending of the C_{60} film for a given bias voltage and film thickness at the set point parameters chosen in Fig. 4.4a ($U_{\mathrm{set}} = 2$ V, $I_{\mathrm{set}} = 50$ pA). For example, when applying a bias voltage of $U_{\mathrm{bias}} = 3$ V on top of an eight layers thick C_{60} film, the absolute voltage drop across the C_{60} film is $U_{\mathrm{C60}} = 1.05$ V.

4.4.4 Shift of LUMO-derived States as a Function of the Vacuum Barrier Thickness

The shift of the LUMO-derived states as a function of the vacuum barrier thickness for a given C_{60} film thickness reflects the change of the voltage drop across the C_{60} film induced by a change of the relative STM tip–sample distance (Δz_{rel}). In other words, the slope of a linear fit of the observed peak positions $U_{\mathrm{LUMO}}^{\mathrm{obs}}$, plotted as a function of Δz_{rel}, equals the change of the voltage drop within the C_{60} layer caused by z-displacement of the STM tip:

$$\frac{\partial U_{\mathrm{LUMO}}^{\mathrm{obs}}}{\partial d_{\mathrm{vac}}} = \frac{\partial U_{\mathrm{C60}}}{\partial d_{\mathrm{vac}}} \tag{4.7}$$

Again, this can be rationalized by the fact that at the observed $\mathrm{d}I/\mathrm{d}U$ peak positions, the voltage drop across the vacuum barrier always matches the zero-field potential of the corresponding LUMO-derived state. Hence, a change in the observed peak position can only result from a change in the voltage drop across the C_{60} film. Figure 4.4d shows two data sets obtained for two different C_{60} film thicknesses. With the observed LUMO peak positions and the fit functions denoted in Fig. 4.4c, the film thickness could be determined as 4 MLs and 8 MLs, respectively. In the case of the 4 MLs thick film the mean value of the fitted slopes in

---

‡A slightly better agreement is obtained when the potential of the LUMO-derived states is extrapolated to zero C_{60} layers.

Fig. 4.4d is $-0.3\,\text{V/nm}$, whereas in the case of the 8 MLs thick film it is $-0.6\,\text{V/nm}$. These values demonstrate that the voltage drop across the 8 MLs thick film is twice as strongly affected by a certain z-displacement of the STM tip than the four layers thick film.

4.4.5 Estimation of the Dielectric Constant of the C$_{60}$ Films

The dielectric constant of the C$_{60}$ film ϵ_r expresses the factor by which its dielectric properties decrease the field in the C$_{60}$ layer (E_{C60}) compared to the one in the vacuum barrier (E_{vac}):

$$E_{\text{C60}} = \frac{E_{\text{vac}}}{\epsilon_r}.$$

(4.8)

By insertion of eq. (4.8) and eq. (4.1) into eq. (4.2) and differentiation with respect to d_{vac}, it can be shown that:

$$\epsilon_r = -\frac{\partial U_{\text{LUMO}}^{\text{obs}}}{\partial d_{\text{vac}}} \cdot \frac{U_{\text{vac}}}{d_{\text{C60}} \cdot E_{\text{C60}}{}^2}.$$

(4.9)

According to eq. (4.4) and eq. (4.7), the dielectric constant of the C$_{60}$ film can thus be obtained from the fitted slopes in Fig. 4.4c and Fig. 4.4d. Along the fitted lines, the voltage drop across the vacuum barrier again equals the zero-field potential of the LUMO-derived states (U_{LUMO}^0). Averaging over the three LUMO-derived states results in a dielectric constant of 8.5 and 9.1 for the 4 and 8 MLs thick C$_{60}$ film, respectively. These values are a factor of two larger than the dc dielectric constant reported for bulk C$_{60}$ ($\epsilon_r = 4.4$[108]). The deviation might indicate a higher dielectric constant for such thin C$_{60}$ films, albeit they could also arise from experimental limitations of the used method. In fact, the data sets in Fig. 4.4c and Fig. 4.4d were acquired with macroscopically different STM tips; hence, the specific shape and strength of the electric field in the STM junction might have been different in both experiments. Therefore, the determined slopes, strictly speaking, cannot be inserted together into eq. (4.9). Additional experiments with both data sets obtained with the same tip could clarify this discrepancy. Furthermore, these experiments could verify whether the dielectric constant of the C$_{60}$ film varies as a function of the film thickness.

4.5 Localized Electronic States Caused by Disorder

This section will show that structural defects in the C$_{60}$ film and local orientational disorder causes the formation of spatially localized electronic split-off states in the band gap of the molecular solid. This will be achieved by mapping the molecular orientations as well as the local electronic structure of C$_{60}$ multilayers by STM. Furthermore, it will be demonstrated that these split-off states act as shallow traps for injected charge carriers, which entails a locally increased (radiative) recombination of electron–hole pairs. Additional tight binding calculations of the films, which are based on the experimentally observed molecular orientations in the surface layer, will be employed to confirm that the existence of these states can be fully explained by local disorder. Beyond that, these calculations offer two additional prospects.

First, they identify local perturbations of the hopping integrals – that is, the spatial orbital overlap between neighboring molecules – as the origin of the split-off state. Second, they might provide a unique way to determine the orientational configuration in the sub-surface layer(s).

Figure 4.6a depicts a typical STM image of the HOMO-derived states of a C_{60} film with more than 6 MLs. Previous STM studies have shown that the orientation of individual C_{60} molecules can be determined by comparing the observed orbital patterns with the calculated projections of a free C_{60} molecule.[124, 128, 129, 140, 142, 143] Three main orientations can be observed in Fig. 4.6a, in which either a hexagonal face (h), a bond between two hexagons (h:h), or a bond between a hexagon and a pentagon (h:p) points toward the STM tip. At negative voltages around -3 V, these three orientations lead to a three-lobed, an oval and a triangular pattern, respectively.[§] On closer inspection, the h-C_{60} occur in two and the h:h-C_{60} as well as the h:p-C_{60} in three variants that deviate from each other by a rotation of 180° and 120° around the surface normal, respectively. The precise orientational configuration of the surface molecules in Fig. 4.6a is schematically depicted in Fig. 4.6b. In the upper part, the molecules form a clear (2×2) superlattice (red parallelogram), which has been also observed for C_{60} multilayer on Si(100)[124] and on thin NaCl films.[70] The molecular orientation in this case matches the fully equilibrated and (111)-terminated low-temperature bulk structure of C_{60}.[107] Within this structure, each of the four molecules can be described by a rotation around one of the four equivalent crystallographic [111] axes, with only one general setting angle for all of these four molecules (see section 4.1). Later diffraction experiments have shown that in addition to this (H) configuration, a small fraction of molecules reside in a second, only ~10 meV less stable (P) configuration, which can be described by a second setting angle along the same [111] axes.[110] The arbitrary distribution of both configurations eventually results in a glass state and is the major source of disorder at low temperatures. On closer inspection of

[§]Although these three orientations can be well distinguished by imaging the LUMO-derived states of the molecules (positive voltages), it is very difficult to determine the precise azimuthal angle of the h:p-C_{60} molecules around the surface normal due to the radial symmetry of their orbital patterns.
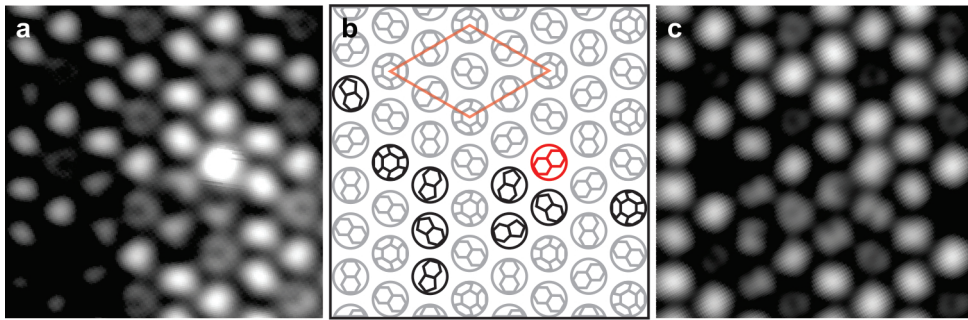
Fig. 4.6: Orientation of the surface molecules of a 6–9 MLs thick C_{60} film on Ag(111). (a) Constant height current image of the HOMO-derived states ($U_{set} = -3$ V). (b) Schematic representation of the orientation of the surface molecules determined from the STM image in panel a. Gray pictograms indicate molecules oriented in the thermodynamically most stable (H) orientation forming a (2×2) superstructure (red parallelogram), while black pictograms indicate molecules in the slightly less stable (P) orientation. The molecule depicted in red deviates from the two possible configurations and appears slightly higher in topography images compared to the other surface molecules. (c) Calculated STM image of the HOMO-derived states based on the orientation of the surface molecules in panel a and b.

Fig. 4.6b, the orientations of the molecules depicted by the black pictograms fully agree with this second most stable configuration. The only exception is the molecule represented by the red pictogram. In constant height topography images, this molecule appears slightly higher and exhibits an orbital pattern typical for an h:h-C$_{60}$. The origin of this deviation might be an uncharged impurity underneath the surface layer, which is discussed below.

The HOMO and LUMO of C$_{60}$ are primarily linear combinations of the $2p_z$ orbitals pointing radially out from each C atom. Hence, for the calculations a basis set consisting of these 60 $2p_z$ orbitals per C$_{60}$ molecule is used.[183] The resulting five-fold degenerate HOMO and the three-fold degenerate LUMO per C$_{60}$ molecule are then employed as a basis set for the calculation of the solid. The parameters of the following tight-binding calculations have been adjusted to band structure calculations.[184] This approach has been shown to accurately reproduce a full band structure calculation.[185] For the present calculation, a (111) surface of an fcc lattice is considered with $12 \times 12 \times 6$ molecules and periodic boundary condition in the lateral directions. The orientation of each molecule is defined as described below. To obtain the STM spectrum and images, the eigenfunctions are calculated at a distance $z = 1$ nm outside the surface, describing each C $2p$ orbital according to the Slater rules.[186] The spectra and images are then generated by an averaging of the resulting local density of states (LDOS) in space (0.1 nm) and energy (images: 2 meV, spectra: 5 meV).

Figure 4.6c displays the calculated STM image of the HOMO-derived band based on the molecular orientation in Fig. 4.6b. The remaining molecules of the calculated slab outside the printed area are oriented in the most stable H configuration. The best agreement between the experimental and calculated images is obtained by a pair of setting angles of 98° and 38° for the H and P configuration, respectively. The molecule represented by the red pictrogram in Fig. 4.6b is oriented identically to its upper left and lower right neighbors and lifted by 0.02 nm compared to the remaining molecules in the surface layer. The calculated image nicely reproduces the intensity ratios and symmetries of the individual molecules in the experimental STM image.

When reducing the bias voltage to values close to the HOMO- or LUMO-derived band onsets, individual localized states appear near both band edges (Fig. 4.7a,b). Whereas the state close to the LUMO-derived band (Fig. 4.7b) possesses its spatial maximum on the slightly raised C$_{60}$ molecule **1**, the much more intensive state close to the HOMO-derived band (Fig. 4.7a) is mostly localized on the neighboring molecule **2**. dI/dU spectra on both molecules, as well as on C$_{60}$ molecules further away (gray curve in Fig. 4.7c) demonstrate that these states lie in the band gap of the C$_{60}$ multilayer. Moreover, the splitting of the HOMO-derived state is much larger than the one of the LUMO-derived state.

When calculating the electronic structure close to the band edges, it is observed that the energy and localization of the highest occupied state sensitively depends on the exact orientational configuration of the molecules in the second layer beneath the surface layer. Therefore, the electronic structure of the system has been calculated for all permutations of the two possible orientations for the twelve nearest neighbors of molecule **2** in the second layer. Interestingly, only 19 out of the 2^{12} possible permutations result in a predominant localization of the highest occupied state as well as an STM intensity maximum on molecule **2**. In the majority of cases, the highest LDOS occurs on other surface molecules, most often on the slightly lifted molecule **1**. For the reverse succession of the fcc layers, none of the 2^{12} permutations result in an LDOS maximum on molecule **2**. These results suggest that the combination of the experiments
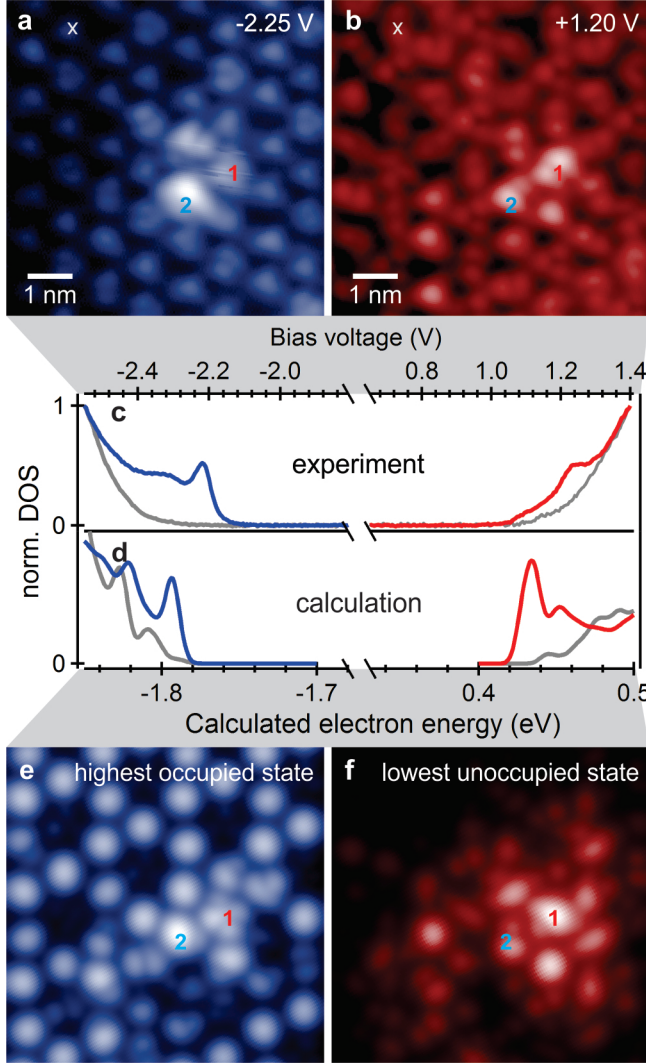
Fig. 4.7: Electronic structure at the band edge of the HOMO- and LUMO-derived states in the same area as depicted in Fig. 4.6. (a) Constant height current map of the HOMO-derived split-off state and (b) the LUMO-derived split-off state. The bias voltage is denoted at the top right of each map. (c) Differential conductance (dI/dU) spectra acquired on molecule **1** (red) and **2** (blue). The gray curve shows the dI/dU spectrum on a reference molecule in an idealized ordered region marked by the white cross. (f) Calculated dI/dU spectrum, (g) map of the highest occupied electronic state and (h) map of the lowest unoccupied state.

and the calculations enables the determination of both the position and the orientation of the molecules in the second layer. The calculated STM map of the highest occupied state and the lowest unoccupied state of the system for the configuration that leads to the best agreement with the experimental data is displayed in Fig. 4.7e and Fig. 4.7f, respectively. The corresponding orientation of the molecules in the surface and the second layer is encoded in Fig. 4.8. Both simulated STM images as well as the simulated dI/dU spectra (Fig. 4.7d) on the equivalent lateral positions qualitatively agree with the experiment. The different energy scales in both the experiment and the calculation primarily have two origins. On the one hand, the calculated band gap is underestimated as many-body effects are neglected. On the other hand, the experimental band gap is overestimated because of the band bending of the C_{60} states due to the electric field between the STM tip and the metal substrate (see section 4.4).

In the following, the origin of the observed split-off states will be discussed. As mentioned above, the majority of C_{60} molecules are in the thermodynamically most stable P orientational configuration. Therefore, the electronic structure of the C_{60} film is primarily determined by

the charge carrier hopping between P molecules. Molecules in the slightly less stable H configuration can be regarded as perturbations to the periodic electronic structure by varying the local hopping integrals, that is, the spatial overlap of the wavefunctions between neighboring molecules. The larger the local changes of the hopping integrals caused by a deviating orientation, the larger is the local perturbation and thus the splitting of the localized state from the band center. Figure 4.8 depicts the local changes of the hopping integrals for the HOMO- and the LUMO-derived states compared to the perfectly ordered structure. In the case of the HOMO-derived states (Fig. 4.8a), each colored segment represents the summed squares of 25 hopping integrals resulting from the five-fold degeneracy of the C_{60} HOMO. In the case of the LUMO-derived states (Fig. 4.8b), each colored segment represents the summed squares of 9 hopping integrals resulting from the three-fold degeneracy of the C_{60} LUMO.

As expected, all molecules in an H configuration (black circles) cause a change in the local hopping integrals and thus a perturbation of the local electronic structure. The strongest variation of the HOMO-derived hopping integrals (Fig. 4.8a) arise around molecule **1** and **2**, with the maximum change (black segment) occurring exactly between these two molecules. This explains the observation of the highest occupied state in this region. For the LUMO-derived states (Fig. 4.8b), none of the changes of the hopping integrals is particularly high. Instead, the maximum changes occur on *all* h:p-C_{60} – that is, molecules with a hexagon-pentagon bond facing the STM tip. Compared with these C_{60} molecules, the perturbation on molecule **1**, which leads to the highest STM intensity both in experiment and calculation, is weaker. Therefore, the higher STM intensity is expected to result from the geometrically higher position of molecule **1** instead of a higher LDOS. It is noteworthy that the absolute changes of the LUMO-derived hopping integrals are only about half as large as in the case of the HOMO-derived states (see color scales in Fig. 4.8). This observation might arise from the lower degeneracy of the involved states and might explain the weaker localization of the
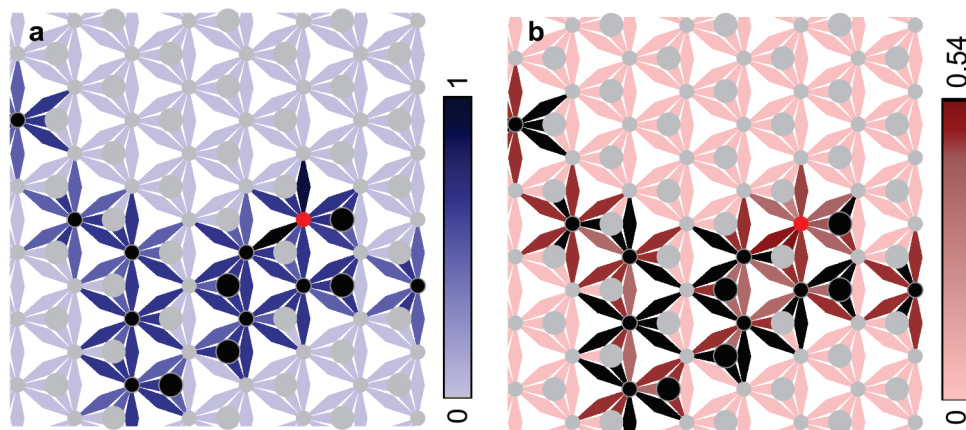
Fig. 4.8: Changes in hopping integrals due to local disorder. (a) Summed squares of the changes in the hopping integrals for the HOMO-derived states and (b) for the LUMO-derived states expressed by color saturation (in arbitrary units). Rhombic areas between the small circles refer to hopping integrals between molecules within the surface layer, triangular areas between a small and a larger circle refer to hopping integrals between molecules in the surface and the second layer. The color of the circles reflect whether the corresponding molecule is in the thermodynamically most stable H configuration (gray) or in the slightly less stable P configuration (black). The red circle marks molecule 1 from Fig. 4.8.

LUMO-derived split-off state (Fig. 4.7b) as well as its weaker splitting from the LUMO-derived band compared to the HOMO-derived split-off state.

Finally, it is demonstrated that the observed HOMO- and LUMO-derived split-off states act as local charge carrier traps that, due to their close proximity to each other, locally enhance the formation and recombination of electron–hole pairs (excitons). Optical spectra acquired with the STM tip positioned over different defect states exhibit a sharp emission line, whose energy varies between 1.69 and 1.78 eV. This variation in the emission energy indicates variations in the depth of the local carrier traps. Very similar STM-induced emission spectra have been observed for C_{60} layers on thin NaCl films and have been interpreted as the recombination of electron–hole pairs.[42, 70] The specific emission spectrum of the defect state in Fig. 4.6-4.8 is displayed by the yellow curve in Fig. 4.9a. Panel b of this figure shows the spatially resolved photon yield – that is, the total measured light intensity divided by the number of tunneling charge carriers – superimposed on a pseudo-3D topography image of the defect site. Around molecule **1**, the photon yield and thus the formation of electron–hole pairs is enhanced by several orders of magnitude compared to the surrounding area. When removing molecule **1** by STM manipulation, the photon yield reduces substantially, though does not disappear completely (Fig. 4.9c). At the same time, the emission line experiences a blue shift of 17 meV (Fig. 4.9a, brown curve). Both observations – the reduced emission intensity and the blue shift – are clear indications for a reduction in the local trap depth. They further demonstrate that the local trap states can be decisively manipulated by the molecular arrangement in the semiconducting film. Concurrently, the removal of molecule **1** proves that the formation of the localized states does not result from the slightly protruding molecule, such as a chemically modified C_{60} molecule or a C_{70} molecule. Instead, the apparent height of this molecule and its deviating orientation most likely result from an underlying *neutral* impurity. A charged impurity can be excluded by the following considerations. Calculations including an additional charge in different voids between the first and the second C_{60} layer could reproduce
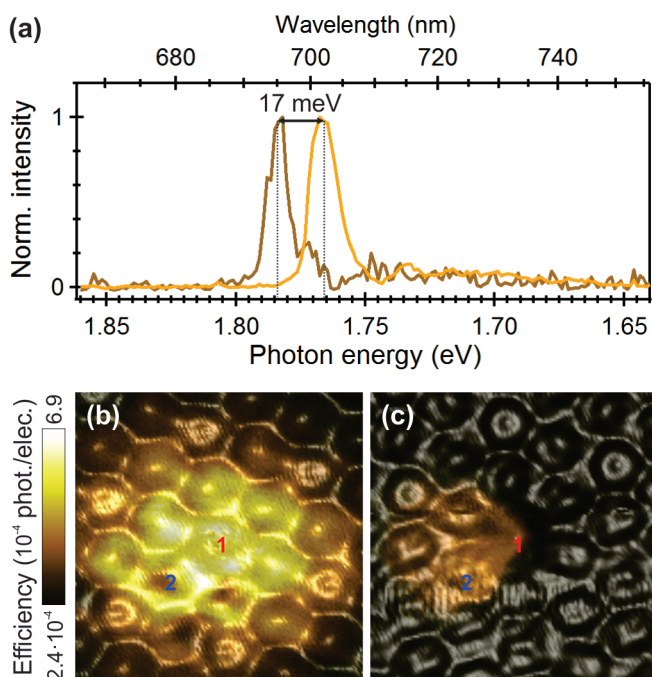
Fig. 4.9: Photon emission at the split-off states imaged in Fig. 4.7. (a) STM-induced emission spectrum on the defects states before (yellow) and after (brown) removing molecule **1** by STM manipulation (U_{set} = −3.0 V, I_{set} = 100 pA). (b) Pseudo-3D topography map of the defect with the color representing the local photon yield before and (c) after removing molecule **1** by STM manipulation (imaging parameters: U_{set} = −3.0 V, I_{set} = 10 pA).

the local splitting of the HOMO-derived states toward lower binding energy only in the case of a negative charge. However, experimentally the presence of such a negative charge is very unlikely because it would require a p-doping of C$_{60}$, known for its high electron affinity. On the other hand, such a negative charge results in an analogous shift of the LUMO-derived states toward lower binding energies, which is at variance with the experimentally observed LUMO-derived split-off states in the band gap.

4.6 Conclusions

After an in-depth literature review of the morphological and electronic structure of C$_{60}$ films, this chapter has shown that the electronic states of C$_{60}$ multilayers studied by STM are subject to a band bending resulting from the electric field between the STM tip and the metal substrate. This band bending linearly increases with C$_{60}$ thickness and decreases with the thickness of the vacuum barrier. This linear relation enables determination of the absolute layer thickness in a given experiment by examining the shifts of the LUMO-derived states as a function of either the C$_{60}$ layer thickness or the vacuum barrier thickness. On the other hand, the shift of the LUMO-derived states allows for a quantification of the absolute band bending within a C$_{60}$ film of given thickness via the empirically derived formula eq. (4.6). Both aspects are necessary prerequisites to explain the STM-induced luminescence of C$_{60}$ multilayers discussed in the next chapter.

The last part of this chapter has demonstrated that local deviations from the idealized ordered structure in the C$_{60}$ multilayers (5–10 MLs) result in spatially localized electronic states within the band gap of the films that split from the HOMO- and LUMO-derived bands. Tight-binding calculations of the films show that these states arise from the local perturbation of hopping integrals and, crucially, depend on the precise orientation of the molecules in the surface layer *and* the layer below. Therefore, the combination of the spatial mapping of these states by STM and their calculation, for example, by the tight-binding approach used in this chapter, enables a prediction of the molecular orientation in the sub-surface layer(s) – information that is usually not directly accessible to STM. Finally, this chapter has proven that the localized electronic states arising from structural defects serve as shallow traps for both injected electrons and holes. When both traps occur in close proximity to each other, these structural defects locally facilitate the formation of electron–hole pairs. A detailed investigation of this and other processes leading to STM-induced luminescence on C$_{60}$ films follows in the next chapter.

Chapter 5

STM-induced Luminescence and Charge Carrier Dynamics in C_{60} Multilayers

Based on the characterization of the local electronic structure of thin C_{60} films in the previous chapter, this chapter will investigate the scanning tunneling microscopy (STM)-induced luminescence of these films. While the STM-induced luminescence on a C_{60} monolayer has been the subject of several previous studies,[36, 37, 187–189] the luminescence on thicker C_{60} films,[42, 70] in particular its spatial dependence, has received less attention. This chapter will present three different processes leading to STM-induced luminescence on 1–10 molecular layers (MLs) thick C_{60} films. Section 5.1 will give a brief overview of these three processes, before they are described in more detail in the sections 5.2–5.4. This chapter continues by investigating the photon statistics of the structural defects introduced in section 4.5 and closes with an examination of their luminescence response to nanosecond voltage pulses sent to the STM tunnel junction. Parts of this chapter will be published in reference [190].

5.1 Overview of the Different Luminescence Processes

Figure 5.1a shows a large-scale STM topograph of a C_{60} pyramid formed by its Stranski-Krastanov-like growth, with the surface color depicting the integrated photon intensity simultaneously measured by one of the two avalanche single photon diodes (APDs). The mean STM height of the six highest terraces measures 0.83 nm, whereas the height of the lowest step edges is 0.52 nm. Previous STM studies have shown that the first C_{60} layer directly adsorbed on coinage metal surfaces appears thinner than the second and subsequent layers[137, 145] due to the higher local density of states (LDOS) on the metal. Therefore, the lowest terrace in Fig. 5.1a can be identified as the uncovered Ag(111) surface. Differential conductance (dI/dU) spectra on this terrace (Fig. 5.1b) confirm this assumption by resolving the Ag(111) surface state.[191] The color scale in Fig. 5.1a shows that the maximum photon intensity occurs on the uncovered Ag(111) surface. A comparison of the emission spectrum on this site (Fig. 5.1c, red curve) with the one observed with the same STM tip on a pristine Ag(111) surface (Fig. 5.1c, gray curve) reveals a substantial intensity reduction around 1.8 eV. This intensity reduction coincides with the absorption onset of bulk C_{60} at 1.80 eV.[192] Hence, it most likely arises from the absorption by the surrounding C_{60} film, when the STM tip is "immersed" in the valley between different C_{60} pyramids. Similar absorption effects have been observed by Schneider *et al.* for porphyrin-covered STM tips.[193]

On the various C_{60} layers, three different luminescence processes can be distinguished that shall be briefly introduced and subsequently described in more detail in the following sections. On the first and second layer, the integrated luminescence intensity is reduced by a factor of
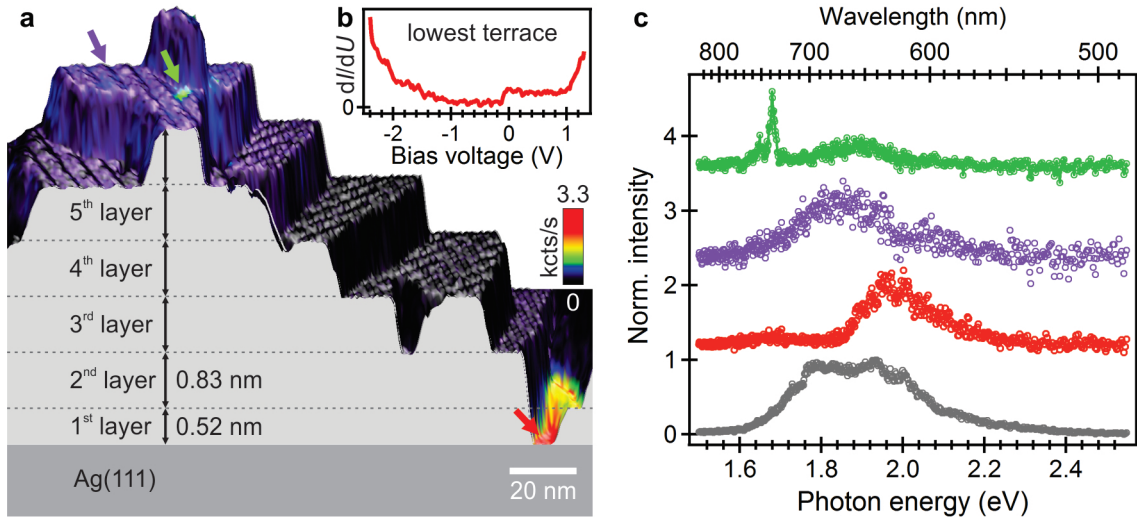
Fig. 5.1: STM-induced luminescence on C_{60} multilayers on Ag(111). (a) STM topography of a C_{60} pyramid consisting of 7 MLs on a Ag(111) substrate where the color represents the integrated STM-induced luminescence intensity simultaneously measured by an avalanche single photon diode (APD) ($U_{set} = -3.0V$, $I_{set} = 20\,pA$). The apparent height of the lowest step edges as well as the identical height difference between the higher terraces are denoted. (b) dI/dU spectrum acquired on the lowest level marked by the red arrow in panel a ($U_{set} = -3.0V$, $I_{set} = 100\,pA$). (c) Emission spectra obtained on a pristine Ag(111) surface (gray, $U_{set} = -3.0V$, $I_{set} = 1\,nA$) and the sites marked by the colored arrows in panel a ($U_{set} = -3.0V$, $I_{set} = 100\,pA$).

~1.5 and ~10, respectively, compared to the intensity on the uncovered Ag(111) surface. Section 5.2 will show that the emitted photons result from the decay of tip-induced surface plasmon polaritons (TIPs) in the tip–sample cavity, similar to that observed on pristine noble metal surfaces.[17] On the first C_{60} layer, TIPs are excited by inelastic tunneling processes between the partially filled lowest unoccupied molecular orbital (LUMO)-derived states (see section 4.3.1) and the empty electronic states of the STM tip. Because these partially filled states are restricted to the first C_{60} layer in direct contact to the metal substrate, each additional layer increases the tunneling distance between those states and the STM tip. As a consequence, the tunneling probability of these inelastic tunneling processes, and thus the plasmon excitation, drops dramatically with each additional layer. At typical tunneling parameters of $U_{set} \sim -3\,V$ and $I_{set} \sim 20\,pA$, this first luminescence process is only observable on C_{60} mono- and bilayers. On thicker films, however, this process is negligible.

Section 5.3 will show that the band bending of electronic states within the C_{60} film, which was discussed in section 4.4, opens a second TIP excitation channel via the LUMO-derived states of the surface layer. It will become obvious that, at the typical tunneling parameters of $U_{set} \sim -3\,V$ and $I_{set} \sim 20\,pA$, the LUMO-derived states of the fifth and higher layer are pulled to or even below the Fermi energy of the substrate ($E_{F,s}$). Therefore, these states can be filled by electrons from the substrate, which again can inelastically tunnel to the STM tip and thereby excite TIPs. Emission spectra on the fifth (Fig. 5.1c, violet curve) and higher layers thus resemble those on the pristine metal surface.

Finally, at the structural and electronic defects described in section 4.5, a third luminescence mechanism exist. There, the lifetime of both types of charge carriers is locally extended so that electrons injected from the substrate into the LUMO-derived states can recombine with holes injected by the STM tip. As a result, luminescence spectra on these sites exhibit a sharp emission line whose precise energy and intensity depend on the specific electronic structure of the defect. As an example, the green curve in Fig. 5.1c displays the emission spectrum on the bright spot in the sixth molecular layer (ML), marked by the green arrow in Fig. 5.1a.

5.2 Plasmonic Luminescence on a C_{60} Monolayer on Ag(111)

Previous studies of the STM-induced luminescence on C_{60} monolayers have primarily used gold substrates, in particular Au(110)[36, 37], Au(111)[187, 189] and a few atomic layers of NaCl on top of a Au(111) surface.[42] On a C_{60} monolayer on Au(111), Geng *et al.* have recently shown by luminescence and dI/dU spectra that the LUMO of the C_{60} molecules is actively involved in the plasmon excitation in the tunnel junction.[189] In this case, the authors observed a two-fold decreased intensity on the C_{60} molecules compared to the depressions between individual molecules, which they ascribed to the varying tip–sample distance.

In contrast, in this thesis constant height photon maps of a C_{60} monolayer on Ag(111) reveal an increased intensity on top of the C_{60} molecules and a submolecular pattern at negative bias polarities (Fig. 5.2a). This pattern in the photon map markedly differs from the simultaneously recorded dI/dU map (Fig. 5.2c). Instead, the photon map reproduces the LDOS close to the Fermi energy of the substrate ($E_{F,s}$), depicted in Fig. 5.2b. The finite density of states near $E_{F,s}$, visible in dI/dU spectra (Fig. 5.2d, blue circle), arises from a charge transfer from the Ag(111) substrate into the C_{60} LUMO-derived states, which thereby get partially filled

(see section 4.3.1). As will be discussed in more detail in chapter 8, such electronic states close to $E_{F,s}$ act as locally and energetically defined "gates" for the excitation of surface plasmon polaritons (SPPs) in tunnel junctions by enhancing the probability of inelastic tunneling channels. Consequently, constant height photon maps acquired at negative bias voltage $<-1.5\,V$ reflect the spatial extension of the C$_{60}$ LUMO-derived states, whereas simultaneously recorded dI/dU maps show the highest occupied molecular orbital (HOMO)-derived states.
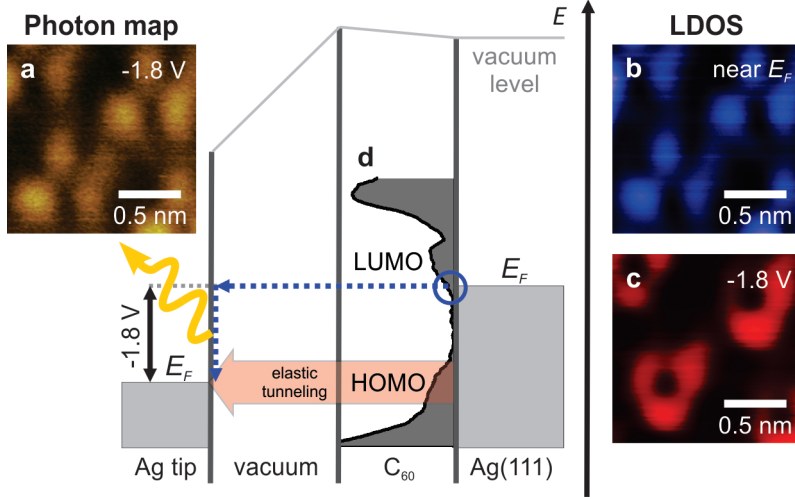
Fig. 5.2: STM-induced luminescence on a C$_{60}$ monolayer on Ag(111). (a) Photon map at $-1.8\,V$, (b) current map at $-0.2\,V$, and (c) dI/dU map at $-1.8\,V$, all recorded at the same constant tip height. (d) Energy diagram together with a measured dI/dU spectrum showing the finite LDOS around zero bias voltage (blue circle).

5.3 Plasmonic Luminescence on C$_{60}$ Multilayers on Ag(111)

As already outlined in section 5.1, the luminescence process observed on a C$_{60}$ monolayer cannot explain the excitation of plasmons on C$_{60}$ films consisting of five or more molecular layers. The distance between the partially filled LUMO-derived states, which are restricted to the first C$_{60}$ layer, and the empty STM tip states is simply too large. Considering the band gap of such thicker C$_{60}$ films, the only process able to provide electrons with a sufficiently high energy to excite TIPs must be based on the injection of electrons into the LUMO-derived states by the metal substrate. In turn, this means that at the typical tunneling parameters of $U_{set} \sim -3\,V$ and a few ten picoamperes, the LUMO-derived states of the fifth C$_{60}$ layer must align with the Fermi energy of the substrate ($E_{F,s}$). Only then, can electrons be injected from the first metallic C$_{60}$ layer into the higher-lying layers. Calculating the energy of the LUMO-derived states within the surface of a 5 MLs thick C$_{60}$ at $-3\,V$ by the empirical formula eq. (4.6) on page 35 reveals that these states should reside ~300 mV above $E_{F,s}$. This deviation could result from

Fig. 5.3: Band banding in a 5 MLs thick C$_{60}$ film at a bias voltage of $-3\,V$, with (gray bars) and without (black bars) an additional hole in the HOMO-derived states in the surface layer.

the use of differently curved STM tips with different electric fields, and the fact that it might be sufficient to align the band onset instead of the band center with $E_{F,s}$. However, it appears more likely that the electron injection into the LUMO-derived states is triggered by a

previous hole injection into the HOMO-derived states by the STM tip. Indeed, the positive potential due to a hole in the HOMO-derived states should result in an additional lowering of the LUMO-derived states that might facilitate an electron injection. Figure 5.3 sketches both energetic situations with (gray bars) and without (black bars) an additional hole in the HOMO-derived states. The electric potential of its positive charge was calculated via the Coulomb potential of one elementary charge, assuming a dielectric constant of $\epsilon_r = 4.4$.[108]

For thicker C$_{60}$ layers, the absolute voltage drop across the C$_{60}$ film increases when keeping the same tunneling parameters. Formally, the LUMO-derived states of the surface layer should thus increasingly shift below $E_{F,s}$. As soon as an electron is injected into the LUMO-derived states, however, its electric field may counteract the bias-induced field within the film, which might pin the LUMO-derived states to $E_{F,s}$. Emission spectra on a 7 MLs thick C$_{60}$ film indicate that such a pinning should be rather weak. Indeed, only when applying bias voltages as high as −3.8 V does the high-energy side of the emission spectrum (second highest curve in Fig. 5.4a) resemble the plasmonic spectrum of the junction obtained on a pristine Ag(111) surface (gray curve, Fig. 5.4a). When decreasing the (negative) bias voltage to −3.0 V (third curve in Fig. 5.4a), the high-energy components of the spectrum are reduced and the spectrum exhibits a smaller quantum cutoff (marked by black arrows). In other words, the maximum energy of the emitted photons is smaller than the high-energy onset of the TIP resonance of the junction. The latter has been determined by a line fit of the high-energy side
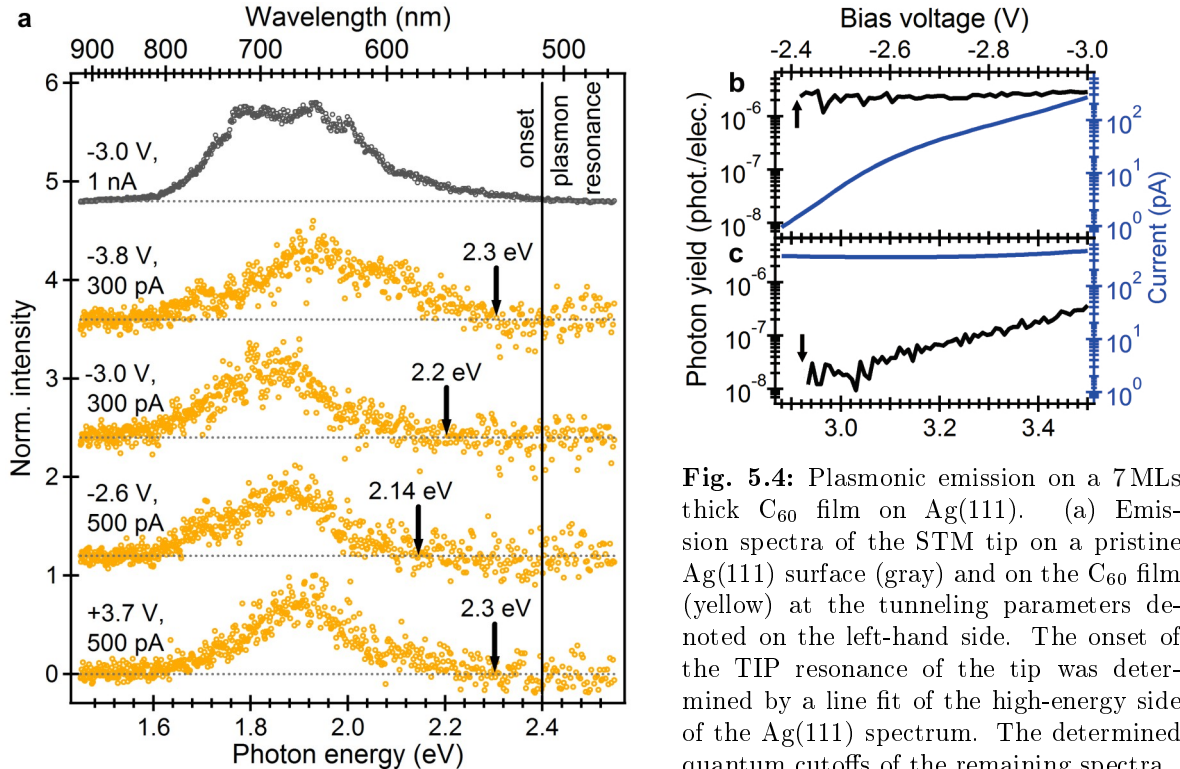
Fig. 5.4: Plasmonic emission on a 7 MLs thick C$_{60}$ film on Ag(111). (a) Emission spectra of the STM tip on a pristine Ag(111) surface (gray) and on the C$_{60}$ film (yellow) at the tunneling parameters denoted on the left-hand side. The onset of the TIP resonance of the tip was determined by a line fit of the high-energy side of the Ag(111) spectrum. The determined quantum cutoffs of the remaining spectra are denoted on the right-hand side. (b) Number of photons detected by the APD per tunneling charge carrier (black, left axis) and measured current (blue, right axis) at negative bias polarity ($U_{set} = -3.0$ eV, $I_{set} = -268$ pA) and (c) at positive bias polarity ($U_{set} = -3.0$ eV, $I_{set} = -268$ pA). Arrows mark the onset of light emission.

of the plasmonic spectrum on a pristine Ag(111) surface and is marked by the vertical line in Fig. 5.4a. Therefore, the quantum cutoff of the emission spectrum can be used to estimate the energy difference between the Fermi energy of the tip ($E_{F,t}$) and the lowest LUMO-derived states of the surface layer, as well as their energy with respect to the Fermi energy of the substrate ($E_{F,s}$). The latter arises as the difference between the applied bias voltage and the high-energy quantum cutoff in the emission spectrum. According to the roughly estimated quantum cutoffs in Fig. 5.4a, at −3.0 V the onset of the lowest LUMO-derived states should lie 0.8 eV below $E_{F,s}$. This observation supports the assumption that the LUMO-derived states in films thicker than 5 MLs lie below $E_{F,s}$. A further reduction of the bias voltage to −2.6 V (forth curve in Fig. 5.4a) weakens the band bending in the C$_{60}$ film so that the energy difference between the applied bias voltage and the photon quantum cutoff – that is, the energy of LUMO-derived states with respect to $E_{F,s}$ – reduces to 0.45 V. In contrast, if the LUMO-derived states of the C$_{60}$ film were pinned to $E_{F,s}$, the quantum cutoff in the emission spectrum should always equal the applied bias voltage multiplied by the elementary charge. For a more precise monitoring of the electronic states, however, additional spectra should be acquired with longer integrations times and better signal-to-noise ratios.

Photon yield–voltage spectra, which show the number of photons detected by the APD per charge carrier tunneling through the vacuum barrier, show only a weak bias dependence of the TIP excitation efficiency at negative bias voltages (Fig. 5.4b, black curve) with a photon yield that slightly increases from 2×10^{-6} at −2.4 V to 3×10^{-6} photons per tunneling charge at −3.0 V. At the same time, the measurable current rises by more than two orders of magnitude (Fig. 5.4b, blue curve). Therefore, every additional charge carrier that, due to the increased bias voltage, tunnels through the vacuum barrier must lead to a proportional increase in the number of TIPs excited in the junction. In other words, the rising current must mostly result from an enhanced electron injection into the LUMO-derived states. If an enhanced hole injection into the HOMO-derived state were responsible for the increasing current, the photon yield would decrease as the injected holes do not have enough energy to excite TIPs in the junction. The bias onset of the luminescence intensity at about +2.4 V may have two different origins: On the one hand, the LUMO-derived states might be located above $E_{F,s}$ below this onset so that an electron injection into the LUMO-derived states via the substrate becomes impossible. On the other hand, the energy of the emitted photons could be smaller than the energy threshold of the APD of about 1.2 eV.

Plasmonic Luminescence at Positive Bias Voltages

At positive bias polarity, photon yield spectra reveal a much stronger bias dependence and an overall lower photon yield on the order of 10^{-8} to 10^{-7} photons per tunneling charge (Fig. 5.4c, black curve). On closer inspection, it turns out that the corresponding luminescence onset at ~2.9 eV, as well as the observed bias dependence of the photon yield, is mostly determined by the sensitivity of the used photon detector. According to eq. (4.6) (page 35), at a bias voltage of ~2.9 eV, the electronic C$_{60}$ states of the surface layer should be up-shifted in energy by ~0.9 eV. When assuming a zero-field energy of the HOMO-derived states of −2.2 eV,[173] these states are located 1.3 eV below the Fermi energy of the substrate and thus are fully occupied. Hence, they cannot contribute to a tunneling process from the STM tip to the sample. Instead, electrons can only tunnel from the occupied STM tip states into unoccupied

C_{60} states. With a zero-field energy of $1\,eV$ (see section 4.4.3), the lowest LUMO-derived state should be located ~$1.9\,eV$ above the Fermi energy of the substrate ($E_{F,s}$) or ~$1\,eV$ below the Fermi energy of the tip ($E_{F,t}$). The latter value essentially corresponds to the energy threshold of the APD (~$1.2\,eV$) used for measuring the luminescence intensity. Therefore, the observed luminescence onset of ~$2.9\,eV$ results from the sensitivity onset of the employed photon detector. With increasing bias voltage, the energy difference between $E_{F,t}$ and the LUMO-derived states increases, and thus the maximum photon energy as well as the total luminescence intensity rise. At a bias voltage of +$3.7\,V$, the high-energy side of the emission (Fig. 5.4a, lowest curve) finally exhibits almost the same shape as the plasmonic spectrum of the junction on a pristine Ag(111) surface (Fig. 5.4a, upper most curve).

5.4 Electron–Hole Pair Recombination at Defect Sites

As discussed in section 4.5, structural defects in the C_{60} films, caused by orientational disorder, substrate dislocations, domain boundaries or impurities, lead to spatially localized electronic states within the band gap of the films. In this and the next section it will be shown that these split-off states act as shallow traps for injected electrons and holes, which thereby experience an extension of their lifetime. When such an electron trap and a hole trap occur in close proximity to each other, the increased lifetime of both charge carriers enhances the probability for the formation and subsequent recombination of electron-hole pairs (see section 4.5). In photon maps these split-off states thus literally come to light as bright spots with a spatial extension over few C_{60} molecules and maximum intensities that exceed the plasmonic background by up to two orders of magnitude. In the vast majority of cases, these luminescence "hot spots" have a circular or near-circular shape with a photon yield that decreases with distance from their center. In rare cases, the bright spots have a triangular shape, which might indicate a localization of the split-off states in subsurface layers. Figure 5.5a shows that the area of enhanced luminescence, as well as the maximum intensity, varies among different bright spots even on the same C_{60} terrace. dI/dU spectra at the emission maxima of the imaged spots (Fig. 5.5b) suggest that the maximum intensity correlates with the energy separation between the valence band edge and its split-off state. Compared to dI/dU spectra in regions that only show a plasmonic luminescence background (gray curve), the two brightest spots 1 and 2 (red and orange curve) show a significant higher LDOS at higher binding energies. On the two dimmest spots 4 and 5 (violet and dark blue curve), on the other hand, the dI/dU spectra resemble those of the dark regions.

5.4.1 Emission Spectra

The emission spectra of the bright spots show a sharp line at negative bias voltages between −2.6 and −3.8 V (full width at half maximum (FWHM): $9\,meV$). Their energy is independent of the applied bias voltage but varies for different bright spots between 1.69 and $1.78\,eV$. The emission spectra of the spots 1, 2 and 5 are displayed in Fig. 5.5c with the same color coding as their labels in panel a. The different emission energies might result from the varying energy difference between the valence band split-off state and the conduction band split-off state. On the low-energy side, the main peak is followed by a vibrational progression consisting of a series of equidistant peaks (marked by arrows) with a mean separation of ~$30\,meV$. For two
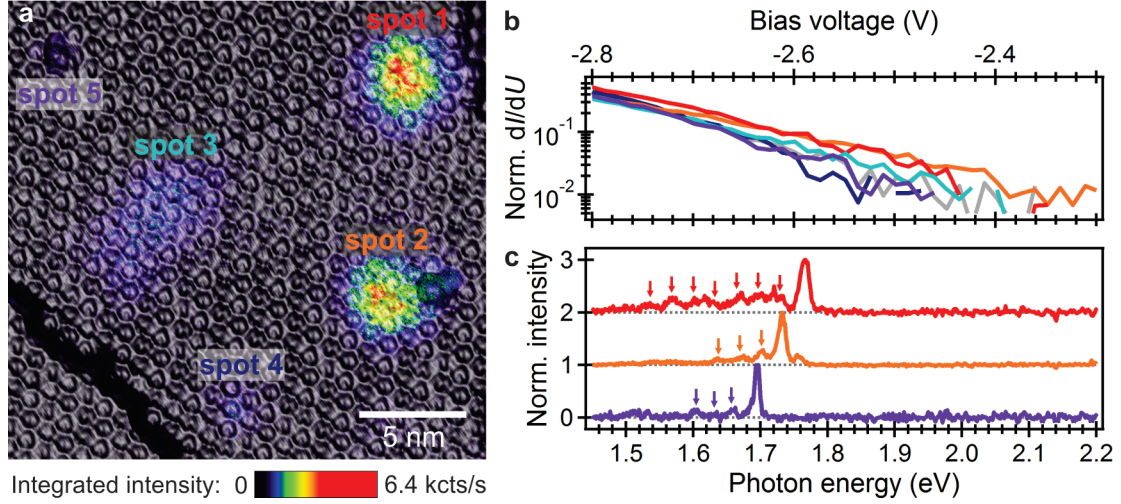
Fig. 5.5: Local electron-hole pair recombination in the surface of a 6 MLs C$_{60}$ film on Ag(111). (a) STM topography with the color reflecting the simultaneously detected integrated luminescence intensity (U_{set} = −3.0 V, I_{set} = 30 pA). Five different luminescence hot spots can be observed. (b) dI/dU spectra acquired on the emission maxima imaged in panel a. The color-coding of the curves equals the labels of the bright spots in panel a. (c) Emission spectra of the bright spots 1 (red), 2 (orange) and 5 (violet) in panel a (U_{set} = −3.0V, I_{set} = 100 pA). The arrows mark equidistant side peaks in the vibrational progression of the main peak.

of ~20 investigated bright spots, including bright spot 2 from Fig. 5.5, the main emission peak was accompanied by an additional peak at slightly higher energy. In a recent theoretical study, such an additional high-energy peak has been found as a fingerprint to distinguish between a singlet emission (fluorescence) and a triplet emission (phosphorescence).[194] According to this theoretical study, most of the bright spots should exhibit phosphorescence. However, time-dependent measurements of the emitted luminescence intensity presented in this work (see section 5.6) disagree with this assumption and reveal only a very weak phosphorescence signal.

When comparing the emission spectra of a bright spot on a 7 MLs thick C$_{60}$ film (colored curves in Fig. 5.6a) with those acquired on the darker regions of the same C$_{60}$ terrace (black curve in Fig. 5.6a), the plasmonic background turns out to be significantly reduced on the defect site (Fig. 5.6a). This observation may be due to the fact that those electrons that recombine with holes injected into the HOMO-derived states are no longer available for inelastic tunneling processes through the vacuum barrier resulting in the excitation of TIPs. Emission spectra acquired at different tunneling parameters further suggest that the applied bias voltage and the tip–sample distance have a crucial influence on the photon yield of both luminescence processes. Compared to the emission spectrum obtained at −3 V and 100 pA (yellow curve, Fig. 5.6a), the electron–hole pair emission clearly drops when increasing the bias voltage to −3.8 V (blue curve, Fig. 5.6a) or decreasing the tip–sample distance to a tunneling current of 300 pA (red curve, Fig. 5.6a). At the same time, the broad plasmonic emission feature between 1.8 and 2.0 eV seems to slightly increase. The energy integrals of the plasmonic components within the region marked by the dashed lines in Fig. 5.6a is denoted at the corresponding spectra. The plasmonic component does not rise in the same way as the electron–hole pair emission reduces because the photon yields of both processes differ by two orders of magnitude
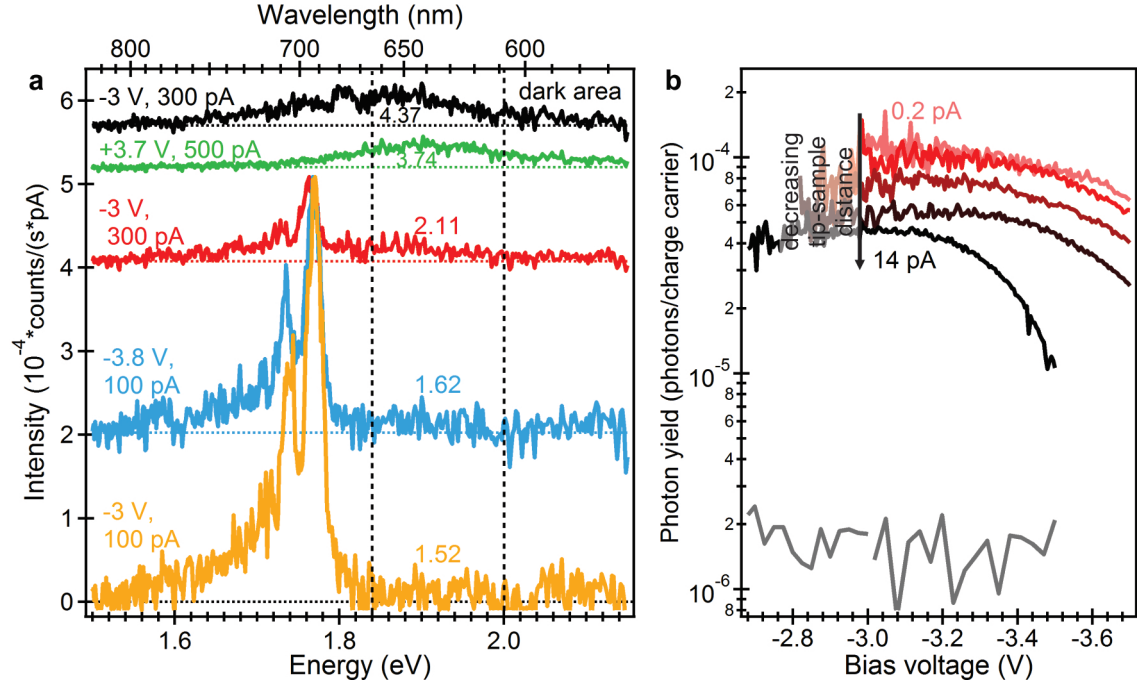
Fig. 5.6: Emission spectra and photon yield on structural defects in C_{60} multilayers as a function of the bias voltage and the tip–sample distance. (a) Emission spectra on a bright spot in the surface of a 7 MLs thick C_{60} film on Ag(111) (colored curves) at various tunneling parameters indicated on the left-hand side as well as on a defect-free region on the same C_{60} terrace (black curve). For clarity, the three lowest curves are shifted vertically such that their intensity maxima coincide. Horizontal dotted lines show the zero intensity line. The numbers on the right-hand side denote the integral of the corresponding spectra in the interval marked by the vertical dashed lines (in units of $10^{-6}\,\text{counts}/(\text{s} \cdot \text{pA} \cdot \text{eV})$). (b) Total photon yield on a bright spot on a 8 MLs thick C_{60} film (upper curves) and a defect-free region on the same C_{60} terrace (lower gray curve) as a function of the applied bias voltage and the tip–sample distance. The numbers in the upper part denote the measured tunneling current at the largest and the smallest tip–sample distance at $-3.0\,\text{V}$.

(cf. previous section 5.3). However, for an accurate determination of the increasing plasmonic emission channel as a function of the applied bias voltage and the tip–sample distance, further emission spectra with better signal-to-noise ratios should be acquired. At positive bias voltages, the emission spectra at the defect sites solely exhibit a plasmonic component (green curve, Fig. 5.6); hence, an electron–hole pair recombination seems to be impossible – at least in the investigated bias regime. The origin of this observation most likely lies in the lack of hole injection into the HOMO-derived states because these are still located below the Fermi energy of the substrate (see section 5.3).

5.4.2 Photon Yield

The important role of the applied bias voltage and the tip–sample distance is also evident in photon yield–voltage curves (Fig. 5.6b). Whereas the photon yield of the plasmonic background in the defect-free regions (gray curve) is rather independent of the applied voltage, the photon yield at the defect sites drastically reduces with increasing negative voltage, in

particular at small tip–sample distance, i.e. large tunneling currents. In fact, the maximum photon yield of 10^{-4} photons per tunneling charge carrier is astonishingly close to the observed photoluminescence quantum efficiency of C_{60} films of 7×10^{-4},[195] when assuming a photon collection efficiency of the used set-up of ~10%.[73] This might indicate that, at small negative bias voltages and large tip–sample distances, most of the charge carriers that contribute to the measurable current lead to corresponding electron–hole pairs. Additional time-dependent measurements and quantitative simulations of the underlying time constants (see section 5.6) would clarify this assumption. According to the discussion in the previous section 5.3, an increased negative bias voltage should mostly enhance the electron injection by the substrate, while the hole injection by the tip should be rather constant. This larger electron injection rate might enhance the tunneling of injected electrons to the STM tip and/or enhance an annihilation of electron–pairs. Both factors should result in a reduced photon yield.

5.4.3 Lateral Dependence

Figure 5.7 summarizes a detailed characterization of the electronic structure and the luminescence from bright spot 2 in Fig. 5.5 as a function of the lateral STM tip position. At the investigated positions marked by the colored crosses, the emission line varies by $4\,\mathrm{meV}$ (Fig. 5.7b). It is worth noting that the main peak energy does not monotonously increase
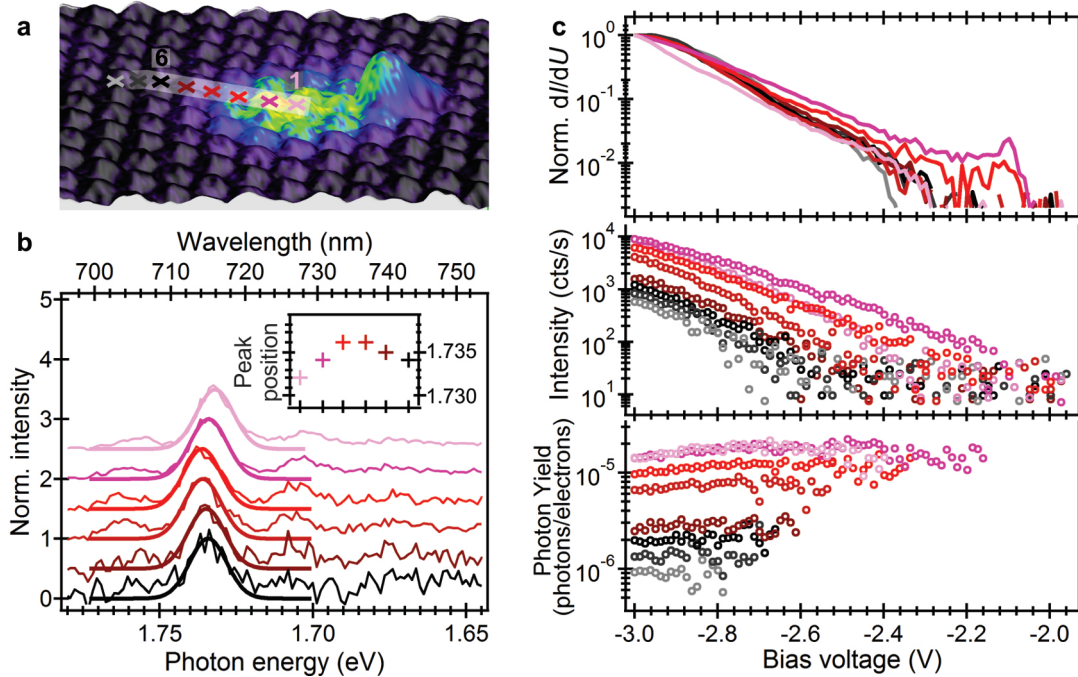
Fig. 5.7: Spatial dependence of the STM-induced luminescence and the electronic structure of a bright spot on a $6\,\mathrm{MLs}$ thick C_{60} film on Ag(111). (a) Detailed STM topography of the bright spot 2 from Fig. 5.5 where the color represents the simultaneously detected integrated luminescence intensity ($U_{\mathrm{set}} = -3.0V$, $I_{\mathrm{set}} = 30\,\mathrm{pA}$). The colored crosses mark the position of the emission spectra in (b) as well as the dI/dU, the intensity, and the photon yield spectra in (c). The inset in b displays the energy of the main peak fitted by a Gaussian function.

with distance from the emission maximum, as it would be expected from a Stark shift, but passes through a maximum of $1.736\,\text{eV}$. The corresponding $\mathrm{d}I/\mathrm{d}U$ and photon intensity spectra (Fig. 5.7c), however, follow two different trends. In accordance with the spatial mapping of the valence band split-off state in section 4.5, this state only occurs on position 2 and 3 (magenta and red curve). The total luminescence intensity and photon yield, on the other hand, gradually decreases with the distance from the emission maximum.

5.4.4 Model of the Emission Processes on C_{60} Multilayers
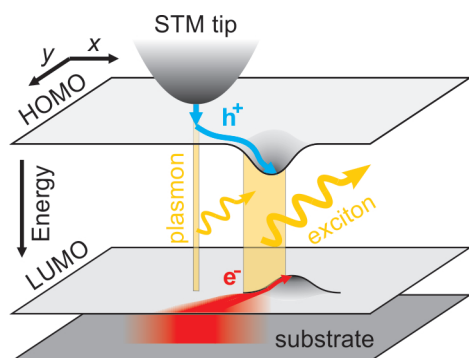
Fig. 5.8: Luminescence process on structural defects in C_{60} multiayers. For explanation see text.

The sum of all these observations suggests the energy diagram sketched in Fig. 5.8. It depicts the local energy of the HOMO- and LUMO-derived states plotted upside down together with the two possible luminescence processes. When the tip is placed on top or close to an area with both a split-off state of the HOMO- and LUMO-derived bands, electrons injected by the substrate and holes injected by the STM tip can diffuse to the corresponding split-off states and be locally trapped. Whereas the hole injection by the tip is highly localized, the electron injection by the planar substrate occurs over a much larger area, as this is determined by the electric field in the junction. When both an electron and a hole are trapped by the corresponding states, the lifetime of both charge carriers in the C_{60} film rises and they can recombine as an electron–hole pair under emission of a photon. Section 4.5 showed that the bottom of both trap states are not necessarily localized on identical C_{60} molecules. Although the most effective trap for the electron–hole pairs could, in principle, be located on a third position, its most likely position might be the site where the product of the probability to find an injected hole and an injected electron is maximal. In addition to the radiative decay of electron–hole pairs, electrons injected by the substrate into the LUMO-derived states can tunnel inelastically to the STM tip and thereby excite TIPs in the junction that in turn also decay as photons. When the STM tip is laterally moved away from both split-off states, less injected charge carriers, in particular, less holes, are trapped. As a consequence, the photon yield of the electron–hole recombination gradually decreases while the plasmonic component slightly increases with the lateral distance from the trap states.

5.5 Photon Statistics – Proof of the Single Photon Emission at the Defect Sites

Measuring the photon statistics of the emitted light – that is, the intensity fluctuations in a given time period – provides valuable information, whether the photons are generated in an uncorrelated manner or one after the other. This section will show that for the electron–hole recombination at the defect sites, the latter is the case or, in other words, the defect sites act as single photon sources similar to nitrogen vacancy centers in diamond.[196, 197] In fact, the presented experiments are the first of their kind in the sense that they demonstrate that photons can be generated in STM one after the other.

Emitted light can be classified into three groups: perfectly coherent light as produced by a laser; chaotic light, for example created by a discharge lamp; and non-classical light, in which photons are emitted one after the other. These three sorts of light differ in the magnitude of their intensity fluctuations in a given time period with respect to the mean intensity. Typically, such fluctuations of a statistical distribution $P(n)$ around its mean value $\overline{n}$ are quantified in form of the variance:

$$var(n) = (\Delta n)^2 = \sum_{n=0}^{\infty} (n - \overline{n})^2 \cdot P(n) \qquad (5.1)$$

For a perfectly coherent light source, the photon emission rate (n_{phot}) exhibits a Poisson distribution, that is, the variance of the photon emission rate equals the mean emission rate: $(\Delta n_{\text{phot}})^2 = \overline{n}_{\text{phot}}$. An incoherent or chaotic light source, on the other hand, exhibits super-Poisson photon statistics, which means that the intensity fluctuations are larger than the mean intensity: $(\Delta n_{\text{phot}})^2 > \overline{n}_{\text{phot}}$. When the photons are emitted one after the other, finally, the photon statistics follows a sub-Poisson statistics, that is, $(\Delta n_{\text{phot}})^2 < \overline{n}_{\text{phot}}$.

Experimentally, the photon statistics of an emission process is accessible by continuously measuring the time delay between the detection of two emitted photons. Technically, this can be done by an intensity interferometer consisting of two photon detectors that, according to its inventors Robert Hanbury Brown and Richard Twiss,[198] is also referred to as a Hanbury Brown Twiss interferometer. Details about the set-up used in this thesis can be found in section 2.3.3. The number of correlation events as a function of the time delay between the detection of the first and the second photon reflects the second-order intensity correlation function ($g^2(\Delta t)$), as long as the number of correlation events is much smaller than the number of start signals from the first APD. For a single-photon emission process, it can be shown that $g^2(\Delta t)$ vanishes when $\Delta t \to 0$.[199]

Figure 5.9a displays the measured intensity correlation on a bright spot at a bias voltage of $-3.2\,\text{V}$ and different tunneling currents (denoted on the left-hand site). At the smallest tunneling current, that is, at the largest tip–sample distance, the correlation signal at time zero exhibits an anti-bunching and reduces by 67% compared to the uncorrelated signal at larger time delays. As this value is above 50%, this is a clear indication that the structural defect acts as a single photon emitter. The correlation signal does not reach zero because of the limited time resolutions of the detectors (FWHM: $1.2\,\text{ns}$). When correcting for the instrumental broadening by a deconvolution with the detector function, $g^2(\Delta t)$ exponentially
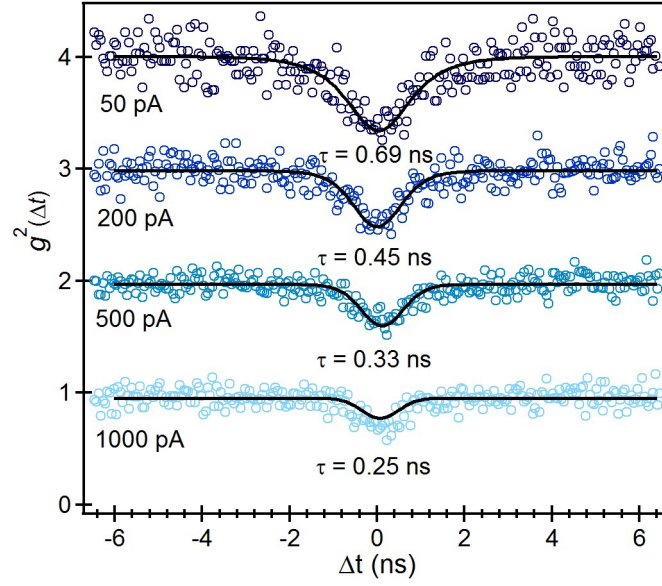
Fig. 5.9: (a) Measured second-order intensity correlation function ($g^2(\Delta t)$) on a defect site in the surface of a C_{60} multilayer as a function of the tunneling current (indicate on the left-hand side). For clarity, the data are shifted vertically. The solid lines display a fit of the data, assuming a single photon emission convoluted by the detector time resolution function (FWHM: 1.2 ns). The number below the correlation minima denotes the time constants from the corresponding fits. (b) Plot of the inverse determined time constants as a function of the tunneling current.

increases around time zero. The determined exponential time constants τ at the various tunneling currents are denoted below the corresponding correlation minima. With increasing current, the correlation minimum becomes less pronounced and the observed time constant continuously reduces from 0.69 ns at a current of 50 pA to 0.25 ns at a current of 1 nA. As long as the defect site can accommodate only one single electron–hole pair, the observed lifetime reflects the lifetime of this electron–hole pair at the experimental conditions, that is, at the given bias voltage and the given tip–sample distance. In the following it is shown that the decline in the observed decay constant and thus the lifetime of the electron–pair can be understood by an enhanced non-radiative quenching of electron–hole pairs. In this context, the observable decay rate of an electron–hole pair (k_{ex}) can be described as the sum of a radiative decay rate $k_{\mathrm{ex}}^{\mathrm{rad}}$ and a non-radiative rate constant $k_{\mathrm{ex}}^{\mathrm{non\text{-}rad}}$:

$$k_{\mathrm{ex}} = k_{\mathrm{ex}}^{\mathrm{rad}} + k_{\mathrm{ex}}^{\mathrm{non\text{-}rad}} \tag{5.2}$$

Expressed by the corresponding time constants, this means:

$$\frac{1}{\tau} = \frac{1}{\tau_{\mathrm{ex}}^{\mathrm{rad}}} + \frac{1}{\tau_{\mathrm{ex}}^{\mathrm{non\text{-}rad}}} \tag{5.3}$$

When assuming a non-radiative quenching of the electron–hole pairs by the charges tunneling through the vacuum barrier, $k_{\mathrm{ex}}^{\mathrm{non\text{-}rad}}$ should be proportional to the measurable tunneling

current $k_{\mathrm{ex}}^{\text{non-rad}} = \alpha \cdot I$, with α as the corresponding proportionality constant. Hence, eq. (5.3) can be rewritten as:

$$\frac{1}{\tau} = \frac{1}{\tau_{\mathrm{ex}}^{\mathrm{rad}}} + \alpha \cdot I \tag{5.4}$$

A plot of the inverse of the observed time constant (τ) as a function of the measured tunneling current should therefore result in a linear function. Figure 5.9b confirms such a linear relation and thus proves an exciton annihilation by the charge carriers tunneling through the vacuum barrier. The unperturbed lifetime of electron–hole pairs at the specific defect site can be determined from the intercept of this linear fit as τ=0.75 ns.

5.6 Charge Carrier Dynamics

This section focuses on the luminescence time response of the structural defect sites in C_{60} multilayers on nanosecond voltage pulses sent to the STM tunnel junction. Technical details about the experimental set-up and the procedure to generate rectangular voltage pulses with rising and falling edge of 3 ns at the tunnel junction can be found in section 2.3.3 and chapter 3, respectively.

5.6.1 Characteristics of the Luminescence Time Response

Figure 5.10a depicts the luminescence response of an electronic defect within the surface of an 8 MLs thick C_{60} film (Fig. 5.10c) at various tip–sample distances to a train of 222 ns voltage pulses. The relative tip–sample distance is denoted on the right-hand side of Fig. 5.10a. The emission spectrum at this defect site is displayed in Fig. 5.10b. For the pulse experiments, the DC bias offset was chosen such that it coincides with the luminescence onset (-2.8 V, 45 fA) determined by intensity–voltage curves. During the pulses, the bias voltage increases from -2.8 V to -3.3 V, which corresponds to a tunneling current of 1.76 pA and 9.09 pA at the smallest and largest tip–sample distance, respectively. The energy shift of the LUMO-derived states as well as the photon yield at this defect site as a function of the relative tip–sample distance are displayed on the right-hand side of Fig. 4.4d (page 33) and Fig. 5.6b (page 51), respectively.

Compared to the voltage pulse arriving at the tunnel junction (red curve), the intensity transients on top of the defect reveals several additional features and time constants. Considering the distance-dependence of the rising edge, two different regimes can be distinguished: In the large distance regime (two lowest curves in Fig. 5.10a), the rising edge exhibits one fast slew rate followed by a slower one, whose time constant decreases with decreasing tip–sample distance. In the short distance regime (three upper most curves in Fig. 5.10a), on the other hand, the rising edge shows an intensity overshoot. While the decay time from this overshoot to the equilibrium intensity decreases with decreasing tip–sample distance, its amplitude increases. A zoom-in on the pulse rising edges (Fig. 5.10d) further shows a delay of the luminescence intensity with respect to the voltage pulse in both regimes. The magnitude of this delay reduces with decreasing tip–sample distance. Interestingly, the luminescence flank follows the time

integral of the ohmic current (blue curves in Fig. 5.10b); in other words, the luminescence intensity reflects the tunneling probability for charge carriers to tunnel through the vacuum barrier. The ohmic current was determined from the known voltage pulse shape and the current–voltage curve at the corresponding tip–sample distances.

In contrast to the rising edge, the characteristics of the falling luminescence edge do not show two different tip–sample distance regimes. Instead, the falling edge always exhibits a fast and a
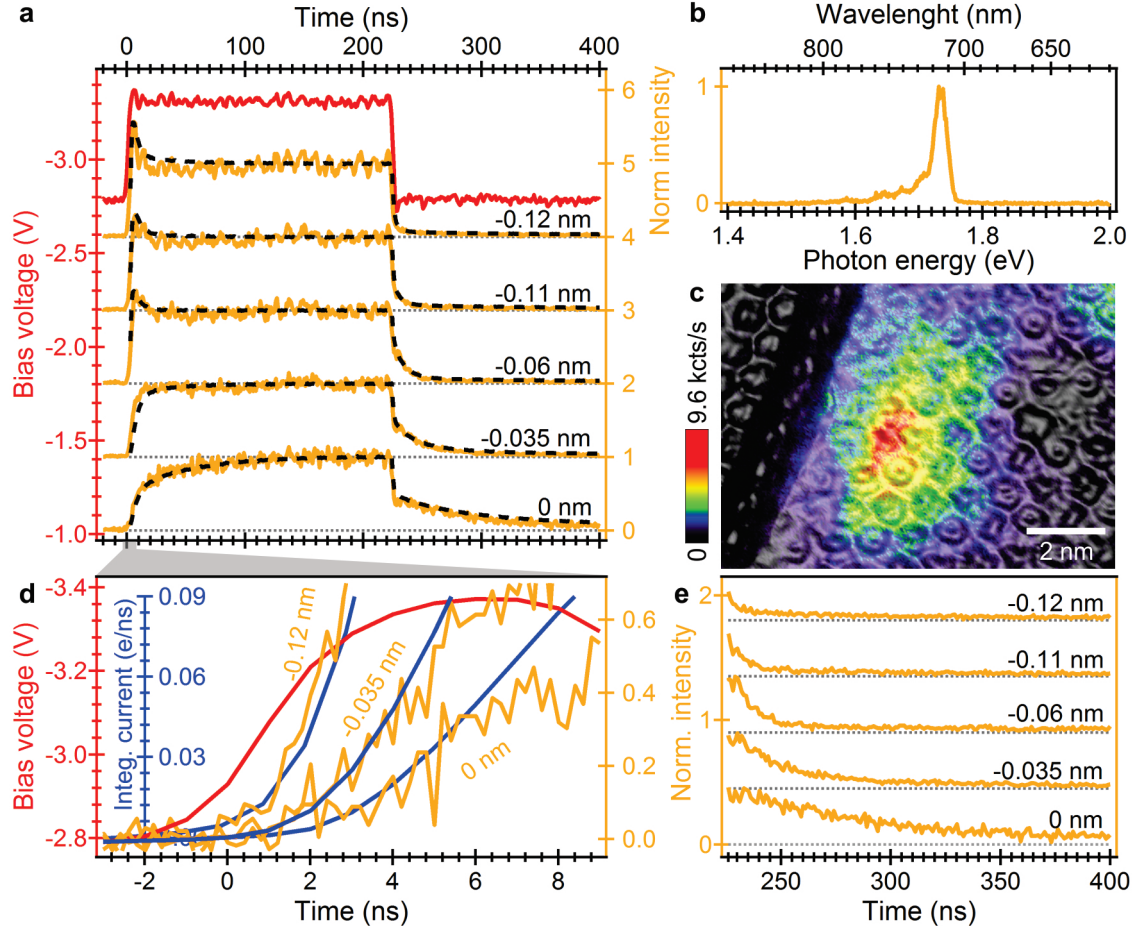
Fig. 5.10: Luminescence response of a defect site in the surface of an 8 MLs thick C_{60} film to a 222 ns voltage pulse. (a) Time-dependent bias voltage at the STM tunnel junction (red) mapped by the procedure described in chapter 3 and normalized time-dependent luminescence intensity (yellow) as a function of the relative tip–sample distance (Δz_{rel}, denoted on the right-hand side). The intensity transients are normalized to the mean intensity at the end of the voltage pulse and are shifted for clarity. Dotted lines indicate zero intensity. The dashed lines display the results of Monte Carlo simulations discussed in section 5.6.2. (b) Emission spectrum ($U_{set} = -3.5$ V, $I_{set} = 15$ pA) and (c) pseudo-3D topography of the defect site where the color reflecting the integrated luminescence intensity measured by an APD ($U_{set} = -3.5$ V, $I_{set} = 15$ pA). (d) Detailed view of the rising edge of the voltage pulse (red) and the luminescence intensity (yellow) of the data shown in panel a. The blue curves depict the time integral of the ohmic current (in electrons per nanosecond) derived from the used voltage pulse and a current–voltage curve at the corresponding tip–sample distance. (e) Detailed view of the falling edge of the luminescence intensity at the denoted Δz_{rel}. Again, dotted lines indicate zero intensity. Time bins: 0.2 ns. In panel a and e the intensity is binned to 1 ns.

slow intensity decay, whose decay constant substantially decreases with deceasing tip–sample distance. On closer inspection, this slower decay in turn is followed by an approximately 200 ns period of non-zero intensity (Fig. 5.10c), which suggests an additional, even slower and distance-independent intensity decay process. Finally, with reducing tip–sample distance, the weak voltage oscillations during the pulses cause an increasing modulation of the luminescence intensity. These only few ten millivolts weak voltage oscillations result from an insufficient compensation of pulse reflections within the bias line (see chapter 3). When using 5 ns voltage pulses on the same defect, similar voltage oscillations occur after the voltage pulses (red curve, Fig. 5.11), which substantially modulate the luminescence decay of the falling edge (yellow curve, Fig. 5.11). A fit of this decay by an exponential function multiplied by the transient voltage (dashed line) shows that the modulation strength of these bias voltage oscillations (red number in Fig. 5.11) systematically increases with decreasing tip–sample distance. In the next section it will become apparent that this increased modulation strength results from the enhanced electron injection rate by the substrate.
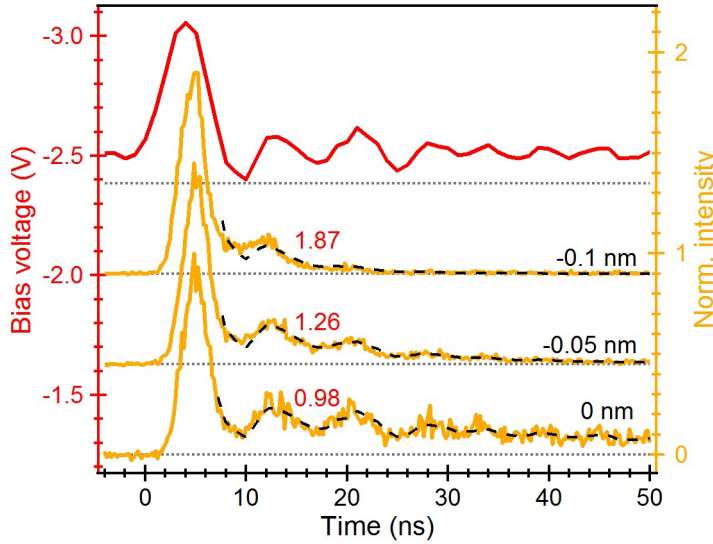
Fig. 5.11: Luminescence response of the defect site in Fig. 5.10 to a 5 ns voltage pulse (red). Yellow curves display the normalized luminescence response for different relative STM tip–sample distances (Δz_{rel}), which are denoted on the right-hand side. The intensity transients are normalized to the peak maximum and are shifted for clarity. Dotted lines indicate zero intensity. The dashed lines display best fits of the falling edges by an exponential function multiplied by the transient voltage. The red numbers denote the strength of the corresponding voltage modulation.

5.6.2 Interpretation of the Observed Time Response

On further consideration, the electron–hole recombination and thus the emission process at the defect sites may follow a multi-step process with a number of different time constants. To make things even more complicated, the precise time constants of the various steps might also depend on whether a hole or an electron is injected first, because the electric potential of the first injected charge carrier will cause an additional band bending and will facilitate the injection of the complementary charge carrier. Figure 5.12 sketches both situations during the voltage pulse. The energetic position of the C$_{60}$ states due to the band bending arising from the applied bias voltage (black bars) are obtained from the empirical formula in eq. (4.6) on page 35. The additional band bending due to the electric potential of the first injected charge carrier (gray bars) are calculated via the Coulomb potential of an elementary charge assuming a dielectric constant of $\epsilon_r = 4.4$.[108]
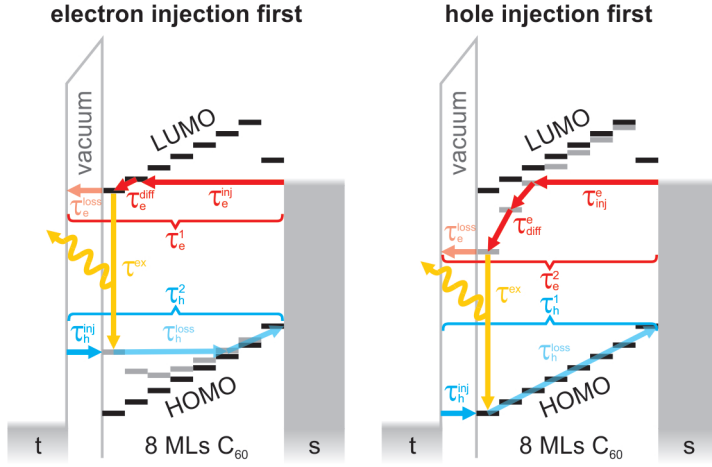
Fig. 5.12: Energy level diagrams of the HOMO- and LUMO-derived states at a defect site in an $8\,\mathrm{MLs}$ thick C_{60} film during the voltage pulses for the two cases that either an electron or a hole is injected first. The time constants involved in the luminescence process are denoted. Black bars depict the energy levels seen by the charge carrier that is injected first, whereas gray bars show the energy levels seen by the second injected charge carrier, which are shifted by the corresponding Coulomb potential of the first charge carrier.

The rather complex dynamics of the emission process can be simplified by the following assumptions. First, in section 5.5 the upper limit for the lifetime of an electron–hole pair (τ_{ex}) at the the defect sites was determined as less than $1\,\mathrm{ns}$. Hence, this process is much faster than the time constants and delay times in Fig. 5.10 so that this time constant can be neglected. Instead, the time constants visible in Fig. 5.10 must be related to the injection and/or diffusion of charge carriers. Second, the time constants for the injection (τ_e^{inj}), diffusion to the surface (τ_e^{diff}) and loss of electrons by tunneling to the STM tip (τ_e^{loss}) can be absorbed in one effective time constant τ_e. The same applies for the injection and loss of holes that can be absorbed in an effective time constant τ_e. Third, the zero intensity before the voltage pulse and the slow luminescence decay after the pulse imply that one of the two charge carriers must be still present after the pulse and can still recombine with its complementary charge carrier. Therefore the emission obeys at least a two-step process, with the first step being possible only during the voltage pulses, while the subsequent step(s) can also occur after the voltage pulses. Finally, the change of the bias voltage at the pulse edges is assumed to be instantaneous.

Based on these four assumptions, the observed luminescence response can be modeled as a combination of two two-step processes – one for the case that an electron is injected first (τ_e^1), which in a second step recombines with an injected hole (τ_h^2), and a second process in which the hole is injected first (τ_h^1) that subsequently recombines with an injected electron (τ_e^2). For the modeling of such a 2×2-step process a Monte

Tab. 5.1: Time constants of the best manual fits of the experimental data in Fig. 5.10a (in ns) at the various STM tip–sample distances Δz_{rel} (in nm). The second column indicates the mean time between two charge carriers tunneling through the vacuum barrier during the pulses (in ns) and is derived from the measured current at the pulse voltage.

| | | electron injected first | | | | hole injected first | | | |
| | | pulse on | | pulse off | | pulse on | | pulse off | |
Δz_{rel}	τ_{tunnel}	τ_e^1	τ_h^2	τ_e^1	τ_h^2	τ_h^1	τ_e^2	τ_h^1	τ_e^2
-0.12	18	600	4	6000	∞	20	1	∞	4
-0.11	20	600	5	9000	∞	30	1	∞	6
-0.06	34	600	6	10000	∞	50	5.5	∞	9
-0.035	49	500	35	∞	37	100	5.5	∞	14
±0	91	600	55	∞	75	550	5.5	∞	27

Carlo simulation is used that numerically solves the corresponding rate equations. The response to the voltage pulses is implemented by periodically switching the corresponding four

time constants (τ_e^1, τ_h^2, τ_h^1, τ_e^2) between two discrete parameter sets. The time for each parameter set is determined by the voltage pulse width and the time between two successive pulses. The best fits of the experimental data in Fig. 5.10a by a manual parameter optimization are displayed by the dashed lines, with the corresponding time constants during and between the voltage pulses being summarized in Tab. 5.1. For this manual parameter optimization only those combinations that fulfill the following two conditions were tested. First, the time constants during the pulses should always be smaller than in between the pulses. Second, during the voltage pulses the time constant referring to the case where a hole is injected first (τ_h^1) must always be larger than the time constant related to the quasi-equilibrium tunneling current measured at the pulse voltage ($-3.3\,\mathrm{V}$). For a more precise determination of the different time constants and their errors, it would be worthwhile to develop an automated fitting procedure that, for example, uses the method of least squares.

A priori it is not clear which time constants of the two two-step processes relates to the case where an electron or an hole is injected first. However, the following arguments will show that the assignment in Tab. 5.1 is plausible. First of all, the time constants τ_h^1 and τ_h^2 during the voltage pulses decrease about one order of magnitude for a reduction of the tip–sample distance by $1\,\text{Å}$. This strong reduction indicates that these time constants are determined by the tunneling processes through the vacuum barrier. In contrast, the time constants τ_e^1 and τ_e^2 change with less than one order of magnitude per $1\,\text{Å}$ tip displacement. Another argument for the correct assignment of the time constants lies in the intensity overshoot at the beginning of the voltage pulses at small tip–sample distances. This overshoot can only be reproduced by the simulation when one time constant referring to the injection of the second charge carrier during the pulse-off phase is much larger than $10\,000\,\mathrm{ns}$. In other words, at small tip–sample distances it must be impossible to inject this type of charge carrier. Considering the band bending within the C$_{60}$ film, a reduction of the tip–sample distance should always facilitate the injection of electrons by the substrate. For the hole injection by the STM tip, however, there might be a specific distance at which the HOMO-derived states are shifted below the Fermi level of the tip. Therefore, below this distance it should be impossible to inject a hole into the HOMO-derived states.

5.6.3 Possible Extensions of the Model Used

Although the assumption of a combination of two two-step processes qualitatively explains the experimentally observed luminescence response, strictly speaking, the determined time constants only provide information on the relative rates of the involved process steps. In the following, a kind of a road map shall be discussed that, step by step, disengages the assumptions in the previous section. This should allow a quantitative simulation of the experimental data and thus a determination of the absolute time constants of the underlying processes.

First, the very slow and distance-independent decay after the voltage pulses visible in Fig. 5.10e can be reproduced by permitting an additional weak phosphorescence channel, with a time constant on the order of $100\,\mathrm{ns}$. Because such a transition from an excited triplet state to a singlet ground state is spin-forbidden, the photon intensity resulting from such a phosphorescence channel should be rather weak. Indeed, time-dependent luminescence spectra of crystalline C$_{60}$ exhibit a phosphorescence signal that is more than a hundred times weaker than the fluorescence signal.[200]

In a second step, the effective time constant for the injection of an electron τ_e^1 and τ_e^2 could each be split into two different constants describing the injection by the substrate τ_e^{inj} and the "loss" of electrons τ_e^{loss} due to their tunneling to the STM tip. This allows for a more stringent boundary condition for the fit of the experimental data, in the sense that the tunneling current measured at the bias voltage during the pulses must always be the sum of all hole currents and the "loss" current of electrons. The corresponding time constants should thus fulfill the relation:

$$\frac{1}{\tau_{\text{tunnel}}} = \frac{1}{\tau_h^1} + \tau_e^1 \frac{1}{\tau_h^2} + \frac{1}{\tau_e^{\text{loss}}} \tag{5.5}$$

Provided that sufficient experimental data is available for a given defect site – for example several luminescence transients at different tip–sample distances and/or different bias voltages – this approach should offer the determination of absolute rate constants for the injection of electrons and holes. At the same time, this might provide a unique way to quantify the fractions of the tunneling current flowing via the HOMO- and LUMO-derived states.

In a third step, one could suspend the assumption of an instantaneous change of the bias voltage. As a consequence, the simulations would not rely on two discrete parameter sets of time constants anymore – one for the situation during the pulses and one between the pulses – but each time constant could be described by a certain voltage-dependence. Although accessing all these, most likely different, voltage dependences seems to be really demanding, specifically designed voltage pulses could probe the dependences of only one or a few specific time constants. For example, the luminescence decay after the pulses must be related to the injection of the second charge carrier at a given offset voltage. The intensity overshoot at the beginning of the pulses at small tip–sample distances should be even more specific. Its decay to the equilibrium intensity during the pulse should directly yield the time constant related to the injection of a hole (τ_h^2) in the presence of a previously injected electron. At the end, this approach should enable a full characterization of the C_{60} tunnel barrier seen by the electrons injected by the substrate, which is not directly accessible by current–voltage curves obtained by STM or transport measurements.

5.7 Conclusions

This chapter has shown that, depending on the thickness of the C_{60} films adsorbed on a Ag(111) surface, three different processes cause STM-induced luminescence at negative bias polarity. All three processes rely on the injection of electrons into the LUMO-derived states of the C_{60} film by the substrate. While for a C_{60} monolayer, this injection "naturally" arises from the high electron affinity of C_{60} and the resulting charge transfer from the metal substrate, the different energy alignment in the thicker C_{60} films requires a band bending of the LUMO-derived states down to the Fermi level of the substrate. As the LUMO-derived states of the surface layer are (partially) filled by electrons from the substrate, they are able to inelastically tunnel to the STM tip and thereby excite tip-induced surface plasmon polaritons (TIPs) in the junction. At structural defects of the C_{60} film, the plasmonic emission process may compete with the radiative decay of electron–hole pairs. As shown in the previous chapter 4, structural defects result in the formation of localized electronic states that may trap both

electrons injected by the substrate and holes injected by the STM tip so that these experience an extension of their lifetime within the C$_{60}$ film.

Measurements of the second-order intensity correlation reveal that these structural defects can accommodate only a single electron–hole pair and thereby act as single photon sources with electron–hole pair lifetimes <0.7 ns. At small tip–sample distances, the observed lifetime reduces due to additional non-radiative quenching processes caused by injected charges. It may be speculated that both photon anti-bunching and electron–hole pair annihilation are related to each other, in the sense that the efficient quenching of the electron–hole pairs by the next injected charge carrier prohibits any biexciton formation and thus ensures a single photon emission. By demonstrating that structural defects alone, in otherwise homogeneous organic films, might be sufficient to guarantee a single photon emission, these experiments may offer entirely new perspectives for the realization of single photon sources.

Investigations of the luminescence response of the structural defects to nanosecond voltage pulses show that the luminescence process can be described by a combination of two two-step processes, in which either a hole is injected first by the STM tip that, in a second step, recombines with an electron injected by the substrate or, vice versa, the electron is injected first and the hole follows. While the injection rate of the electrons by the substrate is rather independent of the tip–sample distance, the hole injection rate by the STM tip exponentially rises with decreasing tip–sample distance. Hence, the specific injection rates of electrons and holes, and thus the currents flowing via the LUMO- and HOMO-derived states, can be controlled by the tunneling parameters. Conversely, the observed luminescence response may be used for a detailed characterization of the injection barrier at the C$_{60}$-substrate and other organic interfaces, which cannot be derived from simple current–voltage curves.

Chapter 6

Electronic Structure of Ir(ppy)$_3$ Adsorbed on Metallic Surfaces

The previous chapter has shown that the highly localized tunneling current in scanning tunneling microscopy (STM) can be employed to locally inject individual charge carriers into thin molecular films that are able to radiatively recombine as electron–hole pairs. The original goal of the following chapters was to transfer this concept to a single molecule, that is, to locally contact and excite the luminescence of an individual molecule. In fact, the successful realization of electroluminescence from an individually contacted molecule[38, 71, 201] can be counted on the fingers of one hand. In searching for a suitable molecule, the choice fell on the green emitter *fac*-tris(2-phenylpyridine)iridium(III) [Ir(ppy)$_3$].[202] Organic light emitting diodes (OLEDs) with emission layers of a few percent of Ir(ppy)$_3$[203] diluted in a matrix material have shown quantum efficiencies near unity.[20–22] In order to electronically decouple the single Ir(ppy)$_3$ molecules from the metallic substrate necessary for STM, in this thesis the molecules should be deposited on a semiconducting C$_{60}$ multilayer. Prior to the discussion of the electronic structure of single Ir(ppy)$_3$ molecules on C$_{60}$ multilayers in chapter 7 and their STM-induced luminescence in chapter 8, the current chapter shall lay the groundwork for these investigations. It will review the most important properties of Ir(ppy)$_3$ and analyze its electronic structure on the coinage metal surfaces Ag(111) and Au(111) as well as on a C$_{60}$ monolayer adsorbed on these metal surfaces.

6.1 Ir(ppy)$_3$ – A Model Emitter for Second-Generation Light Emitting Diodes

OLEDs successfully found their way into the displays of most mobile devices and superseded former liquid-crystal displays (LCDs) therein. The key benefits of OLED display, such as larger contrast ratios and lower power consumption, arises from the fact that the individual pixels themselves emit light and do not require a background light source. The light emitting layer of such first-generation OLEDs consists of fluorescent organic molecules, in which the injection of electrons and holes leads to the formation of electron–hole pairs (excitons) that decay through emission of light. For large-area lighting elements, however, these OLEDs are not yet efficient enough because the injected charge carriers recombine radiatively only as long as the recombining electrons and holes have antiparallel spins, thus, forming singlet excitons. According to quantum-mechanical spin statistics, however, in 75% of all cases both charge carriers have parallel spins and thus form triplet excitons. Since their decay into the electronic ground state is spin-forbidden and possible only via non-radiative processes, most of the generated excitons in first-generation OLEDs are lost and cannot emit light.

Second-generation OLEDs, on the other hand, employ phosphorescent organo-transition metal complexes containing heavy transition metals like platinum, iridium, or osmium. The heavy transition metal of such complexes induces a strong spin–orbit coupling (SOC), which leads to an efficient mixing of singlet and triplet states.[5] Therefore, the spin-forbiddance of these transitions is lifted. As a result, such phosphorescent emitters can harvest all electron-hole pairs for photon emission and thus reach very high quantum efficiencies. One of the leading examples is the green emitter *fac*-tris(2-phenylpyridine)iridium(III) (Ir(ppy)$_3$)[202, 203] due to its particularly high quantum efficiency of almost 100%[20–22] and its, compared to other triplet emitters, fast radiative rates.[22] In the following, its properties and characteristics are briefly summarized.

6.1.1 Chemical Structure

fac-tris(2-phenylpyridine)iridium(III) [Ir(ppy)$_3$] consists of a central iridium metal atom that is octahedrally coordinated by three 2-(pyridin-2-yl)phenyl (ppy) ligands (see Fig. 6.1). Each of the three ligands form two coordination bounds to the central metal; one via the nitrogen of the pyridyl ring and a second one via the 2-C of the phenyl ring. As a result, the molecule exhibits a propeller-like shape. The precise arrangement of the three ligands leads to two different isomers: In the facial or *fac* isomer the three pyridyl groups occupy one face of the octahedral coordination sphere (Fig. 6.1), whereas in the meridional or *mer* isomer they lie on a plane through

Fig. 6.1: Chemical structure of *fac*-tris(2-phenylpyridine)iridium(III). (a) Natta projection. (b) Space-filling model with the pyridine rings in light gray and the phenyl rings in dark gray.

the metal center. This thesis exclusively focuses on the *fac* isomer. X-ray diffraction (XRD) measurements of single Ir(ppy)$_3$ crystals grown by sublimation[204] show that the molecules crystallize in a $P\overline{4}2_1c$ space group and that the precise arrangement of their ligands leads to
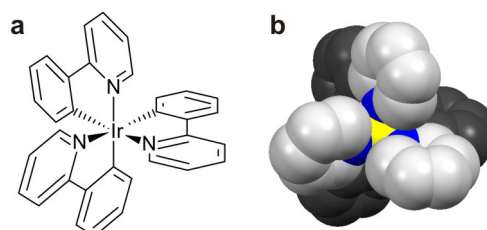
small distortions from a perfect C_3 symmetry. The latter could be also confirmed by optical spectroscopy[22] and density functional theory (DFT) calculations of the free Ir(ppy)$_3$ molecule (see section 6.1.3).

6.1.2 Emission Characteristics

Whereas the luminescence quantum yield of pure Ir(ppy)$_3$ films only lies in the range of 1% due to strong self-quenching,[203,205] organic films doped by a few percent of Ir(ppy)$_3$ can reach quantum yields of almost 100%, even at ambient temperature.[20–22] The most common host matrices are 4,4',bis(N-carbazolyl)biphenyl (CBP),[20,203,205] poly(methyl methacrylate) (PMMA),[20,22] and polystyrene[205] as well as solid organic solvents, such as tetrahydrofuran (THF)[206] and dichloromethane (CH$_2$Cl$_2$).[22] Photoluminescence and electroluminescence spectra exhibit two peaks in the green at about 510 and 540 nm, whose exact position depend on the host material and temperature. As an example, Fig. 6.2a shows the electroluminescence spectrum of 6%wt Ir(ppy)$_3$ in a CBP matrix. Both peaks arise from the combined emission of the lowest triplet term into the singlet ground state.[22] The spin-forbiddance of these transitions is lifted by Herzberg–Teller and Franck–Condon coupling of the involved triplet states to higher lying singlet states. This leads to vibrational satellites at energies slightly below the 0–0 transitions, albeit most of these satellites overlap with each other due to low-energy local phonon modes and electron–phonon coupling to the host matrix. In the end, only two broad emission bands can be resolved.

According to group-theory considerations, the lowest triplet term T_1 of an octahedral complex with a symmetry lower than C_3 should split into three triplet substates (T_1^{I}, T_1^{II}, T_1^{III}).[22] The 0–0 transitions from these three triplet substates have been observed in high-resolution photoluminescence spectra of Ir(ppy)$_3$ doped in a CH$_2$Cl$_2$ matrix at 4 K (Fig. 6.2b). At this temperature, only the two lowest substates T_1^{I} and T_1^{II} can be thermally populated and
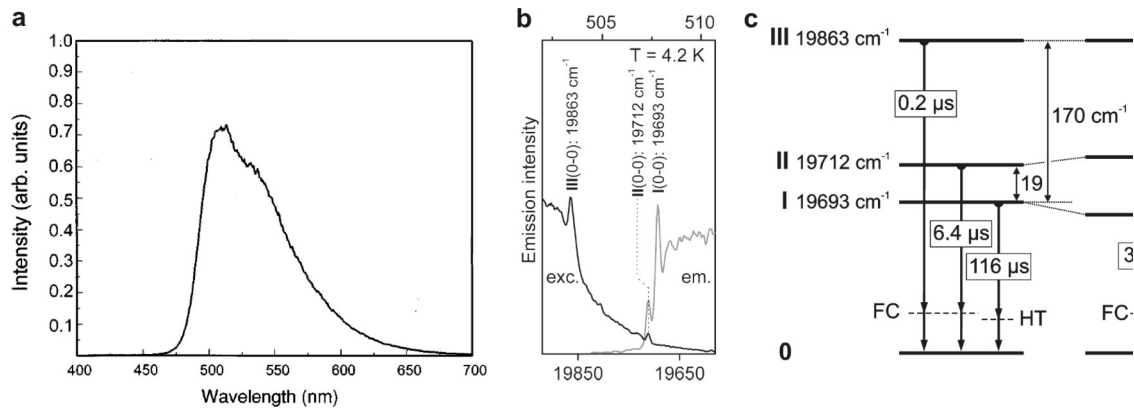
Fig. 6.2: Emission characteristics of Ir(ppy)$_3$. (a) Electroluminescence spectrum of 6%wt Ir(ppy)$_3$ in a CBP matrix obtained from ref. [203]. (b) High-resolution photoluminescence of Ir(ppy)$_3$ in CH$_2$Cl$_2$ ($c \approx 2 \times 10^{-5}$ mol/l) obtained from ref. [22]. The black curve shows an excitation spectrum (exc.) at a detection wavelength of 526.32 nm; the gray curve display an emission spectrum (em.) at an excitation wavelength of 503.45 nm. (c) Energy level diagram and emission decay times of Ir(ppy)$_3$ in CH$_2$Cl$_2$ obtained from ref. [5].

thus decay into the singlet ground state S_0. Hence, emission spectra only show the $T_1^I \rightarrow S_0$ (507.79 nm) and $T_1^{II} \rightarrow S_0$ (507.31 nm) transition, with the intensity following Boltzmann statistics. Excitation spectra, on the other hand, exhibit a pronounced transition from the highest triplet substate $T_1^{III} \rightarrow S_0$ (503.45 nm), a much lower $T_1^{II} \rightarrow S_0$ transition and lack a $T_1^I \rightarrow S_0$ transition. The reason lies in the varying degree of "forbinddance" for the three substates: Whereas the two highest substates, and especially the T_1^{III} substate, mainly couples to higher-lying singlet states that facilitate spin-allowed transitions, the lowest T_1^I substate primarily couple to other triplet states. This trend manifests itself also in the radiative rates of the three substates, which differ by almost four orders of magnitude. For example, in CH_2Cl_2 the rate constants are: $\tau_I = 116\,\mu s$, $\tau_{II} = 6.4\,\mu s$, $\tau_{III} = 200\,ns$.[22] For other matrices such as THF or PMMA slightly different rate constants have been observed due to matrix-cage induced geometry variations.

6.1.3 Electronic Structure

The electronic structure of Ir(ppy)$_3$ has been studied experimentally by ultraviolet photoelectron spectroscopy (UPS)[207] and theoretically by density functional theory (DFT)[208–212] employing different hybrid exchange–correlation functionals. HeI photoelectron spectra of CBP composite films with an Ir(ppy)$_3$ content of 56% reveal three occupied states at energies of about 5.8, 6.4, and 7.2 eV with respect to the vacuum level (Fig. 6.3d).[207] From the concurrence of the high-energy cutoff of both the composite Ir(ppy)$_3$:CBP films and a pure CBP film, the authors deduced a vacuum level alignment of the Ir(ppy)$_3$ guest molecules with respect to the CBP host molecules. For pure Ir(ppy)$_3$ films a 0.2 eV shift of the vacuum level toward lower binding energies was observed compared to the composite Ir(ppy)$_3$:CBP films.

DFT calculations of free Ir(ppy)$_3$ in its electronic ground state are in good agreement with the experimental data. Calculations of electronically excited or ionized states generally require higher theory levels, such as time-dependent functional theory (TDDFT), and consideration of SOC.[210,211] Figure 6.3 summarizes the results of a DFT calculation of a free Ir(ppy)$_3$ molecule in form of a molecular orbital (MO) diagram. The geometry optimization (without symmetry constrains) and the calculation of the molecular orbitals of the Ir(ppy)$_3$ complex as well as its ppy ligands was carried out with Orca[213] using the hybrid exchange–correlation functional B3LYP.[214] In the case of the ppy ligand, which contains an odd number of electrons and thus represents and open-shell system, the necessary exact exchange was calculated by an unrestricted Hartree-Fock (UHF) calculation. For the iridium center of the complex Hay-Wadt's LANL2DZ[215] double-zeta basis was employed that includes a relativistic core potential. For the other atoms a 6-311G(d,p)[216] triple-zeta basis was applied.

The molecular orbitals of the Ir(ppy)$_3$ complex can be considered as a linear combination of the ppy ligand orbitals and the atomic orbitals of the iridium center. Since the Ir(ppy)$_3$ complex contains three ppy ligands, most of its orbitals co-locate in groups of three with very similar energies. In fact, the small deviations from a C_3 symmetry (see section 6.1.1) causes a splitting of the Ir(ppy)$_3$ orbitals resulting from equivalent ligand orbitals into one two-fold degenerate state and one slightly higher- or lower-lying state. The orbital energies of the three highest occupied groups of states are in good agreement with the ionization energies obtained by UPS measurements[207] (Fig. 6.3d), even though the experimental energies are shifted by about 0.5 eV toward higher binding energies. The latter might be

explained by many-body final-state effects due to the ionization of the molecules in the experiment. The three highest occupied Ir(ppy)$_3$ orbitals ($d\pi_1^*$, $d\pi_{2a}^*$, $d\pi_{2b}^*$) exhibit a comparatively high 5d character of 51% in the case of the highest occupied molecular orbital (HOMO) and 43% in the case of the next lower, two-fold degenerate states (Fig. 6.3c). A comparison of the orbital shape with those of the ppy-ligand orbitals suggests that these states result from an anti-bonding combination of the 5d iridium orbitals with the HOMO−1 of the ppy-ligands. The corresponding bonding combination of both the 5d iridium orbitals

MO	Ir	Py	Ph
π_{4a}^*	1.1	86.6	12.3
π_{4b}^*	1.1	86.6	12.3
π_3^*	1.6	87.8	10.6
π_{2a}^*	4.9	72.1	23.0
π_{2b}^*	4.9	72.1	23.0
π_1^*	0.7	70.2	29.0
$d\pi_1^*$	51.3	9.4	39.4
$d\pi_{2a}^*$	43.1	10.7	46.2
$d\pi_{2b}^*$	43.1	10.7	46.2
π_{1a}	2.7	25.3	72.0
π_{1b}	2.7	25.3	71.9
π_2	2.9	24.0	73.1
$d\pi_1$	24.1	19.2	56.7
$d\pi_{2a}$	28.2	13.4	58.3
$d\pi_{2b}$	28.3	13.4	58.4
σ_1	13.0	15.4	71.6
σ_{2a}	18.8	23.8	57.4
σ_{2b}	18.9	24.7	56.4
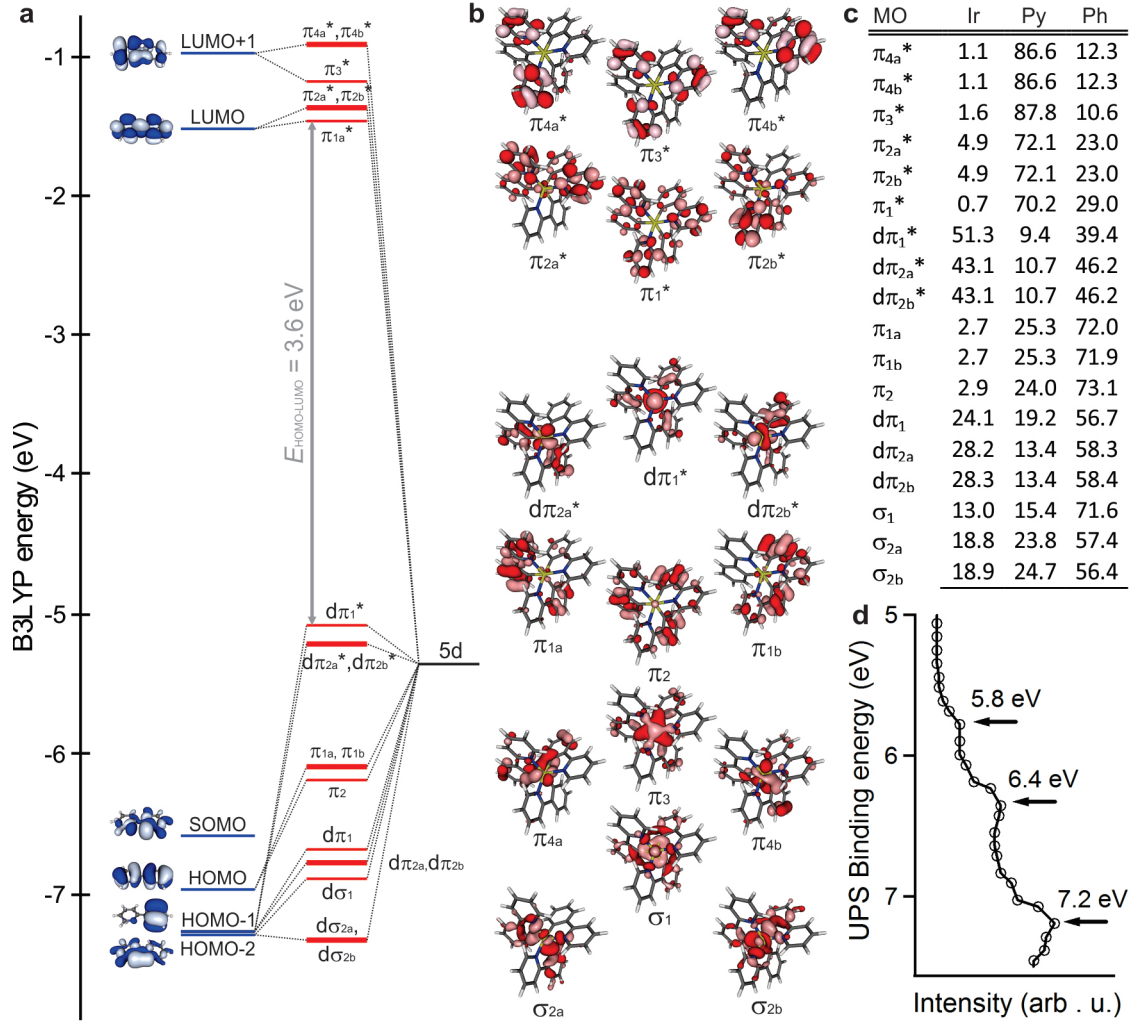
Fig. 6.3: Electronic structure of Ir(ppy)$_3$. (a) Molecular orbital (MO) diagram showing the six lowest unoccupied molecular orbitals and the twelve highest occupied molecular orbitals of Ir(ppy)$_3$ as a linear combination of the ppy ligand orbitals (left-hand side) and the iridium 5d orbitals (right-hand side). The molecular orbitals of the Ir(ppy)$_3$ complex and its ppy ligands were calculated by DFT with the B3LYP exchange–correlation functional. (b) Spatial distribution of the electron density and (c) percentage of the electron density on the iridium center (Ir), the pyridine moieties (Py), and the phenyl moieties (Ph) for the orbitals shown in panel a. (d) HeI spectrum of an Ir(ppy)$_3$:CBP composite film with an Ir(ppy)$_3$ content of 56% (reproduced from ref. [207]). The binding energy in panel a and d is referenced to the vacuum level.

and the ligand HOMO−1 leads to the Ir(ppy)$_3$ orbitals $d\pi_1$, $d\pi_{2a}$, and $d\pi_{2b}$. For symmetry reasons, the ppy-HOMO cannot overlap with the iridium orbitals. Hence, these ligand orbitals form the (almost) non-bonding Ir(ppy)$_3$ orbitals π_{1a}, π_{1b}, and π_2. The three lowest occupied Ir(ppy)$_3$ states depicted in Fig. 6.3 (σ_1, σ_{2a}, σ_{2b}), finally, result from a σ-overlap of the HOMO−2 ligand orbitals with admixtures of the singly occupied ppy-ligand orbitals (SOMO). Besides 5d orbitals, the states σ_1, σ_{2a}, σ_{2b} also involve 6s and 6p iridium orbitals.

In contrast to the highest occupied molecular orbitals, the six lowest unoccupied Ir(ppy)$_3$ orbitals (π_1^*, π_{2a}^*, π_{2b}^*, π_3^*, π_{4a}^*, π_{4b}^*) nearly exclusively arise from the ppy-LUMO and the ppy-LUMO+1 with only weak anti-bonding contributions from the iridium 5d orbitals. As the ppy-HOMO, both the ppy-LUMO and ppy-LUMO+1 are basically unable to overlap with the 5d orbitals of the iridium due to their different symmetries. Therefore, the resulting complex orbitals might be considered as non-bonding orbitals as well. Furthermore, the electron density distribution on the ligands distinctly differs from the occupied states. Whereas most of the electron density of the six lowest unoccupied states is localized on the pyridine moieties, all the occupied states depicted in Fig. 6.3 are predominately localized on the phenyl moieties. Consequently, each phenyl-ring in total withdraws about half of an electron from the iridium center. The pyridine groups, on the other hand, remain almost neutral. As a result, the facial isomer of Ir(ppy)$_3$ exhibits a fairly high dipole moment of 6.2 D, which is more than three times larger than that of water.

6.2 Ir(ppy)$_3$ Directly Adsorbed on Coinage Metal Surfaces

Single Ir(ppy)$_3$ molecules have been investigated by STM on Cu(111) by Yokoyama *et al.*[217,218] and on Au(111) within the scope of a previous PhD thesis by Theresa Lutz.[47] On Cu(111) it was noticed that, above a critical density of 0.24 nm^{-2}, Ir(ppy)$_3$ forms crystalline multilayer islands. In contrast, below this critical density the Ir(ppy)$_3$ molecules arrange in a highly dispersed phase. In this dispersed phase, the molecule–substrate interaction between the single Ir(ppy)$_3$ molecules and the Cu(111) substrate was observed to be relatively weak, compared to other molecules with similar sizes, due to the propeller-like shape of the molecule and the small contact area. As a result, the single Ir(ppy)$_3$ molecules diffuse on the surface and undergo rotational and structural changes even at temperatures as low as 80 K.[218] In topography maps the single Ir(ppy)$_3$ molecules appear with three, ~0.25 nm high protrusions in a triangular arrangement, which were ascribed to the three ppy ligands of the Ir(ppy)$_3$ complex. The majority of molecules have exhibited a symmetric height distribution of these three protrusions, while 10% of the single molecules have shown an asymmetric height distribution, which was attributed to a metastable adsorption geometry. From these submolecular patterns, Yokoyama *et al.* conclude that most of the Ir(ppy)$_3$ molecules adsorb with a parallel alignment of their dipole moment to the surface normal. Among the two possible adsorption geometries, additional semi-empirical PM3 calculations indicate that an adsorption via the three pyridine groups is energetically more favorable than an adsorption via the three phenyl groups.

6.2.1 Single Ir(ppy)₃ Molecules at Au(111) Step Edges

In accordance with the previous studies by Yokoyama *et al.* on Cu(111), most of the Ir(ppy)₃ molecules deposited at room temperature on a Au(111) surface diffuse to the substrate step edges. There, the molecules can maximize their contact area and thus the molecule–substrate interaction. As visible in the topography scan in Fig. 6.4a,b, most of the molecules appear separated from each other, most likely due to the strong repulsive dipole–dipole interactions between them. However, occasionally molecular dimers can be observed, like in the upper left region of Fig. 6.4a,b. In this case, the molecular dipole moments might align in an antiparallel fashion. High-resolution topography maps reveal at least three different adsorption geometries (see dotted rectangle in Fig. 6.4b. Whereas single Ir(ppy)₃ molecules adsorbed on flat Au(111) terraces exhibit an apparent height of ~0.2 nm, similar to that observed on Cu(111),[217] the molecules adsorbed at the step edges possess an apparent height of 0.67 to 0.79 nm (at U_{set} = −3.0 V, I_{set} = 20 pA) depending on their specific adsorption geometry. The overall larger apparent height might be caused by a stronger hybridization of the molecules with the metal substrate due the nearly parallel alignment of the π system of the ligands with respect to the metal surface (see below). The diverse heights of the different adsorption
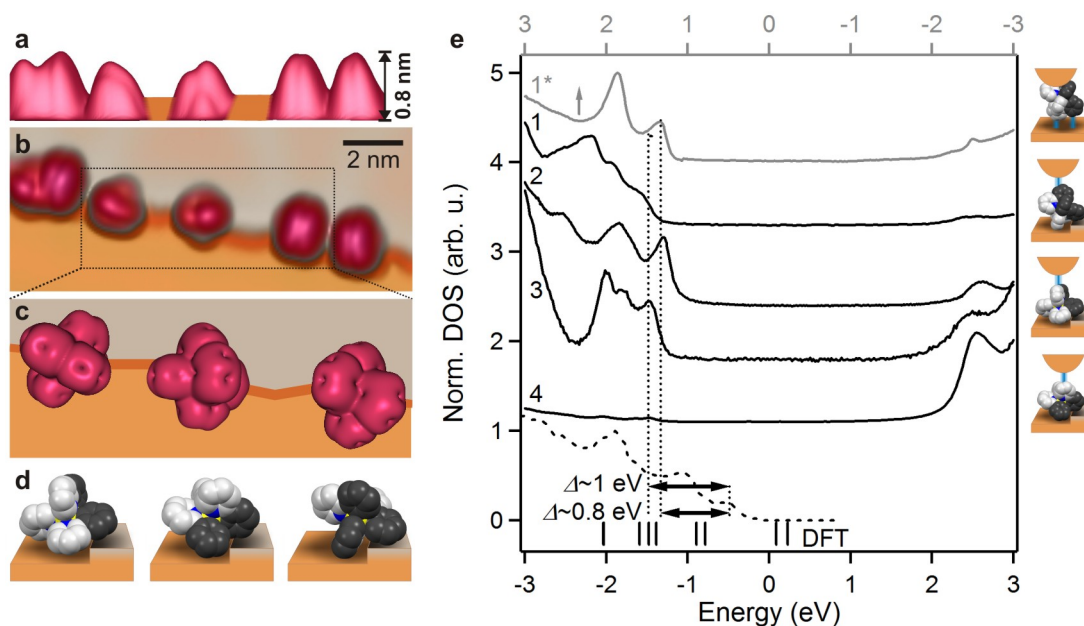
Fig. 6.4: Single Ir(ppy)₃ molecules at a Au(111) step edge. (a) Side-view and (b) top view of the same STM topography image showing individual Ir(ppy)₃ molecule in different adsorption geometries (U_{set} = −3.0 V, I_{set} = 20 pA). (c) Iso-surface plot of the electron density of the first ten occupied molecular orbitals calculated in section 6.1.3 and (d) space-filling model of the possible adsorption geometries of the molecules marked by the dotted rectangle in panel b. The phenyl groups are shown in dark gray, the pyridine groups in light gray. (e) dI/dU spectra on four different Ir(ppy)₃ molecules (spectra 1–4) and on a flat gold terrace (spectrum 1*) after picking up the molecule leading to spectrum 1. The possible adsorption geometries are depicted on the right-hand side. As a comparison, the lower part shows an UPS spectrum of Ir(ppy)₃ in a CBP matrix (dotted line, reproduced from ref. [207]) and the results of the DFT calculation from section 6.1.3 (vertical bars). In both cases, a vacuum level alignment of the molecules with the gold substrate and a work function of 5.3 eV were assumed.

geometries might be the result of a varying orientation of the phenyl and pyridine groups. For example, at negative bias voltages, electrons tunnel from the occupied Ir(ppy)$_3$ states to the STM tip. Since the highest occupied Ir(ppy)$_3$ orbitals are mainly localized on the phenyl groups of the Ir(ppy)$_3$ complex (section 6.1.3), they should appear slightly higher than the pyridine groups in STM. Figure 6.4c depicts the possible orientations of the molecules by showing the iso-surface plots of the summed squares of the ten highest occupied Ir(ppy)$_3$ orbitals calculated in section 6.1.3. The distribution of the calculated electron density nicely reproduces the features observed in the topography map. Therefore, the hybridization with and the perturbation by the metal substrate might be rather weak. The side view of the corresponding space-filling models (Fig. 6.4d) reveal that always three aromatic rings of the complex bind to the metal surface, either two pyridine moieties and one phenyl moiety or vice versa. In contrast to the flat substrate terraces, at substrate step edges, the π-system of the complex ligands can align nearly parallel to the surface. This might enable additional metal-π interactions, which could explain the preferred adsorption of the molecules at step edges.

dI/dU spectra on various single molecules show similar features as those observed by Theresa Lutz on Au(111) terraces.[47] Overall, four different types of dI/dU spectra with slightly varying peak positions and different peak intensity ratios between the occupied and unoccupied states could be observed (Fig. 6.4e). The origin of these differences is discussed below. In the range between −3 and +3 V, one unoccupied state at 2.5 V and up to four occupied states at −1.5, −1.75, −2.05, and −2.6 V can be resolved. Fitting these peaks reveals a clear Lorentzian line shape. Hence, the peak width is determine by the lifetime of the tunneling electrons through the corresponding orbitals. With a full width at half maximum (FWHM) of 0.45 V the lowest unoccupied molecular orbital (LUMO) peak appears slightly broader than the peaks of the occupied states with a FWHM of 0.3 V. The origin might be a stronger coupling of the LUMO to the substrate and/or a partial overlap of closely spaced energy levels, as indicated by the DFT calculation of the free molecule.

The bottom of Fig. 6.4e displays a HeI spectrum of Ir(ppy)$_3$ in a CBP matrix[207] (dashed line) as well as the calculated energy levels of free Ir(ppy)$_3$ from section 6.1.3 (vertical bars) both shifted by the work function of a Au(111) surface of 5.3 eV. Hence, this data depicts an energetic situation when the Ir(ppy)$_3$ molecules would align to the vacuum level of the substrate. The comparison with the measured dI/dU spectra indicates a shift of the occupied states by −1 eV for the spectra 1, 3 and 4 and a shift by −0.8 eV for the spectra 1* and 2. The energy differences between the HOMO and LUMO peak, on the other hand, exhibit a constant value of about 4 eV. The shift of the electronic states suggests the formation of an additional interface dipole barrier or, in other words, a lowering of the work function of the metal substrate upon adsorption of the single Ir(ppy)$_3$ molecules. Similar effects have been observed for many other adsorbate–substrate systems, especially on high work function metals such as gold, and have been ascribed to various origins.[219] In the present case, the lack of electronic states around the Fermi energy of the substrate ($E_{\mathrm{F,s}}$) precludes a possible charge transfer as well as the involvement of additional surface states. Furthermore, a simple attenuation of the electron cloud tailing into the vacuum (*pillow effect*) should cause much smaller shifts. Instead, the major origin of the work function shift might be the strong dipole moment of the Ir(ppy)$_3$ molecules. Similar shifts have been observed, for example, for alkanethiols of varying molecular dipole moments.[220] The reduction of the work function implies that the dipole moment of the Ir(ppy)$_3$ molecules point from the substrate to the vacuum side, in contrast to the conclusions drawn by Yokoyama *et al.* on Cu(111).[217,218] Therefore, for different orientations of the single

molecules, the work function should be lowered by different degrees, which might explain the distinct shifts for the dI/dU spectra displayed in Fig. 6.4e. The calculated orbital energies are shifted by further $0.7\,\text{eV}$ towards lower binding energy and lead to a HOMO–LUMO gap of $3.6\,\text{eV}$. Hence, the calculated gap is slightly lower than the gap determined from dI/dU spectra. These differences might be caused by many-body final state effects and the fact that, strictly speaking, dI/dU spectra obtained in STM do not reflect the energy levels of the electronic ground state but correspond to the positive ion resonance (PIR) and negative ion resonance (NIR), respectively.

Besides the different height profiles of the Ir(ppy)₃ molecules observed in topography maps, the distinct dI/dU spectra recorded on various single molecules are a clear indication for the existence of different adsorption geometries. As discussed in section 6.1.3, the occupied Ir(ppy)₃ orbitals are mostly localized on the phenyl groups, whereas the lowest unoccupied orbitals are predominantly confined to the pyridine groups. Therefore, the intensity ratio of the occupied and unoccupied states measured by dI/dU spectra at a constant STM tip height will depend on whether the tip is positioned on a phenyl group, a pyridine group, or the link between the two. Hence, spectra with a high density of occupied states (for example, spectrum 1 in Fig. 6.4e) might correspond to measurements on top of a phenyl group, spectra with a high density of unoccupied states (for example, spectrum 4 in Fig. 6.4e) to measurements on top of a pyridine group, and spectra with a more or less equal intensity of occupied and unoccupied states (for example, spectrum 2 and 3 in Fig. 6.4e) might result from an intermediated position between one or several phenyl and pyridine and groups.

When picking up the molecule leading to spectrum 1 in Fig. 6.4e by the STM tip, the subsequent spectrum 1* on a flat gold terrace resembles spectrum 2, which was measured on a molecule in another adsorption geometry. Note that spectrum 1* is plotted with reverse bias voltage (top axis) to account for the reverse tunneling through the vacuum barrier. Provided that the picked-up molecule changes its orientation only marginally while attaching it to the tip, such spectra might offer information about the bottom part of the adsorbed molecule, which binds to the substrate. Hence, this simple trick might double the information about the adsorption geometry of the adsorbed molecule. The modifications of the electronic structure after changing the contacting of the singles molecule once again demonstrate that their orientation and the molecular site with the smallest tunnel barrier strongly affect the current transport through the molecules. In conclusion, a systematic study of dI/dU spectra with the molecules being contacted by the substrate and the STM tip should provide a way to uncover the precise orientation of the single Ir(ppy)₃ molecules and also other non-planar, rigid molecules adsorbed on surfaces. Such studies could be further complemented by calculations including the metal substrate.

6.2.2 Single Ir(ppy)$_3$ Molecules on Ag(111) Terraces

On flat Ag(111) terraces, single Ir(ppy)$_3$ molecules exhibit an apparent height of ~0.2 nm, similar to that on Cu(111)[217, 218] and Au(111).[47] dI/dU spectra of the molecules on a Ag(111) surface resemble those of the single Ir(ppy)$_3$ molecules adsorbed at the gold step edges. However, the spectra reveal an additional tail of unoccupied states extending down to $E_{F,s}$ (Fig. 6.5). Similar tails have been observed for C$_{60}$ on coinage metals (see section 4.3.1) and are ascribed to a charge transfer from the metal substrate to the molecule. Hence, the adsorption of the Ir(ppy)$_3$ molecules on a Ag(111) surface might result in an analogous charge transfer.
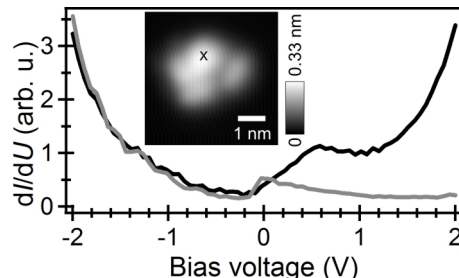
Fig. 6.5: dI/dU spectrum on a single Ir(ppy)$_3$ molecule (black) adsorbed on a Ag(111) surface and the bare Ag(111) surface next to it (gray). The inset shows a topography map of and the position of the spectrum on top of the molecule marked by the cross.

6.2.3 Ir(ppy)$_3$ Layers on Ag(111)

At slightly higher coverages, highly-ordered domains with lateral dimensions of a few tens of nanometers could be occasionally observed. Their apparent height of 0.8 nm with respect to the clean Ag(111) surface equals the height of the single molecules at the Au(111) step edges. Therefore, the found domains might correspond to small patches of an Ir(ppy)$_3$ monolayer. Alternatively, the observed Ir(ppy)$_3$ films might consist of Ir(ppy)$_3$ bi- or multilayers, as suggested by Yokoyama *et al.* on Cu(111). Before discussing the precise arrangement of the molecules, their electronic structure will be discussed.

dI/dU spectra of the Ir(ppy)$_3$ layers resemble those of the single molecules on flat Ag(111) terraces and exhibit a similar LUMO tail down to $E_{F,s}$ (Fig. 6.6i) suggesting a charge transfer from the metal to the Ir(ppy)$_3$ molecules. This charge transfer might be the reason for the ~0.2 eV shift of the dI/dU spectra toward smaller bias voltages compared to those of the single molecules at the gold step edges. Considering the work function difference between Au(111) and Ag(111) of −0.55 eV one would actually expect a shift in the opposite direction. The reason for the observed shift of dI/dU spectra might be explained by the rearrangement of the electron density in the substrate surface due to charge transfer discussed above. At the same time, the partial occupation of the LUMO-derived states might reduce the molecular dipole moment. Calculations of the free Ir(ppy)$_3$ anion, for example, show that the additional electron primarily occupies the almost neutral pyridine groups and the molecular dipole moment reduces by 1.4 D to 4.8 D. Both factors − the rearrangement of electron density in the substrate and the attenuation of the molecular dipole moment − decrease the interface dipole barrier, which leads to a weaker lowering of the work function than in the case of the Au(111) substrate. On closer examination, the occupied states of the Ir(ppy)$_3$ layer appear much sharper than those of the single Ir(ppy)$_3$ molecules adsorbed at the gold step edges. Futhermore, the peaks rather show a Gaussian line shape with a FWHM of 80 meV and 100 meV for the HOMO peak and the most intense peak at −2.1 eV, respectively. Both dI/dU

peaks are accompanied by two shoulders at slightly higher negative bias voltage (see arrows Fig. 6.6g,h). These additional states might correspond to progressions of vibrationally excited states or might result from the splitting of the (nearly) degenerate states (see section 6.1.3) by the crystal field of the neighboring molecules in the Ir(ppy)₃ layer. The unoccupied states,
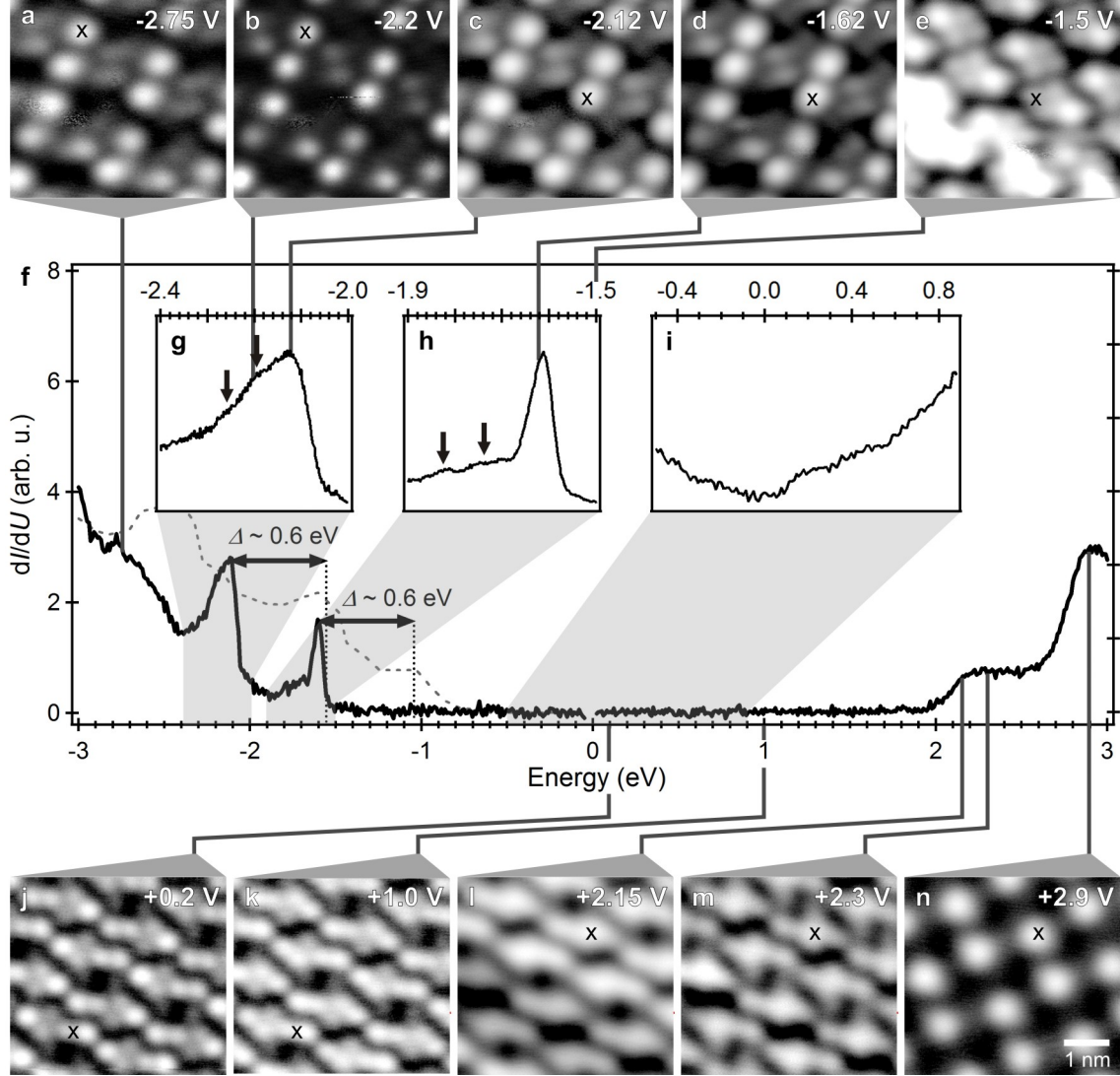
Fig. 6.6: Electronic structure of an Ir(ppy)₃ layer on Ag(111). (a–e) occupied states and (j–n) unoccupied states imaged by constant height dI/dU maps at the denoted bias voltage. The data are plotted with logarithmic gray scale. (f) dI/dU spectrum as a function of bias voltage with detailed spectra in the indicated regions shown in (g–h). The spectrum in panel f consists of two spectra, one recorded at positive bias polarity ($U_{set} = 3.0\,V$, $I_{set} = 40\,pA$) and a second one at negative bias polarity ($U_{set} = -3.0\,V$, $I_{set} = 112\,pA$). The spatial positions of the spectra in the panels f–i are marked in the dI/dU images by black crosses. As a comparison, the dashed curve in panel f depicts the HeI spectrum of Ir(ppy)₃ in a CBP matrix (obtained from ref. [207]), assuming a vacuum level alignment with the metal substrate and a work function of 4.75 eV. The horizontal arrows indicate the energy difference between the dI/dU and the UPS peaks (Δ) and thus the strength of the interfacial dipole. The arrows in panel g and h indicate two weaker peaks aside to the main peak.

on the other hand, appear slightly broader than in the case of the single Ir(ppy)$_3$ molecules on the gold step edges, most likely because of the stronger hybridization and the charge transfer from the Ag(111) substrate. The panels a–e and j–n of Fig. 6.6 display the spatial distribution of the occupied and unoccupied states of the Ir(ppy)$_3$ layer, respectively, imaged by constant height $\mathrm{d}I/\mathrm{d}U$ maps. The lateral drift during the acquisition of the data is corrected according the procedure described in section 2.3.4. The determined drift amounts to $-91\,\mathrm{pm/h}$ in the x-direction (fast scan direction) and $-253\,\mathrm{pm/h}$ in the y-direction (slow scan direction). Hence, the distortion of the image in the fast scan direction due to drift is negligible. For the distortion correction along the slow scan axis, the images are modified by the total drift during the acquisition of an image ($\sim$512 s, $d_y = -36\,\mathrm{pm}$) divided by the original image size (5 nm), that is by 0.72%. The spatial distribution of the occupied states closely resemble each other and the general pattern in $\mathrm{d}I/\mathrm{d}U$ maps depend only weakly on bias voltage. This observation is in agreement with the calculations of the free Ir(ppy)$_3$ molecule in section 6.1.3, which suggest a predominant localization of the ten highest occupied states on the phenyl moieties. Although the electron density on the iridium center varies substantially among the occupied states, the ratio of electron density on the phenyl and pyridine groups ranges only from 2.8 to 4.6 (see Fig. 6.3, page 67). In contrast, the spatial distribution of the unoccupied states strongly depends on the applied bias voltage (Fig. 6.6j–n). The highest spatial resolution is obtained close to $E_{\mathrm{F,s}}$ (Fig. 6.6j), where the additional
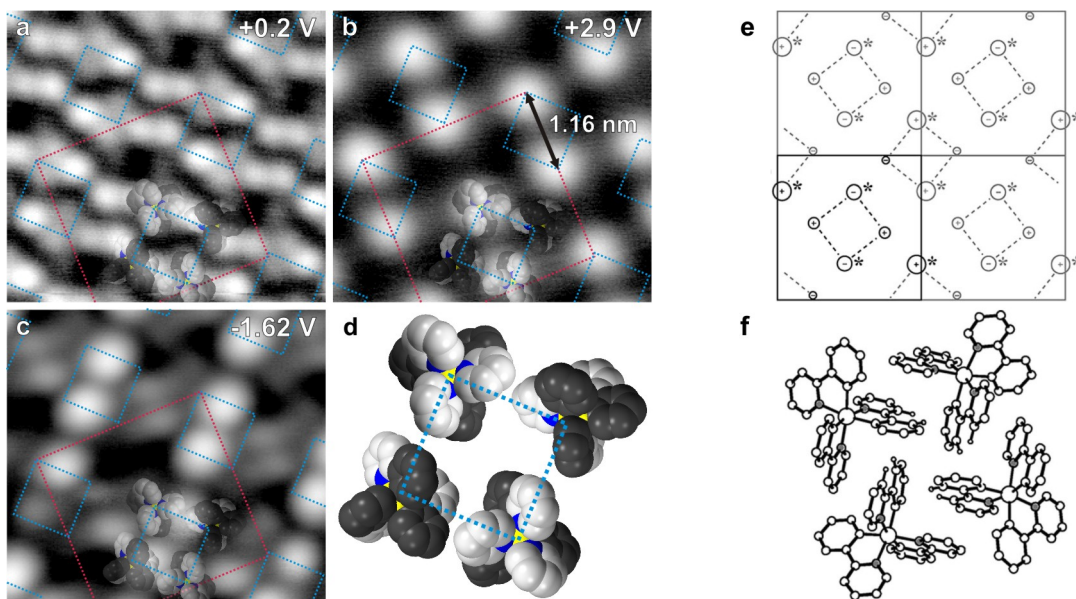
Fig. 6.7: Unit cell of Ir(ppy)$_3$ submonolayers on Ag(111). (a–c) Constant height $\mathrm{d}I/\mathrm{d}U$ maps at the denoted bias voltage plotted with logarithmic gray scale. The larger red squares indicate the unit cell of the adsorption structure; the smaller blue squares mark the tetrameric subunits magnified in (d). Phenyl groups are shown in dark gray, pyridine groups in light gray. The black arrow in panel b indicates the minimum distance between two bright molecules. (e) Four unit cells of bulk Ir(ppy)$_3$ viewed along the crystallographic c axis (obtained from ref. [204]). Large circles correspond to a larger c coordinate while smaller circles correspond to deeper-lying molecules. The plus and minus signs indicate the orientation of the dipole moments, which are either parallel or antiparallel to the c axis. (f) Orientation of the molecules within the tetrameric subunit of bulk Ir(ppy)$_3$ displayed in panel e (obtained from ref. [204]).

electron density due to the charge transfer from the substrate is expected. The dI/dU maps in this bias range exhibit round features with a diameter of 0.3 nm that are arranged in triangular structures. These features might arise form the electron density transfered from the substrate to the individual Ir(ppy)$_3$ ligands; hence, they should depict the interface between the Ir(ppy)$_3$ molecules and the Ag(111) substrate. The highest dI/dU contrast between the molecules is found at a bias voltage of +2.9 eV, which leads to a checkerboard-like pattern with an alternating high and low local density of states on the molecules. The imaged states around +2.9 eV most likely correspond to the second lowest group of unoccupied Ir(ppy)$_3$ states (π_3^*, π_{4a}^*, π_{4b}^*, see Fig. 6.3). Indeed, a population analysis of these states for the free Ir(ppy)$_3$ molecule (Fig. 6.3c) reveal that the electron density on the pyridine groups is ~9 times larger than on the phenyl groups, in accordance with the strong contrast between neighboring molecules. Therefore, the dipole moments of neighboring molecules might be arranged in an antiparallel fashion as well as parallel or antiparallel with respect to the surface normal. Such an arrangement minimizes the electrostatic interactions between the strong dipoles and thus should be favored. An alternating alignment of the dipole moments perpendicular to the surface normal, in contrast, should result in a striped pattern that is not observed.

For a detailed discussion of the molecular arrangement within the layer, the dI/dU maps at −1.62, +0.2 and +2.9 V are shown again in Fig. 6.7. The red squares mark the square unit cell of the molecules with a lattice constant of 2.57 nm. This square unit cell bears a close resemblance with the tetrameric subunits obtained for the bulk structure of Ir(ppy)$_3$ single crystals (Fig. 6.7e,f).[204] Indeed, the observed lattice constant within the Ir(ppy)$_3$ layer is only 11% larger than the lattice vectors along the crystallographic a and b axes of bulk Ir(ppy)$_3$. The less dense unit cell might result from the planar arrangement of the molecules on the flat substrate terraces. In the bulk structure, the molecules pack in weakly associated tetrameric subunits, in which the molecular dipole moments alternate in direction and align roughly parallel or anti-parallel to the c-axis. The dI/dU maps, and particularly the checkerboard-like pattern at +2.9 V, suggest a very similar packing motif. On closer examination, one notices that the distances between the bright molecules of the checkerboard pattern in Fig. 6.7b are not identical along the different directions. Instead, two pairs of molecules per unit cell come slightly closer to each other and exhibit a distance of 1.16 nm (Fig. 6.7b). This distance is basically the same as the one of equally oriented molecules in the bulk tetramers (1.15 nm). On the whole, the Ir(ppy)$_3$ molecules adsorbed on Ag(111) should thus arrange in a similar way as in the bulk. The varying density of states of the round features in Fig. 6.7a and Fig. 6.7c, furthermore, suggests a small tilt angle of the molecular dipole moments with respect to the surface normal. A possible structural model for the observed Ir(ppy)$_3$ layer is shown in Fig. 6.7d.

6.3 Single Ir(ppy)$_3$ Molecules on a C$_{60}$ Monolayer

In order to reduce the interaction between the Ir(ppy)$_3$ molecules and the metal substrate, they were deposited on C$_{60}$ films of various thicknesses. The following sections will show that a C$_{60}$ monolayer primarily acts as a spacer that prevents a direct interaction with the metal substrate. However, as a consequence of the modified interfacial dipole layer at the metal surface, the additional C$_{60}$ monolayer results in a shift of the Ir(ppy)$_3$ states toward lower binding energies.

6.3.1 Topography Maps and Adsorption Geometries

Single Ir(ppy)$_3$ molecules adsorbed on a C$_{60}$ monolayer are observed as only 60 to 120 pm high protrusions in comparison to the highest positions on the C$_{60}$ monolayer; thus, they appear significantly smaller than the molecules directly adsorbed on metal substrates. The main cause for this observation might be the high local density of states (LDOS) of the C$_{60}$ monolayer, as the C$_{60}$ LUMO is three-fold degenerate and the C$_{60}$ HOMO even five-fold degenerate. In addition to this apparent height effects, there might be real height differences. Indeed, the tripod-like shape of the Ir(ppy)$_3$ molecules and the π-system of their ligands might favor an adsorption in which three of the half-ligands enclose one spherical C$_{60}$ molecule.

Overall, three different adsorption geometries can be identified (Fig. 6.8). For bias voltages < -1.5 V, the single molecules exhibit only weak topography features (Fig. 6.8a–c). However, for negative bias voltages ≥ -1.5 V, the molecules show a clear submolecular pattern (Fig. 6.8d,e) similar to those observed by Yokoyama *et al.* on Cu(111).[217,218] At these bias voltages, the topography of the C$_{60}$ layer features the weak extension of the LUMO-derived states to the Fermi energy due to the charge transfer from the metal substrate. Therefore, the reduced spatial resolution for bias voltages < -1.5 V most likely arises from the onset of the C$_{60}$ HOMO-derived states and the resulting coupling between Ir(ppy)$_3$ and C$_{60}$ states. At positive bias voltages up to +3 V, the single Ir(ppy)$_3$ molecules are invisible or appear as very weak depressions, which suggests a lack of unoccupied states in this voltage range.
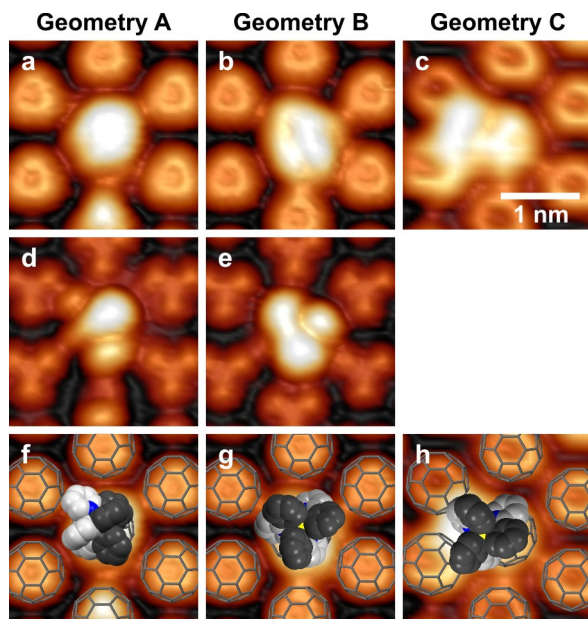
Fig. 6.8: Adsorption geometries of single Ir(ppy)$_3$ molecules on a C$_{60}$ monolayer on Ag(111). (a–c) Pseudo-3D topography map of three differently adsorbed Ir(ppy)$_3$ molecules imaged at a bias voltage of $U_{set} = -3.0$ V. (d,e) Pseudo-3D topography map of the single molecules in the panels a and b imaged at a bias voltage of $U_{set} = -0.9$ V. (f–h) Possible adsorption geometries of the single molecule on the C$_{60}$ lattice. Dark gray parts of the space-filling models show the phenyl groups of the three ppy-ligands, light gray parts the pyridine groups.

The three different adsorption geometries can be clearly discriminated by the submolecular pattern found at bias voltages ≥ -1.5 V. Single molecules in geometry A are characterized by an angled structure with a higher protrusion in the center and two lower outer protrusions, which resembles the "metastable" geometry found by Yokoyama *et al.*[218] The highest protrusion might result from a ppy-ligand whose short axis stands parallel to the surface normal (Fig. 6.8f). The slightly lower protrusions in the lower and upper left part might correspond to a phenyl group and a pyridine group of the other two ppy-ligands, respectively. Single Ir(ppy)$_3$ molecules adsorbed in geometry B, in contrast, exhibit three protrusions of nearly identical

height, which are arranged in a triangular configuration. A similar pattern was also observed by Yokoyama *et al.* on Cu(111).[218] The symmetric pattern suggests that the pseudo-C_3 axis of the Ir(ppy)$_3$ molecules, in this case, is nearly parallel to the surface normal. The partial negative charge on the C$_{60}$ molecules due to the charge transfer from the metal substrate might favor an adsorption of the single Ir(ppy)$_3$ molecule via their neutral pyridine groups (Fig. 6.8g). Besides these two adsorption geometries, photon maps reveal an additional, third geometry C (see Fig. 8.1 on page 99). The submolecular pattern associated with this geometry resembles the one of geometry B; however, the center of the triangular pattern possess a lateral offset with respect to the C$_{60}$ lattice. Therefore, in geometry C the single Ir(ppy)$_3$ molecule might reside in a side-on position on one C$_{60}$ molecule, with its pseudo-C_3 axis slightly tilted referring to the surface normal (Fig. 6.8h).

6.3.2 Electronic Structure

Compared to the single Ir(ppy)$_3$ molecules directly adsorbed on the metal substrate, the electronic states of single Ir(ppy)$_3$ molecules adsorbed on a C$_{60}$ monolayer are shifted by ~1.3 eV toward lower binding energies. This substantial shift and the band gap of > 3.6 eV might explain the absence of unoccupied states and the invisibility of the single molecules at positive voltages up to +3 V. The observed dI/dU spectra slightly vary for the different adsorption geometries, as for the single Ir(ppy)$_3$ molecules at the gold step edges (section 6.2.1). Moreover, the intensity ratio and position of the dI/dU peaks strongly depend on the lateral and vertical position of the STM tip on the single molecules. To illustrate these points, Fig. 6.9a depicts a series of dI/dU spectra along a line across a single Ir(ppy)$_3$ molecule in adsorption geometry A. In addition, Fig. 6.9b shows a series of dI/dU spectra recorded at different tip heights on an Ir(ppy)$_3$ molecules in geometry B. In the latter case, the lateral drift during the acquisition of the data was determined to be < 0.06 nm, so can be neglected. dI/dU spectra of both adsorption geometries exhibit two peaks at -0.2 and -0.9 V. While the molecules in the A configuration exhibit two additional peaks at -1.8 and -2.2 V, molecules in the B configuration show only one additional peak at -1.5 V. The orbital energies of the free Ir(ppy)$_3$ molecule calculated in section 6.1.3 are depicted as vertical bars in Fig. 6.9a,b, assuming a vacuum level alignment with the C$_{60}$-covered surface and a work function of 5 eV.[160, 170] The calculations suggest that the peak closest to the Fermi level at about -0.2 V corresponds to the HOMO of the adsorbed Ir(ppy)$_3$ molecule. Considering the shape of the dI/dU peaks, the HOMO possesses by far the smallest peak width and, in contrast to the remaining peaks, a Lorentzian shape. Indeed, its FWHM of 0.13 eV is less than half as large as the corresponding value for the single Ir(ppy)$_3$ molecules adsorbed at the gold step edges (~0.3 eV), which confirms a certain decoupling from the metal substrate. At the same time, however, the HOMO width is slightly larger than in the case of the Ir(ppy)$_3$ monolayer on Ag(111) (0.08 eV). The widths of the remaining dI/dU peaks are significantly increased (FWHM: 0.46...0.6 eV) compared to the molecules directly adsorbed at the metal substrate, most likely due to the coupling to occupied C$_{60}$ states. Therefore, the C$_{60}$ monolayer merely acts as a thin spacer layer, preventing a direct hybridization with the metal substrate. As an electronic decoupling layer it is, however, less suitable, at least for the decoupling of single Ir(ppy)$_3$ molecules.
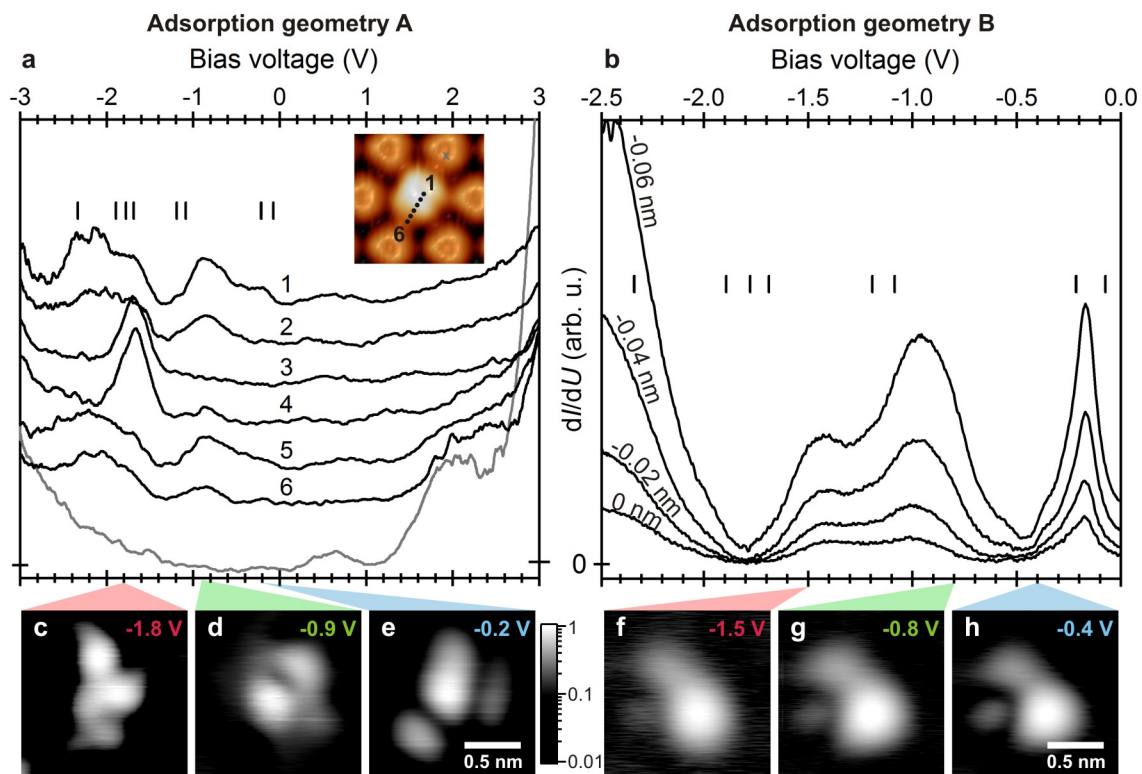
Fig. 6.9: Electronic structure of single Ir(ppy)$_3$ molecules on a C$_{60}$ monolayer on Ag(111). (a) dI/dU spectra along a line across a single Ir(ppy)$_3$ molecule (black solid line) adsorbed in geometry A on a C$_{60}$ monolayer (gray solid line). The lateral position of the spectra is indicated in the inset showing a constant current topography ($U_{set} = -3.0$ V, $I_{set} = 50$ pA). (b) dI/dU spectra on a single Ir(ppy)$_3$ molecule in adsorption geometry B as a function of the relative STM tip–sample distance (denoted aside to the spectra). In both panels, a and b, the vertical bars show the results of the DFT calculation in section 6.1.3 assuming a vacuum level alignment with the C$_{60}$-covered surface (work function: 5 eV[160, 170]). (c–e) Normalized constant height dI/dU map of a single molecule in geometry A and and (f–h) a single molecule in a geometry B, recorded at the denoted bias voltage and plotted with logarithmic gray scale.

Figure 6.9c–e and Fig. 6.9f–h display the orbital shapes of a single Ir(ppy)$_3$ molecule in the A and the B geometry, respectively, imaged by constant height dI/dU maps. For the molecules in the A geometry the observed orbital shapes differs a lot, whereas the imaged electron density of molecules in geometry B changes only marginally with bias voltage. Considering the varying electron density distribution of the different molecular orbitals, as well as their symmetries, geometry B might thus correspond to an orientation in which three equivalent half-ligands – either three phenyl groups or three pyridine groups – pointing toward the STM tip. Geometry A, on the other hand, might correspond to an orientation in which the observed lobes result from phenyl and pyridine moieties. These observations agree with the conclusions drawn above and corroborate the adsorption geometries depicted in Fig. 6.8.

Chapter 7

Single Ir(ppy)$_3$ Molecules on Semiconducting C$_{60}$ Layers – Ir(ppy)$_3$ Embedded in a Double Tunnel Barrier

The previous chapter showed that a C$_{60}$ monolayer is a rather poor electronic decoupling layer for single *fac*-tris(2-phenylpyridine)iridium(III) (Ir(ppy)$_3$) molecules, primarily because of their coupling with the occupied C$_{60}$ states. To prevent a strong interaction of single molecules and atoms with the supporting surface, they are typically deposited on thin insulating layers, such as oxide layers,[38, 221–224] salts,[225–230] or nitrides.[84, 231] However, often the weak interaction with the surface is both a blessing and a curse, as the deposited molecules are quite mobile and hard to image.[47] Chapter 4 showed that the surface of C$_{60}$ films thicker than one monolayer exhibit semiconducting properties with an apparent band gap of ~3 eV. Therefore, in this chapter thin C$_{60}$ films of two and three molecular layers shall be investigated as potential decoupling layers for single Ir(ppy)$_3$ molecules. The motivation behind this is that, due to the π-systems of both the C$_{60}$ and the Ir(ppy)$_3$ molecules, the latter should bind more strongly to the surface, which might enable a detailed characterization of their electronic properties. However, beforehand, the major differences between tunneling through a molecule directly adsorbed on a metallic surface and a molecule on an insulating or semiconducting surface shall be discussed.

7.1 Tunneling Through Molecules on Metallic and Semiconducting Surfaces

All observed differences between the tunneling through a molecule on a metal and a thin semiconducting film can be traced back to two fundamental effects. First, the lack of electronic states within the band gap of the semiconductor reduces the (electronic) coupling between the molecule and the surface. Second, finite bias voltages applied to the junction cause a voltage drop across the semiconductor. The consequences of these two effects shall be briefly discussed in the following subsections.

7.1.1 Lifetime of Transient Charges

Most tunneling processes through a molecule in a scanning tunneling microscope can be considered as a sequential or two-step process: In the first step, one of the electrodes injects a charge carrier – either an electron or a hole – into an unoccupied or occupied electronic state, respectively. In a second step, this charge carrier tunnels to the second electrode. For a molecule directly adsorbed on a metal surface, the initial charge injection can only occur via the STM tip because its electronic states are pinned to those of the substrate (see section 7.1.3). Furthermore, the tunnel barrier between the molecule and a metal substrate is typically extremely thin, such that each injected charge carrier quickly tunnels to the substrate. As a consequence, the residence time of the tunneling charge on the molecule is very short (femto- to picoseconds). When an additional tunnel barrier is inserted between the molecule and the metal substrate, for example, in the form of a thin semiconducting or insulating layer, the charge transfer can be substantially slowed down and the residence time of the additional charge increases respectively. If the second tunneling step in the afore mentioned two-step process is much slower than the first one, the upper limit of the residence time of a charge carrier can be estimated by the mean time between two tunneling charge carriers $\langle t \rangle$ and thus by the measured current:

$$\langle t \rangle = \frac{e}{I} \tag{7.1}$$

with e as the elementary charge. At a measured current of $20\,\text{pA}$, for example, the lifetime of the transient charge on the molecule should be shorter than $8\,\text{ns}$. However, it is important to note that the precise ratio between the measured current and the lifetime of the charged molecule depends considerably on the ratio of the tunneling rates through both tunnel barriers.

7.1.2 Resonant Tunneling Through Vibrationally Excited States

Any polyatomic molecule can be excited to vibrations of its intramolecular bonds and thus possesses a series of vibrational modes, whose number increases with the number of atoms the molecule consists of. Since the corresponding vibrational states couple to the electronic state of the molecule, they lead to a vibrational fine structure of each electronic state (Fig. 7.1), known as vibronic states. When a charge carrier tunnels into one of the higher-lying vibronic

states – for example, of an unoccupied electronic state – the molecule resides in a transiently charged and vibrationally excited state.

A molecule directly adsorbed on a metal surface will typically relax within a few picoseconds into its vibronic ground state.[232] CO molecules on a Pt(111) surface, for instance, exhibit a vibrational relaxation time of 2 ps.[233] The predominant relaxation channel on metal surfaces is the excitation of electron–hole pairs in the metal. When the relaxation time is shorter than the residence time of the additional electron on the molecule, the molecule anion relaxes into its vibrational ground state before the electron tunnels through the second tunnel barrier (Fig. 7.1a). In this case, the tunneling electron always leaves the molecule in its vibrational ground state. In other words, it leaves the molecule with an energy that is smaller than it had before the first tunneling process, irrespective into which vibrationally excited state the electron tunneled before. As a result, the electronic states of a molecule directly adsorbed on a metal surface generally appear as broad, featureless peaks in differential conductance (dI/dU) spectra.*
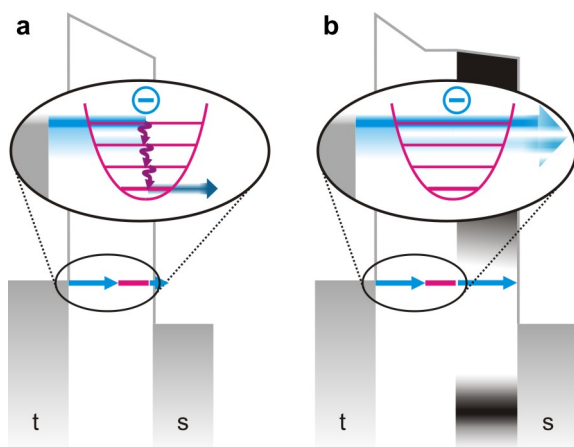
Fig. 7.1: Tunneling through vibrationally excited states. (a) Schematic energy diagram for electrons tunneling from the STM tip (t) through a molecule directly adsorbed on a metal substrate (s) and (b) through a molecule on a thin semiconducting film grown on a metal substrate.

Typical vibrational relaxation times of molecules adsorbed on a semiconducting surfaces lie in the range of a few nanoseconds.[232] For CO on a Si(100) surface, for example, a relaxation time of 2 ns have been observed.[234] In contrast, on insulating NaCl(100) surfaces, even relaxation times of 4 ms have been reported,[235] which is close to the value of the free CO molecule. The dominant decay channel in this case is the excitation of substrate phonons or combination modes with lower frequency adsorbate vibrations.[232] Hence, for molecules adsorbed on thin semiconducting films, the vibrational relaxation times can be comparable or even larger than the residence time of tunneling electrons on the molecules. As a result, the electrons can resonantly tunnel through the vibrationally excited states, without losing energy (Fig. 7.1b). When the Fermi level of the tip is aligned with one of these states, electrons can tunnel more efficiently through the molecule than when the Fermi level is aligned between two vibronic states. Consequently, in this case dI/dU spectra may image the vibrational fine structure of the electronic state. For larger molecules with a multitude of vibrational modes, however, the vibronic states of several modes typically overlap or couple to each other so that the dI/dU spectra nonetheless may only show broad features.

---

*Another origin of the broad dI/dU peaks in this case might follow from the uncertainty principle and the short lifetime of the electron in the molecule. For a significant broadening (>20 meV), however, the electron lifetime must be <100 fs.

7.1.3 Shift of Electronic States by the Electric Field in the Junction

For adsorbed molecules that strongly couple to the electronic states of the surface, such as molecules directly adsorbed on a metal surface, the tunnel barrier between the two is negligible compared to the vacuum barrier. Consequently, the electronic states of the molecules are pinned to the substrate and basically the entire bias voltage applied to the junction drops across the vacuum barrier (Fig. 7.2a). However, this no longer applies when an additional dielectric layer – that is, a thin insulating or semiconducting layer – is inserted between the molecule and the metal substrate. In this case, the dielectric properties of the decoupling layer cause a finite voltage drop between the molecule and the metal substrate (Fig. 7.2b). As described in detail in section 4.4, this finite voltage drop leads to a shift of the electronic states in the surface so that these states appear at a voltage $U_\mathrm{n}^\mathrm{obs}$, which differs from their zero-field potentials U_n^0 by the voltage drop across the decoupling layer:

$$U_\mathrm{n}^\mathrm{obs} = U_\mathrm{n}^0 + U_\mathrm{dec} \tag{7.2}$$
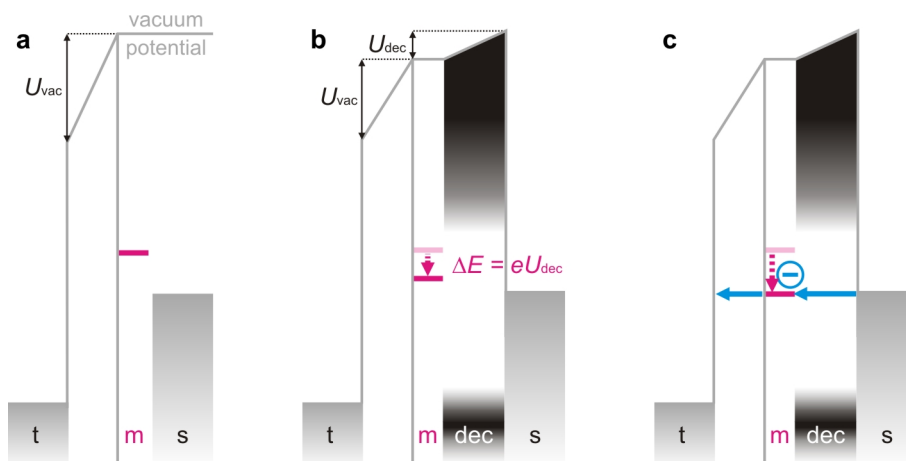
Fig. 7.2: Energy level shift of a single molecule m adsorbed directly on a metal surface and on a thin semiconducting film grown on a metal substrate. (a) On a metal surface, the molecular states are pinned in energy to the substrate s and basically the entire voltage applied to the junction (U_bias) drops across the vacuum barrier (U_vac). (b) For a single molecule adsorbed on a thin decoupling layer dec, U_bias equals the sum of U_vac and the voltage drop across the decoupling layer (U_dec); hence, the molecular states are shifted in energy according to U_dec. (c) As soon as U_dec is larger than the zero-field potential of a molecular state, charge carriers can be injected by the substrate and tunnel from the substrate s to the tip t.

7.1.4 Bipolar Tunneling Through Molecular States

When the voltage drop across the decoupling layer equals the zero-field potential of a molecular state, the state aligns with the Fermi level of the substrate and charge carriers are able to tunnel from the substrate into this state (Fig. 7.2). Hence, the finite voltage drop across the decoupling layer enables an injection of charge carriers from both the STM tip as well as the substrate and thus a bipolar conduction through the molecule.[236] As soon as the

molecular state reaches the Fermi level of the substrate, the conduction through the junction rises dramatically because, technically, the one-step tunneling through the one big barrier consisting of the decoupling layer, the molecule, and vacuum barrier is replaced by a two-step tunneling process through the decoupling layer and the vacuum barrier. In dI/dU spectra, this additional conduction channel manifests itself as a very sharp and intense peak, which generally dominate the spectra.[182, 221, 237] For a molecule directly adsorbed on a metal surface, this additional conduction channel is generally not available because the shift of its molecular states requires very high bias voltages due to the negligible tunnel barrier between the molecule and the substrate.

7.2 Single Ir(ppy)$_3$ Molecules on C$_{60}$ Bilayers

In this section, the electronic characteristics and energy levels of single Ir(ppy)$_3$ molecules on a C$_{60}$ bilayer shall be discussed. The samples were prepared as described in section 2.3.5 on either a Ag(111) or a Au(111) substrate. To avoid confusion, data obtained on a Ag(111) substrate is displayed by gray curves and data acquired on a Au(111) substrate is displayed by brown or black curves. On both substrates, the single Ir(ppy)$_3$ molecules exhibit an apparent height of 100 to 200 pm (at -3 V) and thus appear slightly higher than on a C$_{60}$ monolayer (60 to 120 pm). Similar to the situation on a C$_{60}$ monolayer, photon maps of the single Ir(ppy)$_3$ molecules reveal three different adsorption geometries (see section 8.2). However, dI/dU spectra and dI/dU maps of the single molecules differ markedly from those on the bare metal substrate as well as on a C$_{60}$ monolayer and exhibit a surprisingly large number of spectroscopic features. The following section shall discuss the individual origins of these features. It will become obvious that most of the dI/dU peaks result from two singly occupied molecular orbitals (SOMOs), either a singly occupied C$_{60}$ state or a singly occupied Ir(ppy)$_3$ state. Accordingly, these peaks are denoted either as S_C or S_I peaks. Superscript indices denote whether the underlying tunneling process is connected with the injection of an electron (S^e) or the injection of a hole (S^h).

7.2.1 Charge Injection via the STM Tip

dI/dU spectra on single Ir(ppy)$_3$ molecules on a Au(111)-supported C$_{60}$ bilayer exhibit two distinct peaks (S_I^h, S_I^e, Fig. 7.3a, solid black line) within the band gap of the C$_{60}$ layer (Fig. 7.3a, dotted line) at about -1.75 and 0.8 V. Detailed spectra (Fig. 7.3c,d) show that at smaller tunneling energies both peaks are accompanied by a series of much sharper peaks. Whereas the black spectra in Fig. 7.3c,d are measured at the same lateral position as in Fig. 7.3a, the brown spectra are recorded at the position marked by the brown cross in Fig. 7.3b. In particular for the empty states, the peak width increases substantially with absolute bias voltage, from a full width at half maximum (FWHM) of 22 mV for the lowest unoccupied state S_C^e to 117 mV for the 0.8 V peak. The origin of this trend might be the increasing coupling to C$_{60}$ states. Similar dI/dU spectra are also observed for single Ir(ppy)$_3$ molecules on Ag(111)-supported C$_{60}$ bilayers (Fig. 7.3c,d; gray line), although the exact position of the

first filled state S_C^h and the first empty state S_C^e occur at slightly different bias voltages.[†] On the whole, the energy difference between the highest occupied and lowest unoccupied states on both substrates is considerably smaller than the gap between the highest occupied molecular orbital (HOMO) and the lowest unoccupied molecular orbital (LUMO) observed for Ir(ppy)₃ molecules directly adsorbed on the metal substrates (of ~4 eV, see section 6.2).
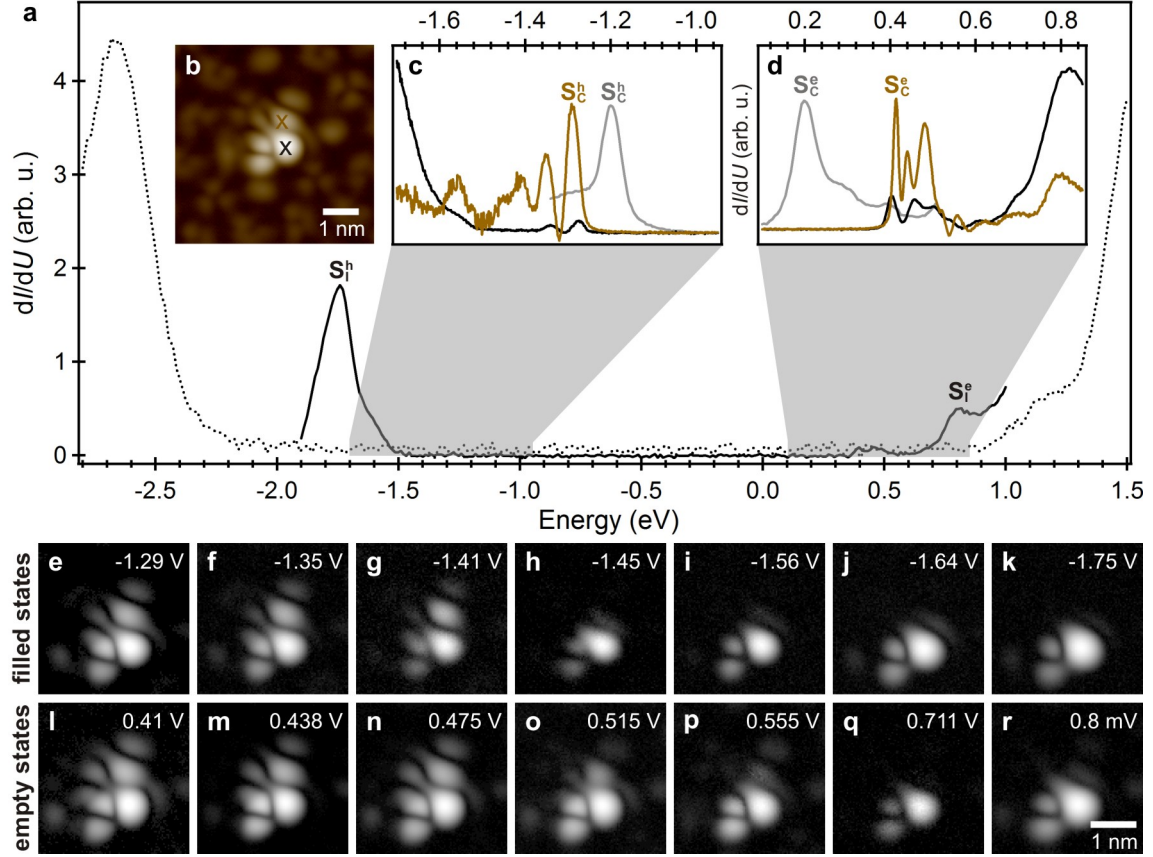
Fig. 7.3: Electronic structure of a single Ir(ppy)₃ molecule on a C₆₀ bilayer. (a) dI/dU spectra of a Au(111)-supported C₆₀ bilayer (dotted curve) and a single Ir(ppy)₃ molecule adsorbed on it (solid black curve). (b) Pseudo-topography image − that is, a constant height current map (U_{set} = 0.711 V) displayed with a logarithmic color scale − of the single molecule in the other panels. (c) Detailed spectra of the highest occupied electronic states and (d) the lowest unoccupied states. The brown and black curves are recorded on slightly different lateral positions, marked by the colored crosses in panel b. The gray curve shows the corresponding states for a single Ir(ppy)₃ molecule on a Ag(111)-supported C₆₀ bilayer. (e–r) Constant height dI/dU maps of the single Ir(ppy)₃ molecule imaged in panel b at the peak energies in the panels c and d.

Constant height dI/dU maps of the S_C^h (Fig. 7.3e) and the S_C^e (Fig. 7.3l) states reveal two additional important aspects: First, the lateral distribution of both states is more than twice as large as a single Ir(ppy)₃ molecule and differs substantially from the molecular orbitals observed for single Ir(ppy)₃ molecules on C₆₀ monolayers. Second, the lateral distribution of both states are very similar to each other and show the same number of nodal planes.

[†]The apparently larger peak widths of the gray curves do not result from an intrinsic effect but instead arises from a larger lock-in modulation amplitude of the bias voltage (20 meV instead of 5 meV).

Consequently, it is very unlikely that the states S$_C^h$ and S$_C^e$ arise from the Ir(ppy)$_3$ HOMO and LUMO, respectively. Instead, both states must arise from the tunneling through the same SOMO. Very similar effects have been reported for other single molecules on thin NaCl films.[227, 229] Indeed, the small energy difference between the Fermi energy of the substrate ($E_{F,s}$) and the Ir(ppy)$_3$ HOMO adsorbed on a C$_{60}$ monolayer, together with the high electron affinity of C$_{60}$, suggests a charge transfer from the Ir(ppy)$_3$ HOMO to the LUMO-derived C$_{60}$ band. As a result, two singly occupied states might develop – one C$_{60}$ SOMO (S_C) and one Ir(ppy)$_3$ SOMO (S_I). On the C$_{60}$ monolayer, such a charge transfer might be hampered by the partial occupation of the C$_{60}$ LUMO-derived states due to the charge transfer from the metal substrate (see section 4.3.1).

Considering a charge injection via the STM tip, each of these two SOMOs should result in a pair of dI/dU peaks.[227] One peak arises at positive bias voltage (S^e) when the tip is able to inject an additional electron into the respective SOMO and thus temporarily creates a fully-occupied state. Another peak at negative bias voltage (S^h) occurs when the tip injects a hole into the respective SOMO, which temporarily creates an fully-unoccupied state. Therefore, the bias voltage of the corresponding dI/dU peaks reflects the energy to load the state with an additional positive or negative charge. The exact charging energies of the C$_{60}$ SOMO for the Au(111) and Ag(111) substrates will be determined in section 7.2.3 and section 7.2.4, respectively.

The dI/dU maps (Fig. 7.3e–r) of the various peaks observed in dI/dU spectra suggest that the lowest-energy peaks S$_C^e$ and S$_C^h$ correspond to the C$_{60}$ SOMO. As mentioned above, the states S$_C^e$ and S$_C^h$ show a substantially larger spatial distribution than expected for a single Ir(ppy)$_3$ molecule. When energetically approaching the S$_I^h$ (Fig. 7.3k) and S$_I^e$ (Fig. 7.3r) states, the orbital pattern increasingly turn into the familiar three-lobe pattern of the Ir(ppy)$_3$ molecules observed on C$_{60}$ monolayers (cf. Fig. 6.9 on page 78). This suggests that the most intense S$_I^h$ and S$_I^e$ peaks correspond to tunneling through the Ir(ppy)$_3$ SOMO. The remaining dI/dU peaks in between can be ascribed to the vibrational progressions of the S$_C^h$ and S$_C^e$ peak, that is, a tunneling through the vibrationally excited states of the C$_{60}$ SOMO (see section 7.2.5).

7.2.2 Charge Injection via the Substrate

When the voltage drop across the C$_{60}$ layer exceeds the potential to charge the C$_{60}$ SOMO, the initial charge carrier injection may occur via the substrate (see section 7.1.4). At negative bias voltages, there might be two competing processes: Either the STM tip initially injects a hole into the SOMO (removes the electron), which temporarily creates a positive charge, or the substrate injects an additional electron into the SOMO, which temporarily leads to a negative charge. The probability for these two processes depends on the tunneling rates through the C$_{60}$ layer and through the vacuum barrier and is therefore adjustable by the tip–sample distance. In either case, the additional conduction channel, i.e. the possibility to first inject a charge carrier from the substrate, leads to a strong increase in the tunneling current, which is equivalent to an intense dI/dU peak. In the following, these peaks are marked by a prime, for example, S$_C^e{}'$. For single Ir(ppy)$_3$ molecules on a Ag(111)-supported C$_{60}$ bilayer, such a charge injection via the substrate occurs at only slightly higher bias voltages than the charge injection via the STM tip. Both processes can be distinguished by the shift of their corresponding dI/dU peaks as a function of the tip–sample distance.[221, 238, 239] With decreasing tip–sample

distance the tip injection peaks S_C^e and S_C^h shift away from $E_{F,s}$ (Fig. 7.4a) due to the reducing relative voltage drop across the vacuum barrier (u_{vac}). At the same time, the larger relative voltage drop across the C_{60} layer (u_{C60}) results in alignment of the S_C^e state with $E_{F,s}$ already at lower bias voltages. Hence, with decreasing tip–sample distance, the substrate injection peak $S_C^{e\prime}$ shifts toward $E_{F,s}$. The approximately ten times stronger shift of the $S_C^{e\prime}$ peak compared to the S_C^e and S_C^h peaks indicates that the voltage drop across the vacuum barrier is much larger than the voltage drop across the C_{60} layer. For the S_C^h peak, no complementary substrate injection peak could be observed because the generation of a positive charge on the C_{60} SOMO requires much higher energies than the generation of a negative charge (~-1.2 eV instead of ~0.2 eV). Using the same voltage ratio as for the S_C^e state, the $S_C^{h\prime}$ peak should appear around -8.5 eV, which is far off the tunneling regime.

For the same reason, the substrate injection peak $S_C^{e\prime}$ for a single Ir(ppy)₃ molecule on a Au(111)-supported C_{60} bilayer occurs at much higher negative bias voltages than for a molecule on a Ag(111)-supported C_{60} bilayer, typically between -3 and -4 V (Fig. 7.4b). At the same time, the approximately 200 meV higher charging potential of the C_{60} SOMO results in a stronger shift of the $S_C^{e\prime}$ peak of -2.50 V/nm. In chapter 8 it will be shown that the weak variation in the charging energy of the C_{60} SOMO has a remarkable influence on the excitation of tip-induced surface plasmon polaritons (TIPs) in the junction.
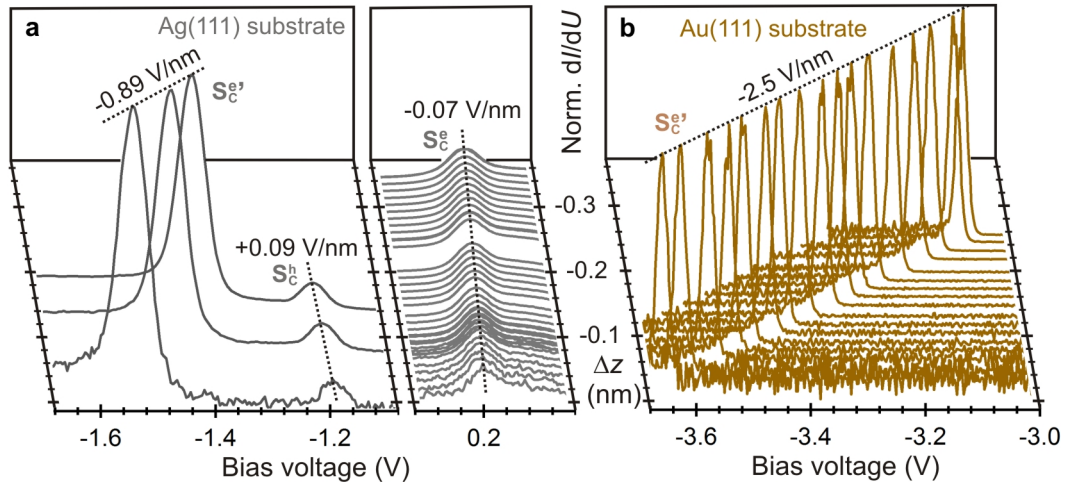
Fig. 7.4: Charge injection via the STM tip and the substrate on a single Ir(ppy)₃ molecule on a C_{60} bilayer. (a) Relative STM tip–sample distance (Δz_{rel}) dependence of the electron (S_C^e peak) and hole injection (S_C^h peak) by the STM tip, as well as the electron injection by the substrate ($S_C^{e\prime}$ peak) into the C_{60} SOMO created upon the adsorption of a single Ir(ppy)₃ molecule on a C_{60} bilayer on Ag(111). (b) Δz_{rel} dependence of the $S_C^{e\prime}$ peak in the case of a single Ir(ppy)₃ molecule on a C_{60} bilayer on Au(111). The shift of the dI/dU peaks as a function of the relative Δz_{rel} is denoted. The depicted data have been drift-corrected according to the procedure described in section 2.3.4.

7.2.3 Charging Potentials of the C₆₀ SOMO on a Au(111) Substrate

In order to determine the exact charging potential of the Ir(ppy)₃ and C_{60} SOMOs, the absolute voltage drops across the vacuum barrier and the C_{60} layer must be taken into account. Therefore, the following three subsections shall briefly describe the general approach for their

calculation using the example of a single $\mathrm{Ir(ppy)_3}$ molecule on a Au(111)-supported C_{60} bilayer. The charging potential of the C_{60} SOMO in the case of a Ag(111)-supported C_{60} bilayer are then determined in section 7.2.4.

Assumptions of the Following Calculations

As is visible in Fig. 7.4, the substrate injection peak $S_C^{e\prime}$ shifts linearly with the relative tip–sample distance Δz_{rel}. Hence, $S_C^{e\prime}(\Delta z_{\mathrm{rel}})$ follows the same distance dependence as the voltage necessary to keep a constant electric field in a plate capacitor. The assumption of a plate capacitor is indeed justified if the curvature of the STM tip is much larger than the tip–sample distance. Considering a finite radius of curvature by an additional quadratic term in the distance dependence of the electric field leads to a negligible error of the field in the junction (see page 88). Furthermore, it is assumed that the dielectric properties of the single $\mathrm{Ir(ppy)_3}$ molecule and the C_{60} bilayer are independent of the electric field in the junction and, thus, independent of the vacuum barrier thickness d_{vac}. With these two assumptions, the bias voltage to charge the C_{60} SOMO by an additional electron from the substrate $(U_{S_C^e}^{\mathrm{obs}\prime})(\Delta z_{\mathrm{rel}})$ can be approximated by a straight line. In the case of the single $\mathrm{Ir(ppy)_3}$ molecule that led to the $\mathrm{d}I/\mathrm{d}U$ spectra depicted in Fig. 7.4b, the best fit function of the $S_C^{e\prime}$ peak is:

$$U_{S_C^e}^{\mathrm{obs}\prime}(\Delta z_{\mathrm{rel}}) = -2.50\,\mathrm{V{\cdot}nm^{-1}}\Delta z_{\mathrm{rel}} - 3.736\,\mathrm{V} \tag{7.3}$$

Potential to Charge the C₆₀ SOMO With an Additional Electron

As discussed in section 7.1.3, non-zero voltages applied to the tunnel junction cause a shift of the electronic states within the double tunnel barrier; hence, their corresponding $\mathrm{d}I/\mathrm{d}U$ peaks are observed at a bias voltage that is enlarged by the respective voltage drop across the decoupling layer, here the C_{60} layer (see eq. (7.2), page 82). According to eq. (4.5) (page 35), the relative C_{60} voltage drop at the onset of electron injection by the STM tip (S_C^e) at a distance $d_{\mathrm{dI/dU}}$ is given by:

$$u_{\mathrm{C60}}(d_{\mathrm{dI/dU}}) = \frac{\Delta U_{S_c^e}}{U_{S_C^e}^{\mathrm{obs}}} = \frac{U_{S_C^e}^{\mathrm{obs}} - U_{S_C^e}^0}{U_{S_C^e}^{\mathrm{obs}}} \tag{7.4}$$

At the $S_C^{e\prime}$ peak, the C_{60} SOMO is charged with an additional electron from the substrate. In this second case, eq. (4.5) becomes:

$$u_{\mathrm{C60}}(d_{\mathrm{vac}}) = -\frac{U_{\mathrm{C60}}}{U_{S_C^e}^{\mathrm{obs}\prime}} = -\frac{U_{S_C^e}^0}{U_{S_C^e}^{\mathrm{obs}\prime}} \tag{7.5}$$

When the progressions of both peaks $S_C^{e\prime}$ and S_C^e are measured at the same tip–sample distance $d_{\mathrm{dI/dU}}$, eq. (7.4) and eq. (7.5) can be equated:

$$u_{C60}(d_{\mathrm{dI/dU}}) = \frac{U_{S_C^e}^{\mathrm{obs}} - U_{S_C^e}^0}{U_{S_C^e}^{\mathrm{obs}}} = -\frac{U_{S_C^e}^0}{U_{S_C^e}^{\mathrm{obs}\prime}} \tag{7.6}$$

After rearranging, the potential necessary to charge the C_{60} SOMO with an additional electron is finally obtained as:

$$U_{S_C^e}^0 = \frac{1}{\dfrac{1}{U_{S_C^e}^{\mathrm{obs}}} - \dfrac{1}{U_{S_C^e}^{\mathrm{obs}\prime}}} \tag{7.7}$$

Generally, the spectra of both peaks S_C^e and $S_C^e{}'$ are recorded at different tip–sample distances because the measured current for both processes differs by several orders of magnitude. However, the fit of the $S_C^e{}'$ peak from eq. (7.3) allows an extrapolation of its energy to the tip–sample distance used during the acquisition of the S_C^e peak spectrum. Insertion of Δz_{rel} of a respective S_C^e spectrum obtained at $\Delta z_{\mathrm{rel}} = -0.58\,\mathrm{nm}$ results in a $S_C^e{}'$ peak position of $U_{S_C^e}^{\mathrm{obs}\prime} = -2.29\,\mathrm{V}$. Together with the position of the S_C^e peak, $U_{S_C^e}^{\mathrm{obs}} = -0.58\,\mathrm{V}$, the potential to charge the C_{60} SOMO with an additional electron arises from eq. (7.7) as: $U_{S_C^e}^0 = 0.46\,\mathrm{V}$.

Effective Thickness of the Vacuum Barrier and the C₆₀ Layer

Assuming that the curvature of the STM tip is much larger than the width of the tunnel junction, the electric field in the junction can be approximated as being homogeneous (plate capacitor geometry). The thickness of the vacuum barrier, d_{vac}, is then accessible by a linear extrapolation of $U_{S_C^e}^{\mathrm{obs}\prime}$ to the negative value of the zero-field charging potential $U_{S_C^e}^0$ (Fig. 7.5). At $d_{0,\mathrm{vac}} = \Delta z_{\mathrm{rel}}(-U_{S_C^e}^0)$, the vacuum barrier formally vanishes and the STM tip would reach the C_{60} SOMO. Hence, the absolute vacuum barrier thickness becomes:

$$d_{\mathrm{vac}}(\Delta z_{\mathrm{rel}}) = \Delta z_{\mathrm{rel}} - d_{0,\mathrm{vac}} = \Delta z_{\mathrm{rel}} + 1.31\,\mathrm{nm} \tag{7.8}$$

In order to estimate the error caused by the assumption of a plate capacitor geometry, the solid blue curve in Fig. 7.5 depicts the best fit of $U_{S_C^e}^{\mathrm{obs}\prime}(\Delta z_{\mathrm{rel}})$ including an additional quadratic term in the distance-dependent electric field. The resulting error of the vacuum barrier thickness arises as $\Delta d_{0,\mathrm{vac}} = 0.07\,\mathrm{nm}$ ($\Delta d_{0,\mathrm{vac}}/d_{0,\mathrm{vac}} = 5\%$) and thus is negligible.

At $d_{\mathrm{tot}} = \Delta z_{\mathrm{rel}}(U_{S_C^e}^{\mathrm{obs}\prime} = 0)$, the STM tip formally touches the metallic substrate. Therefore, the thickness of the C_{60} film (d_{C60}) can be determined by an extrapolation of $U_{S_C^e}^{\mathrm{obs}\prime}$ to zero. Taking the dielectric constant (ϵ_r) of the C_{60} layer into account, which leads to a reduction of the electric field in the layer, the effective thickness of the C_{60} layer is given by:

$$d_{C60} = \epsilon \cdot (d_{\mathrm{tot}} - d_{0,\mathrm{vac}}) \tag{7.9}$$

Using the dielectric constant of bulk C$_{60}$ of ϵ_r = 4.4,[108] the linear fit of $U_{S_C^e}^{obs\prime}$ results in an effective thickness of d_{C60} = 0.81 nm and the quadratic fit of $U_{S_C^e}^{obs\prime}$ leads to d_{C60} = 0.72 nm. In both cases, the effective C$_{60}$ layer thickness thus matches approximately one C$_{60}$ layer (d_{ML} = 0.81 nm). This is plausible insofar as the C$_{60}$ SOMO should be localized within the second C$_{60}$ layer.
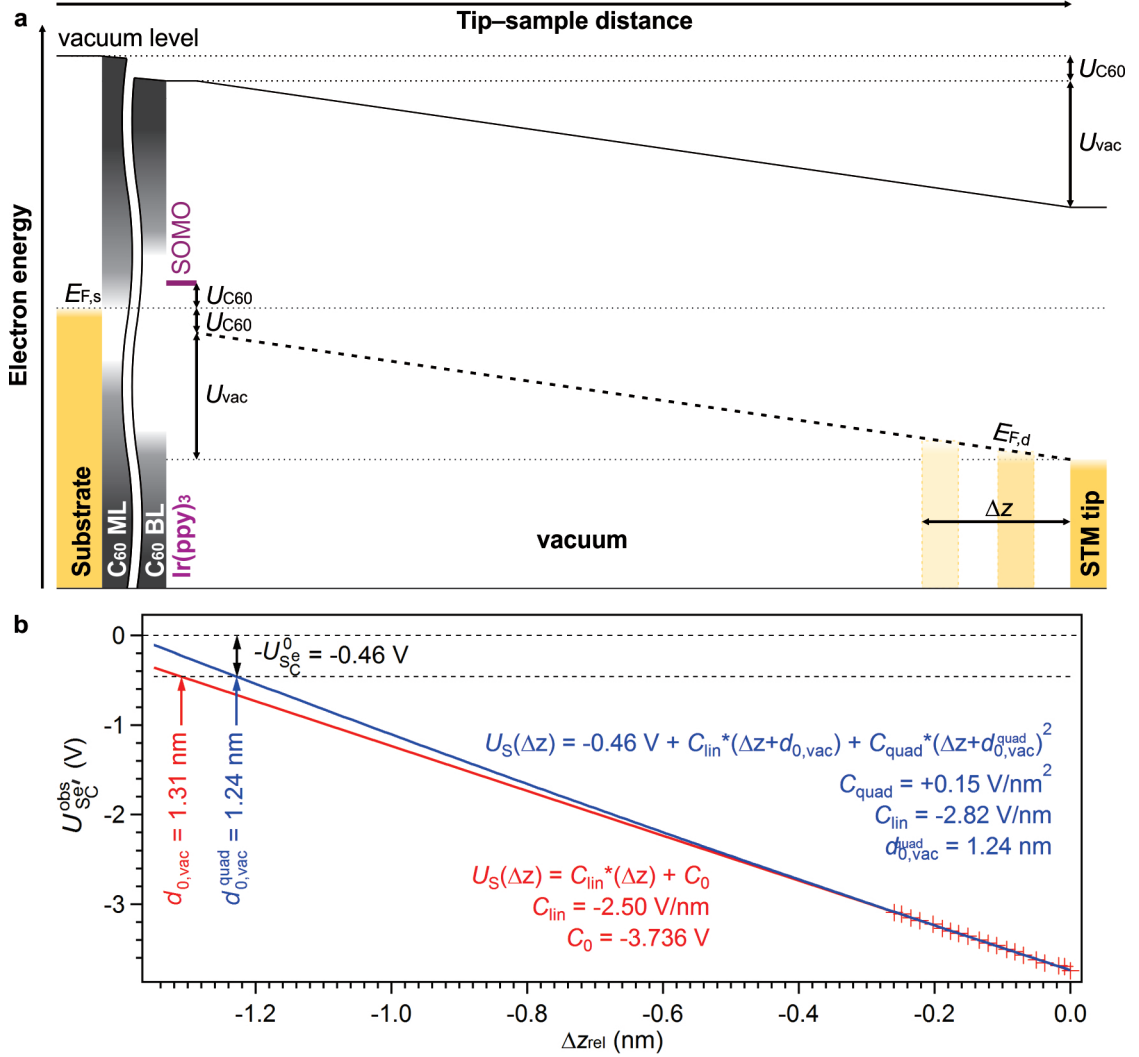
Fig. 7.5: Determination of the absolute vacuum barrier thickness. (a) Schematic energy diagram and density of states of the junction along the tip–sample axis. (b) Plot of the S$_C^e\prime$ peak position from Fig. 7.4b (red crosses) as a function of the relative tip–sample distance, Δz_{rel}. The red and blue curves show a linear and a quadratic fit of the peak position, respectively.

Absolute Voltage Drop across the C$_{60}$ Layer and the Vacuum Barrier

At the S$_C^e\prime$ peak, the absolute voltage drop across the C$_{60}$ barrier (U_{C60}) equals the potential to charge the C$_{60}$ SOMO with an additional electron ($U_{S_C^e}^0$). Knowing its absolute value thus enables determination of U_{C60} for an arbitrary combination of the applied bias voltage and the

vacuum barrier thickness. Insertion of the absolute vacuum barrier thickness from eq. (7.8) into the fit function eq. (7.3) and into eq. (7.5) leads to:

$$u_{C60}(d_{vac}) = -\frac{U^0_{S^e_C}}{U^{obs\prime}_{S^e_C}(d_{vac})} = \frac{1}{5.435\,\text{nm}^{-1} \cdot d_{vac} + 1} \tag{7.10}$$

Typically, the dI/dU spectra of the S^e_C peak are recorded at a set point current of ~40 pA at the bias voltage around the S^e_C peak. In this case, the calculated vacuum layer thickness equals $d_{vac} = 0.8\,\text{nm}$. Insertion into eq. (7.10), therefore, results in a typical relative voltage drop across the C_{60} layer of $u_{C60} = 19\%$. Using eq. (4.5) (page 35), the absolute voltage drop across the C_{60} film for a specific applied bias voltage (U_{bias}) and vacuum layer thickness d_{vac} is obtained as:

$$U_{C60}(d_{vac}, U_{bias}) = \frac{U_{bias}}{5.435\,\text{nm}^{-1} \cdot d_{vac} + 1} \tag{7.11}$$

The voltage drop across the vacuum barrier is accessible via eq. (4.2) (page 34) and is thus given by:

$$U_{vac}(d_{vac}, U_{bias}) = U_{bias} \cdot \left(1 - \frac{1}{5.435\,\text{nm}^{-1} \cdot d_{vac} + 1}\right) \tag{7.12}$$

Electric Field in the Vacuum Barrier

Since the electric field in the junction can be described by a plate capacitor (see page 87), the electric field in the vacuum barrier is given by:

$$E_{vac} = \frac{U_{vac}}{d_{vac}} \tag{7.13}$$

Insertion of eq. (4.2) and eq. (7.10) yields:

$$\begin{aligned} E_{vac} &= \frac{U_{bias} - U_{C60}}{d_{vac}} = \frac{\frac{U_{bias}}{U_{C60}} - 1}{d_{vac}} \cdot U_{C60} \\ &= 5.44\,\text{nm}^{-1} \cdot U_{C60} \end{aligned} \tag{7.14}$$

Hence, the electric field in the vacuum barrier is proportional to the voltage drop across the C_{60} barrier. The insertion of the C_{60} voltage drop at the onset of electron injection by the substrate, $U^0_{S^e_C} = 0.46\,\text{V}$, into section 7.14 results in: $E_{vac} = 5.44\,\text{nm} - 1 \cdot 0.46\,\text{V} = 2.50\,\text{V·nm}^{-1}$. This value perfectly agrees with the slope of $dU^{obs\prime}_{S^e_C}(\Delta z_{rel})/d\Delta z_{rel} = 2.50\,\text{V·nm}^{-1}$ described by eq. (7.3). This proves the full consistency of the calculation of U_{C60} and E_{vac} and corroborates the assumptions on page 87.

Potential to Remove the Electron From the C$_{60}$ SOMO

The potential to remove the electron from the C$_{60}$ SOMO by the STM tip equals the voltage drop across the vacuum barrier at the S$_C^h$ dI/dU peak. On the single Ir(ppy)$_3$ molecule that led to the data depicted in Fig. 7.4b and Fig. 7.5b, the S$_C^h$ peak appears at a bias voltage of $U_{S_C^e}^{obs} = -1.25\,\text{V}$ at a vacuum barrier thickness of $d_{vac} = 0.8\,\text{nm}$. Insertion of both values into eq. (7.12) results in the zero-field charging potential to inject a hole, that is, to remove the electron from the C$_{60}$ SOMO of: $U_{S_C^h}^0 = U_{vac}(0.8\,\text{nm}, -1.25\,\text{V}) = 1.02\,\text{V}$.

7.2.4 Charging Potentials of the C$_{60}$ SOMO on a Ag(111) Substrate

The charging potentials of the C$_{60}$ SOMO in the case of the single Ir(ppy)$_3$ molecules adsorbed on a Ag(111)-supported C$_{60}$ bilayer can be determined analogously to the procedure described in the preceding section 7.2.3. In the following, it is demonstrated that also the shift of the S$_C^e$ peak can be used to calculate all necessary quantities. The best linear fit of the S$_C^e$ peak in Fig. 7.4a is:

$$U_{S_C^e}^{obs}(\Delta z_{rel}) = -0.070\,\text{V·nm}^{-1}\Delta z_{rel} + 0.2025\,\text{V} \tag{7.15}$$

Potential to Charge the C$_{60}$ SOMO With an Additional Electron

Extrapolating $U_{S_C^e}^{obs}(\Delta z_{rel})$ to the relative tip–sample distance of the S$_C^{e}{}'$ peak spectrum ($\Delta z_{rel} = 0.095\,\text{nm}$, $U_{S_C^e}^{obs}{}' = -1.299\,\text{V}$) and insertion into eq. (7.7) result in a zero-field charging potential of the C$_{60}$ SOMO with an additional electron of: $U_{S_C^e}^0 = 0.17\,\text{V}$

Effective Thickness of the Vacuum Barrier

At $U_{S_C^e}^{obs}(\Delta z_{rel}) = U_{S_C^e}^0$, the vacuum barrier formally vanishes again and the STM tip would reach the C$_{60}$ SOMO. Hence, the absolute vacuum barrier thickness is obtained by an extrapolation of $\Delta z_{rel}(U_{S_C^e}^{obs})$ to $U_{S_C^e}^0 = 0.17\,\text{V}$ as:

$$d_{vac}(\Delta z_{rel}) = \Delta z_{rel} - d_{0,vac} = \Delta z_{rel} + 0.462\,\text{nm} \tag{7.16}$$

Absolute Voltage Drop across the C$_{60}$ Layer and the Vacuum Barrier

Insertion of the absolute vacuum barrier thickness from eq. (7.16) into the fit function of the S$_C^e$ peak eq. (7.15) and into eq. (4.5) leads to a relative voltage drop across the vacuum barrier of:

$$u_{vac} = \frac{U_{S_C^e}^0}{U_{S_C^e}^{obs}} = \frac{1}{1.381 - 0.4118\,\text{nm}^{-1} \cdot d_{vac}} \tag{7.17}$$

With eq. (4.5), the resulting absolute voltage drop across the vacuum barrier is:

$$U_{\text{vac}}(d_{\text{vac}}, U_{\text{bias}}) = \frac{U_{\text{bias}}}{1.381 - 0.4118\,\text{nm}^{-1} \cdot d_{\text{vac}}} \tag{7.18}$$

Potential to Remove the Electron From the C$_{60}$ SOMO

The potential to remove the electron from the C$_{60}$ SOMO by the STM tip equals the voltage drop across the vacuum barrier at the S$_C^h$ dI/dU peak. On the single Ir(ppy)$_3$ molecule that led to the data depicted in Fig. 7.4a, the S$_C^h$ peak appears at a bias voltage of $U_{S_C^e}^{\text{obs}} = -1.213\,\text{V}$ at a vacuum barrier thickness of $d_{\text{vac}} = 0.60\,\text{nm}$. Insertion of both values into eq. (7.18) results in the zero-field charging potential to inject a hole into the C$_{60}$ SOMO of: $U_{S_C^h}^0 = U_{\text{vac}}(0.60\,\text{nm}, -1.213\,\text{V}) = -1.07\,\text{V}$.

7.2.5 Vibrational Modes of the C$_{60}$ SOMO

Knowing the absolute thickness of the vacuum barrier, any dI/dU spectrum can be plotted as a function of the voltage drop across the vacuum barrier. For this purpose, the voltage axis merely needs to be multiplied with the relative voltage drop across the vacuum barrier. In the case of the dI/dU spectra on top and aside to a single Ir(ppy)$_3$ molecule on a Au(111)-supported C$_{60}$ bilayer in Fig. 7.3d, the absolute vacuum barrier thicknesses on both positions have been determined as 0.8 and 0.58 nm, respectively. According to eq. (7.10), this corresponds to a relative voltage drop across the vacuum barrier of 81% and 76%. Figure 7.6a,b display both spectra as a function of the vacuum voltage drop minus the potential of the S$_C^e$ peak ($U_{S_C^e}^0$). On closer inspection, the spacing between the S$_C^e$ peak and the first vibrationally excited state deviates from the spacings between the remaining peaks. In addition, the second peak in Fig. 7.6b appears much broader than the other peaks and exhibits a higher intensity than the first vibronic peak.

These observations are incompatible with an excitation of a single vibrational mode. Instead, the observed progression must arise from the interference of at least two different modes. Therefore, the red dashed lines in Fig. 7.6a,b display fits of the obtained spectra by two series of equally-spaced Gaussian functions (green and blue) as well as a peak corresponding to the simultaneous excitation of both modes (turquoise). Interestingly, the frequencies of the excited modes differ on both lateral positions (marked by the colored crosses in Fig. 7.3b). Similar local variations of the excited vibrational modes have been observed by Pradhan *et al.* for a C$_{60}$ monolayer on a thin insulating Al$_2$O$_3$ layer.[240] In that case, the authors ascribed the varying coupling strength of the tunneling electrons with the various intramolecular vibrational modes to the alternating symmetry of the molecular electronic states of individual C$_{60}$ molecules.

In the present case, the high-energy vibrational modes with an energy of 57 and 62 meV may correspond to the $H_g(2)$ (54 meV[108]) and $A_g(1)$ C$_{60}$ mode (62 meV[108]), respectively. Similar vibrational frequencies have been observed for single C$_{60}$ molecules and for C$_{60}$ monolayers on thin Al$_2$O$_3$ films.[240] In particular the $H_g(2)$ mode is known for its strong electron–phonon coupling[241] and has been also observed by inelastic tunneling spectroscopy (IETS) on C$_{60}$ monolayers on Ag(110).[141] The origin of the low-frequency modes in Fig. 7.6 with an energy of

22 and 40 meV, in contrast, is less clear and requires further inquiry. Most likely, these modes correspond to the $H_g(1)$ mode (34 meV[108]), for which a strong electron–phonon coupling has been shown as well.[241] A summary of the found vibronic states in Fig. 7.6a together with the corresponding vibrational quantum numbers is displayed in Fig. 7.6c.
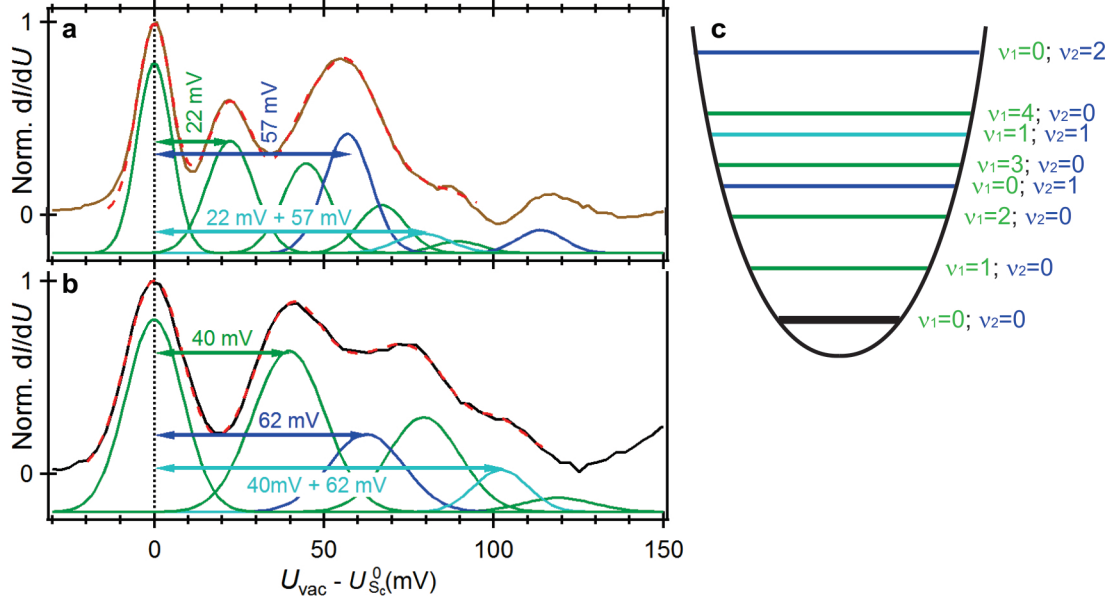

Fig. 7.6: Vibronic spectra of the C$_{60}$ SOMO caused by the adsorption of a single Ir(ppy)$_3$ molecule on a Au(111)-supported C$_{60}$ bilayer. The brown curve in (a) and the black curve in (b) show the same curves as in Fig. 7.3d, but are plotted as a function of the voltage drop across the vacuum barrier (U_{vac}) minus the zero-field charging potential of the C$_{60}$ SOMO ($U_{S_\mathrm{C}^\mathrm{e}}^0$). The dashed red curves show fits of the measured dI/dU spectra by the progressions of two vibrational modes (green and blue) as well the simultaneous excitation of both modes (turquoise). The corresponding Gaussian functions are down-shifted vertically for clarity. (c) Schematic of the vibronic states of the C$_{60}$ SOMO for the spectrum in panel a, together with the respective vibrational quantum numbers.

7.3 Single Ir(ppy)$_3$ Molecules on C$_{60}$ Trilayers

dI/dU spectra on single Ir(ppy)$_3$ molecules adsorbed on a C$_{60}$ trilayer resemble those on a C$_{60}$ bilayer, although the highest occupied state occurs at considerably lower binding energies, typically around +0.4 V. Moreover, the adsorption geometry of the Ir(ppy)$_3$ molecules can be easily modified by currents above ~50 pA. Figure 7.7a depicts two consecutive dI/dU spectra on top of the same Ir(ppy)$_3$ molecule that could be reversibly switched between two different configurations, A and B. The corresponding dI/dU maps of the observed peaks (Fig. 7.7d–k) differ substantially for both configuration, albeit the highest occupied states again exhibit the same pattern as the lowest unoccupied states. As on the C$_{60}$ bilayer, both states of both configurations extend over an area that is larger than the size of a single Ir(ppy)$_3$ molecule. Therefore, they might again arise from a C$_{60}$ SOMO that is created by a charge transfer from the single Ir(ppy)$_3$ molecule to the underlying C$_{60}$ molecules. The S$_\mathrm{C}^\mathrm{e}$ peak thus reflects the energy of an additional electron in the LUMO-derived band in the vicinity of the single

Ir(ppy)$_3$ molecule. As a result of the charge transfer between the Ir(ppy)$_3$ molecule and the C$_{60}$ film, a kind of a zwitterion might form with a negative charge in the C$_{60}$ surface and a positive charge on the Ir(ppy)$_3$ molecule. The latter may causes a split-off of the singly occupied C$_{60}$ state from the LUMO-derived band toward the Fermi level of the substrate (Fig. 7.7l), where the magnitude of this split-off should depend on the distance of the positive charge to the C$_{60}$ SOMO. Because an additional positive charge on the Ir(ppy)$_3$ molecule is predominantly localized on its phenyl group, an adsorption via these phenyl groups should thus lead to a larger split-off than an adsorption via its pyridine groups.

The S$_C^h$ peak at negative bias voltage arises when the single electron in the C$_{60}$ SOMO is able to tunnel to the STM tip or, in other words, when the voltage drop across the vacuum barrier exceeds the potential to remove the electron from the C$_{60}$ SOMO. Therefore, the energy difference between the S$_C^e$ and S$_C^h$ yields the Hubbard energy (U) within the LUMO-derived band.[‡] This energy reflects the summed interactions between two electrons within a specific

---

[‡]Reviewing the literature, this experiment might be the first experimental approach accessing the Hubbard energy of the LUMO-derived band of thin C$_{60}$ films.
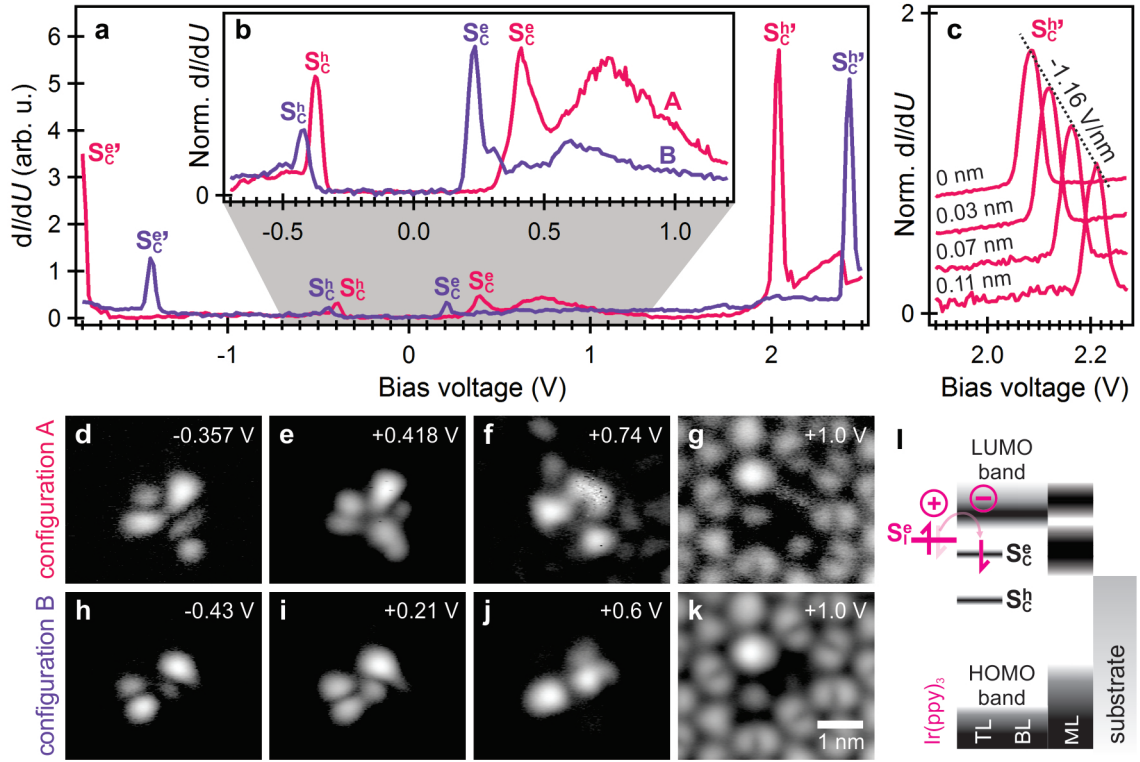
Fig. 7.7: Electronic structure of a single Ir(ppy)$_3$ molecule on a Ag(111)-supported C$_{60}$ trilayer. (a) Consecutively recorded dI/dU spectra on top of the same Ir(ppy)$_3$ molecule before (red, A) and after the single molecule was modified in its adsorption configuration (blue, B). (b) Detailed spectra for both adsorption geometries around the Fermi level of the substrate. (c) Dependence of the S$_C^h{}'$ peak position of the A configuration on the denoted relative tip–sample distances. (d–g) dI/dU maps of the Ir(ppy)$_3$ molecule in its A and (h–k) B configuration at the peak positions observed in panel a and b. (l) Schematic energy level diagram showing the density of states within the different C$_{60}$ layers (ML: first layer, BL: second layer, TL: third layer).

state. In the case of the A configuration, U is slightly larger than for the B configuration. Again, this might be explainable by the different distances of the positive charge on the single Ir(ppy)$_3$ molecule, because a close distance of such a positive charge should facilitate the removal of the single electron in the C$_{60}$ SOMO by the STM tip. Overall, both Hubbard energies of the LUMO-derived band are substantially smaller than the Hubbard energy of the HOMO-derived band of 1.6 eV.[242] The origin of this observation might lie in the larger delocalization and dispersion of the LUMO-derived states[243] and the associated enhanced screening of electric charges. Similar arguments might also explain the larger Hubbard energy of the C$_{60}$ bilayer (see previous section 7.2). In this case, a delocalization of the C$_{60}$ SOMO into the sub-surface layer might be impossible, or at least hindered, by the charge transfer from the metal substrate to the first C$_{60}$ layer (see section 4.3.1). Hence, the C$_{60}$ SOMO should be mostly localized within the topmost layer of the C$_{60}$ bilayer.

As a result of the smaller charging potential necessary to remove the electron from the C$_{60}$ SOMO, this process can now also occur via the substrate, which result in a corresponding $S_C^{h}{}'$ peak around +2 and +3 V (Fig. 7.7a,c). In contrast to the experiments on the C$_{60}$ bilayer, here the precise charging potentials can be directly determined by inserting the observed peak position into eq. (7.7), because the tip injection peaks S_C^{h} and S_C^{e} are recorded within the same spectrum as the substrate injection peaks $S_C^{h}{}'$ and $S_C^{e}{}'$ and thus at the same tip–sample distance. In other words, the position of the substrate injection peaks do not need to be extrapolated as in the case of the C$_{60}$ bilayer. Insertion of the S_C^{e} and $S_C^{e}{}'$ peak position of configuration A and the S_C^{h} and $S_C^{h}{}'$ peak position of configuration B into eq. (7.7) results in a charging potential of $U^0_{S_C^{e},A}$ = +0.18 V and $U^0_{S_C^{h},B}$ = −0.33 V, respectively. The respective potentials to inject the reverse charge carrier into the C$_{60}$ SOMO can be obtained by eq. (7.4) as $U^0_{S_C^{h},A}$ = 0.37 V and $U^0_{S_C^{e},B}$ = 0.35 V. Table 7.1 summarizes all zero-field charging potentials on the C$_{60}$ bi- and trilayer.

The effective thickness of the vacuum barrier and the C$_{60}$ layer can be determined analogously to section 7.2.3 by an extrapolation of one of the substrate injection peaks to the corresponding zero-field charging potential and zero bias voltage, respectively. Using the distance-dependence of the $S_C^{e}{}'$ peak in the B configuration (Fig. 7.7c) results in an effective thickness of the C$_{60}$ layer of 1.28 nm, which is 0.45 nm larger than the corresponding value in the case of the single Ir(ppy)$_3$ molecules on a C$_{60}$ bilayer.

Tab. 7.1: Zero-field charging potentials and Hubbard energy (U) of the C$_{60}$ SOMO due to the adsorption of a single Ir(ppy)$_3$ molecule on various C$_{60}$ layers.

Single Ir(ppy)$_3$ molecule on a ..	Potential to add		U
	an electron [V]	a hole [V]	[eV]
C$_{60}$ bilayer on Au(111)	+0.46	-1.02	1.48
C$_{60}$ bilayer on Ag(111)	+0.17	-1.07	1.24
C$_{60}$ trilayer on Ag(111) (A configuration)	+0.35	-0.33	0.68
C$_{60}$ trilayer on Ag(111) (B configuration)	+0.18	-0.37	0.55

7.4 Conclusions

This chapter has shown that single Ir(ppy)$_3$ molecules adsorbed on a C$_{60}$ bi- or trilayer act as organic dopants for C$_{60}$ films. On both the C$_{60}$ bi- and trilayer, the high electron affinity of C$_{60}$ leads to a charge transfer from the single Ir(ppy)$_3$ molecules to the underlying C$_{60}$ layer, which causes the formation of two singly occupied molecular orbitals (SOMOs) – one at the Ir(ppy)$_3$ molecule and one in the C$_{60}$ layer. Like C$_{60}$ monolayers, also thicker C$_{60}$ layers are thus less suitable as inert electronic decoupling layers, at least for the decoupling of single Ir(ppy)$_3$ molecules.

Despite this fact, the generated SOMOs show the typical characteristics of an individual electronic state within a double tunnel barrier. This includes: an increased lifetime of the tunneling electrons, a resonant tunneling through vibrationally excited states, the shift of the SOMOs by the electric field in the junction, and a bipolar tunneling through the SOMOs. Because such a SOMO can be regarded as both a (partially) occupied and unoccupied state, this state can be both emptied by injecting a hole or filled by adding a second electron by the STM tip or the substrate. The energy difference between both processes equals the Hubbard energy (U) within the corresponding SOMO. The determined Hubbard energies of the C$_{60}$ SOMO in the case of a C$_{60}$ bi- and trilayer are summarized in Tab. 7.1.

Additional calculations could verify the charge transfer between a single Ir(ppy)$_3$ molecule and a C$_{60}$ film as well as the associated formation of two singly occupied states. However, precise calculations, for example density functional theory (DFT) calculations, might be rather expensive due to the large size of the system and the large number of involved atoms.

Chapter 8

Molecular Orbitals: Gates for the Electrical Generation of Plasmons in Tunnel Junctions

Controlling light on the nanoscale and in a similar way as we are able to control electric currents has the potential to revolutionize the exchange and processing of information.[6, 244–247] Although light can be guided on this scale[8] by coupling it to plasmons[248, 249] – that is, collective electron oscillations in metals – their local generation and electronic control remains a challenge. Typically, this coupling, resulting in quasi particles known as surface plasmon polaritons (SPPs), is achieved by prisms,[250, 251] gratings[252] and nanostructures acting as optical antennas,[253] which adjust the different dispersion relations of photons and plasmons with each other. Hitherto less common is the generation of SPPs by high-energy electron beams[254, 255] or inelastically tunneling electrons.[9] Both approaches enable an electrical "dark" generation of SPPs, which does not require the common detour via the irradiation of, usually diffraction-limited, light.

This chapter will focus on the scanning tunneling microscopy (STM)-induced luminescence of single *fac*-tris(2-phenylpyridine)iridium(III) (Ir(ppy)$_3$) molecules adsorbed on one to three molecular layers (MLs) of C$_{60}$. In all these cases, the single Ir(ppy)$_3$ molecules enhance the SPP

excitation in the junction, compared to the pure C_{60} layers. It will become evident that the single $Ir(ppy)_3$ molecules adsorbed on the various C_{60} surfaces provide excellent model systems to study the electrical generation and the electronic control of SPPs in tunnel junctions. Astonishingly, the level of control increases with the number of C_{60} layers as a consequence of the varying electronic structures discussed in the previous two chapters. The observed effects might form the basis for three potential plasmonic devices: A current–SPP converter, in which the electronic states, for example of a single molecule, contacted by a tunnel junction serve as spatially and energetically defined, static nanogates for the SPP excitation (section 8.1);[256] a SPP-emitting transistor, in which these nanogates can be controlled dynamically, for instance, by the electric field in the junction (section 8.2);[257] and an optically readable, non-volatile single-molecule memory, in which the SPP generation can be controlled dynamically and can be reversibly switched between an emitting and a non-emitting state. Details about the sample preparation used in this chapter can be found in section 2.3.5 (page 16). Parts of this chapter have been published in reference [256] and [257].

8.1 Molecular Orbitals as Spatially and Energetically Defined Nanogates – Single $Ir(ppy)_3$ Molecules on a C_{60} Monolayer

Light emission from molecules in tunnel junctions and the question of how they modify the excitation of SPPs in the junction have been interesting scientist for more than two decades.[36] It has been observed that molecules adsorbed on noble metal surfaces can both reduce[36, 258–261] or enhance[40, 189, 262–267] the intensity of excited SPPs and can cause either a red-shift[187, 189, 261] or a blue-shift[263–267] of their spectrum. Three major mechanisms have been discussed to describe the influence of the molecules: (I) They modify the efficiency of the inelastic tunneling process leading to SPP excitations by changing the density of initial or final states[189, 261, 268] or the matrix element;[268] (II) molecules left in an excited state enhance the excitation of SPP modes due to their dynamic dipole,[260, 263, 264, 266, 269] and (III) the dielectric properties of the molecules and the junction geometry alter the field strength of SPP modes.[42, 259, 260, 263, 264, 266–269] A critical assessment of the different mechanisms and their control is decisive for the application of single molecules as ultimate coupling elements for the electrical SPP generation. In contrast to earlier studies, this work employs STM to image individual molecular orbitals[123, 142, 226] and analyzes the local excitation pattern of SPP for the first time in terms of the spatial shape of the present molecular states. The additional spatial information unequivocally proves that molecular orbitals are able to confine the SPP excitation in tunnel junctions spatially and energetically.

8.1.1 Photon Maps

As discussed in section 6.3.1, single $Ir(ppy)_3$ molecules adsorb in three major configurations on a C_{60} monolayer. For bias voltages $U_{bias} < -1.6\,eV$, these three configurations lead to three configuration-specific submolecular patterns in photon maps (Fig. 8.1), which do not change their general shape up to $-3.0\,V$ and resemble the corresponding topography features at $U_{bias} > -1.5\,eV$ (cf. Fig. 6.8 on page 76).* On top of the single $Ir(ppy)_3$ molecules, the

---

*The onset in light intensity at $-1.6\,V$ is mostly determined by the sensitivity onset of the photon detector

photon yield – that is, the number of detected photons per tunneling charge carrier – is about four times larger than on the brightest sites of the pure C_{60} monolayer. In contrast, at positive bias voltages up to +3.0 V, no such enhanced photon emission is observed and the submolecular pattern on top of the single $Ir(ppy)_3$ molecules is similar to the one on the pure C_{60} monolayer.
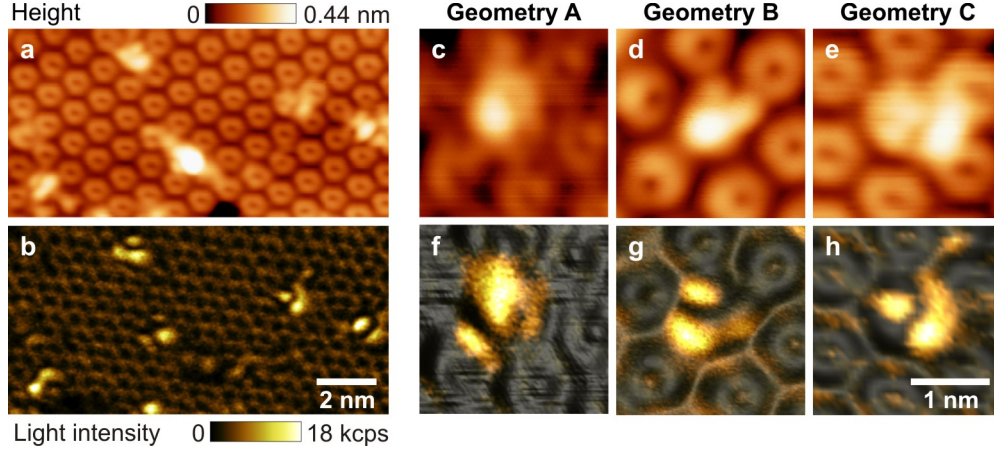

Fig. 8.1: Topography and simultaneously recorded photon map of single $Ir(ppy)_3$ molecules on a C_{60} monolayer on Ag(111). (a,b) Overview scan with various single $Ir(ppy)_3$ molecules. (c–e) Detailed topography scans of three $Ir(ppy)_3$ molecules in different adsorption geometries and (f–h) corresponding photon maps overlaid on a pseudo-3D image of the topography. All images were recorded at $U_{set} = -3.0$ V and $I_{set} = 20$ pA.

8.1.2 Luminescence Spectra

Luminescence spectra obtained with the STM tip on top of the single $Ir(ppy)_3$ molecules indicate that the increased intensity result from an enhanced excitation of tip-induced surface plasmon polaritons (TIPs). The following arguments support this assumption: First, the obtained spectra strongly depend on the geometry of the tip apex (Fig. 8.2a) similar to those observed on pristine noble metal surfaces.[270–272] Second, the specific shape and width of the spectra strongly resemble those recorded on the clean Ag(111) surface and on the pure C_{60} monolayer, for which a plasmonic origin of the emitted photons has been shown earlier.[42, 189] Third, compared to electroluminescence spectra of $Ir(ppy)_3$ in a 4,4',bis(N-carbazolyl)biphenyl (CBP) matrix[203] (Fig. 8.2a, green curve), the spectra are substantially shifted by ~0.5 eV toward lower photon energies. Finally, for electron energies around the TIP resonance of the tip–sample cavity, the spectra on the single $Ir(ppy)_3$ molecules exhibit a quantum cutoff (Fig. 8.2b). In other words, the maximum energy of the emitted photons corresponds to the applied bias voltage: $E_{phot} = e \cdot U_{bias}$ (with e as the elementary charge). The continuous intensity reduction at low energies arises from the diminishing sensitivity of the employed spectrograph (Fig. 8.2b, dashed gray curve). When the spectra on the C_{60} monolayer and the single $Ir(ppy)_3$ molecules are normalized around the quantum cutoff region, the spectra on the $Ir(ppy)_3$ molecules exhibit a significant stronger contribution at smaller photon energies (Fig. 8.2b). In the present case, changes of the tip can be excluded because several successive spectra were recorded on the single molecule and the C_{60} layer. Subtracting the C_{60} spectrum

from the Ir(ppy)$_3$ spectrum reveals two contributions – one from the single Ir(ppy)$_3$ molecule and a second one from the underlying C$_{60}$ monolayer. The contribution from the Ir(ppy)$_3$ molecule thereby exhibits a quantum cutoff that is $0.2\,\text{eV}$ smaller than the one on the C$_{60}$ monolayer. The origin of the different quantum cutoffs will be discussed in the next section.
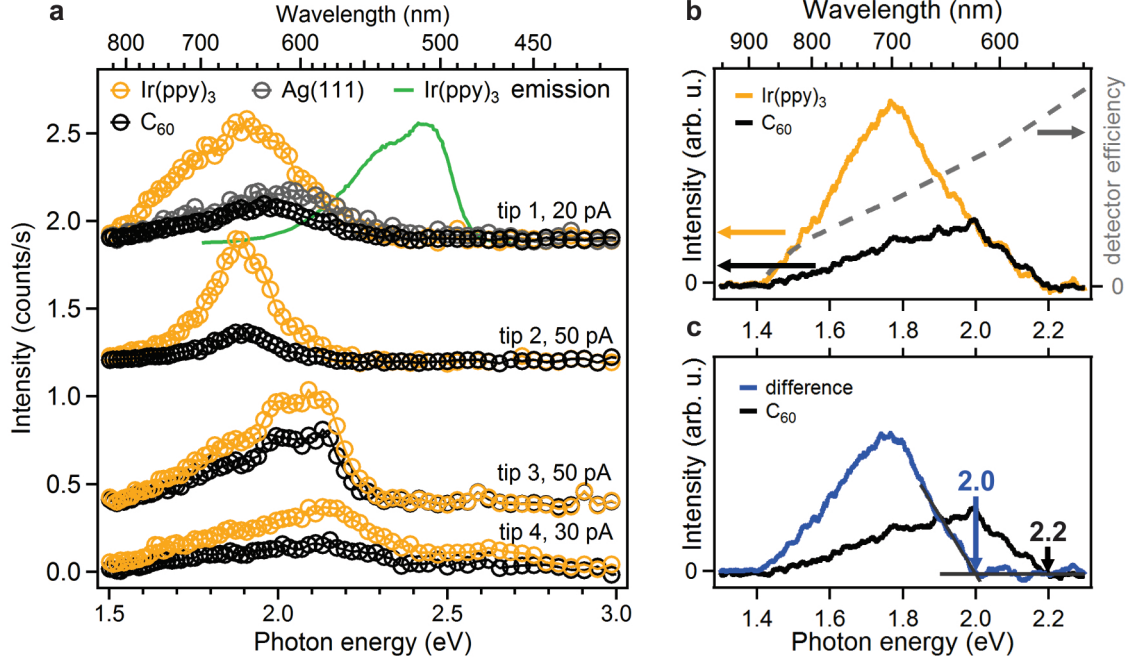

Fig. 8.2: STM-induced luminescence spectra of a C$_{60}$ monolayer on Ag(111) and a single Ir(ppy)$_3$ molecule adsorbed on it. (a) Spectra on the C$_{60}$ monolayer (black) and different single Ir(ppy)$_3$ molecules (yellow) obtained with four different STM tips ($U_{\text{bias}} = -3.0\,\text{V}$, I_{set} is denoted). For tip 1 the corresponding spectrum on the clean Ag(111) surface is displayed in gray. The green curve depicts the electroluminescence spectrum of $6\%wt$ Ir(ppy)$_3$ in a CBP matrix (obtained from ref. [203]). (b) Luminescence spectra at a bias voltage of $-2.2\,\text{V}$ with the same color coding as in panel a (C$_{60}$: $I_{\text{set}} = 100\,\text{pA}$; Ir(ppy)$_3$: $I_{\text{set}} = 50\,\text{pA}$). The dashed gray line depicts the efficiency of the spectrograph. (c) Difference (blue) between the spectra in panel b contrasted with the spectrum on the C$_{60}$ monolayer (black). The high-energy cutoff of both spectra is marked by the colored arrows.

8.1.3 Origin of the Enhanced Surface Plasmon Polariton Excitation

To explore the origin of the submolecular patterns in photon maps, they are compared with the electronic structure of the single Ir(ppy)$_3$ molecules, i.e., the shape of their molecular orbitals. As discussed in detail in section 6.3.2, differential conductance ($\text{d}I/\text{d}U$) spectra of the single Ir(ppy)$_3$ molecules exhibit a series of occupied states (Fig. 8.3a, black curve) within and outside the band gap of the C$_{60}$ monolayer (Fig. 8.3a, gray curve). The highest occupied molecular orbital (HOMO) of the single Ir(ppy)$_3$ molecules appears at a bias voltage of $-0.2\,\text{V}$. A comparison of the constant height photon map at $-1.8\,\text{V}$ (Fig. 8.3b) with the simultaneously recorded orbital pattern (Fig. 8.3c) reveals marked differences. Instead, the light pattern shows a clear similarity to the shape of the HOMO at $-0.2\,\text{V}$ (Fig. 8.3c). A similar congruence between the pattern of enhanced light intensity and the HOMO is also observed for the other adsorption geometries of the Ir(ppy)$_3$ molecules discussed in section 6.3.1. However,

in those cases, the symmetry of the different molecular orbitals look very much alike (cf. Fig. 6.9 on page 78) so that a clear assignment of the orbital that causes the pattern in the photon map is more challenging.

The electronic structure of the single $Ir(ppy)_3$ molecules on the C_{60} monolayer is summarized in the energy level diagram in Fig. 8.3f. Besides the experimentally determined energy levels, the figure additionally contains the energy levels obtained from DFT calculations of a free $Ir(ppy)_3$ molecule (section 6.1.3), assuming a vacuum level alignment with the C_{60}-covered Ag(111) surface (work function: $5\,eV$[160,170]). The energetic positions of these levels agree well with the experimental data. At a bias voltage of $-1.8\,V$, the main tunneling current passes through the C_{60} HOMO. However, the excitation of SPPs (i.e. the recorded luminescence) stems from two inelastic tunneling processes: Path ① is due to electrons that tunnel inelastically from the substrate to the tip, without involving any $Ir(ppy)_3$ states. On the single molecules, the presence of the $Ir(ppy)_3$ HOMO additionally opens an energetically and spatially defined gate ② that substantially enhances the tunneling process at this energy. As a consequence, more tunneling electrons are available with a sufficient energy to excite SPPs in the tunnel junction, which results in a locally enhanced luminescence. Since the spatial shape of the HOMO defines this gate, the photon map always matches the dI/dU map at $-0.2\,V$. The lower-lying $Ir(ppy)_3$ orbitals play no significant role in the luminescence process because of the considerably reduced tunneling probability due to the higher vacuum barrier. This observation is a further clear evidence for the plasmonic origin of the generated photons, in addition to the points mentioned in section 8.1.2. In contrast, an intramolecular radiative transition would
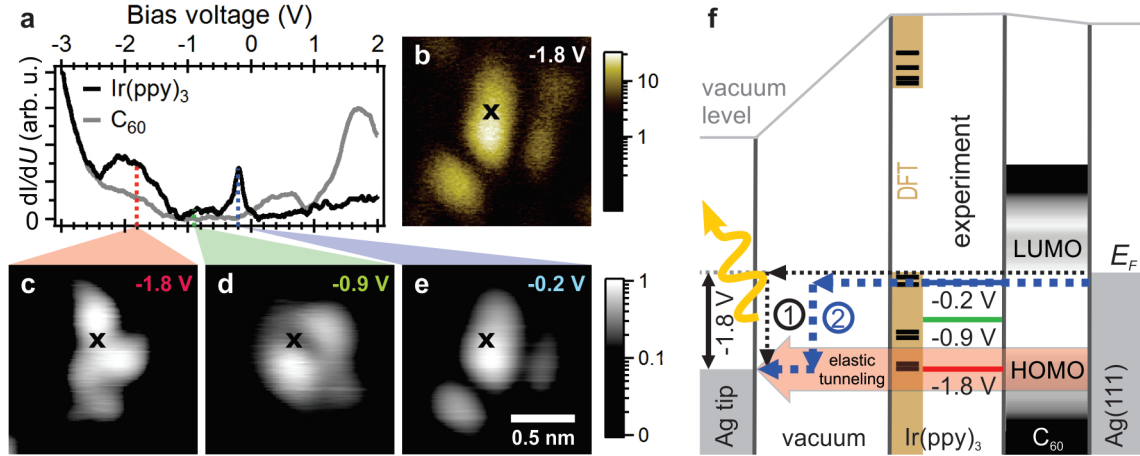
Fig. 8.3: Electronic states and STM-induced luminescence on a single $Ir(ppy)_3$ molecule adsorbed on a C_{60} monolayer on Ag(111). (a) dI/dU spectra on a single molecule (black curve, spatial position marked by the black crosses in the other panels) and the C_{60} monolayer (gray curve). (b) Photon map (in counts/second) and (c–e) normalized constant height dI/dU maps both plotted with logarithmic intensity scale and recorded at the bias voltages indicated in the top right. The constant current topography and photon map of the depicted single molecule is displayed in Fig. 8.1c,f. (f) Schematic energy diagram showing the experimentally observed energy levels of a single $Ir(ppy)_3$ molecule displayed by the color-coded lines (blue, green, red). The black bars in the ocher-colored box show the results of the DFT calculation in section 6.1.3 assuming a vacuum level alignment with the C_{60}-covered surface (work function: $5\,eV$[160,170]). ① and ② represent two inelastic tunneling channels that lead to the excitation of surface plasmon polaritons (SPPs) in the junction.

require the simultaneous injection of an electron and a hole into the molecule. At negative bias voltages, as used here, the hole would be injected by the tip, whereas the electron injection would occur from the substrate. The photon map should thus display the orbital the hole is injected into, that is, either the shape of the −1.8 V orbital or the −0.9 V orbital, because only the hole injection depends on the spatial position of the STM tip. The injection of electrons from the substrate, on the other hand, is rather independent of the tip position on this scale and thus should not contribute to the pattern in the photon map. With a similar argument a possible resonance of excited SPP modes with preexisting electron–hole pairs can be excluded because this would result in a superposition of the −0.2 V and −1.8 V orbital in the photon map. Moreover, such a second-order process, requiring one electron to create the electron–hole pair and a second one to induce the SPP, is not compatible with the perfectly linear dependence of the integrate luminescence intensity with the tunneling current (Fig. 8.4).
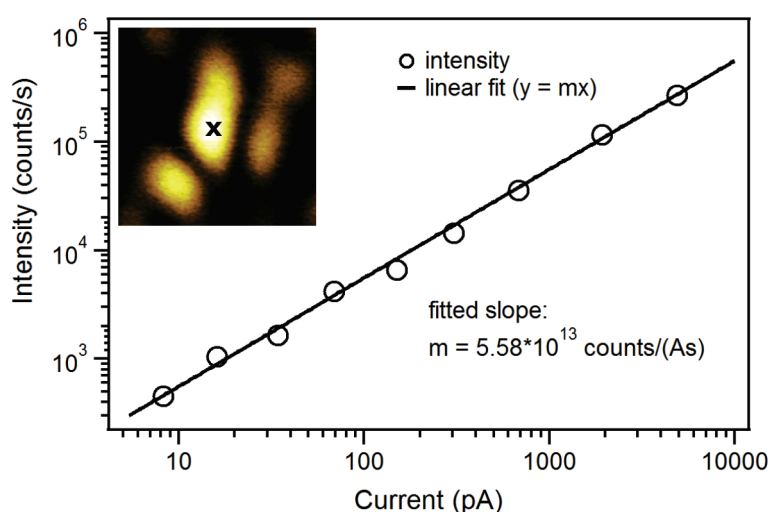

Fig. 8.4: STM-induced luminescence intensity on a single $Ir(ppy)_3$ molecule adsorbed on a C_{60} monolayer on Ag(111) as a function of the tunneling current ($U_{bias} = -1.8$ V). The inset shows the corresponding constant height photon map at the highest current. The black cross marks the spatial position of the plotted intensity.

Consequently, the comparison of submolecularly resolved photon maps with the spatial shape of the molecule's orbitals provides strong evidence for the involved luminescence process. This is important since it may corroborate arguments obtained from optical spectra of the emitted light, such as their width[42,189,260,261,263,264,266,267,269] or the observation of vibrational progressions.[38,40,42,70] It is important to note that an unambiguous correlation of photon maps with the shape of specific molecular orbitals obtained in dI/dU maps is only possible if both maps are recorded in constant height mode. When mapped in constant current mode, as performed in earlier studies,[36,37,189] the tip–sample distance is steadily adjusted in response to spatial variations of the integrated density of states. It has been shown that the tip–sample distance sensitively affects the intensity and the spectrum of excited SPP.[271] Hence, photon maps recorded in constant current mode may contain non-trivial superpositions of several effects that complicate their interpretation.

The different quantum cutoffs of the luminescence spectra on the single $Ir(ppy)_3$ molecules and the C_{60} monolayer at tunneling energies around the SPP resonance of the tip–sample cavity (see section 8.1.2) nicely supports the proposed model. Indeed, the 0.2 eV lower cutoff energy of the difference spectrum (Fig. 8.2c, blue curve) compared to the C_{60} spectrum (Fig. 8.2c, black curve) perfectly agrees with the energetic position of the $Ir(ppy)_3$ HOMO. Finally, section 5.2 has shown that the luminescence process on the C_{60} monolayer directly adsorbed on the metal substrate follows a very similar mechanism. In this case, the electronic states close to the Fermi

level of the substrate, which are responsible for the enhanced SPPs excitation, arise from a charge transfer from the substrate to the lowest unoccupied molecular orbital (LUMO)-derived states of the C_{60} layer (cf. section 4.3.1).

8.2 Dynamic Gating of Plasmon Excitation – Single Ir(ppy)$_3$ Molecules on a C$_{60}$ Bilayer

As discussed in chapter 7, the insertion of a second molecular C_{60} layer between the metal substrate and the single Ir(ppy)$_3$ molecules leads to a substantial change of their electronic structure. The high electron affinity of C_{60} induces a charge transfer from the Ir(ppy)$_3$ HOMO into the LUMO-derived band of the C_{60} layer, which leads to two singly occupied molecular orbitals (SOMOs) – one on the single Ir(ppy)$_3$ molecule and one in the C_{60} film. In particular the charging of the C_{60} SOMO with an additional electron from the STM tip requires bias voltages as small as +0.2 V (Ag(111) substrate) and +0.5 V (Au(111) substrate). At the same time, the C_{60} bilayer acts as a thin semiconducting layer which, in combination with the vacuum tunnel barrier to the STM tip, results in a double tunnel barrier geometry. As a consequence, the electronic states at the surface are no longer pinned to the substrate but shift as a function of the electric field in the junction (see section 7.1.3 and 7.2.2). In this section it will be demonstrated that, depending on the precise energy alignment of the electronic states, the current through and the SPP excitation in the junction are either blocked or permitted. Thus, subtle changes of this energy alignment can result in strong variations in the emitted intensity. It will be shown that this highly sensitive gating works in two ways: On the one hand, it enables following fast dynamic changes of an individual quantum system, by detecting the excited SPPs. On the other hand, weak external manipulations of such a quantum system allow a dynamic control of the SPP generation at its quantum limit. Before elucidating the detailed gating effect in section 8.2.3, the general characteristics of the STM-induced luminescence shall be briefly discussed.

8.2.1 Photon Maps and Photon Yield on the Single Ir(ppy)$_3$ Molecules

With an apparent height of 100 to 200 pm the single Ir(ppy)$_3$ molecules appear slightly higher than on the C_{60} monolayer in constant current topography maps around −3 V. As on the monolayer, three different adsorption geometries can be identified (Fig. 8.5a–c). However, the simultaneously recorded photon maps reveal slightly different submolecular patterns (8.5e–g). The differences might originate from the lower orientational order of the C_{60} molecule in the surface layer favoring slightly different adsorption geometries. Considering the symmetry of the single Ir(ppy)$_3$ molecules, the possible orientation of the molecules and their position on the C_{60} lattice are depicted in 8.5i–k. In contrast to the C_{60} monolayer, single Ir(ppy)$_3$ molecules on an C_{60} bilayer exhibit an enhanced luminescence at negative *and* positive bias voltages. Figure 8.5d,h,l depicts a single Ir(ppy)$_3$ molecule at a bias voltage of +2.5 V that might reside in the same adsorption geometry as the molecule in Fig. 8.5c,g,k.

The enhanced luminescence intensity at negative and positive bias voltages can be also observed in photon yield–voltage spectra (Fig. 8.6a), which show the number of detected photons per tunneling electrons. In accordance with the color coding in this thesis, measurements on
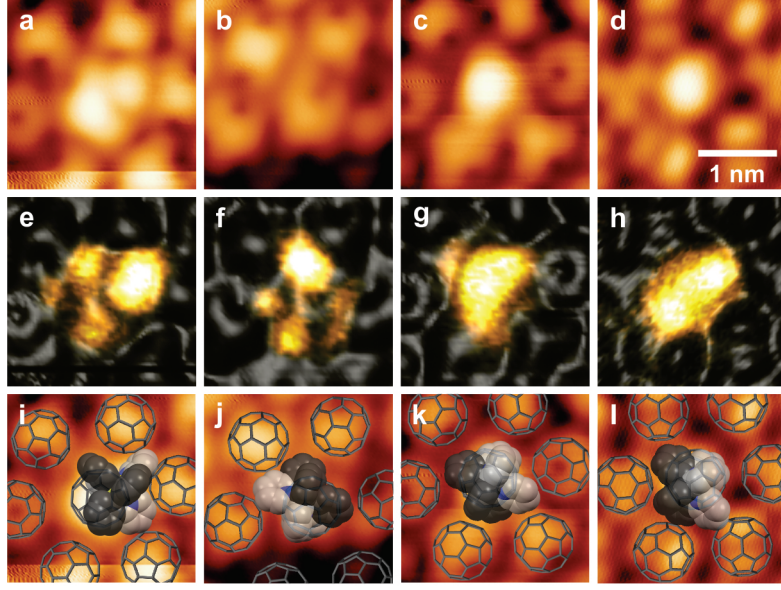
Fig. 8.5: Adsorption geometries of single $Ir(ppy)_3$ molecules on a C_{60} bilayer on Ag(111). (a–d) Constant current topography and (e–h) pseudo-3D topography where the color represents the photon map simultaneously measured by an APD. (i–l) Possible orientations of the single $Ir(ppy)_3$ molecule on the C_{60} lattice. Dark gray parts of the space-filling models represent phenyl groups and light gray parts pyridine groups of the three 2-phenylpyridine ligands. The images in the first three columns are recorded at $U_{set} = -3.5\,V$ and $I_{set} = 10\,pA$; the images in the fourth column show a molecule in the same geometry as in the panels c,g,k and are recorded at $U_{set} = +2.5\,V$ and $I_{set} = 15\,pA$.

a Ag(111) substrate using a silver-coated gold tip are depicted by gray curves, whereas measurements on a Au(111) substrate with a gold tip are displayed by brown curves. Figure 8.6b shows the simultaneously measured dI/dU spectra with the peak notation introduced in section 7.2. In the case of silver electrodes, the photon yield on the single molecule (solid lines) at $+2.5\,V$ is one order of magnitude larger than on the C_{60} bilayer (dotted lines). Compared to the pristine Ag(111) surface (dashed line), the photon yield on the single molecules is one order of magnitude smaller and shifted by approximately $0.5\,V$ toward higher bias voltages. The behavior of the photon yield–voltage curves on clean coinage metal surfaces arises from the vanishing detector efficiency at low photon energies and the vanishing SPP resonance of the tip–sample cavity. Hence, the shift of the photon yield–voltage curve indicates that the excitation of the same SPP modes on the single $Ir(ppy)_3$ molecules requires a higher bias voltage. When assuming the $Ir(ppy)_3$-induced C_{60} SOMO as the final state for inelastically tunneling electrons exciting SPP in the junction, the shift of the photon yield–voltage curve should express the energy position of the C_{60} SOMO at the given tip–sample distance.

At negative bias voltages, the photon yield abruptly increases at the strong $S_C^{e\prime}$ dI/dU peak corresponding to the onset of the electron injection into the C_{60} SOMO via the substrate (see also section 7.2.2). Within the C_{60} band gap, the photon yield on the single $Ir(ppy)_3$ molecule, the pure C_{60} bilayer, and the Ag(111) surface behave surprisingly similar, although the tip–substrate distance might differ by about $2\,nm$. This means that the fractions of tunneling electrons exciting SPP in these three cases are comparable. At bias voltages where the Fermi energy of the tip $(E_{F,t})$ reaches the occupied C_{60} states, the additional elastic tunneling

channels reduce the photon yield on the pure C_{60} bilayer. In the case of a gold tip and a Au(111) substrate, the photon yield is collectively reduced due to the larger internal damping of excited SPPs in the gold surfaces and the larger imaginary part of their dielectric function. Nevertheless, the strong increase of the photon yield at negative bias voltages coincides again with the intense $S_C^{e}{'}$ dI/dU peak corresponding to the onset of the electron injection into the C_{60} SOMO via the substrate.

Photon maps of single $Ir(ppy)_3$ molecules indicate further differences between the single molecules adsorbed on a Ag(111)-supported C_{60} bilayer and a Au(111)-supported C_{60} bilayer. Whereas for the Ag(111) substrate a clear submolecular pattern is observable (Fig. 8.6c), the enhanced luminescence intensity on the Au(111)-supported bilayer extends over an area that is larger than the size of single $Ir(ppy)_3$ molecule and exhibits less pronounced features. The origin of these differences will be discussed in section 8.2.4.
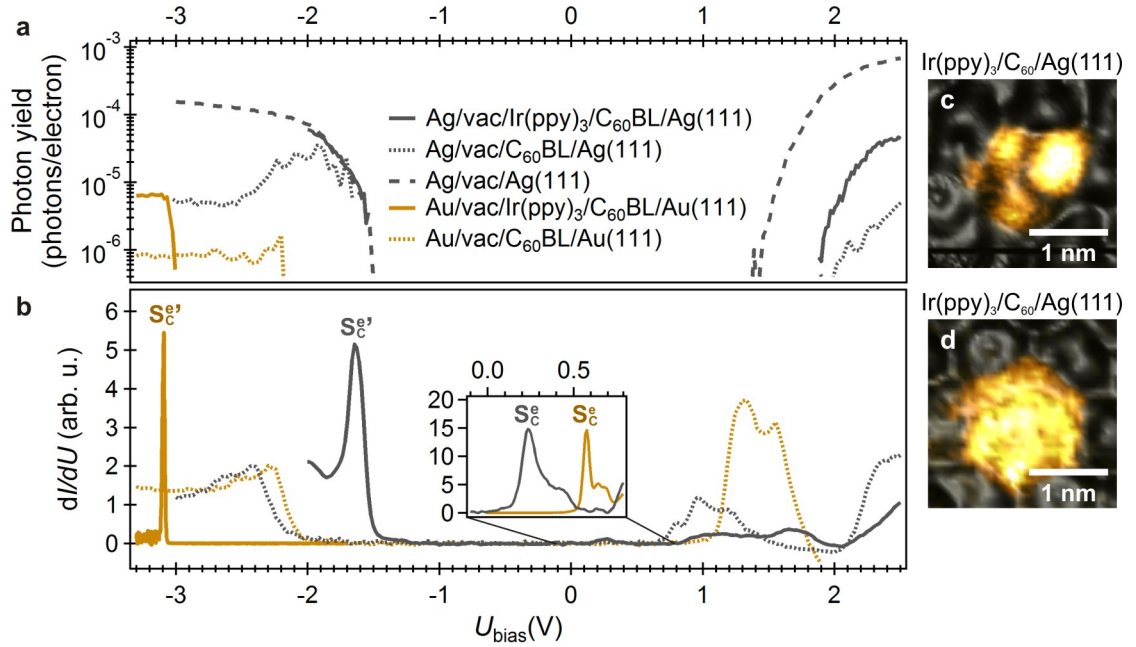
Fig. 8.6: Photon yield and electronic structure on top of a C_{60} bilayer on Ag(111) and Au(111) as well as on top of a single $Ir(ppy)_3$ molecules adsorbed on this. (a) Photon yield and (b) simultaneously recorded differential conductance (dI/dU) as a function of the applied bias voltage U_{bias}. Orange curves correspond to data measured with a Au tip and a Au(111) substrate; grey curves relate to measurements using a Ag-covered Au tip and a Ag(111) substrate. The line style indicates whether the measurement refers to a pure C_{60} bilayer (dotted curves), a single $Ir(ppy)_3$ molecule adsorbed on this (solid curve), or the pristine metal surface (dashed curve). The inset displays a detailed spectrum around the Fermi energy of the substrate. (c) Pseudo-3D topography with overlaid simultaneously recorded photon map (color) of a single $Ir(ppy)_3$ molecule on a Ag(111)-supported C_{60} bilayer and (d) on a Au(111)-supported C_{60} bilayer ($U_{set} = -3.5\,V$; c: $I_{set} = 10\,pA$, d: $I_{set} = 20\,pA$).

8.2.2 Luminescence Spectra

Luminescence spectra on single $Ir(ppy)_3$ molecules adsorbed on a C_{60} bilayer indicate that the emitted light again originates from the excitation of SPPs, as in the case of single $Ir(ppy)_3$

molecules on a C_{60} monolayer. On the whole, the obtained spectra are akin to those of the $Ir(ppy)_3$ molecules on a C_{60} monolayer (Fig. 8.7). Again, the precise shape of the spectra strongly depends on the geometry of the STM tip apex and the spectra exhibit considerably higher contributions at lower photon energies compared to the electroluminescence spectra of $Ir(ppy)_3$ doped in CBP[203] or poly(methyl methacrylate) (PMMA)[273] matrices.

Fig. 8.7: STM-induced luminescence spectra on top of a single $Ir(ppy)_3$ molecule on a C_{60} bilayer (BL, orange) and a C_{60} monolayer (ML, brown). At low photon energy the spectra might vanish due to the decreasing detector efficiency (dashed grey curve). The green curve depicts the electroluminescence spectrum of $6\%wt$ $Ir(ppy)_3$ in a CBP matrix (obtained from ref. [203]).

8.2.3 Surface Plasmon Polariton Excitation as a Function of the Electric Field in the Junction
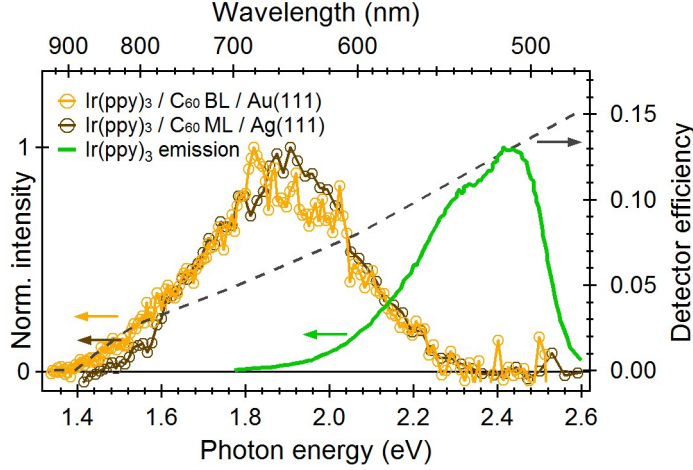
The following section will show that, at negative bias voltages, a single $Ir(ppy)_3$ molecule adsorbed on a C_{60} bilayer behaves like a single-molecule transistor that controls the current through and the SPP excitation in the tunnel junction. In analogy to such a transistor, the metal substrate can be seen as the source, the STM tip as the drain, and the current between both as the source–drain current I_{SD}.

Figure 8.8a,b present the measured plasmonic light intensity P and the tunneling current I_{SD}, respectively, as a function of the applied voltage U_{bias} and the thickness of the vacuum barrier d_{vac}. Both data sets are measured simultaneously by sweeping U_{bias} at different d_{vac}, with the STM tip positioned above a single $Ir(ppy)_3$ molecule on a Au(111)-supported C_{60} bilayer. As an example, Fig. 8.8c,d show a section of P and I_{SD} as a function of U_{bias} and the electric field strength in the junction E. For the determination of the absolute thickness of the vacuum barrier (d_{vac}) and the electric field strength (E) see section 7.2.3 (page 88 and 90). At a bias voltage of ~−3 V, P and I_{SD} abruptly rise by several orders of magnitude. The following arguments will demonstrate that the crucial parameter determining this rise is not the applied voltage but the electric field in the junction. As indicated by the white dashed lines in Fig. 8.8a,b, the switching voltage $U_S(d_{vac})$, assigned to the steepest rise in I_{SD}, shifts linearly with the vacuum barrier thickness (d_{vac}). Calculating the electric field in the vacuum barrier (diagonal gray lines in Fig. 8.8a,b; for details see page 90) reveals that $U_S(d_{vac})$ coincides with a constant field of 2.5 V/nm. The same applies for the gate voltage of the transistor U_G, which here is defined as the potential difference between the $Ir(ppy)_3$-induced S_C^e state and the substrate (source). This potential difference is equivalent to the voltage drop across the C_{60} bilayer $U_G = U_{C60}$. The field-dependent gating becomes even more obvious when the

plasmonic light intensity and the current are plotted as a function of E and U_{bias} (insets Fig. 8.8a,b). In order to account for the exponential decay of the tunneling current with increasing vacuum barrier thickness, the data in the insets of Fig. 8.8a,b are divided by the current at the corresponding switching voltage $U_S(d_{vac})$.

The strong response to the electric field can be rationalized by an analogy to a conventional field-effect transistor. In both devices, crossing of a specific gate voltage threshold opens a conduction channel between the source and the drain. In the present case, however, the conduction channel and the SPP generation are controlled via a particular electronic level instead of the density of charge carriers. In this sense, the mechanism rather resembles a resonant tunneling transistor.[274] We exploit the fact that the $Ir(ppy)_3$-induced S_C^e state can be charged by an additional electron from the STM tip (drain) already at small bias voltages and thus appears close to the Fermi energy of the substrate ($E_{F,s}$) (for details see section 7.2).
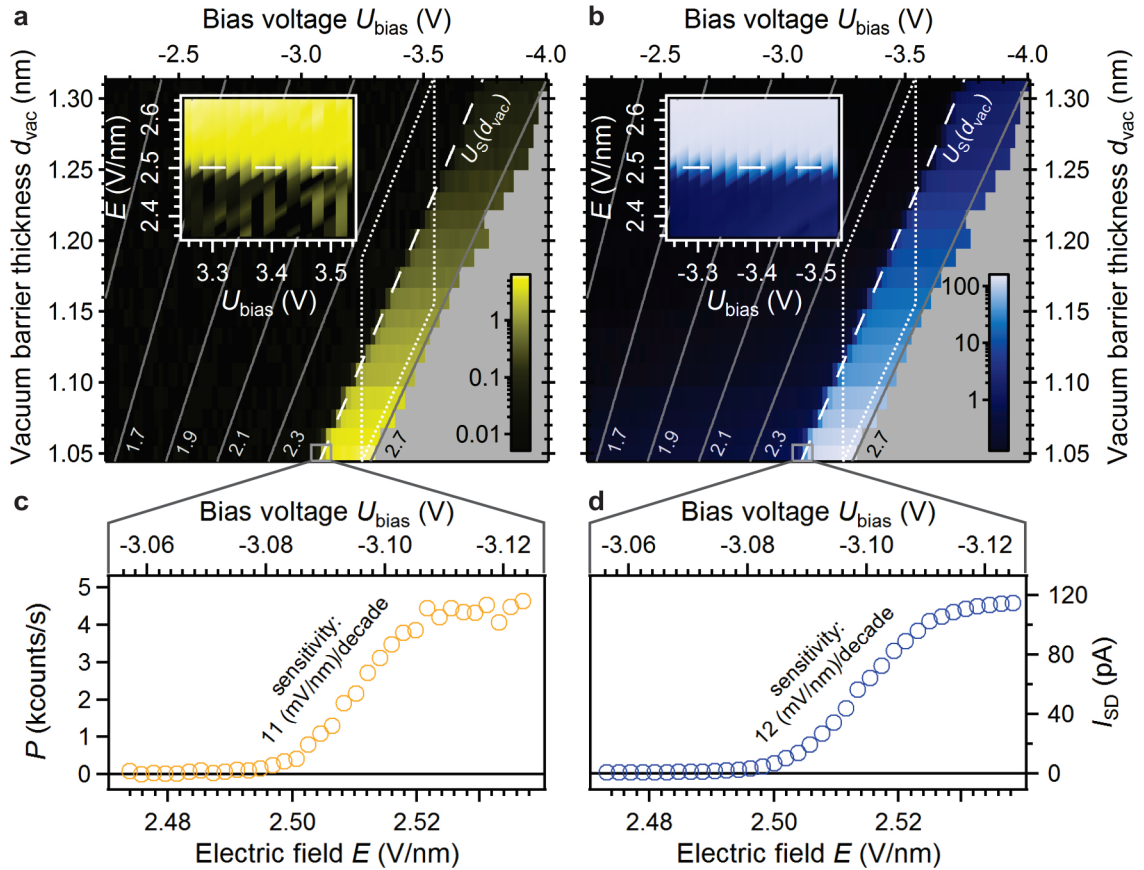
Fig. 8.8: Field dependence of the plasmonic light intensity and the tunneling current through a single $Ir(ppy)_3$ molecule in a vacuum–C_{60} bilayer double tunnel barrier. (a) Color-coded logarithmic plot of the measured plasmonic light intensity (in kcounts/s) and (b) the source–drain current (in pA) as a function of the applied bias voltage and the vacuum barrier thickness. The diagonal lines represent lines of constant electric field strength in the vacuum barrier (in V/nm). The insets show the data within the white dotted rhomboid plotted as a function of U_{bias} and E and divided by the current at the corresponding switching voltage $U_S(d_{vac})$ (in arbitrary units). The small gray rectangles at the bottom mark the section of the plasmonic light intensity displayed in (c) and the source–drain current in (d) at the minimum d_{vac}, respectively. In panel a and b data are binned over 10 points along U_{bias}.
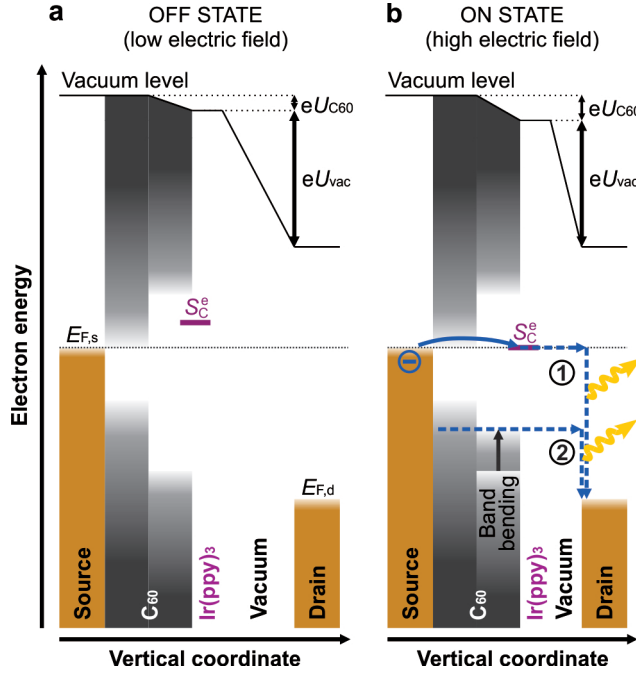
Fig. 8.9: Gating mechanism and density of states within the tunnel junction. (a) OFF state and (b) ON state of the SPP generation. The adsorbed $Ir(ppy)_3$ molecule leads to the formation of a singly occupied C_{60} state (S_C^e) at an energy $E_{S_C^e}^0$ slightly above the Fermi energy of the source contact ($E_{F,s}$). (b) As soon as the voltage drop across the C_{60} layer (U_{C60}) exceeds the charging potential of the S_C^e state, it becomes occupied by an electron from the source electrode and the transistor turns on. This opens two inelastic tunneling channels ① and ② that excite SPP in the junction.

For finite bias voltages, this state is shifted by the corresponding voltage drop (U_{C60}) across the C_{60} barrier. At low negative electric field, the S_C^e state cannot participate in a tunneling process because its charging potential exceeds the voltage drop across the C_{60} barrier (Fig. 8.9). In this case, only electrons from the occupied C_{60} states lead to a marginal tunneling current, which, cannot provide enough energy to excite SPP. U_{C60} rises as the electric field is increased, for example, by decreasing d_{vac} at constant bias voltage. As soon as U_{C60} equals or exceeds the charging potential of the S_C^e state $-U_{C60} \geq U_{S_C^e}^0$, an electron from the source electrode tunnels through the C_{60} barrier and charges the S_C^e state (Fig. 8.9b). While the additional electron occupies the S_C^e state, its charge raises the potential of all electronic states in the junction by the corresponding Coulomb energy and thus inhibits the tunneling of a second electron from the source. Consequently, this process is quantum-limited. At the same time, the transistor turns on and opens two SPP excitation channels: ① The additional electron can tunnel farther to the drain electrode and excite a SPP in the junction. ② The additional charge in the S_C^e state leads to a local band bending[182] in the C_{60} bilayer. This increases the energy of the electrons in the occupied C_{60} states, which now can also tunnel with energies high enough to excite SPPs.

8.2.4 Spatial Dependence of the Suface Plasmon Polariton Excitation

The contribution from channel ② becomes particularly apparent in constant height STM images recorded at bias voltages around $-3\,V$. At this bias voltage, the single molecule is surrounded by an oval region of increased light intensity (Fig. 8.10a) and increased current (Fig. 8.10d) that is larger than the spatial extension of the involved S_C^e state (inset in Fig. 8.10j). Simultaneously recorded dI/dU maps show that this region is encircled by an abrupt jump in differential conductance (Fig. 8.10g), which can be seen as the spatial representation of the sharp $S_C^{e\,\prime}$ peak observed in dI/dU spectra (for details, see section 7.2.2).

Similar ring-like dI/dU features have been observed for silver and alkali metal doped C_{60} monolayers on insulating Al_2O_3 films.[182,237] Aside to the S_C^e state, for example at the white cross in Fig. 8.10, tunneling through this state (channel ①) is not possible and all the current passes through the HOMO-derived C_{60} band. As long as the electric field at the S_C^e state exceeds a threshold of $2.5\,V/nm$, however, it remains charged and sustains the local band bending of the C_{60} bilayer (channel ②). As a result, the size of the ring-like dI/dU, as well as the areas of increased plasmonic light intensity and current, shrink with decreasing electric field in the junction, that is, decreasing bias voltage and increasing vacuum barrier thickness (Fig. 8.10a–i).

In accordance with this interpretation, intensity–voltage curves and current–voltage curves recorded on adjacent C_{60} molecules next to the S_C^e state, for example at the position marked by the white crosses, show a similar switching behavior as on top of this state. Again, the intensity (yellow) and the current (blue circles) abruptly rise at a specific switching voltage. These switching characteristics disappear when the single $Ir(ppy)_3$ molecule is removed by STM manipulation (red and black curve). The voltage offset necessary to overlap both current–voltage curves for $U_{bias} > U_S(d_{vac})$ (gray curve) yields a C_{60} band bending at this position due
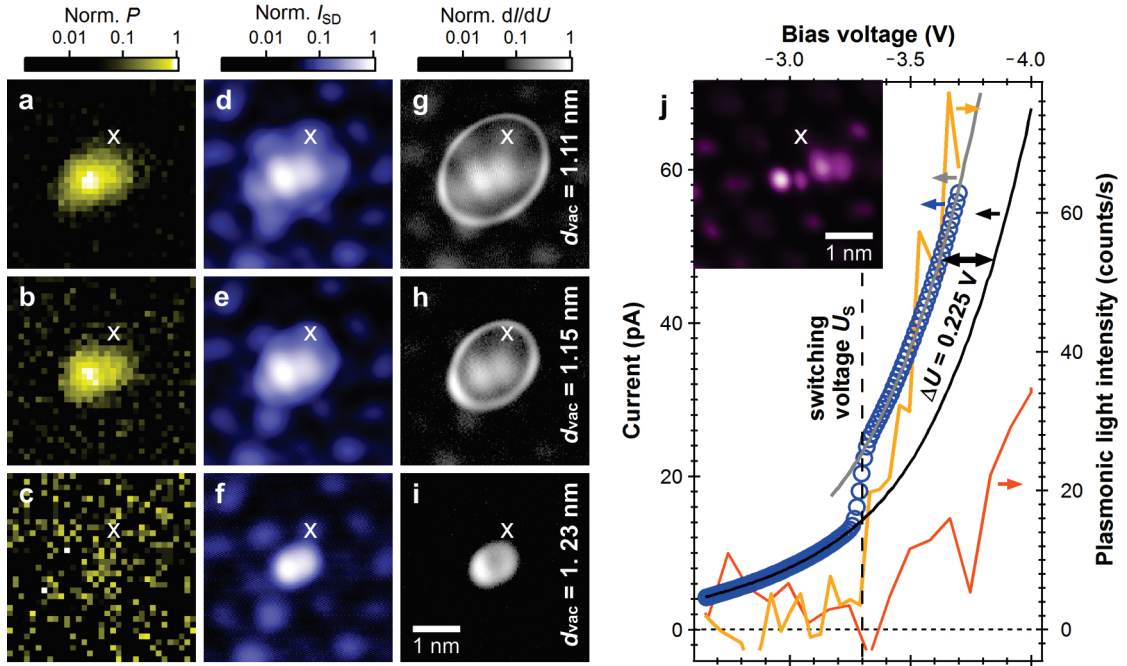
Fig. 8.10: Mapping of the C_{60} band bending. (a–c) Spatial mapping of the normalized plasmonic light emission P, (d–f) the normalized source–drain current I_{SD} and (g–i) the normalized differential conductance dI/dU at a constant bias voltage of $U_{bias} = -3.5\,V$. Images in the same row are recorded simultaneously at the same tip–sample distance, with the vacuum barrier thickness d_{vac} being indicated on the right-hand side. Each map is normalized to its maximum, b: 9 counts/s, c: 168 counts/s, d: 477 counts/s, e: 7 pA, f: 48 pA, g: 136 pA, h: 3.4 pA/V, i: 2.6 pA/V, j: 5.0 pA/V. (j) Current–voltage curve (blue circles) and intensity–voltage curve (yellow line) obtained with the STM tip positioned at the white cross in panel a–i. The switching characteristic in current and intensity disappears when the single molecule is removed by STM manipulation (intensity: red curve; current: black curve). The inset shows the shape of the S_C^e state that gets charged.

to the additional electron in the S_C^e state of $\Delta U = 0.225\,\text{V}$. Consequently, the charging state of the quantum system can be monitored by the intensity of excited SPPs, either directly on top of the quantum system or indirectly at some distance away from it via the local band bending in the semiconducting C_{60} layer.

When using silver instead of gold electrodes, the charging of the S_C^e state occurs already at a bias voltage of about $1.5\,\text{V}$ (cf. Fig. 8.6, page 105). At this voltage, the HOMO-derived C_{60} band lies below the Fermi energy of the drain (STM tip) and cannot contribute to the tunneling current, even when including their band bending. Hence, in this case SPPs are exclusively excited via the quantum-limited channel ①.

8.2.5 Charging Dynamics

To determine the time response of the transistor, the S_C^e state, induced by the single Ir(ppy)_3 molecule, is repeatedly switched between its charged and neutral state by a continuous train of nanosecond voltage pulses (Fig. 8.11, red curve). In this experiment, the STM tip is positioned at a constant height above the Ir(ppy)_3 molecule. The offset voltage, that is, the voltage between the voltage pulses, is chosen to lie below the switching voltage ($U_{\text{bias}}^{\text{DC}} = -2.85\,\text{V}$), while each voltage pulse (amplitude $U_{\text{bias}}^{\text{AC}} = -150\,\text{mV}$) enables the charging of the S_C^e state. Surprisingly, the time-resolved plasmonic light intensity (Fig. 8.11, yellow symbols) raises and decays faster than the voltage pulse charging and discharging the S_C^e state. The reason for this observation lies in the pronounced non-linear intensity–voltage curve (see Fig. 8.8c) and the fact that the generation of SPPs requires the voltage to surpass a specific switching value. Because the offset voltage is chosen to lie below the switching voltage, only a fraction of the voltage pulse edge is used to switch the SPP generation from its on to its off state, or vice versa. For comparison, the dashed line in Fig. 8.11 depicts the intensity expected for an instantaneous response of the system, considering the finite experimental time resolution. The latter is given by two contributions: 1) the bandwidth of the transmission line between the pulse generator
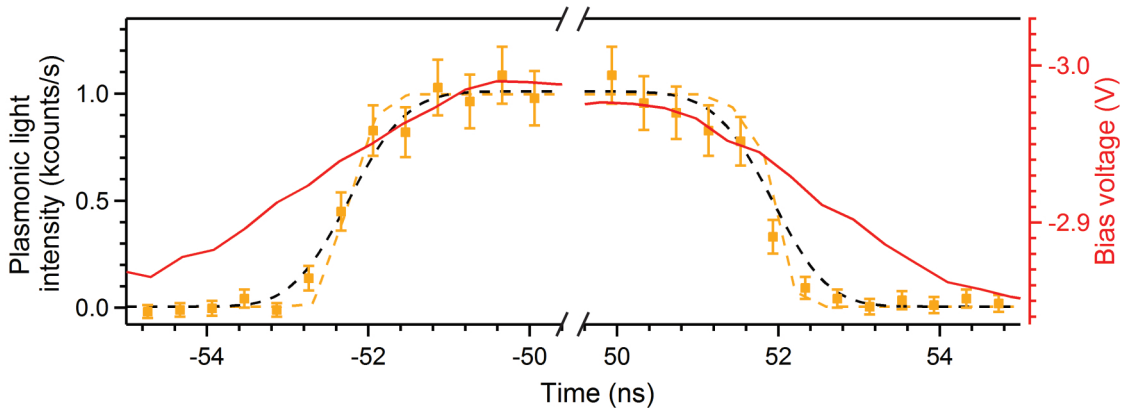
Fig. 8.11: Measured plasmonic light response on top of a single Ir(ppy)_3 molecule on Au(111)-supported a C_{60} bilayer (yellow symbols) to a square voltage pulse (red curve, right vertical axis, $U_{\text{bias}}^{\text{DC}} = -2.85\,\text{V}$, $U_{\text{bias}}^{\text{AC}} = -150\,\text{mV}$, $\langle I_{\text{SD}} \rangle = 10\,\text{pA}$). The dashed yellow curve depicts an instantaneous response to the voltage pulse obtained by an intensity–voltage curve on the single Ir(ppy)_3 molecule. The convolution of this instantaneous response with a Gaussian (FWHM: $1.1\,\text{ns}$) leads to the expected instantaneous response considering the finite experimental time resolution (black dashed curve).

and the STM tunnel junction and 2) the time jitter of the single photon detector. In terms of 1), the instantaneous intensity response to the voltage pulse is determined by the inverse of the procedure described in section 3.1, that is, by calculating the time-dependent intensity from the time-dependent voltage at the junction and the characteristic intensity–voltage curve atop of the single $Ir(ppy)_3$ molecule. In terms of 2), the finite time resolution of the photon detector is taken into account by a convolution of this instantaneous response with a Gaussian (FWHM: 1.1 ns). The perfect agreement of the instantaneous response considering the experimental time resolution with the measured light intensity reveals that both the charging and the discharging of the S_C^e state occur in less than 1 ns. Accordingly, the transistor could be driven well in the gigahertz range. In fact, much higher clock rates might be realizable by using the concepts developed here because both the charging of molecules[275] and the decay of surface plasmon polaritons[18, 19] can occur on subpicosecond time scales.

8.3 Dynamic Gating of Plasmon Excitation With Memory – Single Ir(ppy)$_3$ Molecules on a C$_{60}$ Trilayer

As on the C_{60} bilayer, the adsorption of single $Ir(ppy)_3$ molecules on a C_{60} trilayer causes the formation of two SOMOs, which can be emptied by removing its electron or completely filled by adding an additional electron (see section 7.3). However, the potential to remove the electron from the C_{60} SOMO is about $0.7\,eV$ smaller than on the C_{60} bilayer; hence, the single $Ir(ppy)_3$ molecule leads to one unoccupied state (S_C^e) slightly above the substrate Fermi level ($E_{F,s}$) and one occupied state (S_C^h) slightly below $E_{F,s}$ (Fig. 7.7, page 94). As a consequence, the field-induced gating of the SPP generation occurs at both bias polarities. In other words, the C_{60} SOMO can provide both a sharp initial state (negative bias polarity) *and* a sharp final state (positive bias polarity) close to $E_{F,s}$ for electrons tunneling between the STM tip and the C_{60} surface.

Section 7.3 showed that the single $Ir(ppy)_3$ molecules and thus the $Ir(ppy)_3$-induced S_C^e and S_C^h states can be reversibly switched between two different (adsorption) states, A and B, by applying bias voltages $\geq +2.2\,V$ and $\leq -1.3\,V$ at small tip–sample distances. The slightly different charging potentials of both states have a substantial impact on the SPP excitation efficiency in the junction, in accordance with the effects discussed in the previous sections. In state A, the removal of the C_{60} SOMO electron by the substrate occurs at around $+2.0\,V$ ($S_C^{h'}$ peak, Fig. 8.12a, magenta curve) and is connected to a more than one order of magnitude rise in photon yield (Fig. 8.12b). For the B state, the same onset requires a bias voltage of about $+2.4\,V$ (Fig. 8.12a,b; violet curve). In a similar way, the onset of the electron injection by the substrate determines the rise in photon yield at negative bias voltages, which explains the lack of detectable photons in the case of the A state for bias voltages $> -1.8\,V$. Figure 8.12c-n depict the spatial dependence of the differential conductance (dI/dU) (Fig. 8.12c–e), the SPP excitation (Fig. 8.12g–i), and the measured current (Fig. 8.12k–m) on top a single $Ir(ppy)_3$ molecule in an A state for a constant STM tip–sample distance and increasing bias voltage. As on the C_{60} bilayer, the onset of charge injection by the substrate results in a ring-like feature in dI/dU maps, whose size increase with the electric field strength in the junction; that is, with increasing bias voltage and decreasing tip–sample distance. At the same time, the onset of charge injection determines the area of enhanced photon emission and current.

In the B state, the STM image recorded at the same tip–sample distance does not show any of the characteristics of an additional charge. Instead, the dI/dU map only exhibits a weak electronic state (Fig. 8.12f), the photon map reveals substantially reduced intensity (Fig. 8.12j), and the current map shows only the LUMO-derived band of the topmost C_{60} layer without any indication of the adsorbed $Ir(ppy)_3$ molecule (Fig. 8.12n).

On the whole, the $Ir(ppy)_3$-induced C_{60} SOMO behaves similar to the SPP-emitting transistor introduced in the previous section. In contrast to the latter and any conventional transistor, however, this transistor can be driven at both bias polarities and thus can control electron currents as well as hole currents. Furthermore, its bistability enables a pre-selection of the transistor properties, in particular its threshold voltage between two specific states, by high electric fields and/or larger bias voltages. Similar systems with larger switching energies could provide the basis for optically readable, non-volatile memories. Compared to previously reported concepts for a plasmonic memristor,[276] such a bistable SPP-emitting transistor could directly generate SPP by means of electrical currents. Moreover, such devices could
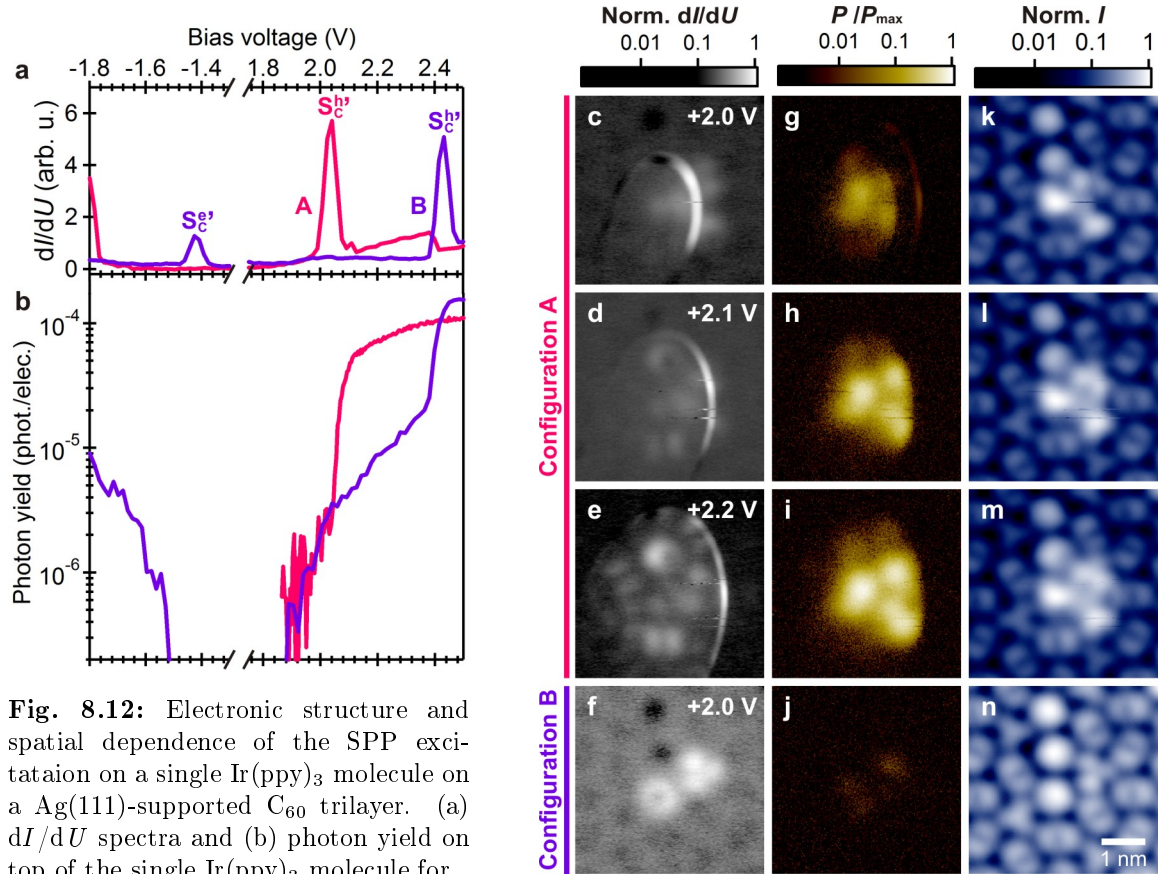
Fig. 8.12: Electronic structure and spatial dependence of the SPP excitataion on a single $Ir(ppy)_3$ molecule on a Ag(111)-supported C_{60} trilayer. (a) dI/dU spectra and (b) photon yield on top of the single $Ir(ppy)_3$ molecule for both adsorptions states A (magenta) and B (violet) of the single $Ir(ppy)_3$ molecule (same as in Fig. 7.7a, page 94). (c–e) Logarithmically plotted constant height dI/dU map, (g–i) photon map, and (k–m) current map of the single molecule in the A state recorded at the same tip–sample distance and the indicated bias voltage. (f) Corresponding dI/dU map, (j) photon map, and (n) current map of the same molecule in the B state. In the panels g–j the maximum intensity always refers to the maximum intensity in panel i.

profit from all the advantages discussed in section 8.2, for example, the high on–off ratios and the fast readout speed.

8.4 Conclusions

The first part of this chapter has demonstrated that resolving both the discrete energy levels of molecules and the local STM-induced luminescence with submolecular spatial resolution allows identification of the inelastic tunneling channels responsible for the excitation of SPP in tunnel junctions. The enhanced intensity and the significant spectral shift on the admolecules can be explained by their electronic structure. Intramolecular transitions and dielectric properties may be of minor importance, at least in the presented case of single $Ir(ppy)_3$ molecule on a C_{60} monolayer. It has been shown that single molecules located in a tunnel junction can act as energetically and submolecularly defined spatial gates for the electrical excitation of SPPs and the emitted luminescence. The intensity and spectral distribution of the generated SPPs are directly related to the spatial shape and the energy of the orbital closest to the Fermi energy. Transferring this concept to other adsorbate systems with known orbital properties may offer the possibility to statically control the electrical excitation of SPPs in a predictable manner.

The second part of this chapter has demonstrated that the SPP excitation can even be dynamically controlled, when the corresponding electronic states reside in a double tunnel barrier and thus their energy can be tuned by the electric field. It has been shown that an individual quantum system is able to dynamically control the electrical SPP generation in a tunnel junction. On the one hand, this enables following subtle dynamic changes of the single quantum system itself via the detection of excited SPP. On the other hand it allows modulating the electrical SPP generation at its quantum limit. For the example of single $Ir(ppy)_3$ molecules on a C_{60} bilayer, it has been shown that the SPP generation can be controlled over three decades with an electric field sensitivity of $11\,mV/nm$ per decade (Fig. 8.8a, page 107) and frequencies well in the gigahertz range. The described effect is expected to be applicable to a large variety of other quantum systems, such as quantum dots or even single atoms, as well as alternative barrier materials. In fact, the SPP gating only relies on the relative alignment of a confined electronic state incorporated in a double tunnel barrier. The specific electronic structure of the junction thereby determines the number of SPP excitation channels that are gated by the quantum system. Therefore, a careful choice of the electronic structure of the junction allows realization of electronically driven and ultrafast gateable single SPP sources. It will be a challenge for future studies to enhance and apply the demonstrated effects in planar tunnel junctions and metal–insulator–metal waveguides. Such quantum interfaces, bridging nano-electronics and nanophotonics, might provide new avenues to realize single-SPP-on-demand sources and to convert electronic qbits into photonic qbits.

The last part of this chapter has provided an outlook by showing that similar quantum systems could also act as plasmonically readable non-volatile memories, as long as they are able to exist in two metastable and electronically different configurations. The presented experiments demonstrated the feasibility of such memories, albeit the specific switching conditions of the single $Ir(ppy)_3$ molecules on C_{60} trilayers should be investigated in more detail and

technological applications might require more robust quantum systems with larger switching energies.

Chapter 9

Conclusions & Perspectives

The results of this thesis provide a bright future for time-resolved scanning tunneling microscopy (STM) and offer a variety of future exciting experiments. This chapter shall briefly discuss some selected perspectives of this work.

9.1 Pushing the Time Resolution of the Developed Methods

Currently, the achievable time resolution of the presented concepts is primarily determined by the time resolution (jitter) of the used single photon detectors and, in the case of the measured luminescence time response, by the maximum speed by which the bias voltage at the STM tunnel junction can be varied. The latter equals the maximum possible edge steepness of voltage pulses arriving at the tunnel junction. This in turn is limited by the employed pulse generator and the bandwidth of the transmission lines leading to the junction. During this thesis the original stainless steel cabling was thus replaced a by high-frequency, semi-rigid wiring with fully impedance matched ($50\,\Omega$) interconnections. While this modification removed the resonance frequencies at 25, 90 and 130 MHz visible in Fig. 3.4b (page 23), it had only small effect on the bandwidth of the set-up, which remained at ~200 MHz. The origin of the limited bandwidth was identified as being due to insufficient shielding of the transmission lines at the microscope head.[277] Saunus *et al.* have shown that proper shielding of the transmission lines up to the thin metal wire forming the STM tip enables voltage pulses on the order of 100 ps.[93] In long term, the shielding of the wiring at the microscope head should thus be reconsidered and adapted.

Section 8.2.5 has shown that the effective time resolution in the emitted light can be higher than the time required to change the bias voltage from its offset value to the pulse value, as long as the investigated system exhibits a strong non-linear intensity–voltage curve, for example, a sharp voltage threshold. In this case, only a fraction of the voltage pulse edge is used to probe the time response of the system. When using voltage pulses whose edges follow the progression of a Gaussian function instead of a linear function, and by choosing appropriate values for the offset and pulse voltage, the limited bandwidth of the transmission lines can be used more effectively. Indeed, the maximum slope of a (normalized) Gaussian function equals about a quarter of its standard deviation. When using Gaussian-shaped pulse edges with a standard deviation of 2.5 ns, for example, the maximum speed by which the bias voltage can be changed equals the inverse pulse amplitude multiplied by 0.625 ns. For maximum

time resolution, the pulse parameters (offset and amplitude) should thus be chosen such that the studied process is provoked at about half of the pulse amplitude. However, neither a modification of the microscope head nor a wily design of the pulses arriving at the tunnel junction is able to overcome the limited time resolution of the single photon detectors. For this reason, the previously used detectors will be replaced in future experiments by detectors with a higher time resolution of 30 ps.

9.2 Single-Electron–Single-Photon Experiments

Chapter 3 has shown that the developed pulse optimization technique enables voltage pulses of a few nanoseconds directly at the point of the experiment, that is, in the tunnel junction. These short voltage pulses imply that, for tunneling currents of a few picoamperes that are restricted to a few nanoseconds, during the pulses statistically less than one charge carrier tunnels through the vacuum barrier. Therefore, the application of a few nanoseconds short voltage pulses enables studying the effect and temporal development of individual charge carriers injected into an investigated system. Indeed, the pulse measurements on the C_{60} defects (section 5.6) can be seen as a first example of such experiments. Modeling the luminescence time response by Monte Carlo simulations have clearly revealed two different scenarios; either a hole is injected first by the STM tip and an electron injected by the substrate follows or, vice versa, the electron is injected first and the hole injection follows.

Thinking one step ahead, the STM tip could also successively inject both types of charge carriers by quickly switching between both bias polarities. In this case, injected electrons and holes may recombine with each other without the generally required charge injection via the substrate. As a consequence, the necessary decoupling layer to the metal substrate could be thicker and could thus prohibit a loss of injected charge carriers to the substrate. The only remaining loss channel would be the tunneling of charge carriers back to the STM tip. In fact, the investigated system could even be pumped with a high-frequency sine wave, which overcomes the limited pulse amplitude of the employed arbitrary wave form generator. However, an important challenge of this approach will be finding a suitable system for these kind of experiments: First, both the highest occupied molecular orbital (HOMO) and the lowest unoccupied molecular orbital (LUMO) must be located within the band gap of the decoupling layer. Second, the adsorption energy of the corresponding molecule or nanostructure to the decoupling layer must be large enough that this withstands the rapidly changing electric fields in the junction.

9.3 Tunable Generation of Monochromatic Surface Plasmon Polaritons

Section 8.2 has shown that the electronic states of molecules in a tunnel junction can both provide sharp initial or final states for electrons inelastically tunneling between both electrodes. In either case, the metallic tip provides a continuum of states, which results in a broad emission spectrum. In contrast, when both the sample and the tip possess sharp electronic states only discrete inelastic tunneling processes should be available. Similar to the intrinsic transitions

within a molecule or nanostructure, the tunneling electrons should thus excite only sharp surface plasmon polariton (SPP) resonances. The corresponding resonance condition and the emission energy would be given by the energy difference between the tip and sample states and would thus be determined by the applied bias voltage. Furthermore, this approach should substantially increase the quantum efficiency – that is, the number of excited SPP per tunneling electron – because it would reduce the number of elastic tunneling channels that cannot contribute to the excitation of SPPs in the tunnel junction. Finally, this approach may also provide a way to quantify the amount of SPPs that radiate as photons and those decaying by non-radiative processes or coupling to propagating SPPs.

9.4 Implementation of the Presented Effects into Solid State Devices

Provided the generally low probability of the inelastic tunneling processes exciting localized SPPs in tunnel junctions could be increased, for example, by the approach discussed in the previous section, this method of electrically generating SPPs would be of paramount technological importance. Various studies have shown that the SPP modes in such nanoscopic tunnel junctions are able to couple to SPP modes propagating along the surface of the electrodes.[278–281] Such nanoscopic junctions offer large arrays of electrically driven and individually addressable SPP sources, necessary, for example, for novel electro-optical computer chips or large arrays of surface plasmon resonance (SPR) sensor for lab-on-the-chip devices. Adding individual quantum systems in such tunnel junctions will only marginally increase the required size, but offer an additional local control of the SPP generation. Therefore, one important challenge is to transfer and apply the effects described in chapter 8 to solid-state devices. In fact, one of the most efficient ways to guide plasmonic light fields on nanometer length scales – the use of metal–insulator–metal waveguides – begs for an implementation of such SPP sources. As already discussed in section 8.4, the specific nature of the quantum system, whether it is a single molecule, a single quantum dot or even a single atom, as well as the specific tunnel barrier, should not affect the presented effects.

9.5 Monitoring the Kinetics of Molecular Rearrangement Processes

Chapter 8 has shown that the electronic states of a molecule in a tunnel junction have a direct influence on the SPP excitation in the junction. When the energy and/or the spatial extension of these states change, for example, due to conformational or configurational changes, such a process should thus directly affect the SPP generation in the junction. Therefore, it may be possible to monitor the dynamics of the corresponding processes via the emitted plasmonic light. Certainly most promising are molecular rearrangement processes that are induced by a change of the redox or charge state of the molecules, as these should be controllable by the applied bias voltage. In fact, several of these *redox-active molecular switches* and *molecular electro-mechanical actuators* have been discussed in the literature. The most prominent members are [8]annuelens[282–285] as well as various biomolecules. One of the most extensively

studied biomolecules is cytochrome c. In solution, the structural relaxations induced by a change of its charge state[286] occurs on the millisecond time scale and 2–3 orders of magnitude faster than the electron transfer.[287] What makes it even more interesting is the fact that its deposition on metal surfaces via ionspray deposition has been investigated within the scope of a previous PhD thesis by Gordon Rinke.[288, 289] Via an already existing vacuum suitcase, similar samples of cytochrome c deposited on a decoupling layer could be also transfered to the microscope used in this thesis without breaking the ultra-high vacuum (UHV) environment.

Bibliography

[1] Shedding light on photonics. *Publ. Serv. Rev. Eur.*, 24, 2012.

[2] United Nations General Assembly resolution. Internationl year of light and light-based technoogies, 2015, 68/221, 20 December 2013.

[3] European Comission. *Key enabling technologies, final report.* 2011.

[4] BMBF, Spectaris, VDMA, and ZVEI. Branchenreport Photonik 2013.

[5] H. Yersin, A.F. Rausch, R. Czerwieniec, T. Hofbeck, and T. Fischer. The triplet state of organo-transition metal compounds. triplet harvesting and singlet harvesting for efficient OLEDs. *Coord. Chem. Rev.*, 255(21-22):2622–2652, 2011.

[6] E. Ozbay. Plasmonics: Merging photonics and electronics at nanoscale dimensions. *Science*, 311(5758):189–193, 2006.

[7] J. A. Schuller, E. S. Barnard, W. Cai, Y. C. Jun, J. S. White, and M. L. Brongersam. Plasmonics for extreme light concentration and manipulation. *Nature Mat.*, 9(3):193–204, 2010.

[8] D. K. Gramotnev and S. Bozhevolnyi. Plasmonics beyond the diffraction limit. *Nat. Photon.*, 4(2):83–91, 2010.

[9] J. Lambe and S. L. McCarthy. Light emission from inelastic electron tunneling. *Phys. Rev. Lett.*, 37(14):923, 1976.

[10] M. Hentschel, R. Kienberger, C. Spielmann, G. A. Reider, N. Milosevic, T. Brabec, P. Corkum, U. Heinzmann, M. Drescher, and F. Krausz. Attosecond metrology. *Nature*, 414(6863):509–513, 2001.

[11] T. Brixner, F. J. García de Abajo, J. Schneider, and W. Pfeiffer. Nanoscopic ultrafast space-time-resolved spectroscopy. *Phys. Rev. Lett.*, 95:093901, 2005.

[12] M. Aeschlimann, M. Bauer, D. Bayer, T. Brixner, F. J. García de Abajo, W. Walter Pfeiffer, M. Rohmer, C. Spindler, and F. Steeb. Adaptive subwavelength control of nano-optical fields. *Nature*, 446:301–304, 2007.

[13] G. Nunes and M. R. Freeman. Picosecond resolution in scanning tunneling microscopy. *Science*, 262(5136):1029–1032, 1993.

[14] Y. Terada, S. Yoshida, O. Takeuchi, and H. Shigekawa. Real-space imaging of transient carrier dynamics by nanoscale pump–probe microscopy. *Nature Phot.*, 4(12):869–874, 2010.

[15] S. Loth, M. Etzkorn, C. P. Lutz, D. M. Eigler, and A. J. Heinrich. Measurement of fast electron spin relaxation times with atomic resolution. *Science*, 329(5999):1628–1630, 2010.

[16] J. K. Gimzewski, J. K. Sass, R. R. Schlitter, and J. Schott. Enhanced photon emission in scanning tunneling microscopy. *Europhys. Lett.*, 8(5):435–440, 1989.

[17] R. Berndt, J. K. Gimzewski, and P. Johansson. Inelastic tunneling excitation of tip-induce plasmon modes on nobel-metal surfaces. *Phys. Rev. Lett.*, 67(27):3796–3799, 1991.

[18] U. D. Keil, T. Ha, J. R. Jensen, and J. M. Hvam. Femtosecond tunneling response of surface plasmon polaritons. *Appl. Phys. Lett.*, 72(23):3074–3076, 1998.

[19] D. Steinmüller-Nethl, R. A. Höpfel, E. Gornik, A. Leitner, and F. R. Aussenegg. Femtosecond relaxation of localized plasma excitations in Ag islands. *Phys. Rev. Lett.*, 68(3):389–392, 1992.

[20] K. Goushi, Y. Kawamura, H. Sasabe, and Adachi C. Unusual phosphorescence characteristics of $Ir(ppy)_3$ in a solid matrix at low temperatures. *Jpn. J. Appl. Phys.*, 43, 2004.

[21] T. Sajoto, P. I. Djurovich, A. B. Tamayo, J Oxgaard, W. A. Goddard, and M. E. Thompson. Temperature dependence of blue phosphorescent cyclometalated Ir(III) complexes. *J. Am. Chem. Soc.*, 131(28):9813–9822, 2009.

[22] T. Hofbeck and H. Yersin. The triplet state of *fac*-$Ir(ppy)_3$. *Inorg. Chem.*, 49:9290–9299, 2010.

[23] X. D. Feng, C. J. Huang, V. Lui, R. S. Khangura, and Z. H. Lu. Ohmic cathode for low-voltage organic light-emitting diodes. *Appl. Phys. Lett.*, 86(14), 2005.

[24] J. Y. Lee. Efficient hole injection in organic light-emitting diodes using C_{60} as a buffer layer for Al reflective anodes. *Appl. Phys. Lett.*, 88(7), 2006.

[25] Y. Y. Yuan, S. Han, D. Grozea, and Z. H. Lu. Fullerene-organic nanocomposite: A flexible material platform for organic light-emitting diodes. *Appl. Phys. Lett.*, 88(9), 2006.

[26] M. G. Helander, Z. B. Wang, and Z. H. Lu. Contact formation at the C_{60}/alkali-metal fluoride/Al interface. *Appl. Phys. Lett*, 93(8), 2008.

[27] J. Bardeen. Tunneling from a many-particle point of view. *Phys. Rev. Lett.*, 6:57, 1961.

[28] A. D. Gottlieb and L. Wesoloski. Bardeen's tunnelling theory as applied to scanning tunnelling microscopy: A technical guide to the traditional interpretation. *Nanotech.*, 17(8):R57, 2006.

[29] C. J. Chen. *Introduction to scanning tunneling microscopy*. Oxford University Press, second edition, 2008.

[30] G. Binnig, H. Rohrer, C. Gerber, and E. Weibel. Surface studies by scanning tunneling microscopy. *Phys. Rev. Lett.*, 49(1):57, 1982.

[31] J. Tersoff and D. R. Hamann. Theory and application for the scanning tunneling microscope. *Phys. Rev. Lett.*, 50(25):1998, 1983.

[32] J. Tersoff and D. R. Hamann. Theory of the scanning tunneling microscope. *Phys. Rev. B*, 31(2):805, 1985.

[33] R. D. Young. Surface microtopography. *Phys. Today*, 24(11):42, 1971.

[34] J. K. Gimzewski, B. Reihl, J. H. Coombs, and R. R. Schlittler. Photon emission with the scanning tunneling microscope. *Z. Physik B*, 72(4):497, 1988.

[35] R. Berndt and J. K. Gimzewski. The role of proximity plasmon modes on noble metal surfaces in scanning tunneling microscopy. *Surf. Sci.*, 269-270:556–559, 1992.

[36] R. Berndt, R. Gaisch, J. K. Gimzewski, B. Reihl, R. R. Schlittler, W.-D. Schneider, and M. Tschudy. Photon emission at molecular resolution induced by a scanning tunneling microscope. *Science*, 262(5138):1425–1427, 1993.

[37] R. Berndt, R. Gaisch, W. D. Schneider, J. K. Gimzewski, B. Reihl, R. R. Schlittler, and M. Tschudy. Photon emission from adsorbed C_{60} molecules with sub-nanometer lateral resolution. *Appl. Phys. A*, 57(6):513–516, 1993.

[38] X. H. Qiu, G. V. Nazin, and W. Ho. Vibrationally resolved fluorescence excited with submolecular precision. *Science*, 299(5606):542–546, 2003.

[39] S. W. Wu, G. V. Nazin, and W. Ho. Intramolecular photon emission from a single molecule in a scanning tunneling microscope. *Phys. Rev. B*, 77(20):205430, 2008.

[40] Z. C. Dong, X. L. Guo, A. S. Trifonov, P. S. Dorozhkin, K. Miki, K. Kimura, S. Yokoyama, and S. Mashiko. Vibrationally resolved fluorescence from organic molecules near metal surfaces in a scanning tunneling microscope. *Phys. Rev. Lett.*, 92(8):086801, 2004.

[41] Z. C. Dong, X. L. Zhang, H. Y. Gao, Y. Luo, C. Zhang, L. G. Chen, R. Zhang, X. Tao, Y. Zhang, J. L. Yang, and J. G. Hou. Generation of molecular hot electroluminescence by resonant nanocavity plasmons. *Nature Phot.*, 4(1):50, 2010.

[42] F. Rossel, M. Pivetta, F. Patthey, and W.-D. Schneider. Plasmon enhanced luminescence from fullerene molecules excited by local electron tunneling. *Opt. Exp.*, 17(4):2714–2721, 2009.

[43] A. Kabakchiev, K. Kuhnke, T. Lutz, and K. Kern. Electroluminescence from individual pentacene nanocrystals. *Chem. Phys. Chem.*, 11(16):3412–3416, 2010.

[44] A. Downes and M. E. Welland. Photon emission from Ag and Au clusters in the scanning tunneling microscope. *Appl. Phys. Lett.*, 72(21):2671–2673, 1998.

[45] N. Nilius, N. Ernst, and H.-J. Freund. Photon emission spectroscopy of individual oxide-supported silver clusters in a scanning tunneling microscope. *Phys. Rev. Lett.*, 84:3994–3997, 2000.

[46] R. Berndt and J. K. Gimzewski. Injection luminescence from $CdS(11\bar{2}0)$ studied with scanning tunneling microscopy. *Phys. Rev. B*, 45:14095, 1992.

[47] T. Lutz, A. Kabakchiev, T. Dufaux, C. Wolpert, Z. Wang, M. Burghard, K. Kuhnke, and K. Kern. Scanning tunneling luminescence of individual CdSe nanowires. *Small*, 7(16):2396–2400, 2011.

[48] J. Lindahl, M. E. Pistol, L. Montelius, and L. Samuelson. Stark effect in individual luminescent centers observed by tunneling luminescence. *Appl. Phys. Lett.*, 68(1):60–62, 1996.

[49] M. J. Romero, J. Van der Lagemaat, I. Mora-Sero, G. Rumbles, and M. M. Al-Jassim. Imaging of resonant quenching of surface plasmons by quantum dots. *Nano Lett.*, 6(12):2833–2837, 2006.

[50] R. Berndt and J. K. Gimzewski. Isochromat spectroscopy of photons emitted from metal surfaces in an STM. *Ann. Physik*, 2(2):133–140, 1993.

[51] H.-M. Benia, P. Myrach, and N. Nilius. Photon emission spectroscopy of thin MgO films with the STM: From a tip-mediated to an intrinsic emission characteristic. *New J. Phys.*, 10(1):013010, 2008.

[52] N. L. Schneider, G. Schull, and R. Berndt. Optical probe of quantum shot-noise reduction at a single-atom contact. *Phys. Rev. Lett.*, 105(2):026601, 2010.

[53] P. Johansson, R. Monreal, and P. Apell. Theory for light emission from a scanning tunneling microscope. *Phys. Rev. B*, 42(14):9210, 1990.

[54] G. Schull, N. Néel, P. Johansson, and R. Berndt. Electron–plasmon and electron–electron interactions at a single atom contact. *Phys. Rev. Lett.*, 102(5):057401, 2009.

[55] R. Berndt, J. K. Gimzewski, and P. Johansson. Electromagnetic interactions of metallic objects in nanometer proximity. *Phys. Rev. Lett.*, 71(21):3493, 1993.

[56] P. Avouris and B. N. J. Persson. Excited states at metal surfaces and their non-radiative relaxation. *J. Phys. Chem.*, 88(5):837–848, 1984.

[57] A. Campion, A. R. Gallo, C. B. Harris, H. J. Robota, and P. M. Whitmore. Electronic energy transfer to metal surfaces: A test of classical image dipole theory at short distances. *Chem. Phys. Lett.*, 73(3):447–450, 1980.

[58] K. Kuhnke, R. Becker, and K. Kern. Dynamics of second harmonic generation at the C_{60}/quartz interface. *Chem. Phys. Lett.*, 257(5–6):569–575, 1996.

[59] K. Kuhnke, R. Becker, M. Epple, and K. Kern. C_{60} exciton quenching near metal surfaces. *Phys. Rev. Lett.*, 79(17):3246–3249, 1997.

[60] X. L. Guo, Z. C. Dong, A.S. Trifonov, K. Miki, Y. Wakayama, D. Fujita, K. Kimura, S. Yokoyama, and S. Mashiko. Nanoscale organic electroluminescence from tunnel junctions. *Phys. Rev. B*, 70(23):233204, 2004.

[61] X. Guo. Tunneling-electron-induced molecular luminescence from a nanoscale layer of organic molecules on metal substrates. *Appl. Phys. Lett.*, 84(6):969–971, 2004.

[62] X.-L. Guo, Z.-C. Dong, A. S. Trifonov, K. Miki, K. Kimura, and S. Mashiko. STM-induced light emission from the surface of H_2TBP porphyrin/PFP porphyrin/Cu(100). *Appl. Surf. Sci.*, 241(1–2):28 – 32, 2005.

[63] X.-L. Guo, Z.-C. Dong, A. S. Trifonov, K. Miki, S. Mashiko, and T. Okamoto. Molecular fluorescence from ZnTBP porphyrin molecular layers on Cu(100) induced by tunnelling currents. *Nanotech.*, 15(6):S402–S405, 2004.

[64] X.L. Guo, Z. C. Dong, A.S. Trifonv, K. Miki, K. Kimura, and S. Mashiko. STM-induced molecular fluorescence from porphyrin molecules on metal substrates. *Appl. Phys. A*, 81:367–370, 2005.

[65] H. Liu, R. Nishitani, Y. Ie, T. Yoshinobu, Y. Aso, and H. Iwasaki. Scanning tunneling microscope (STM)-excited molecular fluorescence from porphyrin thin films. *Jpn. J. Appl. Phys.*, 44(18):566–569, 2005.

[66] H. Liu, Y. Ie, T. Yoshinobu, Y. Aso, and H. Iwasaki. Plasmon-enhanced molecular fluorescence from an organic film in a tunnel junction. *Appl. Phys. Lett.*, 88:061901–1–3, 2006.

[67] H. W. Liu, Y. Ie, R. Nishitani, Y. Aso, and H. Iwasaki. Bias dependence of tunneling-electron-induced molecular fluorescence from porphyrin films on noble-metal substrates. *Phys. Rev. B*, 75(11):115429, 2007.

[68] T. Uemura, M. Furumoto, T. Nakano, M. Akai-Kasaya, A. Saito, M. Aono, and Y. Kuwahara. Local-plasmon-enhanced up-conversion fluorescence from copper phthalocyanine. *Chem. Phys. Lett.*, 448(4–6):232–236, 2007.

[69] H. W. Liu, R. Nishitani, T. Z. Han, Y. Ie, Y. Aso, and H. Iwasaki. STM fluorescence of porphyrin enhanced by a strong plasmonic field and its nanoscale confinement in an STM cavity. *Phys. Rev. B*, 79(12):125415, 2009.

[70] E. Ćavar, M.-C. Blüm, M. Pivetta, F. Patthey, M. Chergui, and W.-D. Schneider. Fluorescence and phosphorescence from individual C$_{60}$ molecules excited by local electron tunneling. *Phys. Rev. Lett.*, 95(19):196102, 2005.

[71] G. Reecht, F. Scheurer, V. Speisser, Y. J. Dappe, F. Mathevet, and G. Schull. Electroluminescence of a polythiophene molecular wire suspended between a metallic surface and the tip of a scanning tunneling microscope. *Phys. Rev. Lett.*, 112:047403, 2014.

[72] G. Hoffmann, R. Berndt, and P. Johansson. Two-electron photon emission from metallic quantum wells. *Phys. Rev. Lett.*, 90(4):046803, 2003.

[73] A. Kabakchiev. *Scanning tunneling luminescence of pentacene nanocrystals.* PhD thesis, Ecole Polytechnique Fédeéral de Lausanne, 2010.

[74] Theresa Lutz. *Scanning tunneling microscopy and luminescence of individual nanostructures.* PhD thesis, Ecole Polytechnique Fédeéral de Lausanne, 2011.

[75] M. Vogelgesang. *Ultrathin KCl films on Cu(110) and Cu(111) studied by low-temperature scanning tunnelling microscopy.* PhD thesis, Ecole Polytechnique Fédeéral de Lausanne, 2005.

[76] J. Hoffman. *A search for alternative electronic order in the high temperature superconductor $Bi_2Sr_2CaCu_2O_{8+\delta}$ by scanning tunneling microscopy.* PhD thesis, University of California, Berkeley, 2003.

[77] K. Kuhnke, A. Kabakchiev, W. Stiepany, F. Zinser, R. Vogelgesang, and K. Kern. Versatile optical access to the tunnel gap in a low-temperature scanning tunneling microscope. *Rev. Sci. Instr.*, 81(11):113102, 2010.

[78] Lake Shore Cryotronics Inc. http://www.lakeshore.com/products/cryogenic-accessories/cable/pages/specifications.aspx, 2015.

[79] K. Kuhnke, A. Kabakchiev, T. Lutz, and K. Kern. Electroluminescence properties of organic nanostructures studied by scanning tunnelling microscopy. *Phys. Stat. Sol. B*, 249(4):644–652, 2012.

[80] K. A. McGee and K. R. Mann. Selective low-temperature syntheses of facial and meridional tris-cyclometalated iridium(III) complexes. *Inorg. Chem.*, 49(19):7800–7809, 2007.

[81] M. Nonoyama. Benzo[h]quinolin-10-yl-n iridium(III) complexes. *Bull. Chem. Soc. Jpn.*, 47(3):767–768, 1974.

[82] R. Berndt and J. K. Gimzewski. Electromagnetic interactions of metallic objects in nanometer proximity. *Phys. Rev. Lett.*, 71(21):3493–3496, 1993.

[83] S. Krause, L. Berbil-Bautista, G. Herzog, M. Bode, and R. Wiesendanger. Current-induced magnetization switching with a spin-polarized scanning tunneling microscope. *Science*, 317(5844):1537–1540, 2007.

[84] S. Loth, S. Baumann, C. P. Lutz, D. M. Eigler, and A. Heinrich. Bistability in atomic-scale antiferromagnets. *Science*, 335(6065):196–199, 2012.

[85] A. A. Khajetoorians, B. Baxevanis, C. Hübner, T. Schlenk, S. Krause, T. O. Wehling, S. Lounis, A. Lichtenstein, D. Pfannkuche, J. Wiebe, and R. Wiesendanger. Current-driven spin dynamics of artificially constructed quantum magnets. *Science*, 339(6115):55–59, 2013.

[86] S. Yoshida, M. Yokota, O. Takeuchi, H. Oigawa, Y. Mera, and H. Shigekawa. Single-atomic-level probe of transient carrier dynamics by laser-combined scanning tunneling microscopy. *Appl. Phys. Exp.*, 6(3):032401, 2013.

[87] Y. Sainoo, Y. Kim, T. Okawa, T. Komeda, H. Shigekawa, and M. Kawai. Excitation of molecular vibrational modes with inelastic scanning tunneling microscopy processes: Examination through action spectra of cis-2-butene on Pd(110). *Phys. Rev. Lett.*, 95(24):246102, 2005.

[88] M. Mehlhorn, H. Gawronski, and K. Morgenstern. Diffusion and dimer formation of CO molecules induced by femtosecond laser pulses. *Phys. Rev. Lett.*, 104(7):076101, 2010.

[89] T. Kumagai, A. Shiotari, H. Okuyama, S. Hatta, T. Aruga, I. Hamada, T. Frederiksen, and H. Ueba. H-atom relay reactions in real space. *Nature Mat.*, 11(2):167–172, 2012.

[90] A. van Houselt and H. J. W. Zandvliet. Colloquium: Time-resolved scanning tunneling microscopy. *Rev. Mod. Phys.*, 82(2):1593–1605, 2010.

[91] M. R. Kan, D. C. Fortin, E. Finley, K. M. Cheng, M. R. Freeman, and W. K. Hiebert. Super-rolloff electron tunneling transduction of nanomechanical motion using frequency downmixing. *Appl. Phys. Lett.*, 97(25):253108, 2010.

[92] G. M. Steeves, A. Y. Elezzabi, R. Teshima, R. A. Said, and M. R. Freeman. Circuit analysis of an ultrafast junction mixing scanning tunneling microscope. *IEEE J. Quantum Electron.*, 34(8):1415–1418, 1998.

[93] C. Saunus, J. R. Bindel, M. Pratzer, and M. Morgenstern. Versatile scanning tunneling microscopy with 120 ps time resolution. *Appl. Phys. Lett.*, 102(5):051601, 2013.

[94] I. Moult, M Herve, and Y. Pennec. Ultrafast spectroscopy with a scanning tunneling microscope. *Appl. Phys. Lett.*, 98(23):233103, 2011.

[95] T. L. Cocker, V. J. Jelic, M. Gupta, S. J. Molesky, J. A. J. Burgess, G. de Los Reyes, L. V. Titova, Y. Y. Tsui, M. R. Freeman, and F. A. Hegmann. An ultrafast terahertz scanning tunneling microscope. *Nature Phot.*, 7:620, 2013.

[96] C. Grosse, M. Etzkorn, K. Kuhnke, S. Loth, and K. Kern. Quantitative mapping of fast voltage pulses in tunnel junctions by plasmonic luminescence. *Appl. Phys. Lett.*, 103, 2013.

[97] A. M. Weiner, J. P. Heritage, and E. M. Kirschner. High-resolution femtosecond pulse shaping. *J. Opt. Soc. Am. B*, 5(8):1563–1572, 1988.

[98] R. F. H. Fischer. *Precoding and Signal Shaping for Digital Transmission.* John Wiley & Sons, New York, 2002.

[99] H. W. Kroto, J. R. Heath, S. C. Obrien, R. F. Curl, and R. E. Smalley. C_{60}: Buckminsterfullerene. *Nature*, 318(6042):162–163, 1985.

[100] W. Krätschmer, L. Lamb, K. Fostiropoulos, and D. R. Huffman. Solid C_{60}: A new form of carbon. *Nature*, 347, 1990.

[101] A. F. Hebard, R. C. Rosseinsky, M. J.and Haddon, D. W. Murphy, S. H. Glarum, T. T. M. Palstra, A. P. Ramirez, and A. R. Kortan. Superconductivity at 18 K in potassium-doped C_{60}. *Nature*, 350:600–601, 1991.

[102] S. Bommel, N. Kleppmann, C. Weber, H. Spranger, P. Schäfer, J. Novak, S. V. Roth, F. Schreiber, S. Klapp, and S. Kowarik. Unravelling the multilayer growth of the fullerene C_{60} in real time. *Nature Comm.*, 2014.

[103] H. Park, J. Park, A. K. L. Lim, E. H. Anderson, A. P. Alivisatos, and P. L. McEuen. Nanomechanical oscillations in a single-C_{60} transistor. *Nature*, 407(6800):57–60, 2000.

[104] C. B. Winkelmann, N. Roch, W. Wernsdorfer, V. Bouchiat, and F. Balestro. Superconductivity in a single-C_{60} transistor. *Nat. Phys.*, 5:876–879, 2009.

[105] M. Arndt, O. Nairz, J. Vos-Andreae, C. Keller, G. van der Zouw, and A. Zeilinger. Wave-particle duality of C_{60} molecules. *Nature*, 401:680–682, 1999.

[106] E. W. Godly and R. Taylor. Nomenclature and terminology of fullerenes: A preliminary survey. *Pure & Appl. Chem.*, 69:1411–1434, 1997.

[107] W. I. F. David, R. M. Ibberson, J. C. Matthewman, K. Prassides, T. J. S. Dennis, J. P. Hare, H. W. Kroto, R. Taylor, and D. R. M. Walton. Crystal-structure and bonding of ordered C_{60}. *Nature*, 353(6340):147–149, 1991.

[108] M. Dresselhaus, G. Dresselhaus, and P. Eklund. *Science of Fullerenes and Carbon Nanotubes*. Academic Press Inc., San Diego, California, USA, 1996.

[109] P. A. Heiney, J. E. Fischer, A. R. McGhie, W. J. Romanow, A. M. Denenstein, J. P. McCauley, A. B. Smith, and D. E. Cox. Orientational ordering transition in solid C_{60}. *Phys. Rev. Lett.*, 66(22):2911–2914, 1991.

[110] W. I. F. David, R. M. Ibberson, T. J. S. Dennis, J. P. Hare, and K. Prassides. Strucutural phase-transition in fullerene C_{60}. *Europhys. Lett.*, 18(3):219–225, 1992.

[111] L. Pintschovius, S. L. Chaplot, G. Roth, M. Haluska, and H. Kuzmany. Diffuse neutron scattering study of the rotational disorder in solid C_{60}. *Phys. Script.*, 1995(T57):102, 1995.

[112] O. Blaschko, G. Krexner, C. Maier, and R. Karawatzki. Determination of molecular orientational angles in the low-temperature phase of C_{60}. *Phys. Rev. B*, 56:2288–2291, 1997.

[113] K.-P. Bohnen and R. Heid. *Ab Initio* intermolecular potential of solid C_{60} in the low-temperature phase. *Phys. Rev. Lett.*, 83:1167–1170, 1999.

[114] M. Hasegawa, K. Nishidate, M. Katayama, and T. Inaoka. Intermolecular potential and the equation of state of solid C_{60}. *J. Chem. Phys.*, 119(3):1386–1396, 2003.

[115] P. J. Benning, F. Stepniak, and J. H. Weaver. Electron-diffraction and photoelectron-spectroscopy studies of fullerene and alkali-metal fulleride films. *Phys. Rev. B*, 48:9086–9096, 1993.

[116] A. Goldoni, C. Cepek, and S. Modesti. First-order orientational-disordering transition on the (111) surface of C_{60}. *Phys. Rev. B*, 54:2890–2895, 1996.

[117] A. Glebov, V. Senz, J. P. Toennies, and G. Gensterblum. Rotational-disordering phase transition of C_{60}(111) epitaxial films grown on GeS(001). *J. Appl. Phys.*, 82(5):2329–2333, 1997.

[118] W. I. F. David, R. M. Ibberson, and T. Matsuo. High-resolution neutron powder diffraction – A case-study of the structure of C_{60}. *Proc. R. Soc. Lond. A*, 442(1914):129–146, 1993.

[119] Y. Z. Li, J. C. Patrin, M. Chander, J. H. Weaver, L. P. F. Chibante, and R. E. Smalley. Ordered overlayer of C_{60} on GaAs(110) studied with scanning tunneling microscopy. *Science*, 252(5005):547–548, 1991.

[120] T. Hashizume, Wang X.-D., Y. Nishina, H. Shinohara, Y. Saito, Y. Kuk, and T. Sakurai. Field ion-scanning tunneling microscopy study of C_{60} on the Si(100) surface. *Jpn. J. Appl. Phys.*, 31(7A):L880, 1992.

[121] H. Wang, C. Zeng, Q. Li, B. Wang, J. Yang, J. G. Hou, and Q. Zhu. Scanning tunneling spectroscopy of individual C_{60} molecules adsorbed on Si(111)-7 × 7 surface. *Surf. Sci.*, 442(2):L1024–L1028, 1999.

[122] J. G. Hou, J. Yang, H. Wang, Q. Li, C. Zeng, H. Lin, W. Bing, D. M. Chen, and Q. Zhu. Identifying molecular orientation of individual C_{60} on a Si(111)-(7 × 7) surface. *Phys. Rev. Lett.*, 83:3001–3004, 1999.

[123] J. I. Pascual, J. Gómez-Herrero, C. Rogero, A. M. Baró, D. Sónchez-Portal, E. Artacho, P. Ordejón, and J. M. Soler. Seeing molecular orbitals. *Chem. Phys. Lett.*, 321(1-2):78–82, 2000.

[124] H. Q. Wang, C. G. Zeng, B. Wang, J. G. Hou, Q. X. Li, and J. L. Yang. Orientational configurations of the C_{60} molecules in the (2×2) superlattice on a solid $C_{60}(111)$ surface at low temperature. *Phys. Rev. B*, 63(8), 2001.

[125] U. D. Schwarz, W. Allers, G. Gensterblum, J.-J. Pireaux, and R. Wiesendanger. Growth of C_{60} thin films on GeS(001) studied by scanning force microscopy. *Phys. Rev. B*, 52:5967–5976, 1995.

[126] D. Zhao, T. Chen, and L. Wang. Observation of electronic correlation effect in C_{60} adsorbed on an (0001) surface of $2H\text{-}MoS_2$ by scanning tunneling microscopy. *Appl. Phys. Lett.*, 66(24):3292–3294, 1995.

[127] R. Schwedhelm, J.-P. Schlomka, S. Woedtke, R. Adelung, L. Kipp, M. Tolan, W. Press, and M. Skibowski. Epitaxial thin-film growth of C_{60} on VSe_2 studied with scanning tunneling microscopy and x-ray diffraction. *Phys. Rev. B*, 59:13394–13400, 1999.

[128] F. Rossel, M. Pivetta, F. Patthey, E. Ćavar, A. P. Seitsonen, and W.-D. Schneider. Growth and characterization of fullerene nanocrystals on NaCl/Au(111). *Phys. Rev. B*, 84(7):075426, 2011.

[129] T. Hashizume, K. Motai, X. D. Wang, H. Shinohara, Y. Saito, Y. Maruyama, K. Ohno, Y. Kawazoe, Y. Nishina, H. W. Pickering, Y. Kuk, and T. Sakurai. Intramolecular structures of C_{60} molecules adsorbed on the Cu(111)-(1×1) surface. *Phys. Rev. Lett.*, 71:2959–2962, 1993.

[130] K. Motai, T. Hashizume, H. Shinohara, Y. Saito, H. W. Pickering, Y. Nishina, and T. Sakurai. C_{60} grown on the Cu(111) 1×1 surface. *Jpn. J. Appl. Phys.*, 32(3B):L450, 1993.

[131] J. K. Gimzewski, S. Modesti, T. David, and R. R. Schlittler. Scanning-tunneling-microscopy of ordered C_{60} and C_{70} layers on Au(111), Cu(111), Ag(110), and Au(110) surfaces. *J. Vac. Sci. Technol. B*, 12(3):1942–1946, 1994.

[132] T. Sakurai, X. D. Wang, T. Hashizume, V. Yurov, H. Shinohara, and H. W. Pickering. Adsorption of fullerenes on Cu(111) and Ag(111) surfaces. *Appl. Surf. Sci.*, 87-88(0):405–413, 1995.

[133] T. Hashizume and T. Sakurai. Fullerenes adsorption on Cu(111) and Ag(111) surfaces. *Surf. Rev. Lett.*, 3(1):905–913, 1996.

[134] W. W. Pai, C.-L. Hsu, M. C. Lin, K. C. Lin, and T. B. Tang. Structural relaxation of adlayers in the presence of adsorbate-induced reconstruction: C_{60}/Cu(111). *Phys. Rev. B*, 69:125405, 2004.

[135] J. A. Larsson, S. D. Elliott, J. C. Greer, J. Repp, G. Meyer, and R. Allenspach. Orientation of individual C_{60} molecules adsorbed on Cu(111): Low-temperature scanning tunneling microscopy and density functional calculations. *Phys. Rev. B*, 77:115434, 2008.

[136] E. I. Altman and R. J. Colton. Determination of the orientation of C_{60} adsorbed on Au(111) and Ag(111). *Phys. Rev. B*, 48(24):18244–18249, 1993.

[137] E. I. Altman and R. J. Colton. The interaction of C_{60} with noble metal surfaces. *Surf. Sci.*, 295(1-2):13–33, 1993.

[138] J. K. Gimzewski, S. Modesti, and R. R. Schlittler. Cooperative self-assembly of Au atoms and C_{60} on Au(110) surfaces. *Phys. Rev. Lett.*, 72:1036–1039, 1994.

[139] T. David, J. K. Gimzewski, D. Purdie, B. Reihl, and R. R. Schlittler. Epitaxial growth of C_{60} on Ag(110) studied by scanning tunneling microscopy and tunneling spectroscopy. *Phys. Rev. B*, 50:5810–5813, 1994.

[140] M. Grobis, X. Lu, and M. F. Crommie. Local electronic properties of a molecular monolayer: C_{60} on Ag(001). *Phys. Rev. B*, 66(16), 2002.

[141] J. I. Pascual, J. Gómez-Herrero, D. Sánchez-Portal, and H.-P. Rust. Vibrational spectroscopy on single C_{60} molecules: The role of molecular orientation. *J. Chem. Phys.*, 117(21):9531–9534, 2002.

[142] X. Lu, M. Grobis, K. H. Khoo, S. G. Louie, and M. F. Crommie. Spatially mapping the spectral density of a single C_{60} molecule. *Phys. Rev. Lett.*, 90(9):096802, 2003.

[143] X. Lu, M. Grobis, K. H. Khoo, S. G. Louie, and M. F. Crommie. Charge transfer and screening in individual C_{60} molecules on metal substrates: A scanning tunneling spectroscopy and theoretical study. *Phys. Rev. B*, 70:115418, 2004.

[144] K. Pussi, H. I. Li, Heekeun Shin, L. N. Serkovic Loli, A. K. Shukla, J. Ledieu, V. Fournée, L. L. Wang, S. Y. Su, K. E. Marino, M. V. Snyder, and R. D. Diehl. Elucidating the dynamical equilibrium of C_{60} molecules on Ag(111). *Phys. Rev. B*, 86:205406, 2012.

[145] E. I. Altman and R. J. Colton. Nucleation, growth, and structure of fullerene films on Au(111). *Surf. Sci.*, 279(1–2):49–67, 1992.

[146] R. Gaisch, R. Berndt, J. K. Gimzewski, B. Reihl, R. R. Schlittler, W. D. Schneider, and M. Tschudy. Internal structure of C_{60} fullerence molecules as revealed by low-temperature STM. *Appl. Phys. A*, 57(2):207–210, 1993.

[147] C. Rogero, J. I. Pascual, J. Gómez-Herrero, and A. M. Baró. Resolution of site-specific bonding properties of C_{60} adsorbed on Au(111). *J. Chem. Phys.*, 116(2):832–836, 2002.

[148] M. Grobis, A. Wachowiak, R. Yamachika, and M. F. Crommie. Tuning negative differential resistance in a molecular film. *Appl. Phys. Lett.*, 86:204102, 2005.

[149] G. Schull and R. Berndt. Orientationally ordered (7×7) superstructure of C_{60} on Au(111). *Phys. Rev. Lett.*, 99:226105, 2007.

[150] X. Zhang, F. Yin, R. E. Palmer, and Q. Guo. The C_{60}/Au(111) interface at room temperature: A scanning tunnelling microscopy study. *Surf. Sci.*, 602(4):885–892, 2008.

[151] G. Schull, N. Néel, M. Becker, J. Kroeger, and R. Berndt. Spatially resolved conductance of oriented C_{60}. *New. J. Phys.*, 10, 2008.

[152] I. F. Torrente, K. J. Franke, and J. I. Pascual. Spectroscopy of C_{60} single molecules: The role of screening on energy level alignment. *J. Phys.: Condens. Mat.*, 20(18), 2008.

[153] J. A. Gardener, G. A. D. Briggs, and M. R. Castell. Scanning tunneling microscopy studies of C_{60} monolayers on Au(111). *Phys. Rev. B*, 80:235434, 2009.

[154] X. Zhang, L. Tang, and Q. Guo. Low-temperature growth of C_{60} monolayers on Au(111): island orientation control with site-selective nucleation. *J. Phys. Chem. C*, 114(14):6433–6439, 2010.

[155] L. Tang, Y. Xie, and Q. Guo. Complex orientational ordering of C_{60} molecules on Au(111). *J. Chem. Phys.*, 135(11), 2011.

[156] L. Tang and Q. Guo. Orientational ordering of the second layer of C_{60} molecules on Au(111). *Phys. Chem. Chem. Phys.*, 14:3323–3328, 2012.

[157] H. Shin, A. Schwarze, R. D. Diehl, K. Pussi, A. Colombier, É. Gaudry, J. Ledieu, G. M. McGuirk, L. N. Serkovic Loli, V. Fournée, L. L. Wang, G. Schull, and R. Berndt. Structure and dynamics of C_{60} molecules on Au(111). *Phys. Rev. B*, 89:245428, 2014.

[158] C. Wöll, S. Chiang, R. J. Wilson, and P. H. Lippel. Determination of atom positions at stacking-fault dislocations on Au(111) by scanning tunneling microscopy. *Phys. Rev. B*, 39:7988–7991, 1989.

[159] L.-L. Wang and H.-P. Cheng. Rotation, translation, charge transfer, and electronic structure of C_{60} on Cu(111) surface. *Phys. Rev. B*, 69:045404, 2004.

[160] L.-L. Wang and H.-P. Cheng. Density functional study of the adsorption of a C_{60} monolayer on Ag(111) and Au(111) surfaces. *Phys. Rev. B*, 69(16):165417, 2004.

[161] I. Hamada and M. Tsukada. Adsorption of C_{60} on Au(111) revisited: A van der Waals density functional study. *Phys. Rev. B*, 83(24), 2011.

[162] A. Fartash. Interfacially ordered C_{60} films on Cu(111) substrates. *J. Appl. Phys.*, 79(2):742–747, 1996.

[163] H. I. Li, K. Pussi, K. J. Hanna, L.-L. Wang, D. D. Johnson, H.-P. Cheng, H. Shin, S. Curtarolo, W. Moritz, J. A. Smerdon, R. McGrath, and R. D. Diehl. Surface geometry of C_{60} on Ag(111). *Phys. Rev. Lett.*, 103:056101, 2009.

[164] A. Fartash. Orientational epitaxy of high-quality C_{60} films on Ag(111). *Phys. Rev. B*, 52:7883–7886, 1995.

[165] A. Fartash. Growth and interfacial evolution of oriented C_{60} overlayers on Au(111). *Appl. Phys. Lett.*, 67(26):3901–3903, 1995.

[166] A. Fartash. In-plane orientational order across $C_{60}(111)/Au(111)$ interfaces. *Thin Solid Films*, 323(1–2):296–303, 1998.

[167] C.-T. Tzeng, W.-S. Lo, J.-Y. Yuh, R.-Y. Chu, and K.-D. Tsuei. Photoemission, near-edge x-ray-absorption spectroscopy, and low-energy electron-diffraction study of C_{60} on Au(111) surfaces. *Phys. Rev. B*, 61:2263–2272, 2000.

[168] J. D. Sau, J. B. Neaton, H. J. Choi, S. G. Louie, and M. L. Cohen. Electronic energy levels of weakly coupled nanostructures: C_{60}-metal interfaces. *Phys. Rev. Lett.*, 101:026804, 2008.

[169] M. de Menech, U. Saalmann, and M. E. Garcia. Energy-resolved STM mapping of C_{60} on metal surfaces: A theoretical study. *Phys. Rev. B*, 73:155407, 2006.

[170] U. Zerweck, C. Loppacher, T. Otto, S. Grafström, and L. M. Eng. Kelvin probe force microscopy of C_{60} on metal substrates: Towards molecular resolution. *Nanotechn.*, 18(8):084006, 2007.

[171] G. Schull, T. Frederiksen, M. Brandbyge, and R. Berndt. Passing current through touching molecules. *Phys. Rev. Lett.*, 103:206803, 2009.

[172] L. H. Tjeng, R. Hesper, A. C. L. Heessels, A. Heeres, H. T. Jonkman, and G.A. Sawatzky. Development of the electronic structure in a K-doped C_{60} monolayer on a Ag(111) surface. *Sol. State Comm.*, 103(1):31–35, 1997.

[173] R. Hesper, L. H. Tjeng, and G. A. Sawatzky. Strongly reduced band gap in a correlated insulator in close proximity to a metal. *Europhys. Lett.*, 40(2):177, 1997.

[174] G. K. Wertheim and D. N. E. Buchanan. Interfacial reaction of C_{60} with silver. *Phys. Rev. B*, 50:11070–11073, 1994.

[175] K.-D. Tsuei, J.-Y. Yuh, C.-T. Tzeng, R.-Y. Chu, S.-C. Chung, and K.-L. Tsang. Photoemission and photoabsorption study of C_{60} adsorption on Cu(111) surfaces. *Phys. Rev. B*, 56:15412–15420, 1997.

[176] T. Kobayashi, C. Tindall, Takaoka O., Y. Hasegawa, and T. Sakurai. Charge-transfer of C_{60} on Cu(111) measured using an STM HREELS system. *J. Kor. Phys. Soc.*, 31, 1997.

[177] T. R. Ohno, Y. Chen, S. E. Harvey, G. H. Kroll, J. H. Weaver, R. E. Haufler, and R. E. Smalley. C_{60} bonding and energy-level alignment on metal and semiconductor surfaces. *Phys. Rev. B*, 44:13747–13755, 1991.

[178] S. J. Chase, W. S. Bacsa, M. G. Mitch, L. J. Pilione, and J. S. Lannin. Surface-enhanced Raman scattering and photoemission of C_{60} on noble-metal surfaces. *Phys. Rev. B*, 46:7873–7877, 1992.

[179] E. Magnano, S. Vandré, C. Cepek, A. Goldoni, A. D. Laine, G.M. Curró, A. Santaniello, and M. Sancrotti. Substrate–adlayer interaction at the C_{60}/Ag(110) interface studied by high-resolution synchrotron radiation. *Surf. Sci.*, 377–379(0):1066–1070, 1997.

[180] M. Pedio, M. L. Grilli, C. Ottaviani, M. Capozi, C. Quaresima, P. Perfetti, P. A. Thiry, R. Caudano, and P. Rudolf. Inverse photoemission studies of C_{60} on Au(110). *J. Elec. Spectr. Rel. Phen.*, 76(0):405–409, 1995.

[181] G. Dutton, D. P. Quinn, C. D. Lindstrom, and X.-Y. Zhu. Exciton dynamics at molecule-metal interfaces: C_{60}/Au(111). *Phys. Rev. B*, 72:045441, 2005.

[182] N. A. Pradhan, N. Liu, C. Silien, and W. Ho. Atomic scale conductance induced by single impurity charging. *Phys. Rev. Lett.*, 94(7):076801, 2005.

[183] O. Gunnarsson. *Alkali-doped fullerides – Narrow-band solids with unusual properties.* World Scientific, Singapore, 2004.

[184] O. Gunnarsson, S. Satpathy, O. Jepsen, and O. K. Andersen. Orientation of C_{60} clusters in solids. *Phys. Rev. Lett.*, 67:3002–3005, 1991.

[185] O. Gunnarsson, S. C. Erwin, E. Koch, and R. M. Martin. Role of alkali atoms in A_4C_{60}. *Phys. Rev. B*, 57:2159–2162, 1998.

[186] J. C. Slater. Atomic shielding constants. *Phys. Rev.*, 36:57–64, 1930.

[187] K. Sakamoto, K. Meguro, R. Arafune, M. Satoh, Y. Uehara, and S. Ushioda. Light emission spectra of the monolayer-island of C_{60} molecules on Au(111) induced by scanning tunneling microscope. *Surf. Sci.*, 502:149–155, 2002.

[188] F. Rossel, M. Pivetta, and W.-D. Schneider. Luminescence experiments on supported molecules with the scanning tunneling microscope. *Surf. Sci. Reports*, 65(5):129, 2010.

[189] F. Geng, Y. Zhang, Y. Yu, Y. Kuang, Y. Liao, Z. Dong, and J. Hou. Modulation of nanocavity plasmonic emission by local molecular state sof C_{60} on Au(111). *Opt. Exp.*, 20(24):26725–26735, 2012.

[190] P. Merino, C. Große, A. Roslawska, K. Kuhnke, and K. Kern. Exciton dynamics of 60-based single photon emitters explored by hanbury brown-twiss scanning tunneling microscopy. *(submitted)*.

[191] P. Heimann, H. Neddermeyer, and H. F. Roloff. Ultraviolet photoemission for intrinsic surface states of the noble metals. *J. Phys. C*, 10(1):L17, 1977.

[192] C. Reber, L. Yee, J. McKiernan, J. I. Zink, R. S. Williams, W. M. Tong, D. A. A. Ohlberg, R. L. Whetten, and F. Diederich. Luminescence and absorption spectra of carbon C_{60} films. *J. Phys. Chem.*, 95(6):2127–2129, 1991.

[193] N. L. Schneider and R. Berndt. Plasmonic excitation of light emission and absorption by porphyrine molecules in a scanning tunneling microscope. *Phys. Rev. B*, 86:035445, 2012.

[194] G. Tian and Y. Luo. Fluorescence and phosphorescence of single C_{60} molecules as stimulated by a scanning tunneling microscope. *Ang. Chem. Int. Ed.*, 52(18):4814–4817, 2013.

[195] P. A. Lane, L. S. Swanson, Q.-X. Ni, J. Shinar, J. P. Engel, T. J. Barton, and L. Jones. Dynamics of photoexcited states in C_{60}: An optically detected magnetic resonance, ESR, and light-induced ESR study. *Phys. Rev. Lett.*, 68:887–890, 1992.

[196] C. Kurtsiefer, S. Mayer, P. Zarda, and H. Weinfurter. Stable solid-state source of single photons. *Phys. Rev. Lett.*, 85:290–293, 2000.

[197] R. Brouri, A. Beveratos, J. P. Poizat, and P. Grangier. Photon antibunching in the fluorescence of individual color centers in diamond. *Opt. Lett.*, 25(17):1294–1296, 2000.

[198] R. Hanbury Brown and R. Q. Twiss. A test of a new type of stellar interferometer on sirius. *Nature*, 178:1046–1048, 1956.

[199] Loudon R. *The quantum theory of light.* Oxford University Press, third edition, 2000.

[200] D. J. van den Heuvel, I. Y. Chan, E. J. J. Groenen, J. Schmidt, and G. Meijer. Phosphorescence of C_{60} at 1.2 K. *Chem. Phys. Lett.*, 231(1):111–118, 1994.

[201] C. W. Marquardt, S. Grunder, A. Blaszczyk, S. Dehm, F. Hennrich, H. v. Löhneysen, M. Mayor, and R. Krupke. Electroluminescence from a single nanotube–molecule–nanotube junction. *Nature Nano.*, 5:863–867, 2010.

[202] K. A. King, P. J. Spellane, and R. J. Watts. Excited-state properties of a triply ortho-metalated iridium(III) complex. *J. Am. Chem. Soc.*, 107(5):1431–1432, 1985.

[203] M. A. Baldo, S. Lamansky, P. E. Burrows, M. E. Thompson, and S. R. Forrest. Very high-efficiency green organic light-emitting devices based on electrophosphorescence. *Appl. Phys. Lett.*, 75(1):4–6, 1999.

[204] R. J. F. Berger, H.-G. Stammler, B. Neumann, and N. W. Mitzel. *fac*-Ir(ppy)$_3$: Structures in the gas-phase and of a new solid modification. *Eur. J. Inorg. Chem.*, 2010(11):1613–1617, 2010.

[205] W. Holzer, A. Penzkofer, and T. Tsuboi. Absorption and emission spectroscopic characterization of Ir(ppy)$_3$. *Chem. Phys.*, 308(1–2):93–102, 2005.

[206] W. J. Finkenzeller and H. Yersin. Emission of Ir(ppy)$_3$. Temperature dependence, decay dynamics, and magnetic field properties. *Chem. Phys. Lett.*, 377(3–4):299–305, 2003.

[207] A. J. Mäkinen, I. G. Hill, and Z. H. Kafafi. Vacuum level alignment in organic guest–host systems. *J. Appl. Phys.*, 92(3):1598–1603, 2002.

[208] P. J. Hay. Theoretical studies of the ground and excited electronic states in cyclometa-lated phenylpyridine Ir(III) complexes using density functional theory. *J. Phys. Chem. A*, 106(8):1634, 2002.

[209] N. G. Park, G. C. Choi, Y. H. Lee, and Y. S. Kim. Theoretical studies on the ground and excited states of blue phosphorescent cyclometalated Ir(III) complexes having ancillary ligand. *Curr. Appl. Phys.*, 6(4):620–626, 2006.

[210] K. Nozaki. Theoretical studies on photophysical properties and mechanism of phosphorescence in [*fac*-Ir(2-phenylpyridine)$_3$]. *J. Chin. Chem. Soc.*, 53(1):101–112, 2006.

[211] E. Jansson, B. Minaev, S. Schrader, and H. Ågren. Time-dependent density functional calculations of phosphorescence parameters for *fac*-tris(2-phenylpyridine) iridium. *Chem. Phys.*, 333(2–3):157–167, 2007.

[212] J. Fine, K. Diri, A.I. Krylov, C. Nemirow, Z. Lu, and C. Wittig. Electronic structure of tris(2-phenylpyridine)iridium: Electronically excited and ionized states. *Mol. Phys.*, 110(15–16):1849–1862, 2012.

[213] F. Neese. The ORCA program system. *WIREs Comput. Mol. Sci.*, 2(1):73–78, 2012.

[214] A. D. Becke. Density-functional thermochemistry. III. The role of exact exchange. *J. Chem. Phys.*, 98(7):5648–5652, 1993.

[215] P. J. Hay and W. R. Wadt. Ab initio effecitve core potentials for molecular calculations – potentials for K to Au including the outermost core orbitals. *J. Chem. Phys.*, 82(1):12, 1985.

[216] R. Krishnan, J.S. Binkley, R. Seeger, and J.A. Pople. Self-consistent molecular-orbital methods. XX. A basis set for correlated wave functions. *J. Chem. Phys.*, 72(1):650–654, 1980.

[217] T. Yokoyama, T. Takahashi, K. Shinozaki, and M. Okamoto. Quantitative analysis of long-range interactions between adsorbed dipolar molecules on Cu(111). *Phys. Rev. Lett.*, 98:206102, 2007.

[218] T. Yokoyama, T. Takahashi, and K. Shinozaki. Surface diffusion of Ir(ppy)$_3$ on Cu(111). *Phys. Rev. B*, 82:155414, 2010.

[219] H. Ishii, K. Sugiyama, E. Ito, and K. Seki. Energy level alignment and interfacial electronic structures at organic/metal and organic/organic interfaces. *Adv. Mat.*, 11(8):605–625, 1999.

[220] I. Campbell, S. Rubin, T. Zawodzinski, J. Kress, R. Martin, D. Smith, N. Barashkov, and J. Ferraris. Controlling Schottky energy barriers in organic electronic devices using self-assembled monolayers. *Phys. Rev. B*, 54:R14321–R14324, 1996.

[221] S. W. Wu, G. V. Nazin, X. Chen, X. H. Qiu, and W. Ho. Control of relative tunneling rates in single molecule bipolar electron transport. *Phys. Rev. Lett.*, 93(23):236802, 2004.

[222] N. Liu, N. A. Pradhan, and W. Ho. Vibronic states in single molecules: C$_{60}$ and C$_{70}$ on ultrathin Al$_2$O$_3$ films. *J. Chem. Phys.*, 120(24):11371–11375, 2004.

[223] X. H. Qiu, G. V. Nazin, and W. Ho. Vibronic states in single molecule electron transport. *Phys. Rev. Lett.*, 92:206102, 2004.

[224] I. G. Rau, S. Baumann, S. Rusponi, F. Donati, S. Stepanow, L. Gragnaniello, J. Dreiser, C. Piamonteze, F. Nolting, S. Gangopadhyay, O. R. Albertini, R. M. Macfarlane, C. P. Lutz, B. A. Jones, P. Gambardella, A. J. Heinrich, and H. Brune. Reaching the magnetic anisotropy limit of a 3d metal atom. *Science*, 344(6187):988–992, 2014.

[225] J. Repp, G. Meyer, F. E. Olsson, and M. Persson. Controlling the charge state of individual gold adatoms. *Science*, 305(5683):493–495, 2004.

[226] J. Repp, G. Meyer, S. M. Stojkovic, A. Gourdon, and C. Joachim. Molecules on insulating films: Scanning-tunneling microscopy imaging of individual molecular orbitals. *Phys. Rev. Lett.*, 94(2):026803, 2005.

[227] J. Repp, G. Meyer, S. Paavilainen, F. E. Olsson, and M. Persson. Imaging bond formation between a gold atom and pentacene on an insulating surface. *Science*, 312(5777):1196–1199, 2006.

[228] P. Liljeroth, J. Repp, and G. Meyer. Current-induced hydrogen tautomerization and conductance switching of naphthalocyanine molecules. *Science*, 317(5842):1203–1206, 2007.

[229] F. Mohn, J. Repp, L. Gross, G. Meyer, M. S. Dyer, and M. Persson. Reversible bond formation in a gold-atom–organic-molecule complex as a molecular switch. *Phys. Rev. Lett.*, 105:266102, 2010.

[230] C. Uhlmann, I. Swart, and J. Repp. Controlling the orbital sequence in individual Cu-phthalocyanine molecules. *Nano Lett.*, 13(2):777–780, 2013.

[231] S. Kahle, Z. Deng, N. Malinowski, C. Tonnoir, A. Forment-Aliaga, N. Thontasen, G. Rinke, D. Le, V. Turkowski, T. S. Rahman, S. Rauschenbach, M. Ternes, and K. Kern. The quantum magnetism of individual manganese-12-acetate molecular magnets anchored at surfaces. *Nano Lett.*, 12(1):518–521, 2012.

[232] H. Arnolds and M. Bonn. Ultrafast surface vibrational dynamics. *Surf. Sci. Rep.*, 65(2):45–66, 2010.

[233] J. D. Beckerle, R. R. Cavanagh, M. P. Casassa, E. J. Heilweil, and J.C. Stephenson. Subpicosecond transient infrared spectroscopy of adsorbates. Vibrational dynamics of CO/Pt(111). *J. of Chem. Phys.*, 95(7):5403–5418, 1991.

[234] K. Laß, X. Han, and E. Hasselbrink. The surprisingly short vibrational lifetime of the internal stretch of CO adsorbed on Si(100). *J. Chem. Phys.*, 123(5), 2005.

[235] H.-C. Chang and G. E. Ewing. Infrared fluorescence from a monolayer of CO on NaCl(100). *Phys. Rev. Lett.*, 65:2125–2128, 1990.

[236] S. Datta, W. Tian, S. Hong, R. Reifenberger, J. I. Henderson, and C. P. Kubiak. Current-voltage characteristics of self-assembled monolayers by scanning tunneling microscopy. *Phys. Rev. Lett.*, 79:2530–2533, 1997.

[237] G. V. Nazin, X. H. Qiu, and W. Ho. Charging and interaction of individual impurities in a monolayer organic crystal. *Phys. Rev. Lett.*, 95:166103, 2005.

[238] G. V. Nazin, X. H. Qiu, and W. Ho. Vibrational spectroscopy of individual doping centers in a monolayer organic crystal. *J. Chem. Phys.*, 122(18), 2005.

[239] N. A. Pradhan, N. Liu, Ch. Silien, and W. Ho. Tuning the bipolar conductance of an alkali-doped C_{60} layer sandwiched between two tunneling barriers. *Nano Lett.*, 5(1):55–59, 2005.

[240] N.A. Pradhan, Ning Liu, and Wilson Ho. Vibronic spectroscopy of single C_{60} molecules and monolayers with the STM. *J. Phys. Chem. B*, 109(17):8513–8518, 2005.

[241] O. Gunnarsson, H. Handschuh, P. S. Bechthold, B. Kessler, G. Ganteför, and W. Eberhardt. Photoemission spectra of C_{60}^-: Electron-phonon coupling, Jahn-Teller effect, and superconductivity in the fullerides. *Phys. Rev. Lett.*, 74:1875–1878, 1995.

[242] R. W. Lof, M. A. van Veenendaal, B. Koopmans, H. T. Jonkman, and G. A. Sawatzky. Band gap, excitons, and coulomb interaction in solid C_{60}. *Phys. Rev. Lett.*, 68:3924–3927, 1992.

[243] M. B. Jost, N. Troullier, D. M. Poirier, J. L. Martins, J. H. Weaver, L. P. F. Chibante, and R. E. Smalley. Band dispersion and empty electronic states in solid C_{60}: Inverse photoemission and theory. *Phys. Rev. B*, 44:1966–1969, 1991.

[244] R. Zia, J. A. Schuller, A. Chandran, and M. L. Brongersma. Plasmonics: the next chip-scale technology. *Mat. Tod.*, 9(20-27), 2006.

[245] T. W. Ebbesen, C. Genet, and S. I. Bozhevolnyi. Surface-plasmon circuitry. *Phys. Tod.*, 61(5):44–50, 2008.

[246] K. F. MacDonald and N. I. Zheludev. Active plasmonics: current status. *Laser Phot. Rev.*, 4(4):562–567, 2010.

[247] V. J. Sorger, R. F. Oulton, R. M. Ma, and X. Zhang. Toward integrated plasmonic circuits. *Mrs Bulletin*, 37(8):728–738, 2012.

[248] K. V. Nerkararyan. Superfocusing of a surface polariton in a wedge-like structure. *Phys. Lett. A*, 237(1-2):103–105, 1997.

[249] J. Takahara, S. Yamagishi, H. Taki, A. Morimoto, and T. Kobayashi. Guiding of a one-dimensional optical beam with nanometer diameter. *Opt. Lett.*, 22(7):475–477, 1997.

[250] E. Kretschmann and H. Raether. Radiative decay of non radiative surface plasmons excited by light. *Z. Naturforsch. Phys.*, A 23(12):1530–1533, 1968.

[251] A. Otto. Excitation of nonradiative surface plasma waves in silver by methode of frustrated total reflection. *Z. Phys.*, 216(4):398–410, 1968.

[252] R. H. Ritchie, E. T. Arakawa, J. J. Cowan, and R. N. Hamm. Surface-plasmon resonance effect in grating diffraction. *Phys. Rev. Lett.*, 21:1530–1533, 1968.

[253] P. Bharadwaj, B. Deutsch, and L. Novotny. Optical antennas. *Adv. Opt. Phot.*, 1(3):438–483, Nov 2009.

[254] M. V. Bashevoy, F. Jonsson, A. V. Krasavin, N. I. Zheludev, Y. Chen, and M. I. Stockman. Generation of traveling surface plasmon waves by free-electron impact. *Nano Lett.*, 6(6):1113–1115, 2006.

[255] D. Rossouw, M. Couillard, J. Vickery, E. Kumacheva, and G. A. Botton. Generation of traveling surface plasmon waves by free-electron impact. *Nano Lett.*, 11(4):1499–1504, 2011.

[256] T. Lutz, C. Große, C. Dette, A. Kabakchiev, F. Schramm, M. Ruben, R. Gutzler, K. Kuhnke, U. Schlickum, and K. Kern. Molecular orbital gates for plasmon excitation. *Nano Lett.*, 13:2846, 2013.

[257] C. Große, A. Kabakchiev, T. Lutz, R. Froidevaux, F. Schramm, M. Ruben, M. Etzkorn, U. Schlickum, K. Kuhnke, and K. Kern. Dynamic control of plasmon generation by an individual quantum system. *Nano Lett.*, 2014.

[258] D. Ino, T. Yamada, and M. Kawai. Luminescence from 3,4,9,10-perylenetetracarboxylic dianhydride on Ag(111) surface excited by tunneling electrons in scanning tunneling microscopy. *J. Chem. Phys.*, 129(1):014701, 2008.

[259] X. Tao, Z. C. Dong, J. L. Yang, Y. Luo, J. G. Hou, and J. Aizpurua. Influence of a dielectric layer on photon emission induced by a scanning tunneling microscope. *J. Chem. Phys.*, 130(8):084706, 2009.

[260] Y. Zhang, X. Tao, H. Y. Gao, Z. C. Dong, J. G. Hou, and T. Okamoto. Modulation of local plasmon mediated emission through molecular manipulation. *Phys. Rev. B*, 79(7):075406, 2009.

[261] N. L. Schneider, F. Matino, G. Schull, S. Gabutti, M. Mayor, and R. Berndt. Light emission from a double-decker molecule on a metal surface. *Phys. Rev. B*, 84(15):153403, 2011. PRB.

[262] W. Deng, D. Fujita, and T. Ohgi. STM-induced photon emission from self-assembled porphyrin molecules on a Cu(100) surface. *J. Chem. Phys.*, 117(10):4995–5000, 2002.

[263] Z. C. Dong, A. Kar, P. Dorozhkin, K. Amemiya, T. Uchihashi, S. Yokoyama, T. Kamikado, S. Mashiko, and T. Okamoto. Tunneling electron induced luminescence from monolayered Cu-TBP porphyrin molecules adsorbed on Cu(100). *Thin Solid Films*, 438(0):262–267, 2003.

[264] Z. C. Dong, A. S. Trifonov, X. L. Guo, K. Amemiya, S. Yokoyama, T. Kamikado, T. Yamada, S. Mashiko, and T. Okamoto. Tunneling electron induced photon emission from monolayered H_2TBP porphyrin molecules on Cu(100). *Surf. Sci.*, 532:237–243, 2003.

[265] X.L. Guo, Z.-C. Dong, A. S. Trifonov, S. Yokoyama, Mashiko S., and T. Okamoto. Light emission from organic molecules on metal substrates induced by tunneling currents. *Jpn. J. Appl. Phys.*, 42(11):6937–6940, 2003.

[266] X. L. Guo, Z. C. Dong, A. S. Trifonov, S. Mashiko, and T. Okamoto. Role of molecules in tunneling-current-induced photon emission from the surface of a perinone derivative molecular monolayer on Au(100). *Phys. Rev. B*, 68(11):113403, 2003.

[267] G. Hoffmann, L. Libioulle, and R. Berndt. Tunneling-induced luminescence from adsorbed organic molecules with submolecular lateral resolution. *Phys. Rev. B*, 65(21):212107, 2002.

[268] R. Berndt and J. K. Gimzewski. Photon emission in scanning tunneling microscopy: Interpretation of photon maps of metallic systems. *Phys. Rev. B*, 48(7):4746–4754, 1993.

[269] Y. Zhang, F. Geng, H. Y. Gao, Y. Liao, Z. C. Dong, and J. G. Hou. Enhancement and suppression effect of molecules on nanocavity plasmon emission excited by tunneling electrons. *Appl. Phys. Lett.*, 97(24):243101, 2010.

[270] J. Aizpurua, S. P. Apell, and R. Berndt. Role of tip shape in light emission from the scanning tunneling microscope. *Phys. Rev. B*, 62(3):2065, 2000.

[271] P. Johansson. Light emission from a scanning tunneling microscope: Fully retarded calculation. *Phys. Rev. B*, 58:10823–10834, 1998.

[272] K. Meguro, K. Sakamoto, R. Arafune, M. Satoh, and S. Ushioda. Origin of multiple peaks in the light emission spectra of a Au(111) surface induced by the scanning tunneling microscope. *Phys. Rev. B*, 65(16):165405, 2002.

[273] M. S. Mehata and N. Ohta. Photo- and field-induced charge-separation and phosphorescence quenching in organometallic complex Ir(ppy)$_3$. *Appl. Phys. Lett.*, 98:181910, 2011.

[274] F. Capasso and R. A. Kiehl. Resonant tunneling transistor with quantum well base and high-energy injection – a new negative differential resistance device. *J. Appl. Phys.*, 58(3):1366–1368, 1985.

[275] T. Hannappel, B. Burfeindt, W. Storck, and F. Willig. Measurement of ultrafast photoinduced electron transfer from chemically anchored Ru-dye molecules into empty electronic states in a colloidal anatase TiO$_2$ film. *J. Phys. Chem. B*, 101(35):6799–6802, 1997.

[276] A. Emboras, I. Goykhman, B. Desiatov, N. Mazurski, L. Stern, J. Shappir, and U. Levy. Nanoscale plasmonic memristor with optical readout functionality. *Nano Lett.*, 13(12):6151–6155, 2013.

[277] R. Froidevaux. Time-resolved STM measurements on organic molecules, 2014. Master thesis, Ecole Polytechnique Fédeéral de Lausanne.

[278] P. Bharadwaj, A. Bouhelier, and L. Novotny. Electrical excitation of surface plasmons. *Phys. Rev. Lett.*, 106(22):226802, 2011.

[279] T. Wang, E. Boer-Duchemin, Y. Zhang, G. Comtet, and G. Dujardin. Excitation of propagating surface plasmons with a scanning tunneling microscope. *Nanotechn.*, 22:175201, 2011.

[280] R. Marty, C. Girard, A. Arbouet, and G. C. des Francs. Near-field coupling of a point-like dipolar source with a thin metallic film: Implication for STM plasmon excitations. *Chem. Phys. Lett.*, 532(0):100–105, 2012.

[281] Z. Dong, H.-S. Chu, D. Zhu, W. Du, Y. A. Akimov, W. P. Goh, T. Wang, K. E. J. Goh, C. Troadec, C. A. Nijhuis, and J. K. W. Yang. Electrically-excited surface plasmon polaritons with directionality control. *ACS Phot.*, 2(3):385–391, 2015.

[282] W. Heinz, H.-J. Räder, and K. Müllen. Changing the size of a cavity via an electron-transfer: synthesis and reduction of 1,5,22,26-tetraoxa-[5,5]-(2,8)-dibenzo[a,e]cylooctatetraenophane. *Tetrah. Lett.*, 30(2):159–162, 1989.

[283] R. Rathore, P. Le Magueres, S. V. Lindeman, and J. K. Kochi. A redox-controlled molecular switch based on the reversible C–C bond formation in octamethoxytetraphenylene. *Angew. Chem. Int. Ed.*, 39(4):809–812, 2000.

[284] M. J. Marsella, R. J. Reid, S. Estassi, and L.-S. Wang. Tetra[2,3-thienylene]: A building block for single-molecule electromechanical actuators. *J. Am. Chem. Soc.*, 124(42):12507–12510, 2002.

[285] R. Shukla, K. Thakur, V. J. Chebny, S. A. Reid, and R. Rathore. Direct observation of electron-transfer-induced conformational transformation (molecular actuation) in a bichromophoric electron donor. *J. Phys. Chem. B*, 114(45):14592–14595, 2010.

[286] A. M. Berghuis and G. D. Brayer. Oxidation state-dependent conformational changes in cytochrome c. *J. Mol. Bio.*, 223(4):959–976, 1992.

[287] S. Boussaad and N.J. Tao. Kinetics of electron transfer-induced conformational changes in cytochrome c immobilized on electrodes studied with surface plasmon resonance. *J. Electroanal. Chem.*, 554–555(0):233–239, 2003.

[288] G. Rinke. *Electrospray ion beam deposition of complex non-volatile molecules.* PhD thesis, Ecole Polytechnique Fédeéral de Lausanne, 2013.

[289] G. Rinke, S. Rauschenbach, L. Harnau, A. Albarghash, M. Pauly, and K. Kern. Active conformation control of unfolded proteins by hyperthermal collision with a metal surface. *Nano Lett.*, 14(10):5609–5615, 2014.

Curriculum Vitae

Name:	Christoph Große
Date/	May 7, 1986,
place of:	Leinefelde, Germany
Nationality:	German

Apr 2011–Jul 2015 **Doctoral Studies**
Ecole Polytechnique Fédéral de Lausanne, Switzerland
Doctoral School in Physics
Research associate in the group of Prof. Klaus Kern at the Max
Planck Institute for Solid State Research, Stuttgart, Germany

Dec 2009–Dec 2010 **Diploma Thesis**
in the group of Prof. Rainer Waser at the Peter Grünberg
Institut (former Institute for Bio- and Nanosystems),
Forschungszentrum Jülich, Germany
"Rastertunnelmikroskopische Untersuchungen zum Adsorptions-
verhalten von N-heterocyclischen Carbenen und Tetrahydro-
furan auf Au(111)"

Oct 2005–Dec 2010 **Diploma Studies**
University of Kassel, Germany
Diploma in Nanostructure and Molecular Science
Research assistant in the group of Prof. Josef Salbeck

Aug 2008–Sep 2008 **Research Stay**
in the group of Prof. Stefan Tautz at the Peter Grünberg Institute
(former Institute for Bio- and Nanosystems), Forschungszentrum
Jülich, Germany

Aug 1998–Jun 2004 **Gymnasium (High School)**
Gottfried–Wilhelm–Leibniz–Gymnasium Leinefelde, Germany

Awards & Honors
Jun 2015   Nottingham Prize

Publications

- <u>C. Große</u>, P. Merino, K. Kuhnke, K. Kern STM-induced Luminescence of C_{60} Multilayers (in preparation)

- <u>C. Große</u>, O. Gunnarsson P. Merino, K. Kuhnke, K. Kern: Real-Space Mapping the Effect of Molecular Disorder on the Local Electronic Structure of Organic Semiconductors (in preparation)

- <u>C. Große</u>, R. Froidevaux, M. Etzkorn, K. Kuhnke, K. Kern: Following the Local Charge Carrier Dynamics in C_{60} Films (in preparation)

- P. Merino, <u>C. Große</u>, A. Roslawska, K. Kuhnke, K. Kern: Exciton dynamics of C_{60}-based single photon emitters (submitted)

- <u>C. Große</u>, A. Kabakchiev, T. Lutz, R. Froidevaux, F. Schramm, M. Ruben, M. Etzkorn, U. Schlickum, K. Kuhnke, and K. Kern: Dynamic Control of Plasmon Generation by an Individual Quantum System, *Nano Lett.* 14, 5693-5697 (2014).

- <u>C. Grosse</u>, M. Etzkorn, K. Kuhnke, S. Loth, and K. Kern: Quantitative mapping of fast voltage pulses in tunnel junctions by plasmonic luminescence, *Appl. Phys. Lett.* 103, 183108 (2013).

- T. Lutz, <u>C. Große</u>, C. Dette, A. Kabakchiev, F. Schramm, M. Ruben, K. Kuhnke, U. Schlickum, and K. Kern: Molecular Orbital Gates for Plasmon Emission, *Nano Lett.* 13, 2846-2850 (2013).

- T. Weidner, J. Baio, A. Mundstock, <u>C. Große</u>, S. Karthäuser, C. Bruhn and U. Siemeling: NHC-Based Self-Assembled Monolayers on Solid Gold Substrates, *Aust. J. Chem.* 64, 1177 (2011).